

Journal of
Mechanics of
Materials and Structures

Volume 3, N° 3

March 2008

 mathematical sciences publishers

JOURNAL OF MECHANICS OF MATERIALS AND STRUCTURES

<http://www.jomms.org>

EDITOR-IN-CHIEF Charles R. Steele
ASSOCIATE EDITOR Marie-Louise Steele
Division of Mechanics and Computation
Stanford University
Stanford, CA 94305
USA

BOARD OF EDITORS

D. BIGONI University of Trento, Italy
H. D. BUI École Polytechnique, France
J. P. CARTER University of Sydney, Australia
R. M. CHRISTENSEN Stanford University, U.S.A.
G. M. L. GLADWELL University of Waterloo, Canada
D. H. HODGES Georgia Institute of Technology, U.S.A.
J. HUTCHINSON Harvard University, U.S.A.
C. HWU National Cheng Kung University, R.O. China
IWONA JASIUŁ University of Illinois at Urbana-Champaign
B. L. KARIHALOO University of Wales, U.K.
Y. Y. KIM Seoul National University, Republic of Korea
Z. MROZ Academy of Science, Poland
D. PAMPLONA Universidade Católica do Rio de Janeiro, Brazil
M. B. RUBIN Technion, Haifa, Israel
Y. SHINDO Tohoku University, Japan
A. N. SHUPIKOV Ukrainian Academy of Sciences, Ukraine
T. TARNAI University Budapest, Hungary
F. Y. M. WAN University of California, Irvine, U.S.A.
P. WRIGGERS Universität Hannover, Germany
W. YANG Tsinghua University, P.R. China
F. ZIEGLER Technische Universität Wien, Austria

PRODUCTION


PAULO NEY DE SOUZA Production Manager
SHEILA NEWBERY Senior Production Editor
SILVIO LEVY Scientific Editor

See inside back cover or <http://www.jomms.org> for submission guidelines.

Regular subscription rate: \$500 a year.

Subscriptions, requests for back issues, and changes of address should be sent to Mathematical Sciences Publishers, 798 Evans Hall, Department of Mathematics, University of California, Berkeley, CA 94720-3840.

©Copyright 2008. Journal of Mechanics of Materials and Structures. All rights reserved.

 mathematical sciences publishers

AN EXTENDED MECHANICAL THRESHOLD STRESS PLASTICITY MODEL: MODELING 6061-T6 ALUMINUM ALLOY

BISWAJIT BANERJEE AND ANUP SATISH BHAWALKAR

The mechanical threshold stress plasticity model of Follansbee and Kocks was designed to predict the flow stress of metals and alloys in the regime where thermally activated mechanisms are dominant and high temperature diffusion effects are negligible. In this paper we present a model that extends the original mechanical threshold stress to the high strain-rate regime (strain rates higher than 10^4 s^{-1}) and attempts to allow for high temperature effects. We use a phonon drag model for moderate strain rates and an overdriven shock model for extremely high strain rates. A temperature dependent model for the evolution of dislocation density is also presented. In addition, we present a thermodynamically-based model for the evolution of temperature with plastic strain. Parameters for 6061-T6 aluminum alloy are determined and compared with experimental data. The strain-rate dependence of the flow stress of 6061-T6 aluminum is found to be in excellent agreement with experimental data. The amount of thermal softening is underestimated at high temperatures (greater than 500 K) but still is an improvement over the original model. We also find that the pressure dependence of the shear modulus does not completely explain the pressure dependence of the flow stress of 6061-T6 aluminum alloy.

1. Introduction

With the advent of powerful computational machines and algorithms, it is now possible to simulate processes such as the accidental impact of vehicles, high-speed machining, high- and hyper-velocity impact and penetration, and explosive forming. These processes typically involve plastic deformations at high strain rates (10^2 s^{-1} to 10^9 s^{-1}) and often temperatures greater than $0.6 T_m$ (T_m is the melting temperature of the material). Adiabatic shear banding often accompanies the process and provides zones where fractures nucleate. A crucial component in the numerical modeling of plastic deformations under these conditions is a model that describes the evolution of the flow stress under a large range of strain-rates and temperatures.

The mechanical threshold stress (MTS) flow stress model [Follansbee and Kocks 1988; Goto et al. 2000; Kocks 2001] was originally developed with two assumptions:

- (1) Thermally activated dislocation motion was dominant and viscous drag effects on dislocation motion were small. This assumption essentially restricts the model to strain rates of 10^4 s^{-1} and less.
- (2) High temperature diffusion effects (such as solute diffusion from inside the grains to grain boundaries) were absent. This assumption limits the range of applicability of the model to temperatures

Keywords: mechanical threshold stress model, 6061-T6 aluminum, high strain rate, high temperature, high pressure.

Funded by the U.S. Department of Energy through the Center for the Simulation of Accidental Fires and Explosions, under grant W-7405-ENG-48.

less than around $0.6 T_m$ (depending on the material). For 6061-T6 aluminum alloy this temperature is approximately 450–500 K.

The aluminum alloy 6061 is composed of 97.5% aluminum, 1.0% magnesium, 0.6% silicon, 0.34% iron, 0.3% copper, 0.2% chromium, and around 0.04% zinc and titanium by weight. The T6 hardening treatment varies by manufacturer but usually involves a solution treatment at 810 K followed by quenching in water and then aging for a few hours at around 450 K. The solution treatment leads to a homogeneous supersaturated solid solution. The quenching step is performed to take the supersaturated solution to a two-phase region of the phase diagram. In the aging step, the magnesium silicide (Mg_2Si) phase is precipitated in such a way that the precipitate is evenly distributed inside the grains. There is also some precipitation of $AlFeSi$ at the grain boundaries. The precipitates inside the grains impede dislocation motion and make the alloy harder. The lightness, strength, weldability, and corrosion resistance of the 6061-T6 alloy makes it ideal for heavy duty structures in marine applications (among other uses). However, at about 550 K, the alloying Mg_2Si precipitates start to diffuse toward the grain boundaries and accumulate at the grain boundaries. As a result, 6061-T6 aluminum softens considerably at high temperatures. More details about the processes involved can be found in [Epler 2002].

Simulations of high velocity sphere-cylinder impact experiments using a MTS model for an aluminum alloy containing 1% magnesium [Puchi-Cabrera et al. 2001] showed that the model underestimated the flow stress at strain rates greater than $10^5 s^{-1}$. Also, high temperature Taylor impact simulations using the same model showed that the flow stress was significantly overestimated for temperatures greater than 450 K [Banerjee 2005b].

In this paper, we extend the MTS model so that it can be used for strain rates greater than $10^4 s^{-1}$ and for temperatures greater than 450 K. To extend the model to the regime of high strain rates, we incorporate a model for viscous drag controlled dislocation motion (which becomes dominant at strain rates greater than $10^4 s^{-1}$). In addition, we incorporate a model for the overdriven shock regime (strain-rates greater than $10^9 s^{-1}$). To account for the effect of thermally assisted diffusion of solutes, we incorporate an empirical modification of the original model for thermally activated mechanisms.

The evolution of temperature with plastic strain can be quite important in some situations (such as the development of adiabatic shear bands). We derive an expression for the Taylor–Quinney coefficient from thermodynamic principles and postulate a temperature dependent model for the evolution of this quantity.

The parameters of the extended MTS model are then fit using experimental stress-strain data for 6061-T6 aluminum from the literature wherever available. The flow stress estimated from the model is then compared with experimental data. Next, predictions of the model for a range of strain rates, temperatures, and levels of plastic strain are discussed. Finally, some concluding remarks are given and potential areas of future work are discussed.

2. The extended mechanical threshold stress model

The original mechanical threshold stress (MTS) model [Follansbee and Kocks 1988; Goto et al. 2000] for the flow stress (σ_y) can be written as

$$\sigma_y(\sigma_e, \dot{\epsilon}, p, T) = [\tau_a + \tau_i(\dot{\epsilon}, T) + \tau_e(\sigma_e, \dot{\epsilon}, T)] \frac{\mu(p, T)}{\mu_0}, \quad (1)$$

where σ_e is an evolving internal variable that has units of stress (also called the mechanical threshold stress), $\dot{\epsilon}$ is the strain rate, p is the pressure, T is the temperature, τ_a is the athermal component of the flow stress, τ_i is the intrinsic component of the flow stress due to barriers to thermally activated dislocation motion, τ_e is the component of the flow stress due to structure evolution (that is, strain hardening), μ is the shear modulus, and μ_0 is a reference shear modulus at 0 K and ambient pressure.

2.1. Athermal component. The athermal component of the yield stress is a function of grain size, dislocation density, distribution of solute atoms, and other long range barriers to dislocation motion. This component may either be constant or may evolve with deformation. A simple model for this component can be written as [Zerilli and Armstrong 1987; Banerjee 2007]:

$$\tau_a = \tau_0 + \frac{k}{\sqrt{d}}, \quad (2)$$

where τ_0 is the component due to far field dislocation interactions and the second term represents contribution due to the Hall–Petch effect where k is a material constant and d is the grain size.

2.2. Intrinsic component. In the MTS model, the intrinsic component of the flow stress is assumed to be dependent only on thermally activated mechanisms in the absence of solute diffusion. This component can be expressed in the phenomenological Arrhenius form given below (see [Kocks et al. 1975, Section 44], for an explanation)

$$\tau_i = S_i \sigma_i, \quad S_i := \left[1 - \left(\frac{k_b T}{g_{0i} b^3 \mu(p, T)} \ln \frac{\dot{\epsilon}_{0i}}{\dot{\epsilon}} \right)^{1/q_i} \right]^{1/p_i}, \quad (3)$$

where σ_i is the intrinsic component of the mechanical threshold stress (flow stress at 0 K), k_b is the Boltzmann constant, b is the magnitude of Burgers vector, g_{0i} is a normalized activation energy, $\dot{\epsilon}_{0i}$ is a constant reference strain rate, and p_i, q_i are constants. The constant p_i can take values between 0 and 1, while q_i can take values between 1 and 2.

In order to fit the high temperature data for 6061-T6 aluminum better, we have found that a better relation for τ_i has the form

$$\tau_i = \sigma_i \left[1 - \left\{ \left(\frac{k_b T}{g_{0i} b^3 \mu(p, T)} \ln \frac{\dot{\epsilon}_{0i}}{\dot{\epsilon}} \right)^{1/q_i} \right\}^2 \right]^{1/p_i}. \quad (4)$$

This relation is equivalent to using values of q_i between 0.5 and 1. If we use such a value in the original MTS model, the value of τ_i tends to become constant as the strain rate is increased. Recall that the original MTS model does not account for the effect of viscous drag at high strain rates, and the model predicts only a small increase in the flow stress with strain rate if q_i is between 1 and 2. The small reduction in the flow stress at high strain rates due to a value of q_i between 0.5 and 1 is easily offset by incorporating a simple model for viscous drag into the MTS model.

2.3. Viscous drag component. To incorporate viscous drag effects due to phonon damping, forest dislocations, and solute atoms, we add a term to the equation for τ_i of the form [Kumar and Kumble 1969;

Frost and Ashby 1971]

$$\tau_v = \frac{2}{\sqrt{3}} \frac{B}{\rho_m b^2} \dot{\epsilon}, \quad (5)$$

where B is the drag coefficient, ρ_m is the mobile dislocation density, and b is the magnitude of the Burgers vector. We assume that a good estimate of the value of the drag coefficient can be obtained if we consider only damping due to phonon scattering [Wolfer 1999]. However, at low temperatures (< 50 K), electron damping can dominate and a model for that should be used in addition to phonon damping (for more details see [Nadgorny 1988] p. 251–260).

The viscous drag coefficient can be written as [Kanel et al. 2001]

$$B \approx \lambda_p B_p = \frac{\lambda_p k_b T \omega_D^2}{\pi^2 \bar{c}^3}, \quad (6)$$

where B_p is the phonon drag coefficient, $\lambda_p \geq 1$ is a correction factor, ω_D is the Debye frequency and \bar{c} is the average sound speed. The Debye frequency is given by

$$\omega_D = \frac{2\pi k_b \theta_D}{h} = 2\pi \bar{c} \left(\frac{3\rho}{4\pi M} \right)^{1/3} = \left(\frac{6\pi^2 \rho}{M} \right)^{1/3} \bar{c}, \quad (7)$$

where θ_D is the Debye temperature, h is Planck's constant, and M is the atomic mass. The average sound speed is defined as

$$\frac{1}{\bar{c}^3} = \frac{1}{3} \left(\frac{2}{c_s^3} + \frac{1}{c_l^3} \right), \quad c_s = \sqrt{\frac{\mu}{\rho}}, \quad c_l = \sqrt{\frac{2\mu(1-\nu)}{\rho(1-2\nu)}}, \quad (8)$$

where c_s is the transverse sound speed, c_l is the longitudinal sound speed, and ν is the Poisson's ratio. Assuming that the Poisson's ratio is $1/3$, we can get an approximation for \bar{c} in terms of the shear sound speed as

$$\bar{c} \approx \left(\frac{24}{17} \right)^{1/3} c_s. \quad (9)$$

Alternatively, we can use Liebfried's model [Kumar and Kumble 1969; Brailsford 1970; Brailsford 1972; Wolfer 1999] for scattering of phonons by dislocations

$$B \approx \lambda_p B_p = \frac{\lambda_p q}{10c_s} \langle E \rangle, \quad (10)$$

where λ_p is a correction factor, q is the cross-section of the dislocation core per unit length and $\langle E \rangle$ is the average internal energy density. From Debye theory, we have

$$\langle E \rangle = \frac{3k_b T \rho}{M} D_3 \left(\frac{\theta_D}{T} \right), \quad \theta_D = \frac{h \bar{c}}{k_b} \left(\frac{3\rho}{4\pi M} \right)^{1/3}, \quad (11)$$

where the Debye function D_3 is defined as

$$D_3(x) := \frac{3}{x^3} \int_0^x \frac{z^3}{\exp(z) - 1} dz. \quad (12)$$

Note that the component of the flow stress due to viscous drag is both temperature and pressure dependent. A closed form expression can be obtained for the Debye integral in terms of polylogarithms (see for example [Truesdell 1945]). However, there is a singularity at $z = 0$ and analytic continuation methods are needed to evaluate the polylogarithms for values of $z > 0$. Alternatively, expansions in terms of Chebyshev polynomials [Ng et al. 1969; MacLeod 1996] may be used. For computational purposes, a look-up table of values (for example [Stegun 1972]) is the most efficient.

The second variable that is needed to compute τ_v is the density of mobile dislocations (ρ_m). The density of mobile dislocations depends on the prior strain history of a material and also on the strain, the temperature, and the strain rate. A simple model for the evolution of mobile dislocations as a function of plastic strain can be written as [Estrin and Kubin 1986; Barlat et al. 2002]

$$\begin{aligned} \frac{d\rho_m}{d\varepsilon_p} &= \frac{M_1}{b^2} \left(\frac{\rho_f}{\rho_m} \right) - I_2(\dot{\varepsilon}, T)\rho_m - \frac{I_3}{b}\sqrt{\rho_f}, \\ \frac{d\rho_f}{d\varepsilon_p} &= I_2(\dot{\varepsilon}, T)\rho_m + \frac{I_3}{b}\sqrt{\rho_f} - A_4(\dot{\varepsilon}, T)\rho_f, \end{aligned} \quad (13)$$

where ρ_f is the density of forest dislocations, b is the magnitude of the Burgers' vector, M_1 is a rate of mobilization of dislocations, I_2 is a rate of immobilization of mobile dislocations due to interactions between mobile dislocations, I_3 is another immobilization rate due to interactions with forest dislocations, and A_4 is the rate of annihilation of forest dislocations due to climb, cross-slip, or diffusion.

To solve the system of differential equations, Equation (13), we need initial values of ρ_m and ρ_f . We may also assume that the density of forest dislocations saturates at a value of ρ_{fs} , that is, $d\rho_f/d\varepsilon_p = 0$ at $\rho_f = \rho_{fs}$. Since the density of forest dislocations is easier to measure than the rate of annihilation A_4 , we use ρ_{fs} to obtain the following expression for A_4 :

$$A_4(\dot{\varepsilon}, T) = I_2(\dot{\varepsilon}, T) \frac{\rho_m}{\rho_{fs}} + \frac{I_3}{b} \frac{1}{\sqrt{\rho_{fs}}}. \quad (14)$$

The rate I_2 and the saturation value ρ_{fs} are, in general, temperature and strain-rate dependent. We assume that the strain rate dependence of these quantities is negligible for aluminum alloys and only consider temperature dependence. Based on the experimental observation that the temperature dependence of the flow stress of aluminum alloys follows a sigmoidal curve [Rosenberg et al. 1986], we assume that I_2 and ρ_{fs} have the following temperature dependence:

$$I_2(T) = I_{20} \left(\frac{\alpha_I}{1 + \exp[-\beta_I(1 - 2\hat{T})]} \right), \quad \rho_{fs}(T) = \rho_{fs0} \left(1 - \frac{\alpha_f}{1 + \exp[\beta_f(1 - 2\hat{T})]} \right), \quad (15)$$

where I_{20} is the value of I_2 at 0 K, ρ_{fs0} is the value of ρ_{fs} at 0 K, $\hat{T} = T/T_m$ where T_m is the melting temperature, α_I, α_f are scaling factors, and β_I, β_f are constants that have values greater than 3.

2.4. Structure evolution component. The evolution of dislocation density could be used to determine the component of the flow stress that depends on the evolution of the structure of a material (see for instance [Barlat et al. 2002]). However, Equations (13) form a stiff system of differential equations and are not ideal for numerical simulations, particularly explicit calculations needed for high rate processes.

Instead, we use the approach originally suggested by [Follansbee and Kocks \[1988\]](#) and describe the component of the flow stress due to structure evolution by

$$\tau_e(\sigma_e, \dot{\varepsilon}, T) = S_e \sigma_e, \quad S_e := \left[1 - \left(\frac{k_b T}{g_{0e} b^3 \mu(p, T)} \ln \frac{\dot{\varepsilon}_{0e}}{\dot{\varepsilon}} \right)^{1/q_e} \right]^{1/p_e}, \quad (16)$$

where σ_e is an internal variable (the structure evolution component of the mechanical threshold stress) that evolves with the deformation, g_{0e} is a normalized activation energy, $\dot{\varepsilon}_{0e}$ is a reference strain rate, and p_e, q_e are constants.

The evolution of σ_e is assumed to be governed by the modified Voce rule

$$\frac{d\sigma_e}{d\varepsilon_p} = \theta_0 \left[1 - \left(\frac{\sigma_e}{\sigma_{es}} \right)^2 \right], \quad (17)$$

where θ_0 is the initial hardening modulus and σ_{es} is the saturation value of σ_e . This equation can be solved in closed form along a constant temperature and strain-rate path to get

$$\sigma_e(\varepsilon_p) = \sigma_{es} \left[\frac{A_\sigma \exp(\beta) + 1}{A_\sigma \exp(\beta) - 1} \right] \quad A_\sigma := \frac{\sigma_{ei} + \sigma_{es}}{\sigma_{ei} - \sigma_{es}}, \quad \beta := \frac{2\theta_0 \varepsilon_p}{\sigma_{es}}, \quad (18)$$

where σ_{ei} is the value of σ_e at zero plastic strain and can be nonzero depending on the prior strain history of the material. For the special case where σ_{ei} is zero, we have

$$\sigma_e(\varepsilon_p) = \sigma_{es} \left[\frac{\exp(\beta) - 1}{\exp(\beta) + 1} \right]. \quad (19)$$

The initial hardening modulus is assumed to be given by a relation of the form

$$\theta_0 = \mu(p, T) \left[a_0 + a_1 \ln \left(\frac{\dot{\varepsilon}_\theta}{\dot{\varepsilon}} \right) + a_2 \widehat{T} + a_3 \widehat{T} \ln \left(\frac{\dot{\varepsilon}_\theta}{\dot{\varepsilon}} \right) \right], \quad (20)$$

where a_0, a_1, a_2, a_3 are constants and $\dot{\varepsilon}_\theta$ is a reference strain rate, and $\widehat{T} = T/T_m$ where T_m is the melting temperature. The value of θ_0 is not allowed to be negative.

The saturation value of structure evolution stress is computed using an Arrhenius type relation of the form

$$\ln \left(\frac{\sigma_{es}}{\sigma_{0es}} \right) = \left(\frac{k_b T}{g_{0es} b^3 \mu(\rho, T)} \right) \ln \left(\frac{\dot{\varepsilon}}{\dot{\varepsilon}_{0es}} \right), \quad (21)$$

where σ_{0es} is the saturation threshold stress for deformation at 0 K, g_{0es} is a normalized activation energy, and $\dot{\varepsilon}_{0es}$ is a reference strain rate.

2.5. Overdriven shock regime. At strain-rates between 10^9 s^{-1} and 10^{12} s^{-1} , the plastic wave overruns the elastic precursor and produces a steeper shock front than is attainable due to adiabatic elastic compression. Such a shock is called *overdriven*. In order to allow for overdriven shocks in our model, we

follow the approach used in the Preston–Tonks–Wallace model [Preston et al. 2003]. The flow stress under overdriven shock conditions (and assuming J_2 plasticity) is given by

$$\sigma_{ys} = \sigma_{ys0} + y_1 \left(\frac{\dot{\epsilon}}{\gamma \dot{\xi}} \right)^{y_2} \mu(p, T), \quad (22)$$

where σ_{ys0} is a lower limit on the flow stress, y_1 , y_2 are material parameters, γ is a scaling factor, and $\dot{\xi}$ is a reference strain rate. The reference strain rate is defined as

$$\dot{\xi} := \frac{1}{2} \left(\frac{4\pi\rho}{3M} \right)^{1/3} c_s, \quad (23)$$

where M is the atomic mass and c_s is transverse sound speed. We assume that there is no hardening in the overdriven shock regime.

2.6. Behavior after melting. After the temperature crosses the melting temperature (T_m), we have to model the material as a liquid. Though, strictly speaking, the behavior of an aluminum alloy melt is nonNewtonian, we use a Newtonian model of the following form to determine the deviatoric stress in the material after it has melted:

$$\sigma_y = \mu_v \dot{\epsilon}, \quad (24)$$

where μ_v is the shear viscosity of the melt. The shear viscosity of aluminum alloys can be estimated by first computing the viscosities of the constituent elements using the Andrade equation [da Andrade 1934; 1952] (alternative approaches can be found in [Kirkwood et al. 1949] and [Dinsdale and Quested 2004]). The viscosity of the alloy can then be calculated using the Moelwyn–Hughes model for binary alloys [Moelwyn-Hughes 1961; Dinsdale and Quested 2004]. However, since we are not interested in the details of the motion of the melt, we simplify our model by using a constant value of $\mu_v = 2.0 \times 10^{-4} \text{Pa} \cdot \text{s}$ in our calculations.

2.7. The extended flow stress model. The final expression for the flow stress is

$$\sigma_y = \begin{cases} \min \left\{ \left[\tau_v + (\tau_a + \tau_i + \tau_e) \frac{\mu}{\mu_0} \right], \sigma_{ys} \right\}, & \text{for } T < T_m, \\ \mu_v \dot{\epsilon}, & \text{for } T \geq T_m. \end{cases} \quad (25)$$

2.8. Shear modulus, melting temperature, EOS, specific heat. To complete the model, we need an expression for the shear modulus as a function of temperature and pressure. We have used a modified form of the Nadal–LePoac model [Nadal and Le Poac 2003] in which the pressure dependence of the shear modulus is determined by the generalized Guinan–Steinberg formula [Burakovsky and Preston 2005; Guinan and Steinberg 1975]:

$$\mu(p, T) = \frac{1}{\mathcal{F}(\widehat{T}, \zeta)} \left[\left\{ \mu_0 + p \frac{\partial \mu}{\partial p} \left(\frac{a_1}{\eta^{1/3}} + \frac{a_2}{\eta^{2/3}} + \frac{a_3}{\eta} \right) \right\} (1 - \widehat{T}) + \frac{\rho}{CM} k_b T \right], \quad (26)$$

$$\eta := \frac{\rho}{\rho_0}, \quad C := \frac{(6\pi^2)^{2/3}}{3} f^2,$$

where \mathcal{F} is a scaling factor that allows for a smooth transition of the shear modulus to melt, $\widehat{T} := T/T_m$, T_m is the melting temperature, ζ is a material parameter, μ_0 is the shear modulus at 0 K and ambient pressure, $\partial\mu/\partial p$ is the slope of the shear modulus versus pressure curve at 0 K, a_1, a_2, a_3 are material constants, ρ_0 is the mass density in the initial state, M is the atomic mass, f is the Lindemann constant, and

$$\mathcal{F}(\widehat{T}, \zeta) := 1 + \exp \left[-\frac{1 + 1/\zeta}{1 + \zeta/(1 - \widehat{T})} \right] \quad \text{for } \widehat{T} \in [0, 1 + \zeta]. \quad (27)$$

For situations where $\rho/\rho_0 < 0.95$ (high hydrostatic tension), we set the shear modulus to the value obtained for $\rho/\rho_0 = 0.95$.

We use the Burakovsky–Greeff–Preston (BGP) model [Burakovsky et al. 2003] to determine the melting temperature. This model improves upon the widely used Steinberg–Cochran–Guinan model [Steinberg et al. 1980] which is also based on the Lindemann criterion. In the BGP model, the Grüneisen gamma is modeled as

$$\Gamma(\rho) = \frac{1}{2} + \frac{\Gamma_1}{\rho^{1/3}} + \frac{\Gamma_2}{\rho^q}, \quad (28)$$

where Γ_1, Γ_2, q are material constants and $q > 1$. This form of $\Gamma(\rho)$ leads to the following expression for the melting temperature as a function of density:

$$T_m(\rho) = T_{m0}\eta^{1/3} \exp \left\{ 6\Gamma_1 \left(\frac{1}{\rho_0^{1/3}} - \frac{1}{\rho^{1/3}} \right) + \frac{2\Gamma_2}{q} \left(\frac{1}{\rho_0^q} - \frac{1}{\rho^q} \right) \right\}, \quad \eta := \frac{\rho}{\rho_0}, \quad (29)$$

where T_{m0} is the melt temperature when $\rho = \rho_0$.

The pressure is calculated using the Holzapfel equation of state [Holzapfel 1991a; 1991b; Burakovsky and Preston 2005] which has the form

$$p(\rho) = 3B_0 [\eta^{5/3} - \eta^{4/3}] \exp \left\{ 1.5(B'_0 - 3) [1 - \eta^{-1/3}] \right\}, \quad \eta := \frac{\rho}{\rho_0}, \quad (30)$$

where B_0 is the bulk modulus at $p = 0$ and B'_0 is the slope of the pressure-density curve at $p = 0$.

We use an empirical temperature-dependent specific heat model and ignore the difference between the values of specific heat at constant pressure and at constant volume. The specific heat model is of the form [Bhawalkar 2006]

$$C_v = \begin{cases} A_1 + B_1 T + C_1 T^2, & \text{for } T < 273 \text{ K}, \\ A_2 + B_2 T, & \text{for } T \geq 273 \text{ K}, \end{cases} \quad (31)$$

where A_1, A_2, B_1, B_2, C_1 are constants.

3. Evolution of temperature due to plastic dissipation

To determine the increase in temperature due to plastic dissipation, we first assume that the deformation gradient (\mathbf{F}) can be split multiplicatively into elastic and plastic parts ($\mathbf{F} = \mathbf{F}_e \cdot \mathbf{F}_p$). We also assume that there is no volume change during the plastic part of the deformation.

The elastic strain measure (\mathbf{E}_e) (with respect to the intermediate configuration) and the plastic strain rate (\mathbf{d}_p) are defined as (see [Wright 2002] for details)

$$\mathbf{E}_e := \frac{1}{2}[\mathbf{F}_e^T \cdot \mathbf{F}_e - \mathbf{1}], \quad (32)$$

$$\mathbf{d}_p := \frac{1}{2}[\mathbf{F}_e \cdot \dot{\mathbf{F}}_p \cdot \mathbf{F}_p^{-1} \cdot \mathbf{F}_e^{-1} + \mathbf{F}_e^{-T} \cdot \mathbf{F}_p^{-T} \cdot \dot{\mathbf{F}}_p^T \cdot \mathbf{F}_e^T]. \quad (33)$$

The stress measure in the intermediate configuration (that is, work conjugate to \mathbf{E}_e) is given by the pull-back of the Cauchy stress by the elastic part of the deformation gradient:

$$\tilde{\mathbf{S}} = \frac{\rho_0}{\rho} \mathbf{F}_e^{-1} \cdot \boldsymbol{\sigma} \cdot \mathbf{F}_e^{-T}. \quad (34)$$

Then the balance of energy can be expressed as

$$\rho T \dot{\eta} = -\nabla \cdot \mathbf{q} + \rho r + \boldsymbol{\sigma} : \mathbf{d}_p - \frac{\rho}{\rho_0} \sum_{n=1}^N Q_n \dot{q}_n, \quad (35)$$

where η is the entropy density, $\nabla \cdot (\bullet)$ denotes the divergence (with respect to the current configuration), r is a internal heat source term, $\boldsymbol{\sigma}$ is the Cauchy stress, and q_n is a set of internal variables. The quantities Q_n are work conjugate to the internal variables q_n and are defined as

$$Q_n := -\rho_0 \frac{\partial g}{\partial q_n}, \quad \text{for } n = 1 \dots N, \quad (36)$$

where $g(\tilde{\mathbf{S}}, T, q_n)$ is the specific Gibbs free energy (per unit mass) and ρ_0 is the density in the intermediate configuration (here assumed to be the same as that in the reference configuration).

The internal variable in the MTS model is σ_e , that is

$$q_1 = \sigma_e, \quad Q_1 = -\rho_0 \frac{\partial g}{\partial \sigma_e}. \quad (37)$$

Under adiabatic conditions which occur for high strain-rate deformations, the heat flux and internal heat sources can be neglected. In that case, the energy equation takes the form

$$\rho T \dot{\eta} = \boldsymbol{\sigma} : \mathbf{d}_p + \rho \frac{\partial g}{\partial \sigma_e} \dot{\sigma}_e. \quad (38)$$

Assuming that the entropy can be derived from the specific Gibbs free energy, it can be shown, after some algebra, that [Wright 2002]

$$\dot{\eta} = \frac{\partial \eta}{\partial \tilde{\mathbf{S}}} : \dot{\tilde{\mathbf{S}}} + \frac{\partial \eta}{\partial T} \dot{T} + \frac{\partial \eta}{\partial \sigma_e} \dot{\sigma}_e = \frac{1}{\rho_0} \frac{\partial \mathbf{E}_e}{\partial T} : \dot{\tilde{\mathbf{S}}} + \frac{C_v}{T} \dot{T} - \frac{1}{\rho_0} \frac{\partial \tilde{\mathbf{S}}}{\partial T} : \dot{\mathbf{E}}_e + \frac{\partial}{\partial T} \left(\frac{\partial g}{\partial \sigma_e} \right) \dot{\sigma}_e. \quad (39)$$

Substitution into the energy equation yields

$$\rho C_v \dot{T} = \boldsymbol{\sigma} : \mathbf{d}_p + \rho \left[\frac{\partial g}{\partial \sigma_e} - T \frac{\partial}{\partial T} \left(\frac{\partial g}{\partial \sigma_e} \right) \right] \dot{\sigma}_e. \quad (40)$$

It is conventional to use a factor χ (called the Taylor–Quinney coefficient) to relate the rate of change of temperature to the plastic work $\mathcal{P}_p := \boldsymbol{\sigma} : \mathbf{d}_p$ using the relation

$$\dot{T} = \frac{\chi \boldsymbol{\sigma} : \mathbf{d}_p}{\rho C_v}. \quad (41)$$

Therefore, from Equation (40), we observe that

$$\chi = 1 - \left[T \frac{\partial}{\partial T} \left(\frac{\partial g}{\partial \sigma_e} \right) - \frac{\partial g}{\partial \sigma_e} \right] \left(\frac{\rho \dot{\sigma}_e}{\boldsymbol{\sigma} : \mathbf{d}_p} \right). \quad (42)$$

Clearly χ evolves with σ_e and T , and cannot be assumed to be around 0.9 as is usually the case. However, the functional form of the Gibbs free energy function is not obvious and we have to make certain assumptions to obtain a function that matches experimental observations (see for instance [Hodowany et al. 2000]).

If we make the assumption that $\boldsymbol{\sigma} : \mathbf{d}_p \approx \sigma_y \dot{\varepsilon}_p$, the expression in Equation (42) reduces to

$$\chi = 1 - \left[T \frac{\partial}{\partial T} \left(\frac{\partial g}{\partial \sigma_e} \right) - \frac{\partial g}{\partial \sigma_e} \right] \left(\frac{\rho}{\sigma_y} \right) \frac{d\sigma_e}{d\varepsilon_p}.$$

Replacing the derivative of σ_e with Equation (17), we get

$$\chi = 1 - \left[T \frac{\partial}{\partial T} \left(\frac{\partial g}{\partial \sigma_e} \right) - \frac{\partial g}{\partial \sigma_e} \right] \left(\frac{\rho \theta_0}{\sigma_y} \right) \left[1 - \left(\frac{\sigma_e}{\sigma_{es}} \right)^2 \right]. \quad (43)$$

To model the specific Gibbs free energy $g(\tilde{\mathcal{S}}, T, \sigma_e)$, we follow the approach of Schreyer and Maudlin [2005] in postulating the following form for the expression involving the derivatives of g (which can be interpreted as a measure of the stored energy of cold work):

$$T \frac{\partial}{\partial T} \left(\frac{\partial g}{\partial \sigma_e} \right) - \frac{\partial g}{\partial \sigma_e} = F_1(T) F_2(\sigma_e), \quad (44)$$

where

$$F_1(T) = \frac{A_\chi}{1 + \exp[-B_\chi(1 - 2\hat{T})]}, \quad F_2(\sigma_e) = \frac{1}{\rho_0} \left(\beta_\chi + \frac{\sigma_e}{\sigma_{es}} \right)^{1/2}, \quad (45)$$

where $A_\chi > 1$, $B_\chi > 1$ are constants, $\hat{T} = T/T_m$, where T_m is the melting temperature, and $0 < \beta_\chi < 1$ is a factor that determines the value of χ at zero plastic strain. We can now calculate the rise in temperature due to plastic dissipation and use that to determine the amount of thermal softening due to plastic deformation. Note that a closed form expression for g that can be evaluated analytically cannot be derived from Equation (44) and further investigation into possible forms of g is needed.

4. Parameter estimation for 6061-T6 aluminum

Before the parameters of the extended MTS model for 6061-T6 aluminum can be estimated, we need the parameters of the shear modulus model. We also need the parameters of the associated melting

temperature model, the equation of state model, and the specific heat model. A detailed exploration of various models, their parameters, and comparisons with experimental data can be found in [Bhawalkar 2006]. The parameters of the models described by Equations (26), (27), (29), (30), and (31) are given in Appendix A, where we also show comparisons with experimental data of the predicted shear modulus, melting temperature, and specific heat.

4.1. Athermal component. In the ASM Handbook on nonferrous alloys [ASM 2002] we find that, for quasistatic tensile loading, at 644 K the yield strength of 6061-T6 aluminum is 12 MPa. The ratio μ/μ_0 for this temperature is 0.65. Hence, the maximum possible value of τ_a at 644 K is 18 MPa. Since this component is athermal, that value must be an upper bound on τ_a . It is possible that the upper bound on τ_a is even lower since the melting temperature of aluminum at ambient pressure is around 933 K. Therefore, it is reasonable to assume that $\tau_a \approx 10$ MPa for 6061-T6 aluminum.

4.2. Intrinsic component. To compute the intrinsic component of the flow stress (τ_i), we have to determine the parameters σ_{0i} and g_{0i} for a particular choice of $\dot{\epsilon}_{0i}$, p_i , and q_i (see Equation (4)). From (25) we see that in the low to moderate strain rate regime, the flow stress at zero plastic strain can be written as

$$\sigma_y = \tau_v + (\tau_a + \tau_i) \frac{\mu}{\mu_0}. \quad (46)$$

To determine τ_i , we need the viscous drag component τ_v and the experimentally determined initial yield stress σ_y . Recent studies [Ogawa 2001; Sakino 2006] show that for strain rates less than 10^4 s^{-1} , the viscous drag component τ_v for 6061-T6 aluminum is small compared to the thermally activated component τ_i . Because the experimental stress-strain data to which have access are for strain rates ranging from 10^{-5} s^{-1} to $8.0 \times 10^3 \text{ s}^{-1}$, we neglect τ_v during the process of computation of σ_i and g_{0i} .

Then, from Equations (4) and (46), we have

$$\left(\frac{\sigma_y}{\mu} - \frac{\tau_a}{\mu_0} \right)^{p_i} = \left(\frac{\sigma_i}{\mu_0} \right)^{p_i} - \left(\frac{\sigma_i}{\mu_0} \right)^{p_i} \left(\frac{1}{g_{0i}} \right)^{2/q_i} \left(\frac{k_b T}{b^3 \mu} \ln \frac{\dot{\epsilon}_{0i}}{\dot{\epsilon}} \right)^{2/q_i},$$

which is of the form $y = A - Bx^2$. A Fisher plot of the experimental data and the model fit is shown in Figure 1. Details of the procedure used to obtain the experimental data and the sources of the data can be found in [Bhawalkar 2006]. The best fit to the experimental data is obtained for $p_i = 0.75$, $q_i = 1.0$, and $\dot{\epsilon}_{0i} = 5.0 \times 10^8 \text{ s}^{-1}$. The Boltzmann constant was taken to be $k_b = 1.38 \times 10^{-23} \text{ J/K}$ and the magnitude of the Burgers' vector was assumed to be $b = 2.86 \times 10^{-10} \text{ m}$ [Wang et al. 1998].

The fit shown in the figure has an R^2 value of 0.6, an F -statistic of 60.7 and Student's t -values of 6.0 and 35.3 for the two coefficients. There are 81 data points. Using a t -value of 1.663 (corresponding to the 95% interval), we get the following range of values for σ_i and g_{0i} :

$$\begin{aligned} \sigma_i \text{ (low)} &= 343.7 \text{ MPa}, & \sigma_i \text{ (fit)} &= 366.6 \text{ MPa}, & \sigma_i \text{ (high)} &= 389.8 \text{ MPa}, \\ g_{0i} \text{ (low)} &= 0.51, & g_{0i} \text{ (fit)} &= 0.59, & g_{0i} \text{ (high)} &= 0.71. \end{aligned}$$

4.3. Viscous drag component. The viscous drag component of the flow stress is given by Equation (5). Two quantities have to be determined before τ_v can be computed: the drag coefficient B and the mobile dislocation density ρ_m .

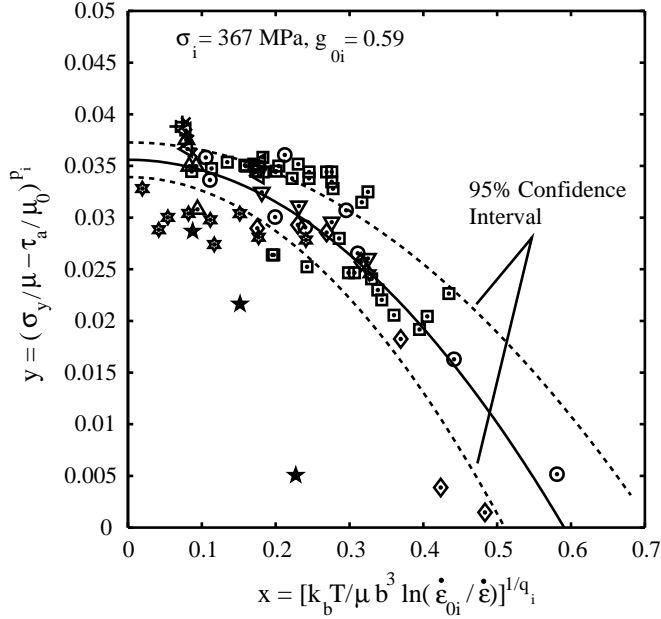


Figure 1. Fisher plot used to determine σ_i and g_{0i} for 6061-T6 aluminum alloy. The solid line shows the model fit to the data. The dotted lines show the range of the model for a confidence level of 95. The symbols represent experimental data. The sources of the experimental data are \circ [Hoge 1966]; \square [Green and Babcock 1966; Eleiche 1972]; ∇ [Davidson 1973]; \star [Rosenberg et al. 1986]; \triangle [Yadav et al. 1995]; \diamond [Brown et al. 1996]; \times [Lee et al. 2000]; $*$ [Ogawa 2001]; $<$ [Cady and Gray III 2001; Fish et al. 2005]; $+$ [Lesuer et al. 2001; Jia and Ramesh 2004].

The drag coefficient can be estimated using either (6) or (10). Figure 2 shows the phonon drag coefficients predicted by the two models. The constants used for the models are:

$$\begin{aligned}
 k_b &= 1.38 \times 10^{-23} \text{ J/K}, & b &= 2.86 \times 10^{-10} \text{ m}, \\
 M &= 26.98 \text{ amu}, & \rho_0 &= 2700 \text{ kg/m}^3, \\
 h &= 6.62 \times 10^{-34} \text{ kg} \cdot \text{m}^2/\text{s}, & q &= 3b.
 \end{aligned}$$

Values of the Debye function (D_3) were calculated using an algorithm given in [MacLeod 1996]. As the pressure increases there is a decrease in B_p . However, the change is small and does not significantly affect the value of τ_v . At temperatures below 50 K, electron drag effects become dominant. Note that this is not reflected by the model in Equation (10). However, since that model predicts a lower value of B_p at high temperatures, we have used (10) in subsequent calculations.

The evolution of dislocation density is harder to quantify. We have chosen parameters for Equation (13) in such a way that, at high strain rates, the viscous drag component of the flow stress approximates

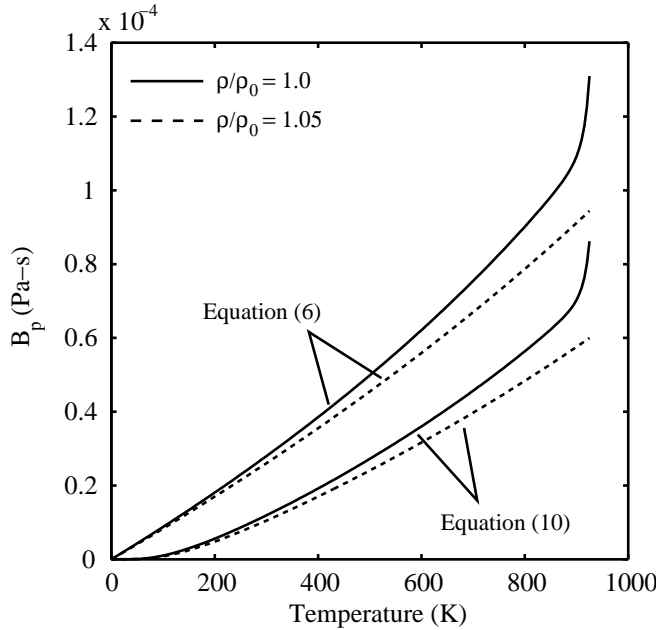


Figure 2. Phonon drag coefficient (B_p) as a function of temperature. The upper curve shows the prediction of the model in Equation (6) and the lower curve shows the values predicted by the model in (10).

experimentally determined yield stress at room temperature. The parameters used for the model are:

$$\begin{aligned}
 b &= 2.86 \text{ m}^{-2}, & M_1 &= 4.14 \times 10^{-7}, & I_{20} &= 5.53 \times 10^3, \\
 I_3 &= 3.81 \times 10^{-2}, & \alpha_I &= 1.0, & \beta_I &= 8.0, \\
 \rho_{f,s0} &= 1.0 \times 10^{14} \text{ m}^{-2}, & \alpha_f &= 0.4, & \beta_f &= 4.0.
 \end{aligned}$$

Using initial values of $\rho_m = 1.0 \times 10^9 \text{ m}^{-2}$ and $\rho_f = 1.0 \times 10^{10} \text{ m}^{-2}$, we get the evolution of the dislocation densities shown in Figure 3. A constant density of $2700 \text{ kg}\cdot\text{m}^{-3}$ has been used in the computation.

The saturation value of ρ_m is approximately $2 \times 10^{11} \text{ m}^{-2}$ at room temperature, which is three orders of magnitude lower than that suggested by Estrin and Kubin [1986]. However, higher values of ρ_m lead to unreasonably low values of the viscous drag component of the flow stress. Also, similar low values of ρ_m are suggested by Kumar and Kumble [1969]. Note that the value of ρ_f is close to the accepted value of total dislocation density in aluminum and its alloys, on the order of $1.0 \times 10^{14} \text{ m}^{-2}$. It can also be observed that the density of forest dislocations decreases with temperature while that of mobile dislocations increases with temperature. Also, our model indicates that the rate of annihilation of forest dislocations is greater than the rate of generation of mobile dislocations as the temperature increases (see Figure 3).

The viscous drag component (τ_v) of the flow stress can now be computed using (5). Figure 4 shows the variation of τ_v with strain rate and temperature (for a plastic strain of 0.2). We have used a value of $\lambda_p = 1$ in the calculations. From the figure it is clear that the viscous drag becomes significant only beyond strain rates of 10^5 s^{-1} . Also, drag effects appear to be negligible at low temperatures.

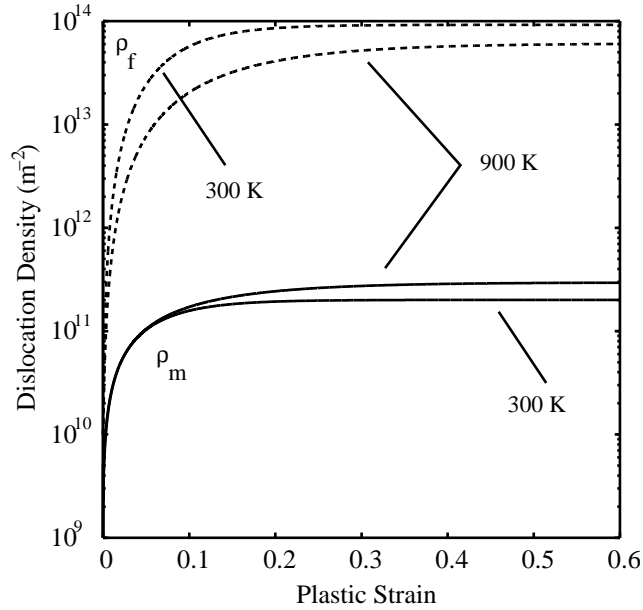


Figure 3. Evolution of dislocation density as a function of plastic strain and temperature. The solid curves show the evolution of ρ_m while the dotted curves show the evolution of ρ_f .

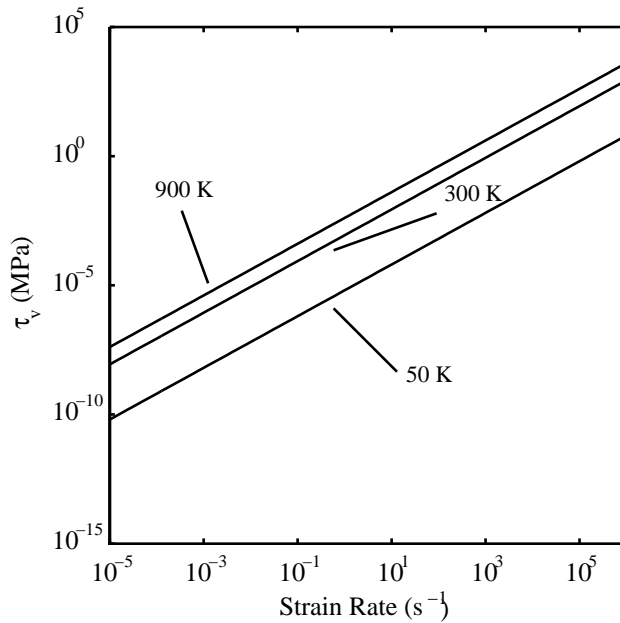


Figure 4. Variation of the viscous drag component of the flow stress of 6061-T6 aluminum with strain rate and temperature for a plastic strain of 0.2.

4.4. Structure evolution component. To determine the structure evolution component (τ_e) of the flow stress we need to compute the evolution of the internal variable σ_e using equation Equation (19). This equation requires two variables: the saturation value σ_{es} of σ_e and the initial hardening rate θ_0 .

To compute σ_{es} using (21), we need the parameters σ_{0es} , g_{0es} , and $\dot{\epsilon}_{0es}$. Given a set of true stress versus true plastic strain curves, the first step in the process of determination of these parameters is to compute the temperature at each point on the curve (for experimental data that are not given in isothermal form). The temperature is computed using (41) with the value of χ being obtained using:

$$\chi = \min\{[0.019 - 0.089 \ln(\varepsilon_p) + 9.23\varepsilon_p^2], 0.9\}, \quad (47)$$

where ε_p is the true plastic strain. Equation (47) is a least squares fit to the experimental data for 2024-T351 aluminum given in [Ravichandran et al. 2001]. The experimental σ_e versus true plastic strain curves are then computed using the relation

$$\sigma_e = \frac{1}{S_e} \left(\sigma_y \frac{\mu_0}{\mu} - \tau_a - \tau_i \right).$$

Note that the quantity τ_i for each curve is the value used to compute the Fisher plot in Figure 1, unlike the procedure used elsewhere [Goto et al. 2000; Banerjee 2007]. The parameters used to compute S_e (see (16)) are:

$$\begin{aligned} k_b &= 1.38 \times 10^{-23} \text{ J} \cdot \text{K}^{-1}, & b &= 2.86 \times 10^{-10} \text{ m}^{-2}, & \dot{\epsilon}_{0e} &= 10^9 \text{ s}^{-1}, \\ g_{0e} &= 3.0, & p_e &= 0.75, & q_e &= 1.0. \end{aligned}$$

The density is assumed to have a constant value of $2700 \text{ kg} \cdot \text{m}^{-3}$ during deformation. Plots of σ_e versus ε_p for all the stress-strain curves used in this work can be found in [Bhawalkar 2006].

After the σ_e versus ε_p curves have been computed, a quadratic polynomial is fit to each curve. The saturation value of σ_e and the temperature at saturation are computed by determining the strain at which the slope of the quadratic curve becomes zero. A Fisher plot can now be drawn to determine the values of σ_{0es} and g_{0es} by writing Equation (21) in the form

$$\ln(\sigma_{es}) = \ln(\sigma_{0es}) - \frac{k_b T}{g_{0es} b^3 \mu} \ln \left(\frac{\dot{\epsilon}_{0es}}{\dot{\epsilon}} \right).$$

To compute the Fisher plot we assume that $\dot{\epsilon}_{0es} = 10^8 \text{ s}^{-1}$ and get the fit shown in Figure 5. The statistics of the fit are: $R^2 = 0.41$, F -statistic = 36.2, t -statistics = 6.0 and 157. There are 52 sample points. Therefore, though the fit is poor, it is statistically significant. The range of values of σ_{0es} and g_{0es} from the fit that are within the 95% confidence interval (corresponding to a t value of 1.675) are:

$$\begin{aligned} \sigma_{0es} \text{ (low)} &= 122.3 \text{ MPa}, & \sigma_{0es} \text{ (fit)} &= 149.5 \text{ MPa}, & \sigma_{0es} \text{ (high)} &= 182.7 \text{ MPa}, \\ g_{0es} \text{ (low)} &= 0.235, & g_{0es} \text{ (fit)} &= 0.30, & g_{0es} \text{ (high)} &= 0.416. \end{aligned}$$

To compute the initial hardening rate (θ_0), we first compute the slopes (θ) of the σ_e versus ε_p curves at each point on the curve. The slope θ is then plotted against $1 - (\sigma_e/\sigma_{es})^2$ and a straight line with zero intercept is fitted to the resulting curve. This model gives a better fit to the experimental data than the more commonly used hyperbolic tangent hardening rule [Follansbee and Kocks 1988; Goto et al. 2000;

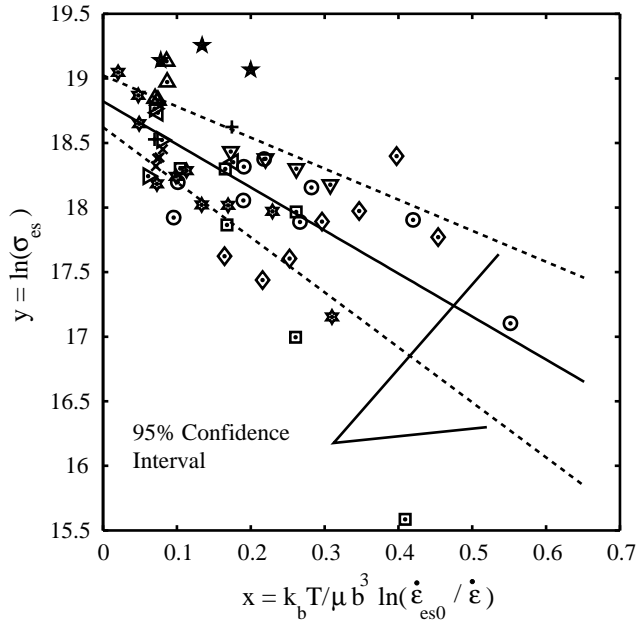


Figure 5. Fisher plot used to determine σ_{0es} and g_{0es} for 6061-T6 aluminum alloy. The solid line shows the model fit to the data. The dotted lines show the range of the model for a confidence level of 95%. The symbols represent experimental data. The sources of the experimental data are \circ [Hoge 1966]; \square [Green and Babcock 1966; Eleiche 1972]; ∇ [Davidson 1973]; \star [Rosenberg et al. 1986]; \triangle [Yadav et al. 1995]; \diamond [Brown et al. 1996]; \times [Lee et al. 2000]; $*$ [Ogawa 2001]; $+$ [Cady and Gray III 2001]; $<$ [Fish et al. 2005]; $>$ [Lesuer et al. 2001; Jia and Ramesh 2004].

[Banerjee 2007]. The slope of the straight line fit gives us the value of θ_0 for each curve. A least squares surface fit of θ_0 as a function of strain rate and temperature (assuming that the parameter $\dot{\epsilon}_\theta = 10^{10} \text{ s}^{-1}$) gives us the following parameters for Equation (20):

$$\begin{aligned} a_0 &= 0.147, & a_1 &= -2.4 \times 10^{-3}, \\ a_2 &= -0.14, & a_3 &= 3.3 \times 10^{-3}. \end{aligned}$$

The spread of the data is quite large and the R^2 value for the fit is 0.38. The F -statistic for the fit is 3.2 which implies that the fit may not be statistically significant. However, comparisons with experimental data show that the predicted flow stresses are reasonable when we use the above parameters. For the details of an alternative approach for modeling the hardening of 6061-T6 aluminum in the context of the MTS model see [Bhawalkar 2006].

4.5. Overdriven shock regime. In the overdriven shock regime, we assume that the flow stress is given by Equation (22) and that the material does not harden. The parameters of the model are determined by fitting a curve to experimental data on 1100 aluminum and 2024 aluminum from [Tonks 1993]. We assume that 6061-T6 aluminum also shows a similar behavior. The fit to the data is shown in Figure 6.

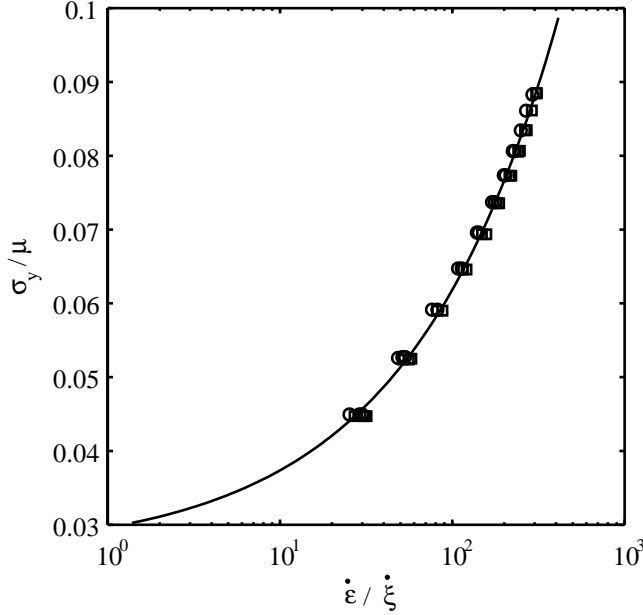


Figure 6. Comparison of the yield stress predicted by the overdriven shock model, [Equation \(22\)](#), with experimental data. The solid line shows the predicted values. The circles show experimental data for 1100 aluminum alloy while the squares show experimental data for 2024 aluminum alloy.

The following parameters have been used in the calculation:

$$\begin{aligned} \rho_0 &= 2700 \text{ kg} \cdot \text{m}^{-3}, & \rho &= 2710 \text{ kg} \cdot \text{m}^{-3}, & T &= 298 \text{ K}, \\ \sigma_{ys0} &= 700 \text{ MPa}, & M &= 26.98 \text{ amu}, & \gamma &= 0.0001. \end{aligned}$$

The parameters determined from the fit are: $y_1 = 3.54 \times 10^{-3}$ and $y_2 = 0.5$.

4.6. Taylor–Quinney coefficient. The Taylor–Quinney coefficient (χ) can be computed using [Equation \(43\)](#). To evaluate this equation we need the parameters A_χ , B_χ , and β_χ in [\(45\)](#). We have determined these parameters by comparing the predictions of our model with experimental data for 2024-T3 aluminum from [\[Hodowany et al. 2000\]](#). [Figures 7 \(left\) and 7 \(right\)](#) show the predicted values of χ for initial temperatures of 300 K and 500 K, respectively. The parameters used for the plots are: $A_\chi = 0.2$, $B_\chi = 12$, and $\beta_\chi = 0.3$. A constant mass density of 2700 kg m^{-3} was used for the calculations. Note that these parameters will change if θ_0 or σ_{es} are changed.

From [Figure 7 \(left\)](#) we observe that, at a temperature of 300 K, the values of χ are nearly the same for strain rates between 0.001 s^{-1} to 3000 s^{-1} . This is similar to the experimental observations in [\[Hodowany et al. 2000\]](#). However, the value of χ increases as the flow stress increases with increasing strain rate due to viscous drag effects. This effect is similar to that observed in rate-dependent α -titanium in [\[Hodowany et al. 2000\]](#). Hence, our model behaves in a reasonable manner at room temperature. On the other hand, the experimental data for 2024-T3 aluminum indicates that low values of χ (less than 0.5) are obtained up to a plastic strain of around 0.3 while our model predicts such values only up to a plastic strain of

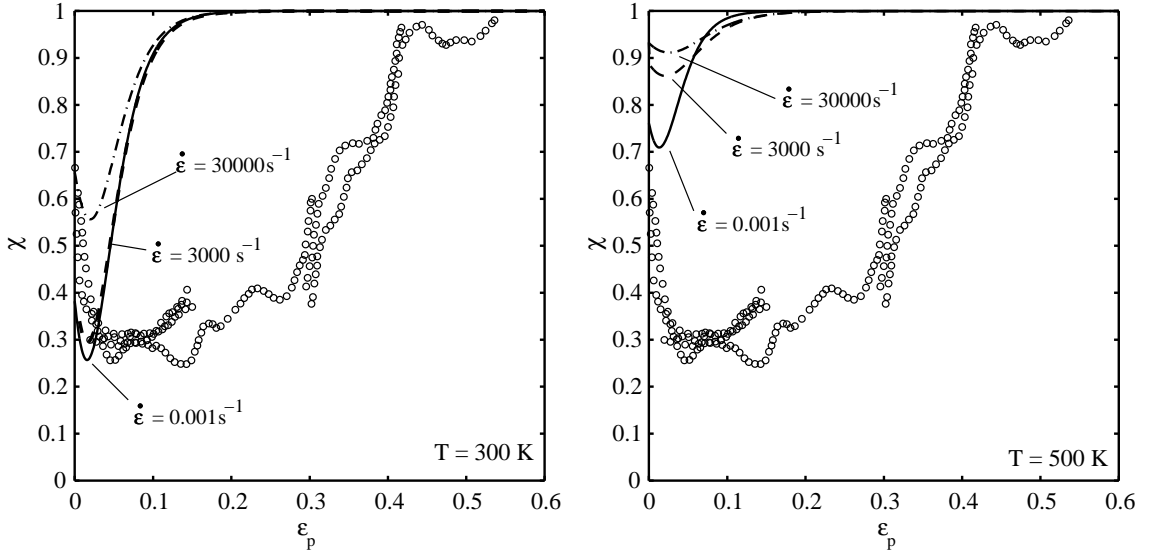


Figure 7. Variation of the Taylor–Quinney coefficient (χ) with plastic strain and strain rate: $T = 300$ K (left), $T = 500$ K (right). The circles show experimental data for 2024-T3 aluminum alloy from [Hodowany et al. 2000] for a strain rate of 3000 s^{-1} and at 300 K. The solid lines represent predicted values for a strain rate of 0.001 s^{-1} . The dashed lines represent predicted values for a strain rate of 3000 s^{-1} and the dash-dot lines represent predictions for a strain rate of $30,000 \text{ s}^{-1}$.

0.05. The width of this zone depends on the initial hardening modulus (θ_0) and on the saturation stress (σ_{es}). The discrepancy between our model for 6061-T6 aluminum and the experimental data for 2024-T3 aluminum indicates that θ_0 for 2024-T3 aluminum might be lower than that for 6064-T6 aluminum. It is also possible that the saturation stress computed by our model is lower than should be expected.

At 500 K (see Figure 7 (right)), the value of χ is considerably higher than at 300 K. We do not have any experimental data to verify that this behavior is reasonable. Experiments at high temperatures are needed to arrive at the correct form of the function $F_1(T)$ in Equation (44). As designed, our the model predicts values of χ close to 1.0 at high temperatures. However, experiments are needed to verify that this is indeed the case for metals and that the stored energy approaches zero at high temperatures.

5. Comparisons of model with experimental data

The verification of the extended MTS flow stress model presented in this paper can be pursued in a number of ways. The strain rate dependence of the model can be verified by computing the flow stress as a function of strain rate (at a constant temperature and plastic strain) and comparing the predicted values with experimental data. A similar comparison of the flow stress as a function of temperature (with the strain rate kept constant) can be used to verify the temperature dependence of the model. Direct comparisons with uniaxial stress-strain curves can also be performed for various strain rates and temperatures.

Numerical simulation is necessary for a more comprehensive validation of the model. Examples of such numerical validation tests have been provided in [Bhawalkar 2006]. Details of the numerical algorithm and various validation tests will be discussed in a forthcoming publication.

5.1. Flow stress as a function of strain rate. Figure 8 shows a comparison of the flow stress predicted by the extended MTS model with experimental data (as a function of strain rate). In the computations performed, the evolution equations for dislocation density were not solved because of the excessive computational cost involved. Rather, a constant value of $\rho_m = 2.0 \times 10^{11} \text{ m}^{-2}$ and a scaling factor of $\lambda_p = 1.0$ were used to compute the component of the flow stress due to viscous drag (τ_v). Adiabatic heating is assumed for strain rates greater than 100 s^{-1} .

Experimental data from [Yadav et al. 1995; Jia and Ramesh 2004; Sakino 2006] for 6061-T6 aluminum alloy suggest that viscous drag effects are small for strain rates up to $3 \times 10^4 \text{ s}^{-1}$. This is in contrast with data given in [Lesuer et al. 2001] which suggests that drag effects become important at strain rates of 10^4 s^{-1} or less. Sakino [2006] has shown quite convincingly that drag effects become important at lower strain rates only in the annealed alloy 6061-O aluminum but not in the hardened 6061-T6 aluminum alloy. Our model slightly overestimates the flow stress for strain rates less than 10^5 s^{-1} but matches quite

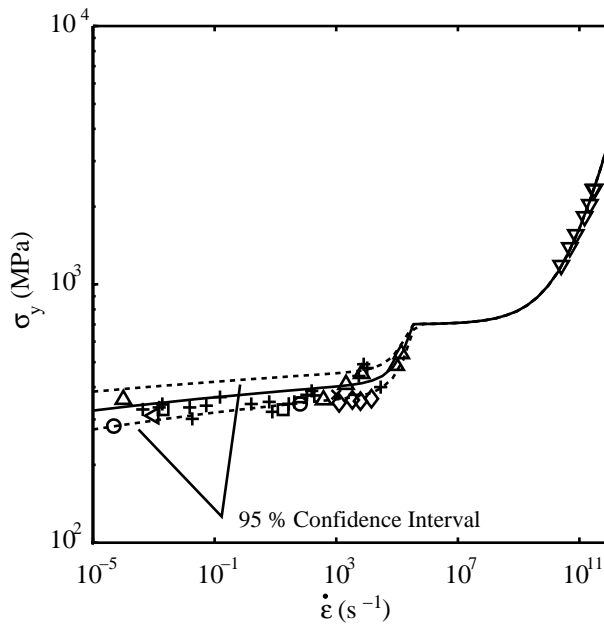


Figure 8. The flow stress of 6061-T6 aluminum alloy as a function of strain rate (at 298 K and a plastic strain of 0.2). The solid line shows the prediction of the extended MTS model. The dashed lines show the range of predicted flow stresses in the 95 % confidence interval. The symbols represent experimental data. The sources of the experimental data are \circ [Hoge 1966]; \square [Green and Babcock 1966; Eleiche 1972]; ∇ [Tonks 1993]; \triangle [Yadav et al. 1995]; \times [Lee et al. 2000]; \triangleleft [Cady and Gray III 2001]; $+$ [Lesuer et al. 2001; Jia and Ramesh 2004]; \diamond [Sakino 2006].

well with the available data for higher strain rates. The 95% confidence interval shown in the figure is based on the low and high values of σ_i , g_{0i} , σ_{0es} , and g_{0es} discussed earlier.

From Figure 8 we can also observe a change in slope of the flow stress-strain rate curve at a strain rate of around 10^6 s^{-1} . Experimental data are not available for the strain rate regime between 10^6 s^{-1} and 10^{10} s^{-1} . The curves for the overdriven shock regime and the moderate strain rate regime can be matched only if there is a change in slope as shown in the figure. A better model for the intermediate strain rate regime can only be determined after experiments (or possibly numerical simulations) have been performed for this regime. In the model that we have presented in this paper, we assume that the viscous drag component of the flow stress saturates when σ_y reaches a value of 700 MPa and any additional increase in the flow stress is due to shock effects as discussed in [Wallace 1981a; 1981b].

5.2. Flow stress as a function of temperature. Figure 9 shows comparisons between experimental data and the flow stress predicted by our model as a function of temperature. At low strain rates (see Figure 9, left), the decrease in flow stress with temperature is predicted quite accurately by the model. Near the melting temperature, the contributions of τ_i and τ_e are close to zero and the flow stress is determined by the athermal component τ_a . Beyond the melting temperature, the stress is computed by the Newtonian fluid model in Equation (24) and the stress is quite small at low strain rates. Adiabatic heat is assumed for the high strain rate calculations.

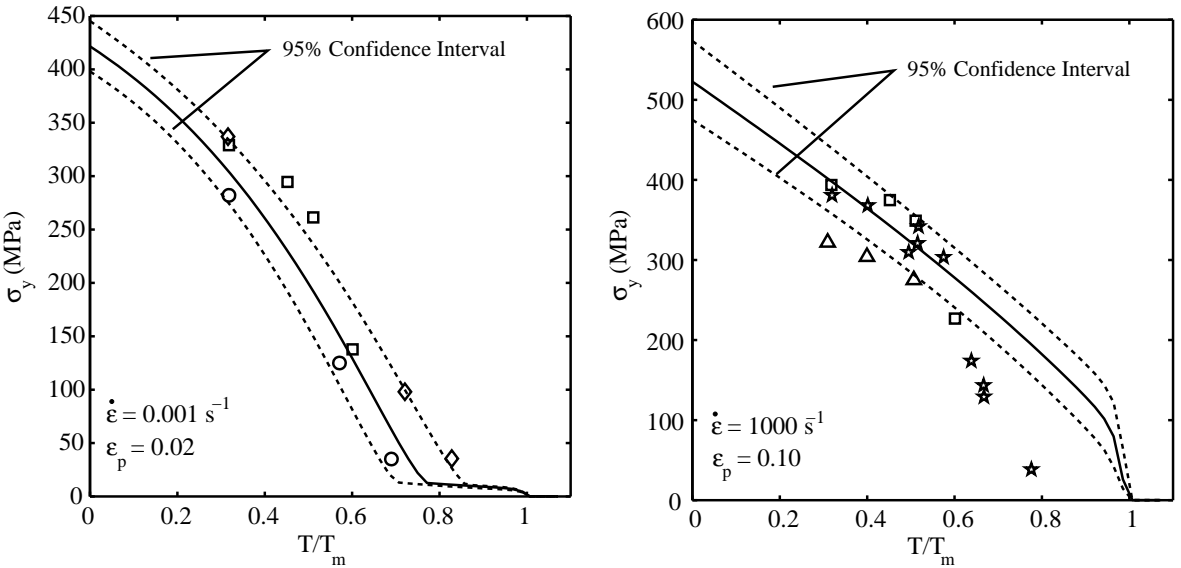


Figure 9. The flow stress of 6061-T6 aluminum alloy as a function of temperature. Left: strain rate = 0.001 s^{-1} and plastic strain = 0.02. Right: strain rate = 1000 s^{-1} and plastic strain = 0.1. The solid lines show the prediction of the extended MTS model. The dashed lines show the range of values predicted if we use the low or high values of the parameters σ_i , g_{0i} , σ_{0es} , and g_{0es} . The symbols represent experimental data. The sources of the experimental data are: \circ [Hoge 1966]; \square [Green and Babcock 1966; Eleiche 1972]; \diamond [Dike et al. 1997]; \star [Rosenberg et al. 1986]; \triangle [Ogawa 2001].

At a strain rate of 1000 s^{-1} , our model predicts the flow stress quite well up to $T/T_m = 0.6$ (see Figure 9, right). At higher temperatures, the flow stress is overestimated. The prediction of our model is reasonable if we consider the full set of data used to arrive at the parameters. It is expected that the predicted temperature dependence of our model can be improved at more experimental data at high temperatures and high strain rates become available.

5.3. Flow stress as a function of pressure. Figure 10 shows the predicted pressure dependence of the flow stress of 6061-T6 aluminum at a strain rate of 0.001 s^{-1} . The increase in flow stress with increasing pressure is underestimated by our model. Since the pressure dependence of the flow stress at low strain rates is determined by the pressure dependence of the shear modulus, the figure shows that the pressure dependence of the shear modulus is not enough to account for the pressure dependence of the flow stress. We also observe that

$$\frac{\partial \sigma_y}{\partial p} \approx 2 \frac{\partial \mu}{\partial p}.$$

This suggests that the pressure dependence of the flow stress in the Steinberg–Cochran–Guinan model [Steinberg et al. 1980] (which is used widely for high strain rate calculations and assumes that $\partial \sigma_y / \partial p \approx \partial \mu / \partial p$) is not correct. We have also observed a similar behavior for OFHC copper [Banerjee 2005a]. An explicit pressure dependence of the initial hardening modulus and the saturation stress is needed to

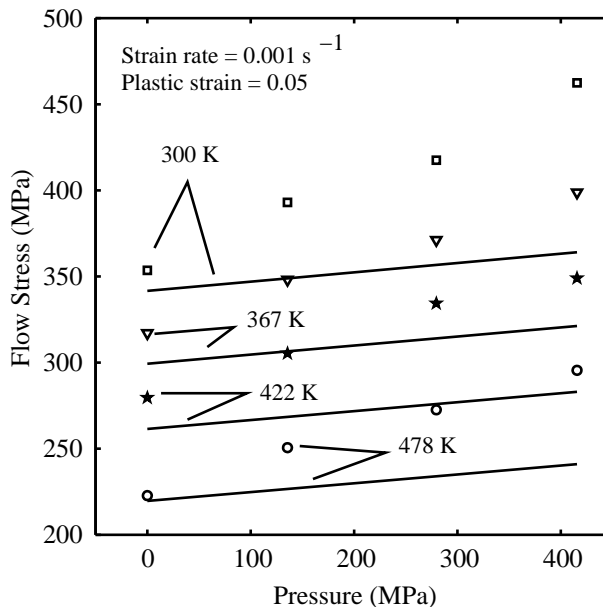


Figure 10. The flow stress of 6061-T6 aluminum alloy as a function of pressure for a strain rate of 0.001 s^{-1} and a plastic strain of 0.05. The solid lines show the predictions of the extended MTS model. The symbols represent experimental data from [Davidson 1973] at the following temperatures range of values predicted if we use the low or high values of □ 300 K, ▽ 367 K, ★ 422 K, and ○ 478 K.

model the plastic behavior of metals under hydrostatic pressure. Such a dependence has to be based on physical considerations and needs further research.

5.4. Uniaxial stress-strain curves. The predicted variation of the flow stress with plastic strain at a strain rate of 0.001 s^{-1} is shown in Figure 11. The calculations were performed using a constant mass density of $2700 \text{ kg}\cdot\text{m}^{-3}$, and a constant mobile dislocation density of $2 \times 10^{11} \text{ m}^{-2}$. Isothermal conditions were assumed.

Figure 11 (left) shows the predicted flow stress at ambient pressure. The flow stress predicted by our model tends to saturate at a lower value than seen in the experimental data. Also the predicted initial hardening modulus is lower than that suggested by the experiments at 367 K and 422 K and higher than experiment at 589 K. However, the initial yield stress predicted by our model is remarkably close to that seen in experiments considering the experimental variability that is observed (for further data on experimental variability at a given temperature and strain rate see [Bhawalkar 2006]). The experimental stress-strain curves show strain softening. A damage model that includes void nucleation and growth can be used to predict that portion of the stress-strain curve. For the sake of simplicity, we do not discuss damage models and their implications in this paper.

Figure 11 (right) shows the predicted flow stress at a pressure of 276 MPa. We notice that the initial yield stress is predicted quite accurately by our model at this pressure for all the temperatures shown in the figure. However, the hardening rate and the saturation stress are underestimated. The error decreases with

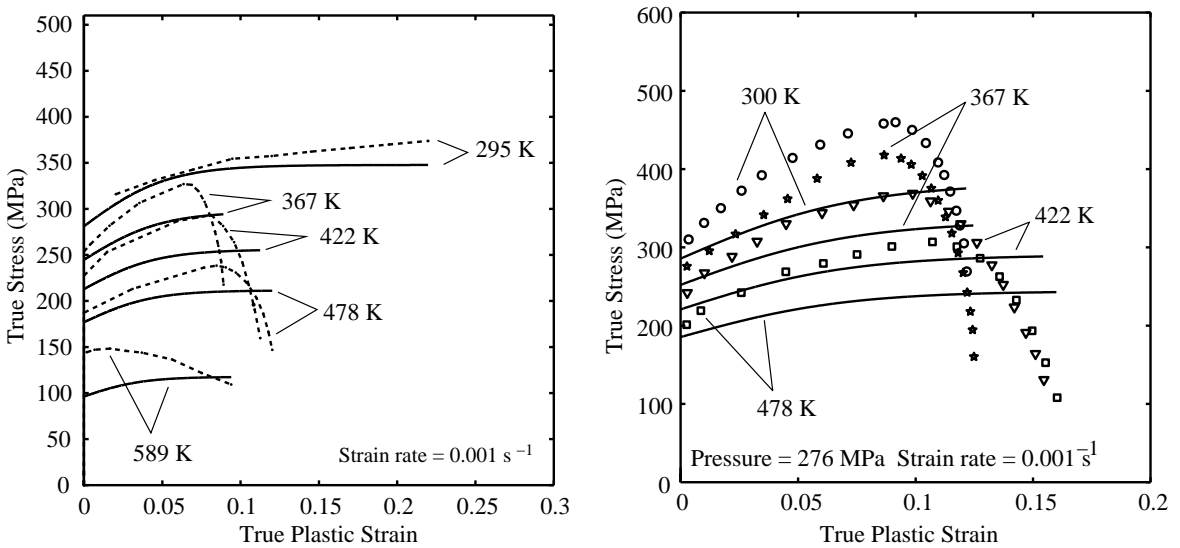


Figure 11. The flow stress of 6061-T6 aluminum alloy as a function of true plastic strain at a strain rate of 0.001 s^{-1} . Left: Ambient pressure; right: pressure = 276 MPa. The solid lines show the prediction of the extended MTS model. On the left side of the figure the dashed lines represent the experimental data. On the right, the symbols represent the experimental data. The data at 295 K are from [Fish et al. 2005]. The data at 300 K, 367 K, 422 K, and 478 K are from [Davidson 1973]. The data at 589 K are from [Green and Babcock 1966; Eliche 1972].

increasing temperature. Similar plots at higher pressures show that the error increases with increasing pressure at a particular temperature (see also Figure 10). As mentioned before, an explicit pressure dependence of the initial hardening rate and the saturation stress is needed to improve our model.

Figure 12 shows the predicted stress-strain curves for strain rates greater than 1000 s^{-1} . The change in mass density due to large pressures that develop at such strain rates has been neglected in our computations. To keep the computations efficient, we have not used the evolution equations for dislocation density and have instead used a constant value of $\rho_m = 2 \times 10^{11} \text{ m}^{-2}$. Adiabatic heating and the resulting thermal softening has been assumed for all these computations.

From Figure 12 (left) we observe that the flow stress predicted by the extended MTS model matches well with the experimental data for temperatures of 77 K and 298 K. At 473 K, the predicted flow stress is higher than experiment and does not capture the strain softening due to accumulating damage in the material. At 618 K, the predicted flow stress is considerably higher than experiments suggest. As observed before, our model does not predict enough thermal softening of 6061-T6 aluminum at higher temperatures— particularly at high strain rates. It is important to note here that 6061-T6 aluminum is a precipitation hardened alloy containing magnesium and silicon as alloying elements. At about 550 K, the solute molecules start to diffuse toward the grain boundaries and the alloy softens considerably. Though the extended MTS model is an improvement over the original MTS model (see [Bhawalkar

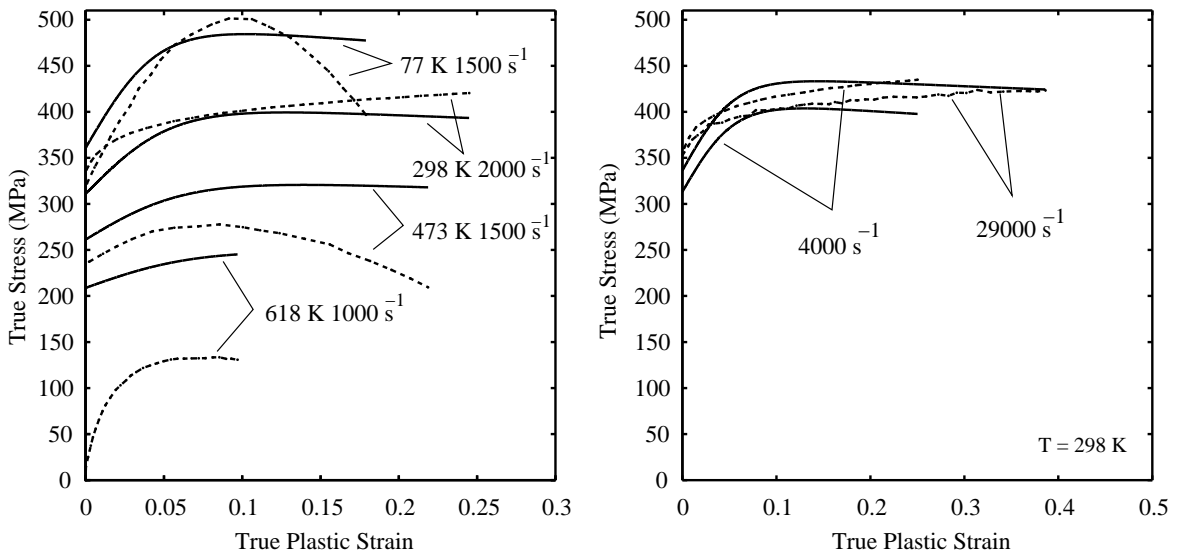


Figure 12. The flow stress of 6061-T6 aluminum alloy as a function of plastic strain at moderately high strain rates. Left: strain rate = $1000\text{--}2000 \text{ s}^{-1}$. Right: temperature = 298 K. The solid lines show the prediction of the extended MTS model. The dashed lines represent the experimental data. The sources of the experimental data are: strain rate = 1000 s^{-1} from [Rosenberg et al. 1986], strain rate = 1500 s^{-1} from [Ogawa 2001], strain rates = 2000 s^{-1} and 4000 s^{-1} from [Lee et al. 2000], strain rate = 29000 s^{-1} from [Jia and Ramesh 2004].

2006] for similar results with the original MTS model), the amount of thermal softening continues to be overestimated by the extended model.

Figure 12 (right) shows that the experimental data does not show any significant strain rate dependence at room temperature (at least up to a strain rate of $29,000 \text{ s}^{-1}$). Our model predicts a small increase in flow stress with strain rate and some thermal softening at strains greater than 0.2. However, the overall match with experiment is quite good. Also the initial rate of hardening appears to be lower than that predicted. However, stress-strain data from split Hopkinson pressure bar experiments are suspect for strains less than 0.1 and conclusions cannot be drawn about the accuracy of our hardening model from this figure.

6. Model predictions

In this section we discuss the predictions of our flow stress model for a large range of conditions. The mass density is assumed to be constant ($2700 \text{ kg}\cdot\text{m}^{-3}$) in our calculations. Since the phonon drag coefficient increases with temperature, assuming a constant mobile dislocation density for all temperatures gives unrealistic flow stresses at strain rates greater than 10^4 s^{-1} . On the other hand, using the evolution equations to determine ρ_m is not computationally efficient. Hence we have used the following equation to determine ρ_m for our calculations in this section:

$$\rho_m \approx \rho_{m0}(1 + \widehat{T})^m,$$

where ρ_{m0} is the dislocation density at 0 K, $\widehat{T} = T/T_m$ where T_m is the melting temperature, and m is a constant. The values of these parameters that we have used are: $\rho_{m0} = 1.3494 \times 10^{11} \text{ m}^{-2}$ and $m = 1.4114$. Using these parameters gives us a value of $\rho_m = 2 \times 10^{11} \text{ m}^{-2}$ at 300 K and $\rho_m = 3.5 \times 10^{11} \text{ m}^{-2}$ at 900 K. The value of ρ_m is not allowed to vary with plastic strain.

Figure 13 (left) shows the flow stress predicted by our model as a function of strain rate at a plastic strain of 0.2 and for a range of temperatures. From the figure we observe that at low strain rates, the flow stress is strongly dependent on temperature. As the strain rate reaches around 10^5 s^{-1} , the model predicts that the temperature dependence of the flow stress decreases until the temperature has hardly any effect.

Figure 13 (right) shows the flow stress as a function of strain rate at a temperature of 400 K and for various levels of strain. In this case we observe that the flow stress saturates rather rapidly (at a plastic strain of around 0.2). This indicates that the material exhibits little strain hardening. However, simulations of Taylor impact tests (see [Bhawalkar 2006]) indicate that we underestimate the amount of hardening in our model. A value of the initial hardening modulus (θ_0) that is around 0.3 of the value that we have used gives a more realistic amount of hardening. However, such a value leads to an underestimation of the flow stress at low strain rates. A better hardening model than the one used is clearly needed if we are to predict the saturation strain more accurately.

Figure 14 (left) shows the flow stress predicted by our model as a function of temperature at a plastic strain of 0.2 and for a range of strain rates. At low strain rates the flow stress decreases rapidly with temperature until it reaches the athermal value. For a strain rate of 10^3 s^{-1} and higher the initial decrease of the flow stress with temperature is small. However, as the temperature reaches the melting temperature, the flow stress drops abruptly to a small value (determined by the constitutive relation for a Newtonian

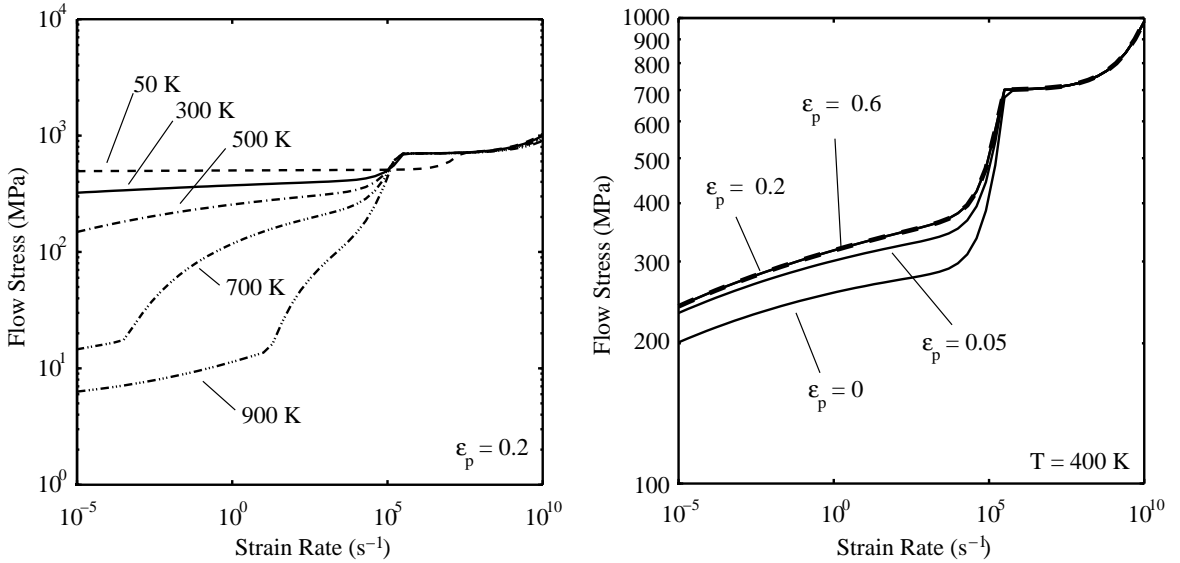


Figure 13. The predicted flow stress of 6061-T6 aluminum alloy as a function of strain rate. Left: Plastic Strain = 0.2. Right: temperature = 400 K.

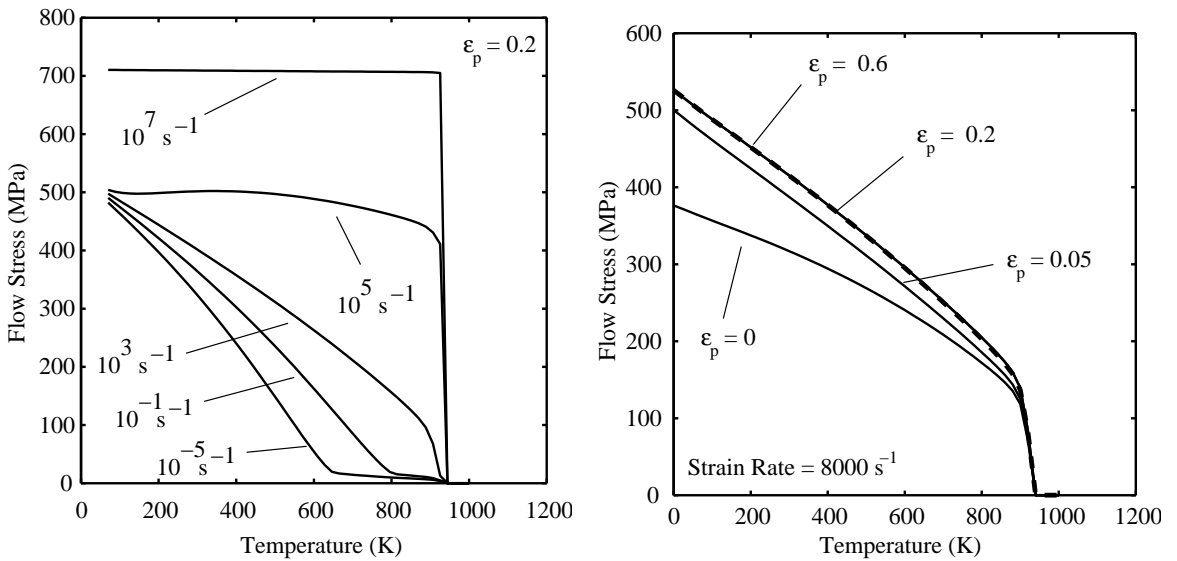


Figure 14. The predicted flow stress of 6061-T6 aluminum alloy as a function of temperature. Left: plastic Strain = 0.2. Right: strain Rate = $8000 s^{-1}$.

fluid). In the absence of experimental data, it is not obvious whether this behavior of our model accurately represents reality.

Figure 14 (right) shows the flow stress as a function of temperature at a strain rate of 8000 s^{-1} and for various levels of strain. Once again, we see that the flow stress saturates at a plastic strain of about 0.2. At low temperatures, the material hardens significantly before saturation. However, as the temperature increases, the amount of hardening decreases until at around 850 K there is essentially no hardening. This is reasonable behavior considering the fact that thermally activated dislocation motion is dominant at a strain rate of 8000 s^{-1} , and enough thermal energy is available at high temperatures to allow slip to occur more readily. The convex nature of the curves shown in the figure also indicate that we are able to capture some of the effects of high temperature solute diffusion in our model.

In Figure 15 (left) we have plotted the predicted flow stress as a function of plastic strain. The strain rate is 8000 s^{-1} and the initial temperatures range from 50 K to 900 K. Adiabatic heating is assumed, and the temperature increases with increasing strain. All the curves show a small amount of thermal softening. We also observe that the initial rate of hardening decreases with temperature. Saturation is reached at higher strains as the temperature increases. If we compare the flow stress at 300 K with those shown in Figure 12 (right), we observe that there is hardly any strain rate dependence at these strain rates. We also observe that the flow stress at 900 K is around 70 MPa which is high considering the fact that the material is close to its melting point.

Figure 15 (right) shows stress-strain plots at various strain rates. The initial temperature of the material is 400 K in these plots. Isothermal conditions were assumed for strain rates lower than 1000 s^{-1} and adiabatic conditions otherwise. Interestingly, the only curve that shows an appreciable amount of thermal softening is the curve at 1000 s^{-1} . At a strain rate of 10^5 s^{-1} , the increase in the drag coefficient with temperature offsets the amount of thermal softening that occurs. The temperature dependence of the flow

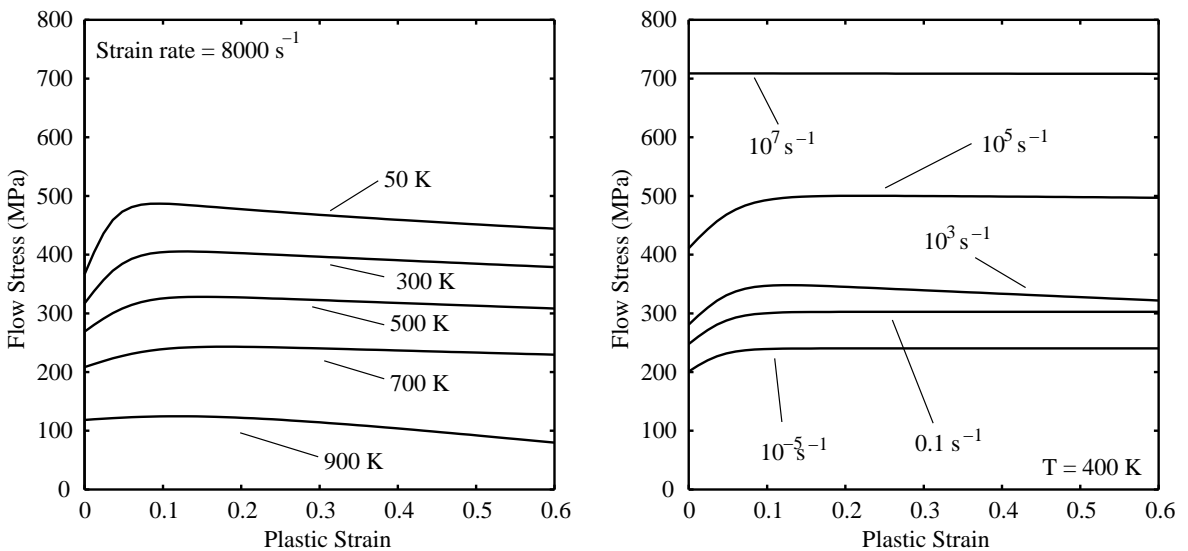


Figure 15. The predicted flow stress of 6061-T6 aluminum alloy as a function of plastic strain. Left: Strain Rate = 8000 s^{-1} . Right: temperature = 400 K.

stress at a strain rate of 10^7 s^{-1} is negligible and hence there is no appreciable thermal softening with increasing strain. The amount of strain that can be achieved at high strain rates is not clear and failure will probably occur before a plastic strain of 0.6 is achieved.

7. Concluding remarks

One of the main shortcomings of the original mechanical threshold stress model was that it was not accurate at strain rates greater than about 10^4 s^{-1} . In this paper we have presented an extended mechanical threshold stress model that is valid for strain rates at which viscous drag effects become dominant. The model has also been extended to the overdriven shock regime. The original model of Follansbee and Kocks was also designed for use in the temperature regime where solute diffusion and other thermally activated diffusion effects could be neglected (typically less than 0.6 of the melting temperature). In the extended model, we allow for higher temperatures by using a modified form of the equation for the intrinsic component of the flow stress. The strain rate dependence of the flow stress is predicted quite accurately by our model. However, the predicted temperature dependence is less accurate and could be improved. Since the density of obstacles inside a crystal decreases with increasing temperature, the activation energy should be a function of the temperature. It is possible that a temperature-dependent model for the activation energy will improve predictions of the flow stress of 6061-T6 aluminum at high temperatures. More high temperature–high strain rate data of the type provided by [Rosenberg et al. \[1986\]](#) are essential before such a model can be developed.

We have provided a detailed description of the procedure for calculating the drag stress. Two methods for computing the viscous drag coefficient have been compared in the paper. We have found that Liebfried's theory provides an estimate of the viscous drag coefficient that better matches experiment. We have also added a temperature dependence to the dislocation evolution equations of Estrin and Kubin and determined new parameters for these equations that fit experimental data. Estrin and Kubin have estimated that the mobile dislocation density is around 10^{14} m^{-2} at saturation. Our results suggest that a more accurate estimate of this quantity is $2 \times 10^{11} \text{ m}^{-2}$.

The evolution equations of the internal variable (mechanical threshold stress) have been simplified and a nondimensional form for the initial hardening modulus has been proposed. The simplified equations allow for an exact expression for the internal variable as a function of plastic strain which can be evaluated efficiently in a computational code. Alternatively, we could have used the equations for the evolution of the dislocation density with the dislocation density as an internal variable. However, the system of equations involved is very stiff and computationally expensive to solve for high strain rate problems. The parameters for 6061-T6 aluminum alloy (needed for the evolution of the internal variable) that we have determined in this paper lead to an underestimation of the saturation stress and the amount of hardening. This effect is particularly noticeable for high hydrostatic pressures. Also, the pressure dependence of the flow stress is not reflected completely by the pressure dependence of the shear modulus (for which a model is presented in the paper). Explicitly pressure–dependent models for the hardening modulus and the saturation stress are clearly needed.

In addition, we have developed an equation for the evolution of temperature with plastic strain based on thermodynamic principles. An expression has been presented for the Taylor–Quinney coefficient as a function of the mechanical threshold stress internal variable. This expression requires a functional

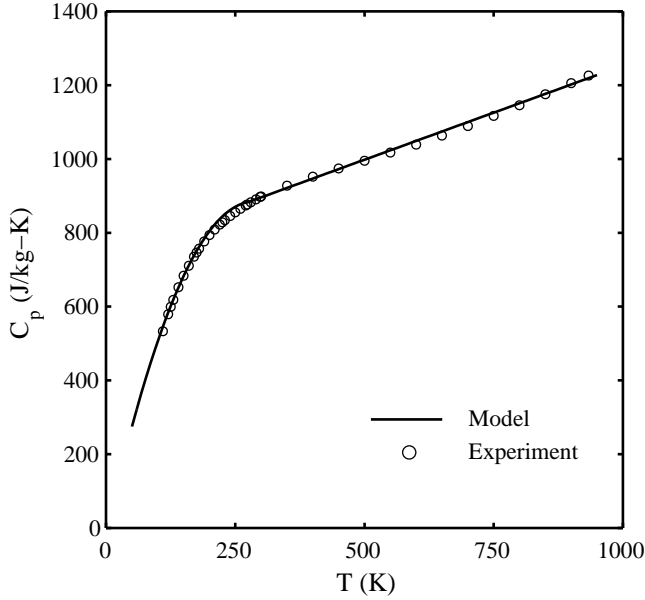


Figure 16. Specific heat of aluminum. The experimental data, shown as open circles, are from [Desai 1987]. The solid line shows the prediction of the model in Equation (31).

representation of the Gibbs free energy density. We have postulated a form of the derivatives of this function that matches experimental data qualitatively. However, further research is needed to arrive at a better form of the Gibbs free energy density function.

Important issues that have not been addressed in this paper are cyclic loading and kinematic hardening models, deformation induced anisotropy in both the elastic and plastic behavior, the appropriate form of the yield condition and the flow rule, and the modeling of void nucleation and growth and the accompanying elastic and plastic damage. Also, in this paper, we have considered only one dimensional analytical verification tests. Consideration of some of the above issues and detailed numerical validation experiments using the material point method Sulsky et al. [1994; 1995] are in progress and will be the subject of a subsequent paper.

Appendix A: specific heat, EOS, melting temperature, shear modulus

Experimental data indicate that the specific heat (at constant pressure) of aluminum increases by around 37% between room temperature and melting [Desai 1987]. A least squares curve fit to the experimental data yields the following parameters for the model given in Equation (31):

$$\begin{aligned} A_1 &= -11.73 \text{ J/kg-K}, & B_1 &= 6.28 \text{ J/kg-K}^2, \\ C_1 &= -0.011 \text{ J/kg-K}^3, & A_2 &= 743.13 \text{ J/kg-K}, \\ & & B_2 &= 0.51 \text{ J/kg-K}^2. \end{aligned}$$

A plot of the fit is shown in Figure 16.

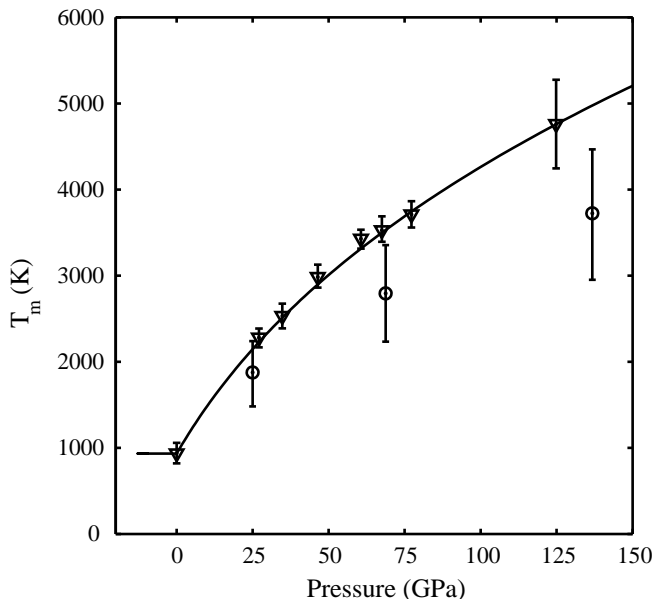


Figure 17. Melting temperature of aluminum. The triangles show experimental data from [Boehler and Ross 1997] and the circles show experimental data collected in [Burakovsky et al. 2000]. The solid line shows the prediction of the model in Equation (29).

The shear modulus model given in Equation (26) requires a pressure. We use the equation of state (EOS) in Equation (30) to compute the pressure for a given change in density. The parameters that we have used for 6061-T6 aluminum are $B_0 = 76.3$ GPa and $B'_0 = 4.29$ [Burakovsky and Preston 2005]. Experimental data for 6061-T6 aluminum alloy [Vaidya and C. 1970], 2024-O aluminum alloy [McQueen et al. 1970], and pure aluminum [Mitchell and Nellis 1981] are closely matched by the EOS model up to a compression ratio (ρ/ρ_0) of 1.4.

Though the alloying content can have a significant effect of the melting temperature of metals, we have assumed in this paper that the melting temperature of 6061-T6 aluminum does not differ significantly from that of pure aluminum. The parameters of the model of melting temperature given in Equation (29) for 6061-T6 aluminum are taken to be

$$T_{m0} = 933.6 \text{ K}, \quad q = 3.3, \\ \Gamma_1 = 0.84(\text{gm/cc})^{1/3}, \quad \Gamma_2 = 45.4(\text{gm/cc})^q.$$

We also assume that for hydrostatic tensile states the melting temperature is equal to T_{m0} . The prediction of the model of Equation (29) is compared with experimental data in Figure 17. An initial density of 2700 kg/m^3 was used while computing the quantities in the figure. The model fits the data from [Boehler and Ross 1997] quite well (triangles) but not the older data collected in [Burakovsky et al. 2000] (circles). The accuracy of the Boehler and Ross data has been confirmed by more recent numerical experiments by Voadlo and Alfe [2002].

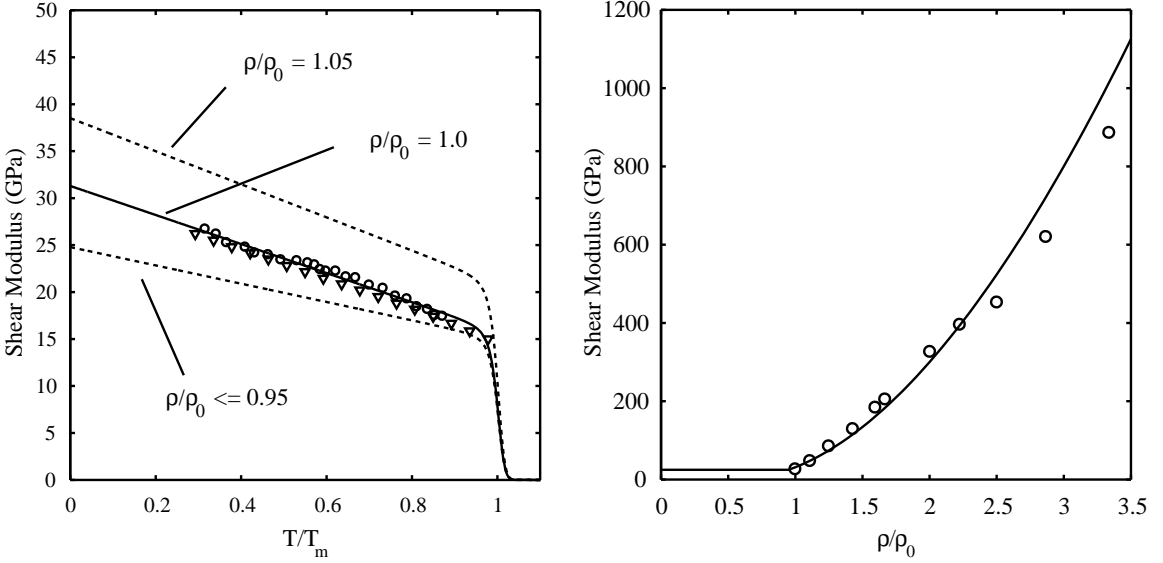


Figure 18. Shear modulus of 6061-T6 aluminum alloy. Left: shear modulus vs. temperature. Right: shear modulus vs. mass density at 0 K. At left, the triangles show experimental data for pure aluminum from [Tallon and Wolfenden 1979] and the circles show experimental data for 6061-T6 aluminum alloy from [Brown et al. 1996]. The solid line shows the prediction of the model in Equation (26) at ambient pressure. The dotted lines show predicted shear moduli under hydrostatic tension and compression. At right, the circles show results from electronic structure calculations [Burakovsky et al. 2003] and the solid line shows the prediction of our model.

The shear modulus model in Equation (26) allows for a smooth transition to zero shear modulus beyond melting. This feature is advantageous in numerical simulations for conditions where melting might occur. The parameters of the shear modulus model for 6061-T6 aluminum are $\mu_0 = 31.3$ GPa, $\partial\mu/\partial p = 1.8$ [Guinan and Steinberg 1974], $a_1 = 0.53$, $a_2 = 0.10$, $a_3 = 0.37$ [Burakovsky and Preston 2005], $C = 0.049$ [Nadal and Le Poac 2003], $\zeta = 0.1$, and $m = 26.98$ amu. The predicted shear modulus as a function of temperature is compared with experimental data in Figure 18 (left). An initial density of 2700 kg/m^3 was used for the calculations in the figure. Further details and comparisons with other models can be found in [Bhawalkar 2006].

The density dependence of the shear modulus at 0 K is compared with computed results in Figure 18 (right). Since the pressure depends directly on the density in the equation of state, this plot may also be considered to be a measure of the pressure dependence of the shear modulus. Our model predicts the shear modulus quite accurately up to $\rho/\rho_0 = 2.2$. Beyond this point the material undergoes a phase transition to the bcc phase and our model overestimates the shear modulus with increasing pressure.

Acknowledgements

The authors wish to thank the anonymous reviewers for pointing out the inconsistencies in the Steinberg–Cochran–Guinan melting temperature model and the data confirming the accuracy of the Burakovsky–Greeff–Preston model.

References

- [da Andrade 1934] E. N. da Andrade, “The theory of viscosity of liquids: I”, *Philosophical Magazine* **17** (1934), 497.
- [da Andrade 1952] E. N. da Andrade, “Viscosity of liquids”, *Proc. R. Soc. Lond. A* **215**:1120 (1952), 36–43.
- [ASM 2002] *American Society of Metals Handbook: Volume 2*, American Society of Metals, New York, 2002.
- [Banerjee 2005a] B. Banerjee, “An evaluation of plastic flow stress models for the simulation of high-temperature and high strain-rate deformation of metals”, *arXiv:cond-mat* **0512466** (2005), 1–43.
- [Banerjee 2005b] B. Banerjee, “Validation of UINTAH: Taylor impact and plasticity models”, in *Proc. 2005 Joint ASME/ASCE/SES Conference on Mechanics and Materials (McMat 2005)*, Baton Rouge, LA, 2005.
- [Banerjee 2007] B. Banerjee, “The Mechanical Threshold Stress model for various tempers of 4340 steel”, *Int. J. Solids Struct.* **44**:3-4 (2007), 834–859.
- [Barlat et al. 2002] F. Barlat, M. V. Glazov, J. C. Brem, and D. J. Lege, “A simple model for dislocation behavior, strain and strain rate hardening evolution in deforming aluminum alloys”, *Int. J. Plasticity* **18** (2002), 919–939.
- [Bhawalkar 2006] A. Bhawalkar, “The mechanical threshold stress plasticity model for 6061-T6 aluminum alloy and its numerical validation”, Master’s thesis, Department of Mechanical Engineering, University of Utah, Salt Lake City, UT, USA, 2006.
- [Boehler and Ross 1997] R. Boehler and M. Ross, “Melting curve of aluminum in a diamond cell to 0.8 Mbar: implications for iron”, *Earth and Planetary Science Letters* **153** (1997), 223–227.
- [Brailsford 1970] A. D. Brailsford, “Phonon component of dislocation drag”, *J. Appl. Phys.* **41**:11 (1970), 4439–4442.
- [Brailsford 1972] A. D. Brailsford, “Anharmonicity contributions to dislocation drag”, *J. Appl. Phys.* **43**:4 (1972), 1380–1393.
- [Brown et al. 1996] W. Brown, H. Mindlin, and C. Y. Ho, *Aerospace structural metals handbook: Volume 3: Code 3206*, CINDAS/USAF CRDA Handbooks Operation, Purdue University, West Lafayette, IN., 1996.
- [Burakovsky and Preston 2005] L. Burakovsky and D. L. Preston, “Generalized Guinan-Steinberg formula for the shear modulus at all pressures”, *Phys. Rev. B* **71** (2005), 184118–1–7.
- [Burakovsky et al. 2000] L. Burakovsky, D. L. Preston, and R. R. Silbar, “Melting as a dislocation-mediated phase transition”, *Phys. Rev. B* **61**:22 (2000), 15011–15018.
- [Burakovsky et al. 2003] L. Burakovsky, C. W. Greeff, and D. L. Preston, “Analytic model of the shear modulus at all temperatures and densities”, *Phys. Rev. B* **67** (2003), 094107–1–9.
- [Cady and Gray III 2001] C. M. Cady and G. T. Gray III, “Influence of strain rate on the deformation and fracture response of a 6061-T6 Al-50 vol. % Al₂O₃ continuous-reinforced composite”, *Material Science and Engineering* **A298** (2001), 56–62.
- [Davidson 1973] P. G. Davidson, *The effects of high pressure and temperature environments on the properties of 6061-T651 Aluminum*, Ph.D. thesis, Department of mechanical engineering, University of Missouri-Rolls, Rolla, MO, 1973.
- [Desai 1987] P. D. Desai, “Thermodynamic properties of aluminum”, *Int. J. Thermophysics* **8**:5 (1987), 621–638.
- [Dike et al. 1997] J. J. Dike, J. A. Brooks, D. J. Bammann, and M. Li, “Thermal-mechanical modeling and experimental validation of weld solidification cracking in 6061-T6 aluminum”, Technical report SAND-97-8582C, Sandia National Laboratories, Albuquerque, New Mexico, 1997.
- [Dinsdale and Quested 2004] A. T. Dinsdale and P. N. Quested, “The viscosity of aluminum and its alloys - A review of data and models”, *J. Materials Science* **39** (2004), 7221–7228.
- [Eleiche 1972] A. M. Eleiche, “Experimental Investigations in the stress-strain Characteristics of Polycrystalline Metals and Alloys at high Strain-Rates and Elevated Temperatures - Survey”, Master’s thesis, Division of Engineering, Brown University, 1972.

- [Epler 2002] M. Epler, "Structures by precipitation from solid solution", pp. 134–139 in *Metallography and Microstructures. ASM Handbook: Volume 9*, ASM International, New York, 2002.
- [Estrin and Kubin 1986] Y. Estrin and L. P. Kubin, "Local strain hardening and nonuniformity of plastic deformation", *Acta Metall.* **34**:12 (1986), 2455–2464.
- [Fish et al. 2005] J. Fish, C. Oskay, R. Fan, and R. Barsoum, "Al 6061-T6-elastomer impact simulations", 2005. Electronic document.
- [Follansbee and Kocks 1988] P. S. Follansbee and U. F. Kocks, "A Constitutive Description of the Deformation of copper Based on the Use of the Mechanical Threshold Stress as an Internal State Variable", *Acta Metall.* **36** (1988), 82–93.
- [Frost and Ashby 1971] H. J. Frost and M. F. Ashby, "Motion of a dislocation acted on by a viscous drag through an array of discrete obstacles", *J. Appl. Phys.* **42**:13 (1971), 5273–5279.
- [Goto et al. 2000] D. M. Goto, J. F. Bingert, S. R. Chen, G. T. Gray, and R. K. Garrett, "The mechanical threshold stress constitutive-strength model description of HY-100 steel", *Metallurgical and Materials Transactions A* **31A** (2000), 1985–1996.
- [Green and Babcock 1966] S. J. Green and S. G. Babcock, "High strain rate properties of eleven reentry-vehicle materials at elevated temperatures", Technical report AFFDL-TR-67-35, DASA, 1966. Part I of Final Report for DASA contract DA-49-149-XZ-322.
- [Guinan and Steinberg 1974] M. W. Guinan and D. J. Steinberg, "Pressure and temperature derivatives of the isotropic polycrystalline shear modulus for 65 elements", *J. Phys. Chem. Solids* **35** (1974), 1501–1512.
- [Guinan and Steinberg 1975] M. W. Guinan and D. J. Steinberg, "A simple approach to extrapolating measured polycrystalline shear moduli to very high pressure", *J. Phys. Chem. Solids* **36** (1975), 829–829.
- [Hodowany et al. 2000] J. Hodowany, G. Ravichandran, A. J. Rosakis, and P. Rosakis, "Partition of plastic work into heat and stored energy in metals", *Experimental Mechanics* **40**:2 (2000), 113–123.
- [Hoge 1966] K. G. Hoge, "Influence of strain rate on mechanical properties of 6061-T6 aluminum under uniaxial and biaxial states of stress", *Experimental Mechanics* **6** (1966), 204–211.
- [Holzapfel 1991a] W. B. Holzapfel, "Equation of state for ideal and real solids under strong compression", *Europhysics Letters* **16** (1991), 67–72.
- [Holzapfel 1991b] W. B. Holzapfel, "Equation of state for solids under strong compression", *High Pressure Research* **7** (1991), 290–293.
- [Jia and Ramesh 2004] D. Jia and K. T. Ramesh, "A rigorous assessment of the benefits of miniaturization in the Kolsky bar system", *Expt. Mechanics* **44**:5 (2004), 445–454.
- [Kanel et al. 2001] G. I. Kanel, S. V. Razorenov, K. Baumung, and J. Singer, "Dynamic yield and tensile strength of aluminum single crystals at temperatures up to the melting point", *J. Appl. Phys.* **90**:1 (2001), 136–143.
- [Kirkwood et al. 1949] J. G. Kirkwood, F. P. Buff, and M. S. Green, "The statistical mechanical theory of transport processes: III. T coefficients of shear and bulk viscosity of liquids", *The J. Chem. Phys.* **17**:19 (1949), 988–994.
- [Kocks 2001] U. F. Kocks, "Realistic constitutive relations for metal plasticity", *Materials Science and Engrg.* **A317** (2001), 181–187.
- [Kocks et al. 1975] U. F. Kocks, A. S. Argon, and M. F. Ashby, "Thermodynamics and Kinetics of Slip", pp. 1–289 in *Progress in Materials Science: Volume 19*, edited by B. Chalmers et al., Pergamon Press, Oxford, 1975.
- [Kumar and Kumble 1969] A. Kumar and R. G. Kumble, "Viscous drag on dislocations at high strain rates in copper", *J. Appl. Phys.* **40**:9 (1969), 3475–3480.
- [Lee et al. 2000] W. S. Lee, J. Shyu, and S. T. Chiou, "Effect of strain rate on impact response and dislocation substructure of 6061-T6 aluminum alloy", *Scripta Materialia* **42** (2000), 51–56.
- [Lesuer et al. 2001] D. R. Lesuer, G. J. Kay, and M. M. LeBlanc, "Modeling large-strain, high-rate deformation in metals", Technical report UCRL-JC-134118, Lawrence Livermore National Laboratory, Livermore, CA, 2001. Johnson-Cook plasticity model for 6061T6 Aluminum.
- [MacLeod 1996] A. MacLeod, "Algorithm 757, MISCFUN: A software package to compute uncommon special functions", *ACM Transactions on Mathematical Software* **22**:3 (1996), 288–301.

- [McQueen et al. 1970] R. G. McQueen, S. P. Marsh, J. W. Taylor, J. N. Fritz, and W. J. Carter, "The equation of state of solids from shock wave studies", pp. 294–417 in *High Velocity Impact Phenomena*, edited by R. Kinslow, Academic Press, New York, 1970.
- [Mitchell and Nellis 1981] A. C. Mitchell and W. J. Nellis, "Shock compression of aluminum, copper, and tantalum", *J. Appl. Phys.* **52**:5 (1981), 3363–3374.
- [Moelwyn-Hughes 1961] E. A. Moelwyn-Hughes, *Physical Chemistry: 2nd Edition*, Pergamon, Oxford, 1961.
- [Nadal and Le Poac 2003] M.-H. Nadal and P. Le Poac, "Continuous model for the shear modulus as a function of pressure and temperature up to the melting point: analysis and ultrasonic validation", *J. Appl. Phys.* **93**:5 (2003), 2472–2480.
- [Nadgorny 1988] E. Nadgorny, "Dislocation Dynamics and Mechanical Properties of Crystals", pp. 1–530 in *Progress in Materials Science: Volume 31*, edited by J. W. Christian et al., Pergamon Press, Oxford, 1988.
- [Ng et al. 1969] E. W. Ng, C. J. Devine, and R. F. Tooper, "Chebyshev polynomial expansion of Bose-Einstein functions of order 1 to 10", *Mathematics of Computation* **23**:107 (1969), 639–643.
- [Ogawa 2001] K. Ogawa, "Impact tensile characteristics of 6061-T6 aluminum alloy", *Journal of Japan Institute of Light Metals* **51**:3 (2001), 175–181.
- [Preston et al. 2003] D. L. Preston, D. L. Tonks, and D. C. Wallace, "Model of plastic deformation for extreme loading conditions", *J. Appl. Phys.* **93**:1 (2003), 211–220.
- [Puchi-Cabrera et al. 2001] E. S. Puchi-Cabrera, C. Villabos-Gutiérrez, and G. Castro-Fariñas, "On the mechanical threshold stress of aluminum: Effect of the alloying content", *ASME J. Engg. Mater. Tech.* **123** (April 2001), 155–161.
- [Ravichandran et al. 2001] G. Ravichandran, A. J. Rosakis, J. Hodowany, and P. Rosakis, "On the conversion of plastic work into heat during high-strain-rate deformation", pp. 557–562 in *Proc. , 12th APS Topical Conference on Shock Compression of Condensed Matter*, 2001.
- [Rosenberg et al. 1986] Z. Rosenberg, D. Dawicke, E. Strader, and S. Bless, "A new technique for heating specimens in split-Hopkinson-bar experiments using induction-coil heaters", *Exp. Mechanics* **26**:3 (1986), 157–173.
- [Sakino 2006] K. Sakino, "Strain rate dependence of dynamic flow stress considering viscous drag for 6061 aluminum alloy at high strain rates", *J. Phys. IV France* **134** (2006), 183–189.
- [Schreyer and Maudlin 2005] H. L. Schreyer and P. J. Maudlin, "Thermodynamically consistent relations involving plasticity, internal energy and thermal effects", *Phil. Trans. R. Soc. A* **363** (2005), 2517–2541.
- [Stegun 1972] I. A. Stegun, "Miscellaneous Functions", pp. 997–1010 in *Handbook of Mathematical Functions with Formulas, Graphs, and Mathematical Tables*, Dover, New York, 1972.
- [Steinberg et al. 1980] D. J. Steinberg, S. G. Cochran, and M. W. Guinan, "A constitutive model for metals applicable at high-strain rate", *J. Appl. Phys.* **51**:3 (1980), 1498–1504.
- [Sulsky et al. 1994] D. Sulsky, Z. Chen, and H. L. Schreyer, "A particle method for history dependent materials", *Comput. Methods Appl. Mech. Engrg.* **118** (1994), 179–196.
- [Sulsky et al. 1995] D. Sulsky, S. Zhou, and H. L. Schreyer, "Application of a particle-in-cell method to solid mechanics", *Computer Physics Communications* **87** (1995), 236–252.
- [Tallon and Wolfenden 1979] J. L. Tallon and A. Wolfenden, "Temperature dependence of the elastic constants of aluminum", *J. Phys. Chem. Solids* **40** (1979), 831–837.
- [Tonks 1993] D. L. Tonks, "Deviatoric stresses and plastic strain rates in strong shock waves for six metals", Technical report LA-12641, Los Alamos National Laboratory, New Mexico, 1993.
- [Truesdell 1945] C. Truesdell, "On a function which occurs in the theory of the structure of polymers", *The Annals of Mathematics: Series 2* **46**:1 (1945), 144–157.
- [Vaidya and C. 1970] S. N. Vaidya and K. G. C., "Compressibility of 18 metals to 45 kbar", *Phys. Chem. Solids* **31** (1970), 2329–2345.
- [Vocadlo and Alfe 2002] L. Vocadlo and D. Alfe, "Ab initio melting curve of the fcc phase of aluminum", *Physical Rev. B* **65** (2002), 214105–1–12.
- [Wallace 1981a] D. C. Wallace, "Irreversible thermodynamics of overdriven shocks in solids", *Physical Review B* **24**:10 (1981), 5597–5606.

- [Wallace 1981b] D. C. Wallace, “Nature of the process of overdriven shocks in metals”, *Physical Review B* **24**:10 (1981), 5607–5615.
- [Wang et al. 1998] J. Wang, Q. F. Fang, and Z. G. Zhu, “Sensitivity of Ultrasonic Attenuation and Velocity Change to Cyclic Deformation in Pure Aluminum”, *Phys. Stat. Sol.* **169** (1998), 43–48.
- [Wolfer 1999] W. G. Wolfer, “Phonon drag on dislocations at high pressures”, Technical report UCRL-ID-136221, Lawrence Livermore National Laboratory, Livermore, California, 1999.
- [Wright 2002] T. W. Wright, *The Physics and Mathematics of Adiabatic Shear Bands*, Cambridge University Press, Cambridge, UK, 2002.
- [Yadav et al. 1995] S. Yadav, D. Chichili, and K. Ramesh, “The mechanical response of 6061-T6 Al/Al₂O₃ metal matrix composite at high rates of deformation”, *Acta Metall. Mater.* **43** (1995), 4453–4464.
- [Zerilli and Armstrong 1987] F. J. Zerilli and R. W. Armstrong, “Dislocation-mechanics-based constitutive relations for material dynamics calculations”, *J. Appl. Phys.* **61**:5 (1987), 1816–1825.

Received 11 Jan 2007. Revised 3 Jun 2007. Accepted 6 Aug 2007.

BISWAJIT BANERJEE: banerjee@eng.utah.edu

Department of Mechanical Engineering, University of Utah, 50 S. Central Campus Dr., Salt Lake City, UT 84112, United States

ANUP SATISH BHAWALKAR: anup.bhawalkar@utah.edu

Brahma Group, Inc., 570 West 800 South, Salt Lake City, UT 84101, United States

THE EFFECT OF TAPER ON SECTION CONSTANTS FOR IN-PLANE DEFORMATION OF AN ISOTROPIC STRIP

DEWEY H. HODGES, JIMMY C. HO AND WENBIN YU

The variational-asymptotic method is used to obtain an asymptotically-exact expression for the strain energy of a tapered strip-beam. The strip is assumed to be sufficiently thin to warrant the use of two-dimensional elasticity. The taper is represented by a nondimensional constant of the same order as the ratio of the maximum cross-sectional width to the wavelength of the deformation along the beam, and thus its cube is negligible compared to unity. The resulting asymptotically-exact section constants, being functions of the taper parameter, are then used to find section constants for a generalized Timoshenko beam theory. These generalized Timoshenko section constants are then used in the associated one-dimensional beam equations to obtain the solution for the deformation of a linearly tapered beam subject to pure axial, pure bending, and transverse shear forces. These beam solutions are then compared with plane stress elasticity solutions, developed for extension, bending, and flexure of a linearly tapered isotropic strip. The agreement is excellent, and the results show that correction of the section constants using the taper parameter is necessary in order for beam theory to yield accurate results for a tapered beam.

1. Introduction

According to Euler–Bernoulli beam theory for pure bending of a uniform beam made of isotropic material with Young’s modulus E , the strain energy per unit length is given by

$$U = \frac{1}{2}EI\kappa^2,$$

where κ is the curvature of the beam neutral axis (the locus of cross-sectional area centroids) and I is the cross-sectional area moment of inertia. The bending stiffness according to Euler–Bernoulli theory is EI . For nonuniform beams it is typical that the bending stiffness is regarded as $EI(x)$, with x being the beam axial coordinate. For example, for a beam with narrow rectangular cross-section of width $2b$ and thickness t , EI is given by

$$EI = \frac{Et(2b)^3}{12} = \frac{2Et b^3}{3}.$$

Customarily, this expression remains the same regardless of whether or not the beam is uniform. For example, when $b = b(x)$, one just replaces b with $b(x)$; the local taper of the beam $b'(x) = -\tau(x)$ does not further influence the local bending stiffness. [Boley 1963] showed that the accuracy of predictions by beam theory, performed in the described manner, worsened as τ increased.

Keywords: beam theory, asymptotic methods, dimensional reduction, tapered beam.

This research was supported in part by the Army Vertical Lift Research Center of Excellence at Georgia Institute of Technology and its affiliate program through subcontract at Utah State University. The technical monitor is Dr. Michael J. Rutkowski.

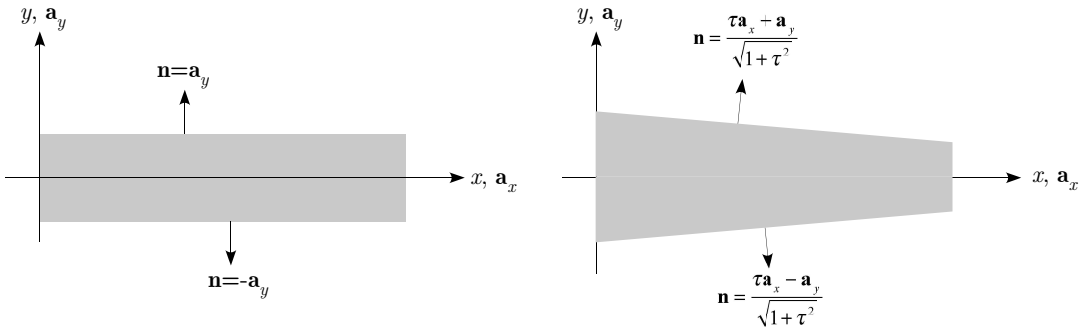


Figure 1. Contrast between a prismatic (left) and a tapered (right) beam.

In reality, taper introduces three-dimensional effects that cannot be accounted for by merely changing the sectional width in this formula. For example, stress at the boundaries of a solid continuum must conform to the traction-stress relationships from Cauchy's formula. Let us now introduce the y -axis as perpendicular to x along with unit vectors, \mathbf{a}_x and \mathbf{a}_y , parallel to x and y respectively. In [Figure 1](#) a prismatic beam is shown beside a linearly tapered beam. Comparing the two cases, one can easily see that neglecting the local taper parameter τ is equivalent to regarding the local upper and lower surface outward-directed normal vectors as parallel to \mathbf{a}_y , which is only true for beams with no taper. Instead, the true outward-directed normal vectors feature a component parallel to \mathbf{a}_x , omission of which means that the surface boundary conditions are erroneous. Cross-sectional analysis (for instance, solutions for the elastic constants used in a beam analysis) of tapered beams performed without consideration of taper would then be incorrect and thereby degrade results from one-dimensional beam analysis. The questions that must be answered are (a) how significant is this effect, and (b) is its inclusion tractable? [Krahula \[1975\]](#) obtained an exact plane stress elasticity solution for a tapered strip-beam undergoing flexure. This solution, along with others developed by [Timoshenko and Goodier \[1970\]](#) for pure extension and bending deformations, all three of which are included herein, provides a means to assess the error associated with omission of taper from the cross-sectional analysis of engineering beam theories for this simple configuration. It will also provide a means to assess the accuracy of more general cross-sectional analyses for spanwise nonuniform beams.

[Andrade and Camotim \[2005\]](#) considered this effect on the lateral-torsional buckling of I-beams. It was reported therein that taper can affect the local cross-sectional stiffnesses, expressions of which, if accurate, demonstrate that its effects are not, in general, negligible. For finite element analysis of linearly tapered I-beams, [Vu-Quoc and Léger \[1992\]](#) derived a flexibility matrix showing a dependence on τ ; however, the basis of their derivation is, at best, only an approximation, in that they assumed that the bending stress equation for a prismatic beam, $\sigma_{xx} = My/I$, remains valid in the presence of taper. For tapered monosymmetric I-beams, [Kitipornchai and Trahair \[1975\]](#) introduced additional section constants to account for taper while leaving the traditional section constants unaltered. [Ronagh et al. \[2000\]](#) also employed this approach for tapered beams of arbitrary cross-sectional geometries. A drawback of introducing additional constants is that it inevitably adds complexity to the beam analysis. There is relatively little other information in the literature regarding the effect of taper on the local

stiffness properties. On the other hand, beam analyses with stiffness (or flexibility) matrices formulated for numerical computations in [To 1981; Karabalis and Beskos 1983; Banerjee and Williams 1986; Cleghorn and Tabarrok 1992; Rajasekaran 1994; Tena-Colunga 1996] are only selected examples of the immense body of research performed on the analysis of tapered beams that does not consider the effect of taper on the cross-sectional constants and stress recovery relations.

Here the effect is examined from the point of view of an analytical treatment. In order to facilitate such a treatment, a tapered strip-beam is analyzed as a plane stress problem undergoing in-plane deformation.

The variational-asymptotic method (VAM) was developed by Berdichevsky and first used in construction of two-dimensional shell theory by dimensional reduction from three-dimensional elasticity theory (see [Berdichevsky 1979]). The VAM finds an asymptotically-exact approximation of the solution, to any desired order of accuracy, in terms of specified small parameters. The suitability of VAM for development of one-dimensional beam theory was shown by Berdichevsky [1981]. [Hodges 2006] and many references cited therein provide sample derivations for applying the VAM to the analysis of beams.

In this paper the VAM is used in Section 2 to analyze the in-plane deformation of a thin strip-beam and obtain its strain energy per unit length. In Section 3, this strain energy is repackaged into a generalized Timoshenko framework. In Section 4, the resulting generalized Timoshenko theory, with its modified bending and shear stiffnesses, is used to analyze the classical pure extension, pure bending, and flexure problems associated with the in-plane deformation of a linearly tapered beam. In Section 5, three elasticity solutions are presented for the pure extension, pure bending, and flexure problems. In Section 6, the elasticity results are compared with the beam solution. Finally, conclusions are drawn.

2. Beam strain energy per unit length

Beam theory requires an expression for the strain energy per unit length in terms of generalized strains that depend only on the axial coordinate. The process of finding this expression, to be rigorous, must begin with the strain energy for the accompanying elasticity problem on which dimensional reduction is being performed. As discussed in [Hodges 2006], and many papers cited therein (for example, [Cesnik and Hodges 1997; Yu et al. 2002]), dimensional reduction is based on the identification and exploitation of various small parameters, and may be rigorously carried out by asymptotic methods. The VAM of [Berdichevsky 1979] allows one to work directly in terms of energy functionals and still take advantage of small parameters.

In this section we develop the strain energy per unit length for a linearly tapered strip-beam such as the one shown on the right side of Figure 1. The undeformed state is described following the methods of [Hodges 2006], where the position vector to an arbitrary point in the undeformed beam is taken to be

$$\hat{\mathbf{r}} = x\mathbf{a}_x + y\mathbf{a}_y = \mathbf{r} + y\mathbf{a}_y,$$

where the x -axis is the reference line of the undeformed beam, taken for convenience as the locus of cross-sectional centroids. The position vector to an arbitrary point in the deformed beam can be written as

$$\hat{\mathbf{R}} = \mathbf{R} + y\mathbf{T}_y + w_x(x, y)\mathbf{T}_x + w_y(x, y)\mathbf{T}_y, \quad (1)$$

where $\mathbf{R} = (x + u)\mathbf{a}_x + v\mathbf{a}_y$, \mathbf{T}_x is a unit vector tangent to the deformed reference line, and \mathbf{T}_y is normal to \mathbf{T}_x in the plane. If we only keep linear terms, then $\mathbf{T}_x = \mathbf{a}_x + v'\mathbf{a}_y$ and $\mathbf{T}_y = -v'\mathbf{a}_x + \mathbf{a}_y$. The

displacement field is thus described in terms of beam variables $u(x)$, $v(x)$ along with warping functions $w_x(x, y)$ and $w_y(x, y)$. For the dimensional reduction, the warping functions are unknown at the outset but are solved for in the procedure. Two constraints on the warping are needed to make the displacement field unique. These constraints are not unique, so we choose to follow [Hodges 2006] in letting

$$\langle \hat{\mathbf{R}} \rangle = 2b\mathbf{R}, \tag{2}$$

where

$$\langle (\bullet) \rangle = \int_{-b(x)}^{b(x)} (\bullet) dy.$$

Equation (2) implies that

$$\langle w_x \rangle = \langle w_y \rangle = 0. \tag{3}$$

The beam is assumed to be homogeneous and isotropic, and the entire development is linear throughout. Under assumption of plane stress, appropriate for a thin body such as this one, twice the strain energy per unit length is given by

$$2U = \frac{Et}{1-\nu^2} \left\langle \Gamma_{xx}^2 + \Gamma_{yy}^2 + 2\nu\Gamma_{xx}\Gamma_{yy} + \frac{(1-\nu)}{2}\Gamma_{xy}^2 \right\rangle, \tag{4}$$

where ν is Poisson’s ratio. According to the displacement field spelled out in Equation (1), the two-dimensional strain components are

$$\Gamma_{xx} = \bar{\epsilon} - y\bar{\kappa} + w'_x, \quad \Gamma_{yy} = w_{y,y}, \quad \Gamma_{xy} = w_{x,y} + w'_y, \tag{5}$$

where (\prime) means the partial derivative with respect to x and $(\prime)_y$ means the partial derivative with respect to y . The one-dimensional generalized strains are $\bar{\epsilon}$ and $\bar{\kappa}$, both functions of x . Here $\bar{\kappa} = v''(x)$ is the usual curvature of the reference line of Euler–Bernoulli beam theory, and $\bar{\epsilon} = u'(x)$ is the stretching of the reference line. The one-dimensional generalized strains are taken as known in the dimensional reduction procedure.

There are three small parameters that can be identified. First, the strain is small compared to unity. It is straightforward to show that both $\bar{\epsilon}$ and $a\bar{\kappa}$ are $O(\epsilon)$, where ϵ denotes the maximum strain, and $a = b(0)$ the maximum value taken on by y in the structure. The second small parameter is a/ℓ where ℓ is the wavelength of deformation along the beam, such that $\partial(\bullet)/\partial x = O(\bullet/\ell)$. Finally, in this study we select the nondimensional taper parameter τ as a small parameter. Because our problem is linear, the strain will only enter the strain energy quadratically, so the smallness of strain has no real effect on the formulation. For simplicity, we take a/ℓ and τ to be of the same order, $O(\delta)$, and will ultimately ignore δ^3 compared to unity.

The VAM procedure is summarized as follows:

- (i) Identify and remove all terms $O(\delta)$ and higher in the strain.
- (ii) Use this resulting zeroth-order approximation of the strain to form the zeroth-order approximation of the strain energy in terms of the warping.
- (iii) Minimize the zeroth-order approximation of strain energy with respect to the warping to obtain the zeroth-order approximation of the warping.

- (iv) Perturb the resulting zeroth-order warping by one order of δ and use the perturbed warping to express the strain components to a sufficiently high order approximation so that the energy contains all $O(\delta^2)$ terms and all higher-order terms are dropped.
- (v) Minimize this second-order approximation of the energy with respect to the warping function perturbations.
- (vi) Substitute the result for the warping back into the original strain energy and discard all terms of orders higher than $O(\delta^2)$.

The result is the asymptotically-exact strain energy per unit length.

To begin we write twice the zeroth-order approximation of the energy, tantamount to ignoring δ altogether, as

$$2U_0 = \left\langle \frac{Et}{1-\nu^2} \left[(\bar{\epsilon} - y\bar{\kappa})^2 + 2\nu w_{y,y} (\bar{\epsilon} - y\bar{\kappa}) + \frac{(1-\nu)w_{x,y}^2}{2} + w_{y,y}^2 \right] - 2\lambda_x w_x - 2\lambda_y w_y \right\rangle,$$

where Lagrange multipliers λ_x and λ_y are used to enforce constraints on the warping. The warping field that minimizes U_0 can be found as

$$w_x = 0, \quad w_y = -\nu\bar{\epsilon}y + \frac{\nu\bar{\kappa}}{2} \left(y^2 - \frac{b^2}{3} \right).$$

Plugging this warping field back into the expression for $2U_0$, one obtains twice the zeroth-order energy as

$$2U_0 = 2Ebt\bar{\epsilon}^2 + \frac{2}{3}Etb^3\bar{\kappa}^2, \quad (6)$$

which is consistent with Euler–Bernoulli theory. Note that Equation (6) is derived without ad hoc assumptions such as assuming the cross section to be rigid in its own plane or assuming that $\nu = 0$. Such assumptions are sometimes used to derive classical beam theory, but they are neither necessary nor correct.

For the next approximation to the one-dimensional energy, we first perturb the above approximation of warping to arrive at

$$w_x = v_x, \quad w_y = -\nu\bar{\epsilon}y + \frac{\nu\bar{\kappa}}{2} \left(y^2 - \frac{b^2}{3} \right) + v_y,$$

where v_x is the perturbation of w_x , and v_y is the perturbation of w_y ; v_x and v_y are of one order higher in δ than w_x and w_y .

This new warping field is then substituted into the strain components from (5), at which point a new expression for the two-dimensional strain energy arises from (4) by virtue of the new strain components. Here one must be careful to retain all terms up through $O(\delta^2)$ and drop all terms of higher order in the energy, so now we find

$$2U_2 = \frac{Et}{1-\nu^2} \left\{ \frac{1-\nu}{2} \left\langle \left[\frac{\nu\tau b\bar{\kappa}}{3} - y\nu\bar{\epsilon}' + \frac{\nu(3y^2-b^2)\bar{\kappa}'}{6} + v_{x,y} \right]^2 \right\rangle + \left\langle v_{y,y}^2 + 2v'_x(1-\nu^2)(\bar{\epsilon} - y\bar{\kappa}) \right\rangle \right\}.$$

Expressions for the perturbation variables, v_x and v_y , that minimize U_2 subject to the constraints in (3) must be found; the constraints are again enforced by use of Lagrange multipliers, Λ_x and Λ_y ,

respectively. The stationary point of U_2 is found by setting its first variation equal to zero, which leads to the two Euler–Lagrange equations

$$\frac{\partial U_2}{\partial v_x} - \left(\frac{\partial U_2}{\partial v'_x} \right)' - \left(\frac{\partial U_2}{\partial v_{x,y}} \right)_{,y} = \Lambda_x, \quad \frac{\partial U_2}{\partial v_y} - \left(\frac{\partial U_2}{\partial v_{y,y}} \right)_{,y} = \Lambda_y, \quad (7)$$

along with corresponding natural boundary conditions

$$\frac{\partial U_2}{\partial v_{x,y}} \Big|_{y=\pm b(x)} = 0, \quad \frac{\partial U_2}{\partial v_{y,y}} \Big|_{y=\pm b(x)} = 0. \quad (8)$$

According to Saint-Venant’s principle, boundary conditions, the warping at the beam ends (not shown) does not affect the behavior of the warping inside the beam and is not used in the solution of Equations (7) and (8).

Although both the Euler–Lagrange equations and boundary conditions for v_x and v_y look almost identical, the actual equations obtained are not. The Euler–Lagrange equation for v_y , the second equation of (7), reduces simply to $v_{y,yy} = 0$; from this and the second equation of (8), which requires $v_{y,y}$ to vanish at $y = \pm b$, one obtains by inspection that $\Lambda_x = v_y = 0$. On the other hand, the resulting Euler–Lagrange equation in v_x , the first part of Equation (7), can be simplified to

$$Et [(2 + \nu)(\bar{\epsilon}' - y\bar{\kappa}') + v_{x,yy}] + 2(1 + \nu)\Lambda_x = 0, \quad (9)$$

and the natural boundary conditions simplify to

$$\frac{y\tau(\bar{\epsilon} - y\bar{\kappa})}{b} + \frac{2\nu(\tau b\bar{\kappa} - 3y\bar{\epsilon}') + \nu(3y^2 - b^2)\bar{\kappa}' + 6v_{x,y}}{12(1 + \nu)} \Big|_{y=\pm b(x)} = 0. \quad (10)$$

Solving Equations (9) and (10) simultaneously gives the Lagrange multiplier as

$$\Lambda_x = Et \left(\frac{\tau\bar{\epsilon}}{b} - \bar{\epsilon}' \right),$$

and v_x as

$$v_x = \frac{\tau}{3b} [(1 + \nu)(b^2 - 3y^2)\bar{\epsilon} + y(5\nu + 6)b^2\bar{\kappa}] + \frac{1}{6} \{ \nu(3y^2 - b^2)\bar{\epsilon}' + [y^3(\nu + 2) - y(5\nu + 6)b^2]\bar{\kappa}' \}.$$

Note that the first term is $O(\tau)$ and the second is $O(a/\ell)$, so that the perturbation is indeed $O(\delta)$. It can also be easily checked that the traction-free boundary conditions are satisfied asymptotically to the order of the perturbation variables, $O(\delta)$.

With both perturbation variables now known, the second-order energy is also known. The strain energy per unit length, asymptotically correct up to second order in δ , is then the sum of U_0 and U_2 , and is equal to

$$U = Etb \left[1 - \frac{2}{3}(\nu + 1)\tau^2 \right] \bar{\epsilon}^2 + \frac{2Et\nu\tau b^2}{3} \bar{\epsilon}\bar{\epsilon}' + \frac{Etb^3}{9} [3 + 2(14\nu + 15)\tau^2] \bar{\kappa}^2 - \frac{4Et\tau(8\nu + 9)b^4}{9} \bar{\kappa}\bar{\kappa}' + \frac{4Et(1 + \nu)b^5}{15} \bar{\kappa}'^2 + \frac{2Et(11\nu + 12)b^5}{45} \bar{\kappa}\bar{\kappa}'', \quad (11)$$

which is of the same form as the refined beam theory presented in [Hodges 2006], namely

$$2U = S\bar{\epsilon}^2 + 2G\bar{\epsilon}\bar{\epsilon}' + A\bar{\kappa}^2 + 2B\bar{\kappa}\bar{\kappa}' + C\bar{\kappa}'^2 + 2D\bar{\kappa}\bar{\kappa}'', \quad (12)$$

with A , B , C , D , S , and G being scalars identified from Equation (11); they are implicit functions of x through the varying width $b(x)$ and explicit functions of τ . It is easy to see that terms A and S without τ correspond to those of Euler–Bernoulli theory. Terms with τ are the corrections from taper, and other terms from which τ is absent (C and D) pertain to shear deformation of prismatic beams.

3. Transformation to generalized Timoshenko form

The strain energy function developed in the previous section is not suitable for use as an engineering beam theory because of the presence of derivatives of $\bar{\epsilon}$ and $\bar{\kappa}$. It is known, however, that the form of (11) can be transformed into a generalized Timoshenko theory, which is the main objective of this section. Thus, the strain energy will be put into the form

$$2U^* = W\kappa^2 + 2X\kappa\gamma + Y\gamma^2 + Z\epsilon^2, \quad (13)$$

where W , X , Y , and Z are scalars, and with W , X , and Z being functions of τ , while γ is the one-dimensional beam engineering transverse shear measure. The shear strain measure γ turns out to be one order higher in δ than the classical measures of strain; therefore the energy from (11), which is second-order accurate, is sufficient to construct a generalized Timoshenko model. Note that after being put in this form the energy will no longer be asymptotically correct, because information is lost in the conversion process. Also, because γ is $O(\delta)$, Y will not have corrections from the taper parameter in a second-order correct strain energy. By inspection of (12), extension $\bar{\epsilon}$ is coupled only with its own derivative, hence we expect it will not be coupled with any other strain measures in (13).

The major difference between classical and Timoshenko theories is that classical theory neglects transverse shear strain while the generalized Timoshenko theory includes it, so the relationship between the two theories is established here. (The term *generalized* is used to emphasize the fact that the theory is not Timoshenko theory, nor is it based on any of the myriad assumptions of that theory. Moreover, the present theory includes the bending-shear coupling effect embodied in X .) As depicted in Figure 2, T_x

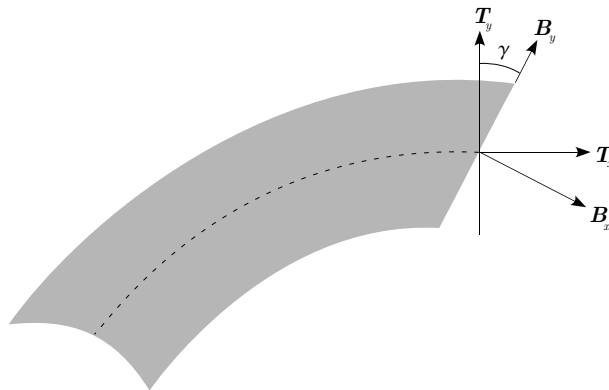


Figure 2. Coordinate systems used for transverse shear formulation.

and \mathbf{T}_y collectively represent the dyad associated with classical theory, whereas \mathbf{B}_x and \mathbf{B}_y represent the dyad associated with generalized Timoshenko theory. \mathbf{T}_x and \mathbf{T}_y are aligned as parallel to and normal to the beam reference axis respectively. \mathbf{B}_x and \mathbf{B}_y are then rotated clockwise by an angle from \mathbf{T}_x and \mathbf{T}_y so that \mathbf{B}_x is normal to the cross-sectional plane (which may be either defined as an average or at a point), so that

$$\mathbf{B}_x = \mathbf{T}_x - \gamma \mathbf{T}_y, \quad \mathbf{B}_y = \gamma \mathbf{T}_x + \mathbf{T}_y.$$

Following the procedure of [Hodges 2006], which assumes that the strain components are small, the axial force strain measure is identical for the two theories so that $\bar{\epsilon} = \epsilon$ and the relationship of moment strain between the two theories is given by

$$\bar{\kappa} = \kappa + \gamma'. \tag{14}$$

Due to the presence of the derivatives in $\bar{\kappa}$ in Equation (12), we also mention that the derivatives are

$$\bar{\kappa}' = \kappa' + \gamma'', \quad \bar{\kappa}'' = \kappa'' + \gamma''', \tag{15}$$

and that $v' = \theta + \gamma$, where θ is the total section rotation and $\kappa = \theta'$.

The derivatives of ϵ , κ , and γ must be written in terms of ϵ , κ , and γ , since the form of (13) contains no derivatives. The approach for eliminating the derivatives adopted here is to make use of the equilibrium equations. At each section the axial force (F), shear force (V), and bending moment (M) are, respectively,

$$F = \frac{\partial U^*}{\partial \epsilon} = Z\epsilon, \quad V = \frac{\partial U^*}{\partial \gamma} = X\kappa + Y\gamma, \quad M = \frac{\partial U^*}{\partial \kappa} = W\kappa + X\gamma.$$

In the absence of applied loading within the beam, the equilibrium equations are then

$$\begin{aligned} F' &= Z\epsilon' + Z'\epsilon = 0, \\ V' &= Y\gamma' + X\kappa' + Y'\gamma + X'\kappa = 0, \\ M' + V &= X\gamma' + W\kappa' + (X' + Y)\gamma + (W' + X)\kappa = 0. \end{aligned} \tag{16}$$

The above represents a system of equations which can be used to solve for ϵ' , γ' , and κ' in terms of ϵ , γ , and κ . The higher derivatives can then be obtained, in terms of ϵ , γ , and κ , by directly taking derivatives of (16). The resulting expressions are too lengthy to include here, but suffice it to say that the procedure is not at all challenging for symbolic computational tools such as Mathematica.

The desired strain energy of the beam, in the form of (13), can now be obtained by substituting Equations (14) and (15), along with the described approach for eliminating derivatives, into (12). Comparing the resultant second-order approximation to the strain energy with (13), one obtains the section constants as

$$\begin{aligned} W &= \frac{2Et b^3}{3} \left[1 + \frac{(\nu - 48)\nu - 45}{45(\nu + 1)} \tau^2 \right], & X &= \frac{Et(5\nu + 3)b^2\tau}{9(\nu + 1)}, \\ Y &= \frac{5Et b}{6(\nu + 1)}, & Z &= 2Et b \left(1 - \frac{2\tau^2}{3} \right). \end{aligned}$$

The terms involving $\tau = -b'(x)$ are the corrections from our having included taper. From these expressions, we can observe that W is proportional to b^3 and is a quadratic polynomial in τ , X is proportional

to b^2 and is linear in τ , Y is proportional to b and is independent of τ , and Z is proportional to b and is a quadratic polynomial in τ^2 .

According to Renton [1991] there is no consensus on the precise definition of shear stiffness; thus, even though the expression for Y corresponds to results from [Washizu 1968; Young 1989; Renton 1991], it may not match those of other definitions.

4. Beam analysis of classical elasticity problems

4.1. Pure extension. In pure extension, a beam of length l is loaded at each end by equal and opposite axial tensile forces of magnitude T , depicted in Figure 3 for $Q = 0$. The potential of the applied loads is thus

$$\Phi = -T[u(l) - u(0)] = -T \int_0^l u' dx = -T \int_0^l \epsilon dx.$$

According to the principle of virtual work, the system is in equilibrium if and only if the variation of its total potential is zero. Upon setting the variation of the total potential equal to zero without imposing any geometric boundary conditions, one obtains

$$\int_0^l (W\kappa\delta\kappa + X\gamma\delta\kappa + X\kappa\delta\gamma + Y\gamma\delta\gamma + Z\epsilon\delta\epsilon - T\delta\epsilon) dx = 0.$$

The above equation requires the internal axial force, F , to be $F = Z\epsilon = T$. One can easily see that the elongation strain is

$$\epsilon = \frac{T}{Z}, \quad (17)$$

knowledge of which allows us to then integrate the kinematical differential equation $u' = \epsilon$ to obtain $u(x)$ for any given spanwise variation of the section constant Z . According to the model obtained from the VAM, the displacement $u(x)$ can be related directly to the elasticity solution in terms of the average axial displacement over the section.

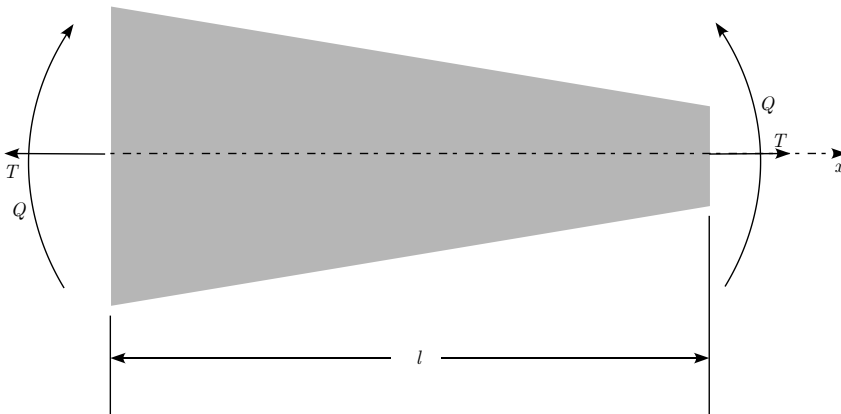


Figure 3. Schematic of beam loaded for either pure extension or pure bending.

4.2. Pure bending. To solve the pure bending problem, we use the kinematical differential equation $\kappa = \theta'$ and apply equal and opposite moments of magnitude Q on the ends of the beam. [Figure 3](#), with $T = 0$, illustrates this case. This yields a potential of the applied loads of the form

$$\Phi = -Q[\theta(l) - \theta(0)] = -Q \int_0^l \theta' dx = -Q \int_0^l \kappa dx.$$

Equilibrium equations can then be found by minimizing the total potential subject to no geometric boundary conditions. The result is

$$\int_0^l (W\kappa\delta\kappa + X\gamma\delta\kappa + X\kappa\delta\gamma + Y\gamma\delta\gamma + Z\epsilon\delta\epsilon - Q\delta\kappa) dx = 0.$$

The resulting Euler–Lagrange equations require that the bending moment and shear force are, respectively,

$$M = W\kappa + X\gamma = Q, \quad V = X\kappa + Y\gamma = 0.$$

Thus, eliminating $\gamma = -X\kappa/Y$, one obtains

$$\left(W - \frac{X^2}{Y}\right)\kappa = Q.$$

The solution can then be written as

$$\kappa = \frac{Q}{W - \frac{X^2}{Y}}, \tag{18}$$

which allows one to integrate the kinematical differential equation, $\theta' = \kappa$, to obtain $\theta(x)$ for any given spanwise variation of W , X , and Y . Unlike the prismatic case, even though Q is constant, κ is not. Moreover, the transverse displacement $v(x)$ can then be obtained by integration of another kinematical differential equation, $v' = \theta + \gamma = \theta - X\kappa/Y$. It is clear that loading by pure bending produces transverse shear deformation in a tapered beam.

4.3. Flexure. For the flexure problem, we load the beam with an equal and opposite transverse force P at each end, and a moment Pl at the left end to counteract the moment of the force at the right end (see [Figure 4](#)). For this loading the potential of the applied loads takes the form

$$\Phi = -P[v(l) - v(0)] + Pl\theta(0) = -P \int_0^l [(v' - \theta) + (l - x)\theta'] dx = -P \int_0^l [\gamma + (l - x)\kappa] dx.$$

Equilibrium equations can then be found by minimizing the total potential subject to no geometric boundary conditions. The result is

$$\int_0^l \{W\kappa\delta\kappa + X\gamma\delta\kappa + X\kappa\delta\gamma + Y\gamma\delta\gamma + Z\epsilon\delta\epsilon - P[\delta\gamma + (l - x)\delta\kappa]\} dx = 0.$$

The resulting Euler–Lagrange equations and boundary conditions require that the bending moment and shear force are, respectively,

$$M = W\kappa + X\gamma = P(l - x), \quad V = X\kappa + Y\gamma = P.$$

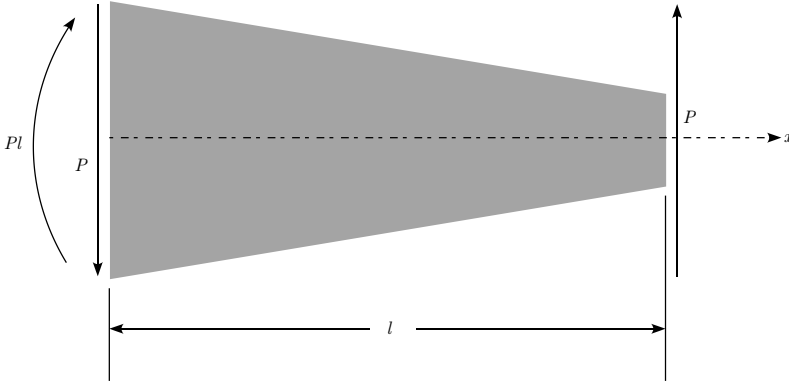


Figure 4. Schematic of beam loaded for flexure.

Thus, one obtains

$$\kappa = \frac{P}{WY - X^2} [Y(l - x) - X], \quad \gamma = \frac{P}{WY - X^2} [W - X(l - x)], \quad (19)$$

which allows one to integrate the same kinematical differential equations as in the pure bending case to obtain the total section rotation $\theta(x)$ and the displacement of the neutral axis $v(x)$ for any given spanwise variation of W , X , and Y . Unlike the prismatic case, although the bending moment is linear, κ is not. Also, although the shear force is constant, γ is not constant.

5. Solutions for classical elasticity problems

This section presents exact solutions for the purpose of comparing with the above beam solutions based on a refined beam theory. These solutions are appropriately based on linear, plane stress elasticity theory for a linearly tapered strip for problems of pure extension, pure bending, and flexure. For all three cases, the components of the stress tensor are presented (σ_{xx} , σ_{xy} , and σ_{yy}). Components of the strain tensor may then be obtained from the plane stress form of Hooke's law. Lastly, the strains can be integrated to obtain displacements, $u_x(x, y)$ and $u_y(x, y)$. In the formulae that ensue, the y -coordinate varies between $\pm b(x)$, where $b = a - x\tau$, a is the half-width of the strip at $x = 0$, $h = a - l\tau > 0$ is the half-width of the strip at $x = l$, t is the thickness of the strip, l is its length (not to be confused with the wavelength ℓ that was previously used), and $s = l - x$.

We now set forth a way to extract information from the elasticity solutions so that the results can be compared with those from the beam solutions. Let us denote the displacement fields from elasticity by $u_x(x, y)$ and $u_y(x, y)$. These can be related to those from beam theory by making use of Equation (1), yielding

$$u_x = u - yv' + w_x, \quad u_y = v + w_y, \quad (20)$$

where we have earlier approximated the warping displacements. Integrating both sides of Equation (20) over y and using the constraints on the warping, one obtains

$$u = \frac{1}{2b} \langle u_x \rangle, \quad v = \frac{1}{2b} \langle u_y \rangle. \quad (21)$$

Multiplying both sides of the first part of Equation (20) by y and integrating allows us to identify

$$\theta = \frac{3}{2b^3} \langle -yu_x \rangle, \quad \gamma = v' - \theta = \frac{3}{2b^3} \langle yw_x \rangle. \quad (22)$$

Finally, the stretching and bending strain measures, $\epsilon = u'$ and $\kappa = \theta'$, along with the shear strain measure γ , can now be compared directly with results from applying the beam theory to a specific problem such as pure extension, pure bending or flexure.

5.1. Pure extension. The solution for the deformation of a wedge described by polar coordinates r and ϕ , presented in [Timoshenko and Goodier 1970, p. 110], is quite simple. The stresses for this case are

$$\sigma_\phi = \sigma_{r\phi} = 0, \quad \sigma_r = \frac{T \cos \phi}{rt (\alpha + \cos \alpha \sin \alpha)},$$

where, referring back to Figure 3, $Q = 0$, T is nonzero, and

$$\alpha = \tan^{-1} \tau, \quad r = \sqrt{y^2 + \frac{b^2}{\tau^2}}, \quad \phi = \tan^{-1} \left(\frac{y\tau}{b} \right).$$

The stresses in the Cartesian system can be found as

$$\sigma_{xx} = \sigma_r \cos^2 \phi - \sigma_{r\phi} \sin 2\phi, \quad \sigma_{xy} = -\sigma_{r\phi} \cos 2\phi - \frac{1}{2} \sigma_r \sin 2\phi, \quad \sigma_{yy} = \sigma_r \sin^2 \phi + \sigma_{r\phi} \cos 2\phi.$$

In terms of the geometric parameters and loads, the stresses finally become

$$\begin{aligned} \sigma_{xx} &= \frac{T\tau b^3 (\tau^2 + 1)}{t (b^2 + y^2 \tau^2)^2 [\tau + (\tau^2 + 1) \tan^{-1}(\tau)]}, & \sigma_{xy} &= -\frac{T y \tau^2 b^2 (\tau^2 + 1)}{t (b^2 + y^2 \tau^2)^2 [\tau + (\tau^2 + 1) \tan^{-1}(\tau)]}, \\ \sigma_{yy} &= \frac{T y^2 \tau^3 b (\tau^2 + 1)}{t (b^2 + y^2 \tau^2)^2 [\tau + (\tau^2 + 1) \tan^{-1}(\tau)]}. \end{aligned}$$

5.2. Pure bending. This case is also shown in Figure 3, here with $T = 0$ and Q nonzero. The stresses in polar coordinates are given by Timoshenko and Goodier [1970, pp. 112–13], as $\sigma_\phi = 0$ and

$$\sigma_r = \frac{2Q \sin 2\phi}{r^2 t (2\alpha \cos 2\alpha - \sin 2\alpha)}, \quad \sigma_{r\phi} = -\frac{Q (\cos 2\phi - \cos 2\alpha)}{r^2 t (2\alpha \cos 2\alpha - \sin 2\alpha)}.$$

Making the above transformation to Cartesian coordinates, one may obtain the stresses as

$$\begin{aligned} \sigma_{xx} &= -\frac{2bQy\tau^3 [b^2 (2\tau^2 + 1) - y^2 \tau^2]}{t (b^2 + y^2 \tau^2)^3 [\tau + (\tau^2 - 1) \tan^{-1}(\tau)]}, & \sigma_{xy} &= -\frac{Q\tau^4 [b^4 - 3y^2 (\tau^2 + 1) b^2 + y^4 \tau^2]}{t (b^2 + y^2 \tau^2)^3 [\tau + (\tau^2 - 1) \tan^{-1}(\tau)]}, \\ \sigma_{yy} &= \frac{2bQy\tau^5 [b^2 - y^2 (\tau^2 + 2)]}{t (b^2 + y^2 \tau^2)^3 [\tau + (\tau^2 - 1) \tan^{-1}(\tau)]}. \end{aligned}$$

To visualize the deformed shape, finite element analysis was performed using ABAQUS. The deformed shape of the structure is shown in Figure 5. To eliminate rigid body motion, the geometric boundary conditions were set as $u_x = u_y = 0$ at the point $(x = 0, y = 0)$ and $u_y = 0$ at the point $(x = l, y = 0)$. Modeling in ABAQUS was done using its CPS8R elements, and its results were validated with the

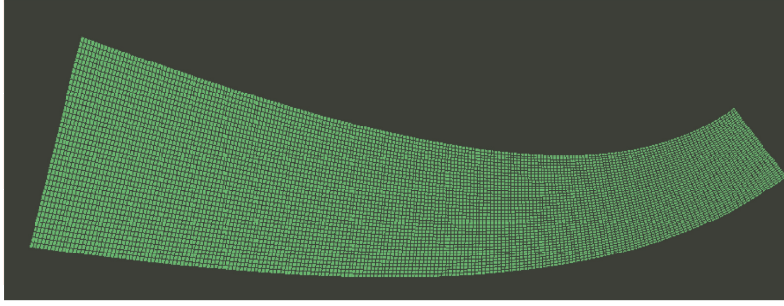


Figure 5. Deformed shape of the tapered strip under pure bending.

l (m)	a (m)	τ	t (m)	E (GPa)	ν	Q (N-m)
20	3	0.1	0.1875	200	0.3	1

Table 1. Dimensions, material properties, and loading for the tapered strip evaluated for ABAQUS calculations.

elasticity solution. The specific dimensions, material properties, and loading chosen are given in Table 1. It is clear that κ increases as the width of the structure decreases.

5.3. Flexure. The stresses of this case, shown in Figure 4, are given in polar coordinates by Krahula [1975], with $\sigma_\phi = 0$ and

$$\sigma_r = \frac{2P}{r^2t} \left[\frac{r \sin \phi}{\sin 2\alpha - 2\alpha} + \frac{(l - a \cot \alpha) \sin 2\phi}{2\alpha \cos 2\alpha - \sin 2\alpha} \right], \quad \sigma_{r\phi} = - \frac{P(\cos 2\phi - \cos 2\alpha) \cot \alpha (a - l \tan \alpha)}{r^2t(\sin 2\alpha - 2\alpha \cos 2\alpha)}.$$

(It is noted that several small printing mistakes in the paper had to be corrected in order to obtain this result.) Making the transformation to Cartesian coordinates, one finds the stresses to be

$$\begin{aligned} \sigma_{xx} &= \frac{bPy\tau^2}{t(b^2 + y^2\tau^2)^3} \left\{ \frac{2h[b^2 + (2b^2 - y^2)\tau^2]}{\tau + (\tau^2 - 1)\tan^{-1}(\tau)} - \frac{b(\tau^2 + 1)(b^2 + y^2\tau^2)}{(\tau^2 + 1)\tan^{-1}(\tau) - \tau} \right\}, \\ \sigma_{yy} &= - \frac{Py\tau^4}{t(b^2 + y^2\tau^2)^3} \left\{ \frac{(\tau^2 + 1)(b^2 + y^2\tau^2)y^2}{(\tau^2 + 1)\tan^{-1}(\tau) - \tau} + \frac{2bh[b^2 - y^2(\tau^2 + 2)]}{\tau + (\tau^2 - 1)\tan^{-1}(\tau)} \right\}, \\ \sigma_{xy} &= - \frac{P\tau^4[b^5 - s\tau b^4 - 4y^2(\tau^2 + 1)b^3 + 3sy^2\tau(\tau^2 + 1)b^2 - y^4\tau^4b - sy^4\tau^3]}{t(b^2 + y^2\tau^2)^3 \left\{ 2\tau \tan^{-1}(\tau) + (\tau^4 - 1) [\tan^{-1}(\tau)]^2 - \tau^2 \right\}} \\ &\quad + \frac{P\tau^3(\tau^2 + 1)[b^5 - s\tau b^4 - 2y^2(\tau^2 + 2)b^3 + 3sy^2\tau(\tau^2 + 1)b^2 + y^4\tau^4b - sy^4\tau^3] \tan^{-1}(\tau)}{t(b^2 + y^2\tau^2)^3 \left\{ 2\tau \tan^{-1}(\tau) + (\tau^4 - 1) [\tan^{-1}(\tau)]^2 - \tau^2 \right\}}. \end{aligned}$$

6. Comparison

In this section we wish to compare the beam section constants obtained by the VAM with results for the same quantities extracted from our elasticity solutions. To do so, the one-dimensional displacement and rotation variables u , v , and θ are extracted from the elasticity solutions above by averaging two-dimensional displacements over y in accordance with Equations (21) and (22). Then these quantities are differentiated with respect to x , leading to the values of one-dimensional generalized strains ϵ , γ , and κ . Finally, effective stiffnesses are found by dividing appropriate applied loads by corresponding one-dimensional generalized strains. These effective stiffnesses are then compared directly with values of the section constants determined from the VAM.

6.1. Pure extension. For pure extension, it is appropriate to compare the quantity T/ϵ using the stiffness constants obtained from the VAM with an expansion of the elasticity solution in τ . The beam solution, from Equation (17), and the second-order asymptotic expansion of the elasticity solution both agree that this quantity is

$$\frac{T}{\epsilon} = Z = 2Etb \left(1 - \frac{2\tau^2}{3} \right).$$

The term involving τ^2 represents the correction to taper. The perfect agreement of these two solutions reflects that the strain energy from the classical model is asymptotically exact for this problem, which is expected because shearing deformations are not involved in pure extension. For a section with a linear taper of $\tau = 0.1763$, which corresponds to 10° taper, and is not uncommon as local taper on rotor blades, the axial stiffness is overpredicted by 2.12% if the taper effect is neglected.

6.2. Pure bending. The quantity to be compared for this problem is Q/κ . The beam solution, from Equation (18) is

$$\frac{Q}{\kappa} = W - \frac{X^2}{Y} = \frac{2Etb^3}{3} - \frac{4Etb^3(4\nu + 9)\tau^2}{45},$$

whereas the second-order asymptotic expansion of the elasticity solution yields

$$\frac{Q}{\kappa} = \frac{2Etb^3}{3} - \frac{4Etb^3(\nu + 3)\tau^2}{15}.$$

For a linear taper of $\alpha = 10^\circ$ and $\nu = 0.3$, the taper effect reduces the bending stiffness by 4.28% and 4.42% from the elasticity and beam solutions respectively. The relative difference between the beam solution and the elasticity solution is $2\nu\tau^2/15$, with the beam solution being softer. This small difference between the asymptotic expansion of the exact solution versus the beam results can be attributed to our having approximated the asymptotically-exact energy, Equation (11), by forcing it into the mold of the generalized Timoshenko model, Equation (13). Obviously, the correction due to taper is itself much larger than the difference between the elasticity and beam solutions.

6.3. Flexure. For the flexure problem we compare the quantities P/κ and P/γ at $x = l$. The beam solution, Equation (19), yields

$$\frac{P}{\kappa} = X - \frac{WY}{X} = -\frac{5Etb^2}{(3 + 5\nu)\tau} + O(\tau), \quad \frac{P}{\gamma} = Y - \frac{X^2}{W} = \frac{5Etb}{6(1 + \nu)} + O(\tau^2) = \frac{5Gtb}{3} + O(\tau^2).$$

An order of magnitude analysis shows that we cannot trust either of the correction terms to these results, because we do not have sufficient data to ensure that we have all the contributions to them. That is to say, the VAM solution would have to be extended to include terms of higher order in τ than we needed to construct the beam model; in particular corrections of third-order to X and second-order to Y would be needed. As expected, the elasticity solution is in agreement with the above P/γ result since it does not involve taper. It should be noted, however, that there is more than one possible result from this exercise. The method of [Yu and Hodges 2004] was used here. The result for P/κ does involve taper and is given by

$$\frac{P}{\kappa} = -\frac{10Et b^2}{3(2+3\nu)\tau} + O(\tau).$$

The beam solution differs from the elasticity solution by less than 4% for practical values of ν . Note that this term tends to infinity as taper decreases and the beam approaches being prismatic.

7. Conclusion

A beam model is constructed using the variational-asymptotic method that is capable of handling extension, in-plane bending, and in-plane shear for a homogeneous, isotropic strip-beam, the width of which is linearly tapered along the span. The resulting beam model reveals that (a) section constants are influenced by the local taper such that $b'(x) = -\tau$ appears explicitly, and (b) bending and shear deformation are coupled by τ in the resulting model. To validate the theory, solutions for the corresponding plane stress elasticity problems for pure extension, pure bending, and flexure are presented, and the corrections caused by $\tau \neq 0$ are found. Excellent agreement is demonstrated between the elasticity solutions and the beam solutions based on the constructed model.

Examples of this influence include a decrease in both axial and bending stiffnesses, the latter being large enough that its neglect cannot be justified for tapered beams. To avoid errors, the taper effect must be accounted for in the cross-sectional analysis prior to performing the beam analysis. The present results will be of practical use in validating general cross-sectional analyses when they are eventually extended to include the influence of taper. In particular, additional work is needed to account for this effect in the cross-sectional analysis of spanwise nonuniform composite beams with arbitrary cross-sectional geometries and to determine asymptotically-exact strain/stress recovery relations.

References

- [Andrade and Camotim 2005] A. Andrade and D. Camotim, “Lateral-torsional buckling of singly symmetric tapered beams: theory and applications”, *J. Eng. Mech.* **131**:6 (2005), 586–597.
- [Banerjee and Williams 1986] J. Banerjee and F. Williams, “Exact Bernoulli-Euler static stiffness matrix for a range of tapered beam columns”, *Int. J. Numer. Meth. Eng.* **23**:9 (1986), 1615–1628.
- [Berdichevsky 1979] V. L. Berdichevsky, “Variational-asymptotic method of constructing a theory of shells”, *PMM* **43**:4 (1979), 664–687.
- [Berdichevsky 1981] V. L. Berdichevsky, “On the energy of an elastic rod”, *PMM* **45** (1981), 518–529.
- [Boley 1963] B. A. Boley, “On the accuracy of the Bernoulli-Euler theory for beams of variable section”, *J. Appl. Mech. (Trans. ASME)* **30** (1963), 374–378.
- [Cesnik and Hodges 1997] C. E. S. Cesnik and D. H. Hodges, “VABS: a new concept for composite rotor blade cross-sectional modeling”, *J. Am. Helicopter Soc.* **42**:1 (1997), 27–38.

- [Cleghorn and Tabarrok 1992] W. Cleghorn and B. Tabarrok, “Finite element formulation of a tapered Timoshenko beam for free lateral vibration analysis”, *J. Sound Vib.* **152**:3 (1992), 461–470.
- [Hodges 2006] D. H. Hodges, *Nonlinear composite beam theory*, vol. 213, Progress in astronautics and aeronautics, American Institute of Aeronautics and Astronautics, Reston, VA, 2006.
- [Karabalis and Beskos 1983] D. Karabalis and D. Beskos, “Static, dynamic and stability analysis of structures composed of tapered beams”, *Comput. Struct.* **16**:6 (1983), 731–748.
- [Kitipornchai and Trahair 1975] S. Kitipornchai and N. Trahair, “Elastic behaviour of tapered monosymmetric, I: beams”, *J. Struct. Div. ASCE* **101** (1975), 1661–1678.
- [Krahula 1975] J. L. Krahula, “Shear formula for beams of variable cross section”, *AIAA J.* **13**:10 (1975), 1390–1391.
- [Rajasekaran 1994] S. Rajasekaran, “Equations for tapered thin-walled beams of generic open section”, *J. Eng. Mech.* **120**:8 (1994), 1607–1629.
- [Renton 1991] J. D. Renton, “Generalized beam theory applied to shear stiffness”, *Int. J. Solids Struct.* **27**:15 (1991), 1955–1967.
- [Ronagh et al. 2000] H. Ronagh, M. Bradford, and M. Attard, “Nonlinear analysis of thin-walled members of variable cross-section, I: theory”, *Comput. Struct.* **77**:3 (2000), 285–299.
- [Tena-Colunga 1996] A. Tena-Colunga, “Stiffness formulation for nonprismatic beam elements”, *J. Struct. Eng.* **122**:12 (1996), 1484–1489.
- [Timoshenko and Goodier 1970] S. P. Timoshenko and J. N. Goodier, *Theory of elasticity*, 3rd ed., McGraw-Hill, New York, 1970.
- [To 1981] C. To, “A linearly tapered beam finite element incorporating shear deformation and rotary inertia for vibration analysis”, *J. Sound Vib.* **78**:4 (1981), 475–484.
- [Vu-Quoc and Léger 1992] L. Vu-Quoc and P. Léger, “Efficient evaluation of the flexibility of tapered I-beams accounting for shear deformations”, *Int. J. Numer. Meth. Eng.* **33**:3 (1992), 553–566.
- [Washizu 1968] K. Washizu, *Variational methods in elasticity and plasticity*, Pergamon Press, Oxford, UK, 1968.
- [Young 1989] W. C. Young, *Roark’s formulas for stress and strain*, 6th ed., McGraw-Hill, New York, 1989.
- [Yu and Hodges 2004] W. Yu and D. H. Hodges, “Elasticity solutions versus asymptotic sectional analysis of homogeneous, isotropic, prismatic beams”, *J. Appl. Mech. (Trans. ASME)* **71**:1 (2004), 15–23.
- [Yu et al. 2002] W. Yu, D. H. Hodges, V. V. Volovoi, and C. E. S. Cesnik, “On Timoshenko-like modeling of initially curved and twisted composite beams”, *Int. J. Solids Struct.* **39**:19 (2002), 5101–5121.

Received 6 Jul 2007. Revised 3 Oct 2007. Accepted 8 Oct 2007.

DEWEY H. HODGES: dhodges@gatech.edu

Daniel Guggenheim School of Aerospace Engineering, Georgia Institute of Technology, Atlanta, GA 30332-0150, United States

<http://www.ae.gatech.edu/~dhodges/>

JIMMY C. HO: jho@gatech.edu

Daniel Guggenheim School of Aerospace Engineering, Georgia Institute of Technology, Atlanta, GA 30332-0150, United States

WENBIN YU: wenbin.yu@usu.edu

Wenbin Yu, Mechanical & Aerospace Engineering Department, Utah State University, Logan, UT 84322-4130, United States

ON LARGE DEFORMATION GENERALIZED PLASTICITY

VASSILIS P. PANOSKALTSIS, LAZAROS C. POLYMENAKOS AND DIMITRIS SOLDATOS

Dedicated to the memory of Juan C. Simo for his seminal contributions to solid and computational mechanics

Large deformation generalized plasticity is presented in a covariant setting. For this purpose, the tensor analysis on manifolds is utilized and the manifold structure of the body as well of the ambient and the state space is postulated. On the basis of the multiplicative decomposition of the deformation gradient into elastic and plastic parts and the use of hyperelastic stress-strain relations, a large deformation elasto-plasticity model is proposed. Computational aspects and the predictions of the model under uniaxial and biaxial straining are also presented.

1. Introduction

Since the time of its initial introduction in [Lubliner 1974], generalized plasticity theory has been elaborated further within the large deformation analysis regime in order to deal with materials with a vanishing elastic domain [Lubliner 1975], the maximum plastic dissipation postulate [Lubliner 1986], and nonisothermal behavior [Lubliner 1987]. In these approaches the theory has been presented largely in an abstract manner dealing with issues appearing primarily in a referential setting. Moreover, even though constitutive models based on the generalized plasticity theory have been proposed and implemented numerically, within the context of the infinitesimal theory [Lubliner et al. 1993; Auricchio and Taylor 1995; Panoskaltis et al. 1997], a model within the context of the finite theory has not been proposed yet.

The objective of this study is threefold: first, to present the theory in a covariant setting. For this purpose manifold structure is considered not only for the body of interest and the ambient space, but also for the state space, that is, the set of all realizable states over a material point. Accordingly, the motion of the body, which is considered as a time dependent mapping within the ambient space, is extended to a local dynamical process by considering the state space as a fiber over the body particles. In turn, the involvement of the standard pull-back/push-forward operations of the tensor analysis on manifolds [Marsden and Hughes 1994, p. 67] leads to the introduction of the convected Lie derivative [Simo and Marsden 1984], which eventually leads to a covariant formulation of the theory. It is noted that the covariant formulation leads to constitutive equations which are invariant under arbitrary spatial diffeomorphisms and the principle of objectivity — invariance under arbitrary spatial isometries — is trivially satisfied. This point of view has been exploited by Simo [1988] within the context of classical plasticity, and seems to have passed largely unnoticed within the literature. Unlike the presentation of

Keywords: large deformation plasticity, generalized plasticity, tensor analysis on manifolds, covariant formulation, Lie derivative, internal variables, metric of the elastically relaxed space, loading-unloading conditions, time integration algorithm, predictor-corrector algorithm.

[Simo 1988], where the covariance principle is applied after the problem kinematics have been specified, the present approach leaves the problem kinematics entirely unspecified.

Second, to propose a rather simple model on the basis of metal plasticity in order to make clear the covariance principle within the generalized plasticity context, in its most simple setting. The proposed model comprises the following components:

- (i) decomposition of the total motion into a plastic motion in some relaxed space endowed with the structure of a Riemannian manifold, followed by an elastic motion, as suggested by Le and Stumpf [1993];
- (ii) flow rule in terms of the Riemannian metric of the relaxed space;
- (iii) Von Mises loading surfaces with both isotropic and kinematic hardening;
- (iv) hyperelastic constitutive equations for the characterization of the elastic response, as proposed in the work of Simo and Ortiz [1985].

Third, to present the computational implementation of a generalized plasticity model in a covariant formulation. Finally, we also present numerical simulations.

2. Constitutive theory

Following the erudite approach of Marsden and Hughes [1994] within the context of nonlinear elasticity, we consider both the body of interest and the ambient space as three-dimensional Riemannian manifolds. In particular, let B be the reference configuration of the body of interest, which is modeled as a three-dimensional manifold with points labeled by (X^1, X^2, X^3) , and define a motion of B as a time dependent mapping $x : B \rightarrow b$, which is given by

$$x^1 = x^1(X^1, X^2, X^3, t), \quad x^2 = x^2(X^1, X^2, X^3, t), \quad x^3 = x^3(X^1, X^2, X^3, t), \quad (1)$$

and maps the points of the reference configuration B onto the points $\mathbf{x} = \mathbf{x}(X, t)$ of the current configuration b . The mapping Equation (1) is assumed to be one to one and twice differentiable, that is, an element of the Einstein group \mathcal{E} [Dyson 1972]. The deformation gradient is defined as the tangent map of Equation (1),

$$\mathbf{F}(X, t) = \frac{\partial \mathbf{x}}{\partial X},$$

with determinant $J = \det \mathbf{F}(X, t) > 0$. Furthermore, let \mathbf{G} and \mathbf{g} be the covariant metrics of the reference configuration and the ambient space, respectively. Next we introduce the right Cauchy–Green tensor, defined as the pull-back of \mathbf{g} ,

$$\mathbf{C} = \mathbf{x}^*(\mathbf{g}) = \mathbf{F}^T \mathbf{g} \mathbf{F},$$

and the Finger deformation tensor, defined as the push-forward of \mathbf{G} ,

$$\mathbf{b}^{-1} = \mathbf{x}_*(\mathbf{G}) = \mathbf{F}^{-T} \mathbf{G} \mathbf{F}^T.$$

In general, the referential metric \mathbf{G} is unknown, and several considerations must be made for its determination, including experimental procedures [Valanis and Panoskaltis 2005]. By means of the adopted manifold structure and the consideration of the referential metric, several internal material structures, including directional densities, curved material structures, preformed materials, and prestressed

reference configurations, can be accounted for by the proposed approach. For a dissipative material, like the elastic-plastic continuum to be discussed here, the referential metric is a function of the history of deformation [Valanis 1995]. The only case where the referential metric is constant in the course of deformation is that of an elastic material, like the one discussed in the covariant approaches of Simo et al. [1988] and Marsden and Hughes [1994].

Generalized plasticity is a local internal variable theory of rate independent behavior which is based primarily on the assumption that plastic deformation takes place on loading but not on unloading [Lubliner 1974; 1975]. In the absence of thermal effects, the material state at the point X with coordinates (X^1, X^2, X^3) is assumed to be determined by the couple (S, Q) , where S denotes the second Piola–Kirchhoff stress tensor and Q denotes the internal variable vector. The latter is assumed to be covariant in the sense that under the mapping Equation (1) it is transformed according to the general tensorial transformation law, as it is given, for instance, in [Marsden and Hughes 1994, p. 67]. On the basis of the previous discussion regarding the referential metric, it is concluded that the latter has to be included in Q . The state space S is assumed to be attached to the point X so that the set $X \times S$ is a fiber of X , and since this set is an open subset of $B \times S$, it is a local manifold. The dimension of this manifold is $6 + r$, where r is the number of independent components of Q .

A local process Ψ in S is defined as a curve in S , that is, as a mapping $\Psi : I \in \mathbb{R} \rightarrow S$, with $\Psi(t) = (S(t), Q(t))$, where $t \in I$. The direction and the speed of the process are determined by the tangent vector $\dot{\Psi} : S \rightarrow TS$, with $\dot{\Psi} = (\dot{S}, \dot{Q})$, where TS is the tangent space of S . Since \dot{S} is always known under stress control, the component \dot{Q} of $\dot{\Psi}$ has to be determined. The latter is assumed to be given by rate equations of the form

$$\dot{Q} = \Pi(S, C, Q, \dot{S}), \quad (2)$$

where $\Pi : S \times TS \rightarrow TS$ is a vector field in TS , which is considered as a tensorial function of the denoted arguments. We note the dependence of the function Π on the (convected) metric C in the reference configuration, which needs to be included not only for a covariant setting of the theory [Simo et al. 1988], but also to account for effects such as pressure dependence of the plastic response [Simo and Ortiz 1985]. Rate independence implies that Equation (2) is invariant under a change of the parameter t by any monotonically increasing, continuously differentiable function $\chi(t)$ (see, for instance, [Lubliner 1987; Lucchesi and Podio-Guidugli 1992]). Then the necessary and sufficient condition for rate independence is that Π is homogeneous to the first degree [Lubliner 1986; 1987], that is

$$\Pi(S, C, Q, c \cdot \dot{S}) = c \cdot \Pi(S, C, Q, \dot{S}), \quad (3)$$

for any positive number c .

A local process is defined as elastic if it lies entirely in a six dimensional submanifold of S , the stress space defined by $Q = \text{constant}$, otherwise it is defined as plastic. The elastic range of a state is defined as a submanifold in stress space comprising the stresses that can be reached elastically from the current stress point [Pipkin and Rivlin 1965; Lucchesi and Podio-Guidugli 1992]. It is assumed further that the boundary of the elastic range is a five-dimensional manifold, the points of which have a coordinate neighborhood on it, which is attached to the interior in much the same way as a face of a cube is attached to the interior. The latter manifold may be defined as a loading surface [Eisenberg and Phillips 1971; Lubliner 1987]. In turn, a state within its elastic range may be defined as plastic if it lies on a loading

surface and as elastic otherwise. On the basis of axioms and results from set theory and topology, Lubliner [1987] showed that the simplest function Π obeying the homogeneity condition Equation (3) consistent with the notion of the loading surface is

$$\Pi(\mathbf{S}, \mathbf{C}, \mathbf{Q}, \dot{\mathbf{S}}) = \Lambda(\mathbf{S}, \mathbf{C}, \mathbf{Q}) \langle N : \dot{\mathbf{S}} \rangle, \quad (4)$$

where N is the outward normal to the loading surface, assumed to be nonvanishing, and $\langle \cdot \rangle$ stands for the Macauley bracket, defined as

$$\langle x \rangle = \begin{cases} x, & \text{if } x \geq 0, \\ 0, & \text{if } x < 0. \end{cases}$$

In view of Equations (2) and (4), the rate equations for the evolution of the internal variables can be written as

$$\dot{\mathbf{Q}} = \Lambda(\mathbf{S}, \mathbf{C}, \mathbf{Q}) \langle N : \dot{\mathbf{S}} \rangle. \quad (5)$$

The inner product $N : \dot{\mathbf{S}}$ of the tangent vector $\dot{\mathbf{S}}$ and the normal vector N (one form) is defined as the loading rate. The loading rate determines the velocity and the direction of the process from a plastic state, relative to its elastic range. If $N : \dot{\mathbf{S}} < 0$, then the elastic range remains invariant under the flow of $\dot{\mathbf{S}}$ (see [Abraham et al. 1988, p. 257]) and the process is elastic. If $N : \dot{\mathbf{S}} > 0$, then the elastic range is not invariant anymore, and a new plastic state at a new value of \mathbf{Q} is initiated. The limiting case, where $N : \dot{\mathbf{S}} = 0$, results in an elastic process and is defined as neutral loading. It is noted that the present formulation presupposes stability under stress control and is limited to work hardening materials. The incorporation of work softening phenomena within the theory can be conducted along the lines presented in this study in conjunction with some developments given in [Lubliner et al. 1993].

The manifold defined by the equation $\Lambda(\mathbf{S}, \mathbf{C}, \mathbf{Q}) = 0$, which comprises all elastic states, may be called the elastic domain, and its boundary, which is assumed to be a submanifold, is called the yield hypersurface. The projection of the elastic domain on the manifold $\mathbf{Q} = \text{constant}$ is called the elastic domain at \mathbf{Q} . In general, the elastic domain at \mathbf{Q} is a submanifold of the elastic range [Lubliner 1987]. The particular case where the two manifolds coincide corresponds to classical plasticity. In this case, the closure of the elastic domain C , which constitutes the whole state space S , is invariant under the action of the plastic flow. More specifically, if the yield hypersurface, which now comprises the totality of plastic states, is assumed to be given by the function $g : C \rightarrow \mathbb{R}$, with $g(\mathbf{S}, \mathbf{C}, \mathbf{Q}) = 0$, then the state space C is defined, for any regular value $\lambda \leq 0$ of g , as the manifold $C = g^{-1}(\lambda)$. Then the invariance of the state space under the action of the plastic flow is equivalent to the invariance of C under the action of the flow of the tangent vector to the process $\dot{\Psi}$. The necessary and sufficient condition for the invariance of C under the flow of $\dot{\Psi}$ (see [Abraham et al. 1988, pp. 256–258]) is

$$\dot{\Psi} : \text{GRAD} g \leq 0. \quad (6)$$

The limiting case $\dot{\Psi} : \text{GRAD} g = 0$ corresponds to a process tangent to the yield hypersurface and constitutes the consistency condition of classical plasticity. This result can be generalized for the case in which the yield hypersurface is not a submanifold, but rather a piecewise smooth surface (see, for instance, [Hartman 1972]), and the multisurface plasticity formulation due to [Koiter 1953] is regained.

Another case of interest arises when the function Λ is a nonvanishing function of its arguments. If this is the case then there are no elastic states, and the elastic domain degenerates to a surface which may be called a quasiyield surface [Lubliner 1975].

With the help of Equation (5) we now define the general (stress-space) loading-unloading conditions explicitly as

$$\left\{ \begin{array}{l} \Lambda(S, C, Q) = 0, \quad \text{elastic state,} \\ \Lambda(S, C, Q) \neq 0, \quad \text{and} \quad \left\{ \begin{array}{ll} N : \dot{S} < 0, & \text{elastic unloading,} \\ N : \dot{S} = 0, & \text{neutral loading,} \\ N : \dot{S} > 0, & \text{plastic loading.} \end{array} \right. \end{array} \right. \quad (7)$$

The equivalent development of the theory in the current configuration can be performed by considering the local vector bundle mapping (see [Abraham et al. 1988, p.167])

$$P : B \times S \rightarrow b \times s \text{ with } P(X, S, Q, t) = (x(X, t), x_*(S), x_*(Q)),$$

which, by keeping the point X fixed, may be identified as a (local) dynamical process. Accordingly, the state space s at the point x with coordinates (x^1, x^2, x^3) is composed by the Kirchhoff stress tensor $\tau = F S F^T$, and the push-forward of the internal variable vector, denoted as $q = x_*(Q)$.

Then, by the application of a push-forward operation to Equation (5) with the mapping Equation (1), we have in an equivalent spatial setting

$$L_v q = \lambda(\tau, g, q, F) \langle n : L_v \tau \rangle, \quad (8)$$

where $L_v(\cdot)$ stands for the Lie derivative, defined as the convected derivative relative to the current configuration (for instance, see [Simo and Marsden 1984; Le and Stumpf 1993]), λ is a vector field in Ts , and n is the outward normal to the loading surface in the current configuration. It is noted that the (invariant) loading rate $N : \dot{S}$ is transformed in the current configuration to $n : L_v \tau$ [Miehe 1998]. We further note the presence of the deformation gradient F among the arguments of λ due to the push-forward operation by which Equation (8) is derived from Equation (5). In view of Equation (8) we formulate the spatial version of the loading-unloading conditions as

$$\left\{ \begin{array}{l} \lambda(\tau, g, q, F) = 0, \quad \text{elastic state,} \\ \lambda(\tau, g, q, F) \neq 0, \quad \text{and} \quad \left\{ \begin{array}{ll} n : L_v \tau < 0, & \text{elastic unloading,} \\ n : L_v \tau = 0, & \text{neutral loading,} \\ n : L_v \tau > 0, & \text{plastic loading.} \end{array} \right. \end{array} \right. \quad (9)$$

Equation (5), along with the mathematical expression for the loading surfaces, which are assumed to be given as a single parameter family of the form $\Phi(S, C, Q) = K$, constitute the simplest version of generalized plasticity in the reference configuration. An equivalent spatial setting consists of Equation (8) and an expression for the loading surfaces of the form $\varphi(\tau, g, q, F) = k$. In order to develop a generalized plasticity model, we have to specify:

- (i) the kinematic assumptions regarding the geometry of deformation,
- (ii) the stress-deformation relations,

(iii) the kind and the number of the internal variables.

These are specified in the forthcoming section, where a rather simple model is proposed.

3. A model problem

Consistent with the covariant formulation employed, the basic kinematical assumption consists of a decomposition of the motion into a plastic motion in some relaxed space B_e , considered as a Riemannian manifold, followed by an elastic motion [Le and Stumpf 1993]. In particular the plastic motion, which will be termed as plastic flow, is defined as the time dependent mapping $\mathbf{x}^P : B \rightarrow B_e$, which is given as

$$x^{p1} = x^{p1}(X^1, X^2, X^3, t), \quad x^{p2} = x^{p2}(X^1, X^2, X^3, t), \quad x^{p3} = x^{p3}(X^1, X^2, X^3, t).$$

Then the total motion Equation (1) can be decomposed as

$$\mathbf{x} = \mathbf{x}^e \circ \mathbf{x}^P, \quad (10)$$

where the motion $\mathbf{x}^e : B_e \rightarrow b$, with

$$x^{e1} = x^{e1}(x^{p1}, x^{p2}, x^{p3}, t), \quad x^{e2} = x^{e2}(x^{p1}, x^{p2}, x^{p3}, t), \quad x^{e3} = x^{e3}(x^{p1}, x^{p2}, x^{p3}, t),$$

constitutes the elastic deformation.

The decomposition Equation (10) of the motion leads to the multiplicative decomposition of the deformation gradient into elastic and plastic parts, $\mathbf{F} = \mathbf{F}^e \mathbf{F}^P$. Such decomposition has been considered by Lee [1969], Mandel [1972], Lubliner [1986], and Simo [1988], among others. Following Le and Stumpf [1993], we introduce the model in the (elastically) relaxed space. A similar approach has been also favored by Lee [1969], Mandel [1972], Dashner [1986], and Dafalias [1998], among others. Accordingly, the state variables are assumed to be the (contravariant) stress tensor \mathbf{S}_e , defined as the push-forward of the second Piola–Kirchhoff stress tensor by the plastic motion $\mathbf{S}_e = \mathbf{F}^P \mathbf{S} \mathbf{F}^{PT}$, and the internal variable vector, which is assumed to be composed of the Riemannian metric in B_e , \mathbf{G}_e and an additional internal variable vector \mathbf{Q}_e . The selection of the metric of the (elastically) relaxed space as a primary state variable is natural and relies on the fact that it is precisely the tensor \mathbf{G}_e and the internal variables which determine the continuously evolving geometry of the relaxed space under the action of the plastic flow. This approach has its origins in the work of Le and Stumpf [1993], is consistent with the necessity of the selection of a measure of plastic deformation as an independent variable according to Naghdi [1990], and takes into account the fact that the referential metric varies in the course of plastic deformation, according to Valanis [1995].

Motivated by classical metal plasticity we introduce a von Mises type of expression for the loading surfaces with both isotropic and kinematic hardening,

$$\Phi(\mathbf{S}_e, \mathbf{C}_e, \alpha, \mathbf{H}_e) = \sqrt{(S_e^{\alpha\beta} - H_e^{\alpha\beta})(S_e^{\gamma\delta} - H_e^{\gamma\delta})C_{e\alpha\gamma}C_{e\beta\delta} - \frac{1}{3}(S_e^{\alpha\beta}C_{e\alpha\beta})^2} - \sqrt{\frac{2}{3}}(\sigma_y + K\alpha), \quad (11)$$

where \mathbf{C}_e is the (convected) metric for the relaxed space, defined as the pull-back of the spatial metric by the elastic deformation $\mathbf{C}_e = \mathbf{F}^{eT} \mathbf{g} \mathbf{F}^e$, where α is a scalar internal variable which controls the size of the loading surfaces, \mathbf{H}_e is a deviatoric stress tensor (that is, $\text{tr}(\mathbf{H}_e \mathbf{C}_e) = 0$), usually termed back stress

which controls the location of the loading surfaces, and σ_y and K are two model parameters designating the uniaxial yield stress and the (isotropic) hardening modulus, respectively.

The evolution of the plastic flow (flow rule) is considered to be normal to the loading surfaces as per

$$L_{VP} \mathbf{G}_e^{-1} = h \mathbf{N}_e \langle \mathbf{N}_e : L_{VP} \mathbf{S}_e \rangle, \quad (12)$$

where $L_{VP}(\cdot)$ is the (convected) Lie derivative along the velocity of the plastic flow; the velocity may be defined as [Le and Stumpf 1993]

$$\mathbf{V}^P = \bar{\mathbf{V}}^P \circ \mathbf{x}^{P-1}, \quad \text{where } \bar{\mathbf{V}}^{P\alpha} = \frac{\partial x^{P\alpha}}{\partial t} (\mathbf{X}, t)|_{X=\text{constant}}.$$

\mathbf{N}_e is the normal vector to the loading surfaces which, in view of Equation (11) [Simo and Ortiz 1985; Simo 1988], is given as

$$\mathbf{N}_e = \frac{\partial \Phi}{\partial \mathbf{S}_e} = \frac{(\mathbf{S}_e - \mathbf{H}_e) - \frac{1}{3} \{(\mathbf{S}_e - \mathbf{H}_e) : \mathbf{C}_e\} \mathbf{C}_e^{-1}}{\|(\mathbf{S}_e - \mathbf{H}_e) - \frac{1}{3} \{(\mathbf{S}_e - \mathbf{H}_e) : \mathbf{C}_e\} \mathbf{C}_e^{-1}\|},$$

where $\|\cdot\|$ is the Euclidean norm and h is a scalar function of the state variables which enforces the defining property of a plastic state. Accordingly, the value of h must be positive at any plastic state and zero at any elastic one. It should be noted that in taking the derivative of the loading function with respect to the stress tensor \mathbf{S}_e , the quantities \mathbf{S}_e and \mathbf{C}_e are treated as independent variables. The relation between the stress tensor \mathbf{S}_e and the metric \mathbf{C}_e , as it is expressed in Equations (24) and (25), is an a posteriori fact related to the choice of the constitutive equations (in this case hyperelastic).

It is emphasized that in the particular case in which the relaxed space is considered as flat, or almost flat, and by noting that

$$L_{VP} \mathbf{G}_e^{-1} = \dot{\mathbf{G}}_e^{-1} - \mathbf{L}_P \mathbf{G}_e^{-1} - \mathbf{G}_e^{-1} \mathbf{L}_P^T,$$

where $\mathbf{L}_P = \dot{\mathbf{F}}^P \mathbf{F}^{P-1}$ is the (true) plastic velocity gradient, the flow rule can be stated as

$$\text{Sym} [\mathbf{G}_e^{-1} \mathbf{L}_P] = -\frac{1}{2} h \mathbf{N}_e \langle \mathbf{N}_e : L_{VP} \mathbf{S}_e \rangle,$$

where $\text{Sym}[\cdot]$ stands for the symmetric part of its argument. For the particular case in which the relaxed space is considered as Euclidean, that is, $\mathbf{G}_e^{-1} = \mathbf{1}$, a flow rule in terms of $\text{Sym}[\mathbf{L}_P]$ is derived. If this is the case, the adopted flow rule resembles the associative flow rule derived by Simo [1988], based on the maximum plastic dissipation postulate, within the context of classical plasticity

$$\text{Sym} [\mathbf{L}_P] = \dot{\gamma} \mathbf{C}_e \mathbf{N}_e, \quad (13)$$

where $\dot{\gamma}$ is the consistency parameter, which can be determined by means of the consistency condition (Equation (6)). It is noted that the flow rule adopted herein (12), differs from the associated flow rule (13) by a factor equal to \mathbf{C}_e and a multiplicative scalar.

In accordance with the classical theory we propose the following evolution equations for the remaining internal variables [Simo and Hughes 1997, p. 90]:

$$\dot{\alpha} = \sqrt{\frac{2}{3}} h \langle \mathbf{N}_e : L_{VP} \mathbf{S}_e \rangle, \quad (14)$$

$$L_{VP} \mathbf{H}_e = \frac{2}{3} H h \mathbf{N}_e \langle \mathbf{N}_e : L_{VP} \mathbf{S}_e \rangle, \quad (15)$$

where H is the (kinematic) hardening modulus.

The referential setting of the model can be determined by applying a pull-back operation to Equations (11), (12), (14), and (15) by the plastic flow as

$$\Phi(\mathbf{S}, \mathbf{C}, \alpha, \mathbf{H}) = \sqrt{(S^{IJ} - H^{IJ})(S^{KL} - H^{KL})C_{IK}C_{JL} - \frac{1}{3}(S^{KL}C_{KL})^2} - \sqrt{\frac{2}{3}}(\sigma_y + K\alpha), \quad (16)$$

$$\dot{\mathbf{C}}^{p-1} = h\mathbf{N}\langle \mathbf{N} : \dot{\mathbf{S}} \rangle, \quad (17)$$

$$\dot{\alpha} = \sqrt{\frac{2}{3}}h\langle \mathbf{N} : \dot{\mathbf{S}} \rangle, \quad (18)$$

$$\dot{\mathbf{H}} = \frac{2}{3}Hh\mathbf{N}\langle \mathbf{N} : \dot{\mathbf{S}} \rangle, \quad (19)$$

where \mathbf{C}^P , \mathbf{H} , and \mathbf{N} are the pull-backs in the reference configuration of the tensors \mathbf{G}_e , \mathbf{H}_e , and \mathbf{N}_e , respectively, by the plastic flow. It is concluded that \mathbf{C}^P , besides being the primary measure of plastic deformation (see Equation (17)), also plays the role of the aforementioned referential metric.

It is noted that unlike the theoretical presentation, which was developed primarily in the reference configuration, the model is developed primarily in the relaxed space. Thus the relaxed space, as well as any other configuration of the body, can also serve as a reference configuration. This point of view enables us to visualize the deeper inside of the notion of spatial covariance, according to which all configurations of the body are practically indistinguishable and the equation forming is a matter of observation. This statement is an interpretation within the generalized plasticity context of the comment by Dyson [1972], ‘‘Einstein based his theory on the principle that God did not attach any preferred labels to the points of space-time.’’ As a result, once the equations describing the state of the body are known in some configuration, they are known in any configuration by employing the covariant transformation laws. An application the equivalent setting of the model in the current configuration can be derived by a push-forward operation to Equations (16), (17), (18), and (19) by the total motion as

$$\varphi(\boldsymbol{\tau}, \mathbf{g}, a, \mathbf{h}) = \sqrt{(\tau^{ij} - h^{ij})(\tau^{kl} - h^{kl})g_{ik}g_{jl} - \frac{1}{3}(\tau^{kl}g_{kl})^2} - \sqrt{\frac{2}{3}}(\sigma_y + Ka), \quad (20)$$

$$L_v \mathbf{b}^e = h\mathbf{n}\langle \mathbf{n} : L_v \boldsymbol{\tau} \rangle, \quad (21)$$

$$\dot{\alpha} = \sqrt{\frac{2}{3}}h\langle \mathbf{n} : L_v \boldsymbol{\tau} \rangle, \quad (22)$$

$$L_v \mathbf{h} = h\frac{2}{3}H\mathbf{n}\langle \mathbf{n} : L_v \boldsymbol{\tau} \rangle, \quad (23)$$

where \mathbf{b}^e , \mathbf{h} , and \mathbf{n} are the push forwards into the current configuration of the referential tensors \mathbf{C}^P , \mathbf{H} , and \mathbf{N} , respectively.

To this end, it is emphasized that the presented covariant approach has been discussed, on the basis of physical grounds, by Dafalias [1998] (see also [Dafalias 1993; 2001]). In particular, it is argued that a rate equation for the evolution of a tensorial internal variable in terms of the convected Lie derivative embodies only the evolutionary characteristics of this internal variable and not its (possible) orientational characteristics related to the material substructure, which must be accounted by the constitutive model. In order to accomplish this goal, Dafalias [1998] adopts a flow rule in the form (see also [Dafalias 1993]) $\text{Sym}[\mathbf{L}_p] = \dot{\gamma}\mathbf{N}_e(\mathbf{T}, a, \mathbf{H}_e)$, where \mathbf{T} is a stress tensor defined in the relaxed space in terms of the

Cauchy stress tensor σ as $T = \det(F^e)F^{e-1}\sigma F^{e-T}$, while for the evolution of the back stress tensor proposes an equation in terms of a corotational derivative as

$$\hat{H}_e = \dot{H}_e - \omega H_e + H_e \omega = \dot{\gamma} M(T, \alpha, H_e),$$

where ω is defined as the constitutive spin and is related to the aforementioned orientational characteristics inherited to the back stress tensor due to the material substructure and M is a tensorial function, which, due to invariance requirements, is considered as isotropic. The determination of ω lies crucially on the fact that, in the absence of plastic deformation ($\dot{\gamma} = 0$), one has $\hat{H}_e = \mathbf{0}$, and H_e just spins by ω . By noting further that, in the absence of plastic deformation, the relaxed space spins by the antisymmetric part of the plastic velocity gradient L_p , $\text{ant}[L_p]$, it is proposed that ω can be determined by an expression of the form

$$\text{ant}[L_p] = \omega + W^p = \omega + \dot{\gamma} \Omega(T, \alpha, H_e),$$

where W^p is defined as the plastic spin and Ω is an isotropic function of the state variables. From the authors' point of view, noting that both the convected and the corotational mode of evolution for the internal variables are different manifestations of the Lie derivative concept [Marsden and Hughes 1994, p.100], the adequate form of evolution has to be decided on the basis of the experimentally observed behavior. It should become clear that, unlike the Lie derivative concept, which is a purely kinematical one, the constitutive and plastic spin concepts require the existence of a substructure whose kinematics may be different from those of the continuum. These issues, together with a possible extension of the proposed covariant formulation, in order to account for crystal plasticity and crystal defects, are a subject of our ongoing research. Finally, the stress response is assumed to be hyperelastic, governed by an isotropic strain energy function proposed within the context of nonlinear elasticity by Ciarlet [1988] and utilized in a somewhat different format within the context of classical plasticity in [Simo and Hughes 1997, p. 258],

$$W = \lambda \frac{I_{e3} - 1}{4} - \left(\frac{\lambda}{2} + \mu \right) \ln \sqrt{I_{e3}} + \frac{1}{2} \mu (I_{e1} - 3),$$

where $I_{e1} = \text{tr}(C_e G_e^{-1})$ and $I_{e3} = \det(C_e G_e^{-1})$ are the first and third invariants of $C_e G_e^{-1}$, and λ and μ are material parameters to be interpreted as Lamé constants. Then the stress response in the relaxed space is determined by

$$S_e = 2 \frac{\partial W}{\partial C_e}, \tag{24}$$

which yields

$$S_e = \lambda \frac{I_{e3} - 1}{2} C_e^{-1} + \mu (G_e^{-1} - C_e^{-1}). \tag{25}$$

By employing once more the standard pull-back and push-forward operations, Equation (25) may be equivalently written in the forms

$$S = \lambda \frac{I_3 - 1}{2} C^{-1} + \mu (C^{p-1} - C^{-1}), \quad \tau = \lambda \frac{i_3 - 1}{2} g^{-1} + \mu (b^e - g^{-1}), \tag{26}$$

where I_3 and i_3 are the third invariants of the tensors CC^{p-1} and gb^e , respectively.

4. Computational aspects

The numerical implementation of a generalized plasticity based model relies crucially on the fact that, unlike the classical elastoplastic case, the internal variables are no longer constrained to lie within the closure of the elastic domain. Accordingly, unlike the classical elastoplastic case where the evolution equations define a unilaterally constrained problem of evolution, in the case of generalized plasticity the evolution equations form a differential system, which must obey the continuous form of the loading-unloading conditions (see Equations (7) and (9)) [Panoskaltis et al. 1997].

As a result it is concluded that, from a theoretical point of view, by means of the continuous form of the loading-unloading conditions one has a complete characterization not only of the current state of the material (elastic or plastic), but also, in the case the material state is plastic, of the type of the applied loading process (elastic unloading, neutral loading, plastic loading). From a computational point of view, the crucial requirement for the numerical implementation of an elastoplastic model, simply consists of the unambiguous knowledge of whether plastic loading takes place. For the classical elastoplastic case this requirement is provided by the introduction of the Kuhn–Tucker conditions of the theory of optimization, which, as it is noted in [Simo and Hughes 1997, p.84], imply the generalization of the loading-unloading criteria of the strain-space plasticity as they are given, for instance, in [Naghdi 1990]. Unlike this case, in our case the aforementioned requirement can be provided directly from the stress-space loading-unloading conditions by means of the (algorithmic) parameters $\mathbf{Z} = \mathbf{\Lambda} \langle \mathbf{N} : \dot{\mathbf{S}} \rangle$ and $\mathbf{z} = \lambda \langle \mathbf{n} : L_v \boldsymbol{\tau} \rangle$. By use of these parameters, and in view of the basic evolution equations (see Equations (5) and (8)), we state the algorithmic loading-unloading conditions as if $\mathbf{Z} = \mathbf{0}$ then $\dot{\mathbf{Q}} = \mathbf{0}$, if $\mathbf{Z} \neq \mathbf{0}$ then $\dot{\mathbf{Q}} \neq \mathbf{0}$, or, equivalently, if $\mathbf{z} = \mathbf{0}$, then $L_v \mathbf{q} = \mathbf{0}$, if $\mathbf{z} \neq \mathbf{0}$ then $L_v \mathbf{q} \neq \mathbf{0}$.

From now on, our analysis will be focused on the rather simple model proposed in Section 3. The concepts which will be presented on the basis of this model can be extended, with some computational cost, in more sophisticated models encompassing nonconstant elasticities, nonnormality flow rules, multiple hardening mechanisms, and damage.

The time integration procedure may in principle be formulated equivalently with respect to the reference or the current configurations. Since we deal with large scale plastic flow, the kinematics of the problem, together with the principle of covariance, suggest that a numerical formulation in terms of the Kirchhoff stress and its convected derivative (see Equations (20), (21), (22), (23), and (26)) is more fundamental. Further, in the current configuration the spatial metric usually has a diagonal form, which makes the computations simpler than those in the reference configuration, where the (convected) metric \mathbf{C} is fully populated [Miehe 1998]. The details of the implementation procedure follow.

Let $I = [0, T]$, the time interval of interest. It is assumed that at time $t_n \in I$, the configuration of the body of interest b_n , defined as $b_n = \{\mathbf{x}_n = \mathbf{x}_n(\mathbf{X}) \mid \mathbf{X} \in B\}$, along with the state variables $\{\mathbf{x}_n, \boldsymbol{\tau}_n, \mathbf{b}_n^e, \alpha_n, \mathbf{h}_n\}$, are the known data at time t_n .

Assume a time increment Δt_n , which drives the time to $t_{n+1} = t_n + \Delta t_n$, and the body configuration to

$$b_{n+1} = \{\mathbf{x}_{n+1} = \mathbf{x}_{n+1}(\mathbf{X}) \mid \mathbf{X} \in B\},$$

where

$$\mathbf{x}_{n+1}(\mathbf{X}) = \mathbf{x}_n(\mathbf{X}) + \mathbf{U}(\mathbf{X}) = \mathbf{x}_n(\mathbf{X}) + \mathbf{u}(\mathbf{x}_n(\mathbf{X})),$$

and \mathbf{u} is the incremental displacement field, which is assumed to be given. Then the algorithmic problem at hand is to update the stress tensor and the internal variables to the time step t_{n+1} in a manner consistent with the continuous Equations (20), (21), (22), (23), and (26). To this end the continuous equations will be discretized by the backward Euler scheme which is first order accurate and unconditionally stable. Because of the presence of Lie derivatives within the continuous equations, adequate approximations for these objects are derived on the basis of their defining property and the general tensorial transformation law. In particular, the defining relation for the Lie derivative of a tensor \mathbf{q} of type $\binom{r}{s}$ in the b_{n+1} configuration is

$$L_v \mathbf{q}_{n+1} = \mathbf{x}_{n+1*} \left(\frac{\partial}{\partial t} \mathbf{x}_{n+1}^* (\mathbf{q}) \right). \quad (27)$$

By performing a pull-back operation, Equation (27) can be written consecutively as

$$\mathbf{x}^* L_v \mathbf{q}_{n+1} = \frac{\partial}{\partial t} (\mathbf{x}^* (\mathbf{q}_{n+1})) = \dot{\mathbf{Q}}_{n+1} \doteq \frac{1}{\Delta t_n} (\mathbf{Q}_{n+1} - \mathbf{Q}_n),$$

which in turn may be written in component form on the basis of the general tensorial transformation law as

$$\begin{aligned} \left[\frac{\partial X^{I_1}}{\partial x_{n+1}^{i_1}} \dots \frac{\partial X^{I_r}}{\partial x_{n+1}^{i_r}} \frac{\partial x_{n+1}^{j_1}}{\partial X^{J_1}} \dots \frac{\partial x_{n+1}^{j_s}}{\partial X^{J_s}} \right] L_v (q^{i_1 \dots i_r}_{j_1 \dots j_s})_{n+1} &= \frac{1}{\Delta t_n} [(\mathbf{Q}^{I_1 \dots I_r}_{J_1 \dots J_s})_{n+1} - (\mathbf{Q}^{I_1 \dots I_r}_{J_1 \dots J_s})_n] \\ &= \frac{1}{\Delta t_n} \left[\frac{\partial X^{I_1}}{\partial x_{n+1}^{k_1}} \dots \frac{\partial X^{I_r}}{\partial x_{n+1}^{k_r}} \frac{\partial x_{n+1}^{l_1}}{\partial X^{J_1}} \dots \frac{\partial x_{n+1}^{l_s}}{\partial X^{J_s}} (q^{k_1 \dots k_r}_{l_1 \dots l_s})_{n+1} - \frac{\partial X^{I_1}}{\partial x_n^{k_1}} \dots \frac{\partial X^{I_r}}{\partial x_n^{k_r}} \frac{\partial x_n^{l_1}}{\partial X^{J_1}} \dots \frac{\partial x_n^{l_s}}{\partial X^{J_s}} (q^{k_1 \dots k_r}_{l_1 \dots l_s})_n \right], \end{aligned}$$

from which $L_v (q^{i_1 \dots i_r}_{j_1 \dots j_s})_{n+1}$ can be determined as

$$L_v (q^{i_1 \dots i_r}_{j_1 \dots j_s})_{n+1} = \frac{1}{\Delta t_n} \left[(q^{i_1 \dots i_r}_{j_1 \dots j_s})_{n+1} - \frac{\partial x_{n+1}^{i_1}}{\partial x_n^{k_1}} \dots \frac{\partial x_{n+1}^{i_r}}{\partial x_n^{k_r}} \frac{\partial x_n^{l_1}}{\partial x_{n+1}^{j_1}} \dots \frac{\partial x_n^{l_s}}{\partial x_{n+1}^{j_s}} (q^{k_1 \dots k_r}_{l_1 \dots l_s})_n \right], \quad (28)$$

where the tensor, with components

$$(f^i_j)_{n+1} = \frac{\partial x_{n+1}^i}{\partial x_n^j} = \frac{\partial x_{n+1}^i}{\partial X^I} \frac{\partial X^I}{\partial x_n^j} = (F^i_I)_{n+1} ((F^{-1})^I_j)_n,$$

is defined as the relative deformation gradient with respect to the configuration b_{n+1} [Simo and Hughes 1997, p. 279]. It is interesting to note that since any objective derivative of a tensorial quantity \mathbf{q} differs for its convected Lie derivative by terms depending on \mathbf{q} and the Lie derivative of the spatial metric \mathbf{g} (see [Atluri 1984] and [Marsden and Hughes 1994, p. 100]), (28) can be used as a basis for the objective approximation of other objective derivatives, which may be used in place of the convected derivative, used herein.

By means of Equation (28) a (covariant) approximation for a contravariant $\binom{0}{2}$ tensor \mathbf{q} , like the tensors $\boldsymbol{\tau}$, \mathbf{b}^e , and \mathbf{h} , participating in the proposed model is derived as

$$L_v (q^{ij})_{n+1} = \frac{1}{\Delta t_n} \left[(q^{ij})_{n+1} - \frac{\partial x_{n+1}^i}{\partial x_n^k} \frac{\partial x_{n+1}^j}{\partial x_n^l} (q^{kl})_n \right],$$

or equivalently

$$L_v \mathbf{q}_{n+1} = \frac{1}{\Delta t_n} (\mathbf{q}_{n+1} - \mathbf{f}_{n+1} \mathbf{q}_{n+1} \mathbf{f}_{n+1}^T).$$

Accordingly, the time discrete counterparts of Equations (21), (22), (23) and (26) are

$$\frac{1}{\Delta t_n} (\mathbf{b}_{n+1}^e - \mathbf{f}_{n+1} \mathbf{b}_n^e \mathbf{f}_{n+1}^T) = h_{n+1} \mathbf{n}_{n+1} l_{n+1}, \quad (29)$$

$$\frac{1}{\Delta t_n} (\alpha_{n+1} - \alpha_n) = \sqrt{\frac{2}{3}} h_{n+1} l_{n+1}, \quad (30)$$

$$\frac{1}{\Delta t_n} (\mathbf{h} - \mathbf{f}_{n+1} \mathbf{h}_n \mathbf{f}_{n+1}^T) = \frac{2}{3} H h_{n+1} \mathbf{n}_{n+1} l_{n+1}, \quad (31)$$

$$\boldsymbol{\tau}_{n+1} = \lambda \frac{\det(\mathbf{g}_{n+1} \mathbf{b}_{n+1}^e) - 1}{2} \mathbf{g}_{n+1}^{-1} + \mu (\mathbf{b}_{n+1}^e - \mathbf{g}_{n+1}^{-1}), \quad (32)$$

where

$$\mathbf{g}_{n+1} = \mathbf{g}(\mathbf{x}_{n+1}),$$

$$h_{n+1} = h(\mathbf{g}_{n+1}, \boldsymbol{\tau}_{n+1}, \mathbf{b}_{n+1}^e \mathbf{h}_{n+1}),$$

$$l_{n+1} = \left\langle \mathbf{n} : \frac{1}{\Delta t_n} (\boldsymbol{\tau}_{n+1} - \mathbf{f}_{n+1} \boldsymbol{\tau}_n \mathbf{f}_{n+1}^T) \right\rangle$$

and

$$\mathbf{n}_{n+1} = \frac{(\boldsymbol{\tau}_{n+1} - \mathbf{h}_{n+1}) - \frac{1}{3} \{(\boldsymbol{\tau}_{n+1} - \mathbf{h}_{n+1}) : \mathbf{g}_{n+1}\} \mathbf{g}_{n+1}^{-1}}{\|(\boldsymbol{\tau}_{n+1} - \mathbf{h}_{n+1}) - \frac{1}{3} \{(\boldsymbol{\tau}_{n+1} - \mathbf{h}_{n+1}) : \mathbf{g}_{n+1}\} \mathbf{g}_{n+1}^{-1}\|},$$

are quantities expressed in terms of the basic variables, subjected to the time discrete counterpart of the algorithmic loading-unloading conditions, which can be written as:

$$\text{If } z_{n+1} = 0, \text{ then } \begin{cases} \mathbf{b}_{n+1}^e &= \mathbf{f}_{n+1} \mathbf{b}_n^e \mathbf{f}_{n+1}^T, \\ \alpha_{n+1} &= \alpha_n, \\ \mathbf{h}_{n+1} &= \mathbf{f}_{n+1} \mathbf{h}_n \mathbf{f}_{n+1}^T, \end{cases} \quad (33)$$

and

$$\text{If } z_{n+1} \neq 0, \text{ then } \begin{cases} \mathbf{b}_{n+1}^e &\neq \mathbf{f}_{n+1} \mathbf{b}_n^e \mathbf{f}_{n+1}^T, \\ \alpha_{n+1} &\neq \alpha_n, \\ \mathbf{h}_{n+1} &\neq \mathbf{f}_{n+1} \mathbf{h}_n \mathbf{f}_{n+1}^T, \end{cases} \quad (34)$$

where $z_{n+1} = h_{n+1} l_{n+1}$. It is observed that Equations (29), (30), (31) and (32), subjected to the time discrete algorithmic loading-unloading conditions of Equation (33), form a system of four equations in four unknowns (\mathbf{b}_{n+1}^e , α_{n+1} , \mathbf{h}_{n+1} , and $\boldsymbol{\tau}_{n+1}$). The solution of this system can be performed by a predictor-corrector algorithm like the one presented by Panoskaltzis et al. [1997], in conjunction with some developments proposed within the context of large deformation computational plasticity, by Simo and Ortiz [1985] and Auricchio and Taylor [1999]. It is noted that, unlike the classical elastoplastic case, the consistency condition and accordingly the consistency parameter are absent from the model governing equations. Due to this absence the resulting system is simpler than in the classical elastoplastic case and more computer power is preserved.

5. Numerical simulations

The predictions of the model introduced in [Section 3](#) will be illustrated by considering two problems of large scale plastic flow, namely a simple shear test and the biaxial extension of a material block. The model will be implemented numerically by following our development in [Section 4](#). The model parameters are $\lambda = 330$, $\mu = 150$, $\sigma_y = 20$, $K = 15$, and $H = 0$.

The function h is set as

$$h = \frac{\langle \Phi \rangle}{\beta |\Phi|} \quad \text{and} \quad \frac{1}{\beta}$$

for $\Phi = 0$, where β is a model parameter.

In this case the elastic domain is the manifold defined by the set

$$D(C, S, \alpha, H) = \{(C, S, \alpha, H) / \Phi(C, S, \alpha, H) < 0\},$$

while the elastic range E is defined at any material state, by noting the one to one correspondence which exists between the end point of a vector of constant origin and the vector itself, as

$$E(C^*, S^*)|_{(\alpha, H)=\text{constant}} = \left\{ (C^*, S^*) \setminus \begin{cases} C^* = C + \dot{C}, S^* = S + \dot{S}, & \text{if } \Phi(C, S, \alpha, H)|_{(\alpha, H)=\text{constant}} < 0 \\ \text{or } N : \dot{S} \leq 0 \end{cases} \right\}.$$

The elastic domain at the state in question is defined as

$$D(C^*, S^*)|_{(\alpha, H)=\text{constant}} = \{(C^*, S^*) \setminus \Phi(C^*, S^*, \alpha, H)|_{(\alpha, H)=\text{constant}} < 0\},$$

which is clearly a submanifold of $E(C^*, S^*)|_{(\alpha, H)=\text{constant}}$.

The limit $\beta \rightarrow 0$ corresponds to classical plasticity. In this case the initial loading surface defined by $\Phi = 0$ coincides with the yield surface of classical plasticity [[Eisenberg and Phillips 1971](#)], while the limit $h_{\beta \rightarrow 0}$ is determined by the consistency condition (6).

The particular case where h is considered as a positive function of the state variables (for example, constant, exponential, hyperbolic) corresponds to a model with a quasiyield surface. In this model every state is a plastic state, plastic loading appears from the initiation of loading, and every reloading process, following (elastic) unloading, results in plastic response.

The simple shear problem [[Gurtin 1981](#), p. 115] is defined by

$$x^1 = X^1 + \gamma X^2, \quad x^2 = X^2, \quad x^3 = X^3,$$

where γ is the shearing parameter. This problem has been used extensively as a testing problem (see, for example, [[Lee et al. 1983](#); [Dafalias 1983](#); [Haupt and Tsakmakis 1986](#); [Atluri 1984](#)]) within the context of large deformation plasticity.

The predictions of the model for different values of the parameter β are shown in [Figure 1](#). We note that for large values of β the predicted response is identical to that of a perfectly plastic material. Furthermore, the oscillating behavior, which is reported in [[Atluri 1984](#)] in finite shear, even in the case of classical isotropic hardening plasticity, does not appear.

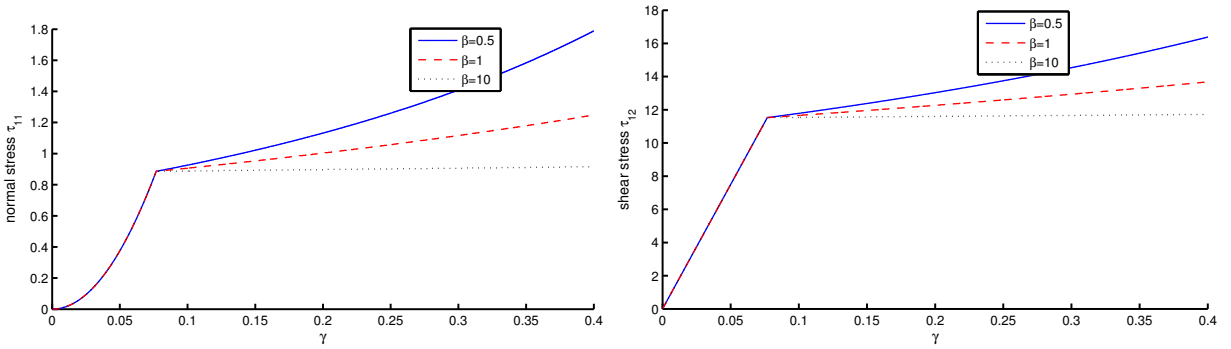


Figure 1. Normal (left) and shear (right) stresses versus the shearing parameter.

The second problem is the biaxial extension of a material block. The straining occurs along the X^1 and X^2 axes while the block is assumed to be fixed along the X^3 direction. This problem is defined as

$$x^1 = (1 + \lambda)X^1, \quad x^2 = (1 + \omega)X^2, \quad x^3 = X^3,$$

where λ and ω are the straining parameters. The predictions for the normal stresses for different interrelations of the straining parameters are shown in Figure 2.

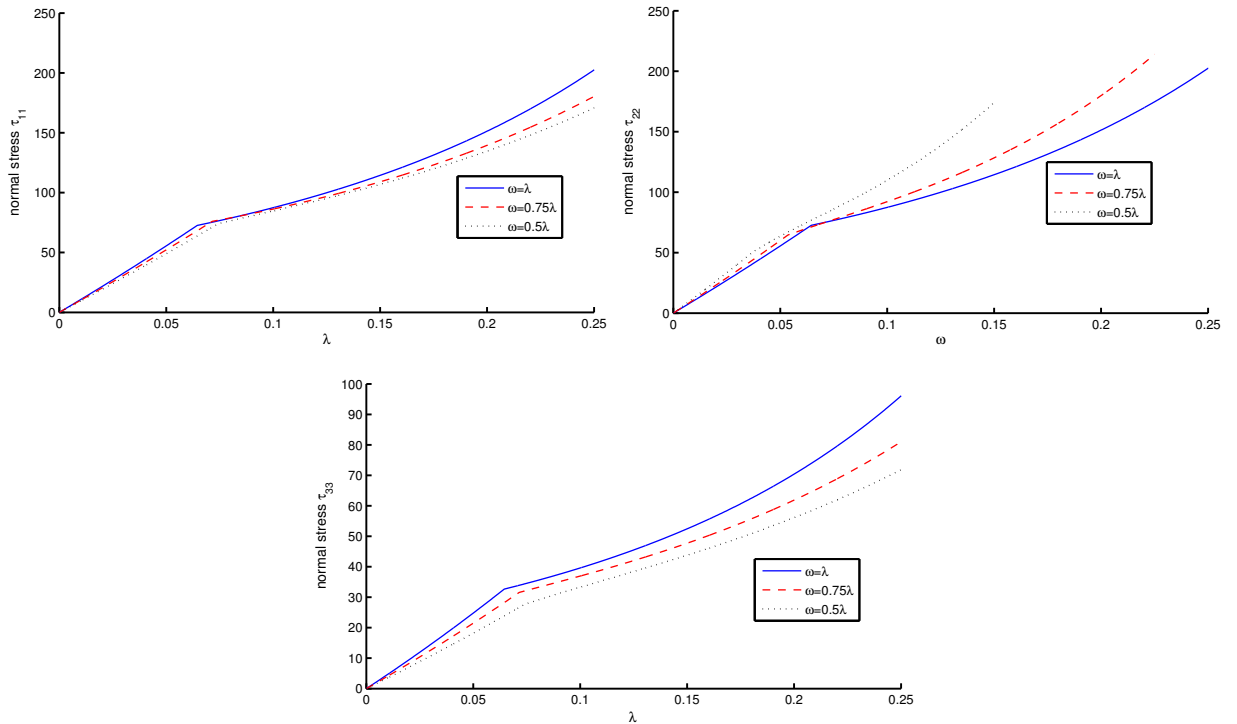


Figure 2. Biaxial extension of a material block: normal stresses versus straining parameters.

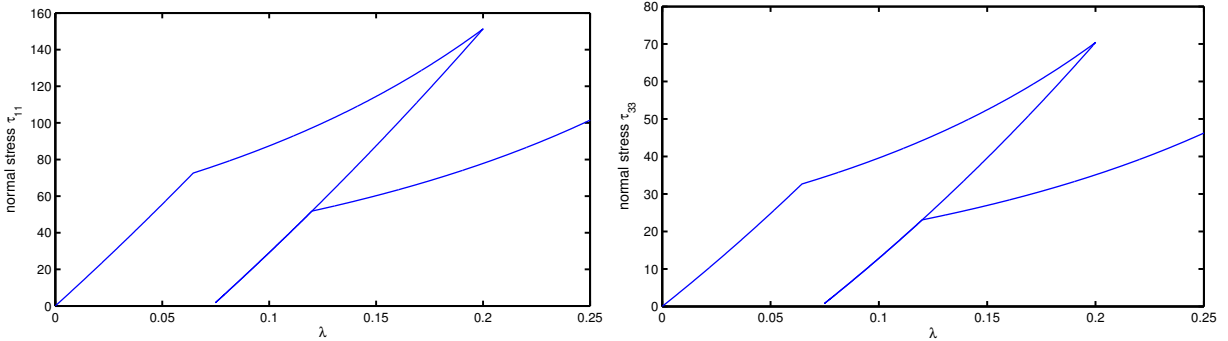


Figure 3. Biaxial extension of a material block: initial loading, unloading, and reloading.

A second loading history comprising loading, unloading from a plastic state, and reloading is given for $\lambda = \omega$ in Figure 3. We note that, consistently with a generalized plasticity based model, during reloading, after unloading from a plastic state, plastic behavior appears before attaining the state where the unloading began.

6. Conclusions

One of the main contributions of this paper is the presentation of the (stress space) covariant formulation of rate independent generalized plasticity. For this purpose, the manifold structure of the body, as well as of the ambient and the state space, is postulated. In the course of the development of the theory, and based on geometry of manifolds, the consistency condition of classical plasticity is derived. A rather simple model is proposed in order to emphasize the covariant presentation of the generalized plasticity concept in its most simple setting. The model is developed in the (elastically) relaxed space. By employing the pull-back and push-forward operations the model is also derived in the reference and current configurations, respectively. A time integration algorithm, in the current configuration, is developed in detail. Appropriate algorithmic approximations of the Lie derivatives of the tensorial quantities entering the algorithm are derived. Also, algorithmic loading-unloading conditions are derived. The proposed model is tested numerically in the solution of two problems of large scale plastic flow.

Further research directions comprise the derivation of more sophisticated models that include rate, thermal, and anisotropic effects for the accurate description of solid behavior, as well as the development of the additional necessary computational tools for the implementation of those models within the context of the finite element method.

References

- [Abraham et al. 1988] R. Abraham, J. E. Marsden, and T. Ratiu, *Manifolds, tensor analysis and applications*, 2nd ed., Springer-Verlag, New York, 1988.
- [Atluri 1984] S. N. Atluri, “On constitutive relations at finite strain: Hypo-elasticity and elasto-plasticity with isotropic or kinematic hardening”, *Comput. Methods Appl. Mech. Eng.* **43** (1984), 137–171.
- [Auricchio and Taylor 1995] F. Auricchio and R. L. Taylor, “Two material models for cyclic plasticity: non-linear kinematic hardening and generalized plasticity”, *Int. J. Plast.* **11** (1995), 65–98.

- [Auricchio and Taylor 1999] F. Auricchio and R. L. Taylor, "A return-map algorithm for general associative isotropic elastoplastic materials in large deformation regimes", *Int. J. Plast.* **15** (1999), 1359–1378.
- [Ciarlet 1988] P. Ciarlet, *Mathematical elasticity, Volume 1: Three dimensional elasticity*, North-Holland Publishing Company, Amsterdam, 1988.
- [Dafalias 1983] Y. F. Dafalias, "Co-rotational rates for kinematic hardening at large plastic deformations", *J. Appl. Mech. (Trans. ASME)* **40** (1983), 561–565.
- [Dafalias 1993] Y. F. Dafalias, "On multiple spins and texture development. Case study: kinematic and orthotropic hardening", *Acta Mech.* **100** (1993), 171–194.
- [Dafalias 1998] Y. F. Dafalias, "Plastic spin: necessity or redundancy?", *Int. J. Plast.* **14**:9 (1998), 909–931.
- [Dafalias 2001] Y. F. Dafalias, "Physico-geometrical coupling in finite strain elastoplasticity", pp. 65–77 in *Proceedings of Euromech Colloquium 430 on Formulations and Constitutive Laws for Very Large Strains*, edited by J. Plešek, October 3–5 2001.
- [Dashner 1986] P. A. Dashner, "Invariance considerations in large strain elasto-plasticity", *J. Appl. Mech. (Trans. ASME)* **53** (1986), 55–60.
- [Dyson 1972] F. J. Dyson, "Missed opportunities", *Bulletin of American Mathematic Society* **78** (1972), 635–652.
- [Eisenberg and Phillips 1971] M. A. Eisenberg and A. Phillips, "A theory of plasticity with non-coincident yield and loading surfaces", *Acta Mech.* **11** (1971), 247–260.
- [Gurtin 1981] M. E. Gurtin, *An introduction to continuum mechanics*, Academic Press., 1981.
- [Hartman 1972] P. Hartman, "On invariant sets and on a theorem of Wazewski", *Proceedings of the American Mathematical Society* **32**:2 (1972), 511–520.
- [Haupt and Tsakmakis 1986] P. Haupt and C. Tsakmakis, "On kinematic hardening and large plastic deformations", *Int. J. Plast.* **2** (1986), 279–293.
- [Koiter 1953] W. T. Koiter, "Stress-strain relations, uniqueness and variational theorems for elastic-plastic materials with a singular yield surface", *Quart. Appl. Math.* **11** (1953), 350–354.
- [Le and Stumpf 1993] K. H. Le and H. Stumpf, "Constitutive equations for elastoplastic bodies at finite strain: thermodynamic implementation", *Acta Mech.* **100** (1993), 155–170.
- [Lee 1969] E. H. Lee, "Elastic-plastic deformations at finite strains", *J. Appl. Mech. (Trans. ASME)* **36** (1969), 1–6.
- [Lee et al. 1983] E. H. Lee, R. L. Mallet, and T. B. Wertheimer, "Stress analysis for anisotropic hardening in finite-deformation plasticity", *J. Appl. Mech. (Trans. ASME)* **50** (1983), 554–560.
- [Lubliner 1974] J. Lubliner, "A Simple theory of plasticity", *Int. J. Solids Struct.* **10** (1974), 313–319.
- [Lubliner 1975] J. Lubliner, "On loading, yield and quasi-yield hypersurfaces in plasticity theory", *Int. J. Solids Struct.* **11** (1975), 1011–1016.
- [Lubliner 1986] J. Lubliner, "Normality rules in large-deformation plasticity", *Mech. Mater.* **5** (1986), 29–34.
- [Lubliner 1987] J. Lubliner, "Non-isothermal generalized plasticity", pp. 121–133 in *Thermomechanical Coupling in solids*, edited by H. D. Bui and Q. S. Nyugen, 1987.
- [Lubliner et al. 1993] J. Lubliner, R. L. Taylor, and F. Auricchio, "A new model of generalized plasticity and its numerical implementation", *Int. J. Solids Struct.* **30**:22 (1993), 3171–3184.
- [Lucchesi and Podio-Guidugli 1992] M. Lucchesi and P. Podio-Guidugli, "Materials with elastic range: a theory with a view toward applications: Part II", *Archive of Rational Mechanics and Analysis* **110** (1992), 9–42.
- [Mandel 1972] J. Mandel, *Plasticité classique et viscoplasticité*, Springer-Verlag, Vienna, New York, 1972. (CISM, Udine 1971).
- [Marsden and Hughes 1994] J. E. Marsden and T. J. R. Hughes, *Mathematical foundations of elasticity*, Dover Publications, New York, 1994.
- [Miehe 1998] C. Miehe, "A constitutive frame of elastoplasticity at large strains based on the notion of a plastic metric", *Int. J. Solids Struct.* **35**:30 (1998), 3859–3897.

- [Naghdi 1990] P. M. Naghdi, “A critical review of the state of finite plasticity”, *Zeitschrift Für Angewandte Mathematic und Physic* **41** (1990), 315–387.
- [Panoskaltzis et al. 1997] V. P. Panoskaltzis, S. Bahuguna, and D. Soldatos, “A general consistent integration scheme for rate-independent generalized plasticity”, pp. 540–547 in *Computational plasticity*, edited by D. R. J. Owen et al., Barcelona, Spain, 1997.
- [Pipkin and Rivlin 1965] A. C. Pipkin and R. S. Rivlin, “Mechanics of rate-independent materials”, *Zeitschrift für Angewandte Mathematik und Physik* **16** (1965), 313–326.
- [Simo 1988] J. C. Simo, “A framework for finite strain elastoplasticity based on maximum plastic dissipation and multiplicative decomposition Part I: Continuum formulation”, *Comput. Methods Appl. Mech. Eng.* **66** (1988), 199–219.
- [Simo and Hughes 1997] J. C. Simo and T. J. R. Hughes, *Computational inelasticity*, Springer-Verlag, New York, 1997.
- [Simo and Marsden 1984] J. C. Simo and J. E. Marsden, “On the rotated stress tensor and the material version of the Doyle-Ericksen formula”, *Archive of Rational Mechanics and Analysis* **86** (1984), 213–231.
- [Simo and Ortiz 1985] J. C. Simo and M. Ortiz, “A unified approach to finite deformation elastoplastic analysis based on the use of hyperelastic constitutive equations”, *Comput. Methods Appl. Mech. Eng.* **49** (1985), 221–245.
- [Simo et al. 1988] J. C. Simo, J. E. Marsden, and P. S. Krishnaprasad, “The Hamiltonian structure of elasticity. The convected representation of solids, rods and plates”, *Archive for Rational Mechanics and Analysis* **104** (1988), 125–183.
- [Valanis 1995] K. C. Valanis, “The physical metric in thermodynamics”, *Acta Mech.* **113** (1995), 169–184.
- [Valanis and Panoskaltzis 2005] K. C. Valanis and V. P. Panoskaltzis, “Material metric, connectivity and dislocations in continua”, *Acta Mech.* **175** (2005), 77–103.

Received 30 Sep 2006. Accepted 25 Oct 2007.

VASSILIS P. PANOSKALTSIS: vpp@nestor.cwru.edu

Department of Civil Engineering, Case Western Reserve University, Cleveland, OH, 44106-7201, United States

LAZAROS C. POLYMENAKOS: lcp@ait.edu.gr

Autonomic & Grid Computing, Athens Information Technology, Peania 19002, Greece

DIMITRIS SOLDATOS: jsol@ait.gr

Department of Civil Engineering, Case Western Reserve University, Cleveland, OH, 44106-7201, United States

ADVANCED POSTBUCKLING AND IMPERFECTION SENSITIVITY OF THE ELASTIC-PLASTIC SHANLEY–HUTCHINSON MODEL COLUMN

CLAUS DENCKER CHRISTENSEN AND ESBEN BYSKOV

The postbuckling behavior and imperfection sensitivity of the Shanley–Hutchinson plastic model column introduced by Hutchinson in 1973 are examined. The study covers the initial, buckled state and the advanced postbuckling regime of the geometrically perfect realization as well as its sensitivity to geometric imperfections.

In Section 1, which is concerned with the perfect structure, a new, simple explicit upper bound for all solutions to the problem is found when the tangent modulus at bifurcation vanishes compared to the linear elastic (unloading) modulus. The difference between the upper bound and the solution to an actual problem is determined by an asymptotic expansion involving hyperbolic trial functions (instead of polynomials) which fulfill general boundary conditions at bifurcation and infinity. The method provides an accurate estimate of the maximum load even if it occurs in an advanced postbuckling state. Finally, it is shown that the maximum load is often considerably larger than the bifurcation load.

Section 2 presents a new asymptotic expansion which is utilized to study the imperfection sensitivity of the Shanley–Hutchinson elastic-plastic model column. The method is mainly characterized by three novel features. Firstly, unlike other expansions which are performed around one or maybe two points, ours takes the total postbuckling path of the geometrically perfect structure as its basis, that is, the equilibrium of an imperfect path is written as the postbuckling path of the perfect structure plus an asymptotic contribution. Secondly, the expansion parameter is chosen as the buckling mode amplitude minus its value at initiation of elastic unloading. In this connection, the asymptotic expansion of initiating elastic unloading to the lowest order given by Hutchinson serves as a kind of boundary value for the asymptotic expression. Thirdly, a new and more suitable set of base functions is introduced to enhance the accuracy of the asymptotic expansion for large imperfection levels without compromising the asymptotic behavior for small imperfections. If an asymptotically exact postbuckling solution for the perfect structure around the maximum load has been obtained by some method, be it numerical or asymptotic, then the prediction of the imperfection sensitivity is asymptotically correct.

Introduction

Today, elastic-plastic stability of structures, including their imperfection sensitivity, may be examined by means of numerical methods. Such procedures may, however, suffer some major disadvantages. A complete analysis of the behavior of a perfect or a geometrically imperfect structure often becomes very time consuming, and in the vicinity of singularities, for example bifurcation, the equilibrium equations may become numerically unstable which might lead to divergence. This is one reason why analytical

Keywords: elastic-plastic stability, asymptotic expansion, imperfection sensitivity.

The present study was initiated when the first author was a graduate student and the second author was a member of the faculty at the Technical University of Denmark, Department of Structural Engineering and Materials.

investigation of stability problems is still important. Another, maybe even more important, ground for the interest in analytic methods is the desire to better understand elastic-plastic stability and imperfection sensitivity. It is therefore important to establish an analytic method for treatment of plastic stability.

For more than half a century, Koiter's general asymptotic theory of initial postbuckling and imperfection sensitivity of elastic structures has been available [Koiter 1945]. Development of a similar and as widely applicable theory of stability in the plastic range presents more difficulties, mainly due to the fact that, contrary to the case of elastic structures, the maximum load of a geometrically perfect elastic-plastic structure rarely occurs at bifurcation. To date, the most successful method has been established by Hutchinson [1973b]. However, as pointed out by Hutchinson himself, the method has a rather limited range of applicability for certain types of structures (see also [Hutchinson 1974]).

A short survey of plastic buckling. The history of analytical treatment of elastic-plastic stability is only a little more than one hundred years old, beginning with the work of Engesser [1889], who proposed a formula for the plastic bifurcation load, later known as the *tangent modulus load*, of a column. His formula was subjected to criticism and Engesser derived another formula under the tacit assumption that bifurcation occurs under constant load, the so-called *reduced modulus load*. It appears that over the next 60 years almost any professor of structural mechanics had his own formula for plastic column buckling. In retrospect it seems clear that these formulas are just weighted averages of the two loads mentioned above, and sometimes the *Euler buckling load* is also included in the weighting. Based on experiments on aluminum columns and by analyzing the initial postbifurcation behavior of a simple model column, which we refer to as the *Shanley column*, Shanley [1947] showed that the tangent modulus load was indeed the most meaningful of the previously suggested plastic buckling loads and that at that load, bifurcation takes place under increasing load. Soon after, Duberg and Wilder [1952] introduced imperfections in the Shanley model column, and later Hill [1957] established the minimum energy criterion of stability for a rigid plastic body.

While the works mentioned above were mainly concerned with determination of the correct plastic bifurcation load and to some extent also with the initial postbifurcation behavior, analytic determination of the maximum load-carrying capacity of geometrically perfect and imperfect structures received much less attention. Not until the work by Hutchinson [1973b], and the survey article [Hutchinson 1974] was an asymptotic method in the spirit of Koiter established. Hutchinson introduced terms of fractional powers in the asymptotic expansion in order to handle elastic unloading. Hutchinson's method and ideas were further explored by, among others, Needleman and Tvergaard [1976] and van der Heijden [1979].

Hutchinson [1972; 1973a] and van der Heijden [1979] prescribe that elastic unloading initiates at bifurcation for the perfect structure. The point of initiating elastic unloading of the imperfect structure is determined by a simple one-term elastic asymptotic expansion. Hutchinson uses this point as basis for an asymptotic expansion similar to the one he suggested for the perfect structure, while van der Heijden also uses the point of initiating elastic unloading to construct solutions in the spirit of his perfect solution. Both these solutions tend to be considerably more complicated than their perfect counterparts but suffer the same shortcoming: relatively accurate estimates of the load-carrying capacity is only found when the maximum load occurs very close to bifurcation. This is, however, rarely the case in plastic stability problems. Note that neither of the solutions predicts asymptotically correct maximum loads for small imperfections.

Hutchinson and Budiansky [1976] discovered that when the critical load of an elastic-plastic structure coincides with the reduced modulus load the maximum loads in the presence of imperfections sometimes coincide with the maximum loads of the hypoelastic comparison structure, and a theory rather similar to the simpler elastic asymptotic Koiter theory yields exact asymptotic estimates of these maximum loads. Needleman and Tvergaard [1976] suggested that even when the maximum load of the imperfect structure is found after initiating elastic unloading a hypoelastic theory may still yield sufficiently precise results. They base their idea on the fact that the larger the imperfections the less significant elastic unloading becomes. Comparison with numerical results shows that when the equilibrium of the geometrically perfect structure is not significantly influenced by plasticity this method estimates the imperfection sensitivity extremely well, but when the added stiffness of the elastic unloading zone dominates postbuckling a hypoelastic theory cannot be used for accurate estimates.

Thus, when plasticity is included the imperfection sensitivity analysis becomes even more complex, partly because the maximum load of both the perfect and the imperfect structure may be far from bifurcation, and partly due to the fact that each equilibrium path of the imperfect structure has a singularity where elastic unloading initiates. Probably for these reasons it seems that very few new approaches to analytic treatment of plastic postbuckling and imperfection sensitivity have been proposed since the above mentioned studies and none appears to have led to much improvement over the existing methods. Thus, a simple and universally accurate method for handling imperfection sensitivity of plastic structures has not yet been established. In this connection it may be worth mentioning that Ming and Wenda [1990] postulated to have improved Hutchinson's asymptotic method by choosing a different perturbation parameter. However, a closer examination of their work reveals that they determine the asymptotic coefficients correctly, but that their asymptotic plots do not match these coefficients at all. The correct curves do not approximate the maximum load any better (or worse) than Hutchinson's did. The article by Scherzinger and Triantafyllidis [1998] is concerned with an asymptotic analysis of stability of elastic-plastic structures, but their expansion parameter ε describes the slenderness of the beams investigated rather than a displacement variable, as is the case in the present study.

Since the Sixties, great effort has been spent on nonlinear numerical investigations of more realistic elastic-plastic structures. In spite of their own merits, numerical investigations rarely lead to a deeper understanding of the phenomenon of elastic-plastic buckling, at least not unless a large number of computations are carried out.

Main objectives. The maximum loads, denoted P_{\max} , of the analytical methods mentioned above are all fairly well predicted when the maximum load occurs very close to the point of bifurcation, even though the matching buckling amplitude is sometimes rather poorly determined. When P_{\max} lies far from the point of bifurcation the accuracy deteriorates rapidly. The main reason for including elastic unloading is the enhanced load-carrying capacity in postbuckling. Thus, an accurate determination of the postbuckling load reserve is of great importance, in particular when the maximum load becomes considerably higher than the bifurcation load.

In order to reduce the complexity of the problems as much as possible without loss of plastic characteristics, Hutchinson [1974] used a slightly modified version of the Shanley column which only differs from the original by being supported by a continuous row of springs and a nonlinear spring at the top in order to introduce various kinematic nonlinearities; see Figure 1. In the present paper we investigate both

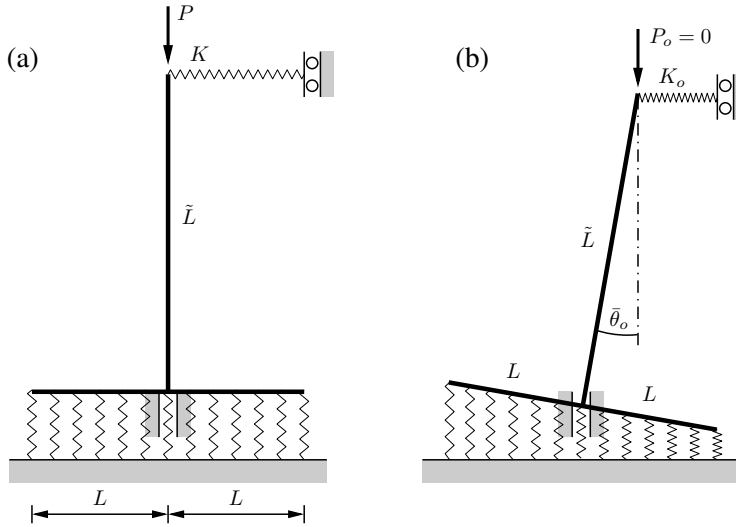


Figure 1. The continuous Shanley–Hutchinson column: (a) geometrically perfect; (b) geometrically imperfect.

the geometrically perfect and the geometrically imperfect version of the *Shanley–Hutchinson Column* and develop analytic methods which predicts the load-carrying capacity of the geometrically imperfect Shanley–Hutchinson elastic-plastic model column (see [Figure 1\(b\)](#), and for the the maximum load of its geometrically perfect counterpart, see [Figure 1\(a\)](#)) and concentrate on cases where P_{\max} does not occur close to bifurcation.

The ultimate goal of the investigation of plastic stability is, of course, to allow plastic stability to be included in maximum load calculations for more realistic structures, but that is not within the scope of the present paper.

1. Geometrically perfect model column

1.1. Preliminary analysis. In order for a solution to the plastic postbuckling problem to be considered satisfactory, we require that its prediction of the maximum load be accurate compared to the postbuckling load reserve and that the results be stable in the sense that the solution should be valid for all relevant cases. Furthermore, it is important that the solution be relatively simple and straightforward to apply to real structures.

Before 1970 the models considered—for example, the original Shanley column—were so simple that it was possible to give explicit solutions, but with the continuous Shanley–Hutchinson column and other more realistic models the complexity of the solutions made this impossible. We emphasize that by an explicit solution we do not necessarily mean the exact equilibrium, rather *explicit* is used in the sense of an *approximation* which does not invoke incremental steps. By this definition Hutchinson’s and van der Heijden’s solutions are also explicit. Such explicit solutions are subject to some limitations with regard to generality which will also be present in this paper:

- No other singularity can be present after the bifurcation singularity and before maximum load (for example, mode interaction, extension of the unloading zone all the way through the cross-section, Bauschinger effects, etc.).
- Unloading must start at bifurcation, which it will do in most relevant stability cases; see, for example, [Hutchinson 1974], and certainly for the Shanley–Hutchinson column.

The first limitation can be overcome by splitting the solutions into parts between singularities. The latter problem rarely occurs because unloading usually starts at bifurcation.

Before we proceed the search for a solution valid far from bifurcation, we discuss the merits of the most important existing methods.

Hutchinson's asymptotic expansion. The asymptotic expansion for initial postbuckling in the plastic range due to Hutchinson [1974] is the foundation for later asymptotic approaches to plastic stability. It is the natural, albeit not as obvious, extension of the elastic asymptotic theory by Koiter [1945] except for the fact that fractional powers are present in the expansions. It accounts for elastic unloading and material nonlinearities, but is still, like its elastic counterpart, fairly straightforward to apply to structural problems. The disadvantage of the method and the reason that new analytic plastic methods are still interesting is that it furnishes rather crude estimates of the maximum load and its associated displacements, unless the maximum occurs very close to bifurcation. This fact was already pointed out by Hutchinson [1974]. Later, van der Heijden [1979] showed that expanding Hutchinson's method further often produces less accurate approximations of the maximum load due to the unpredictable range of convergence for ordinary asymptotic methods.

The reduced modulus solution by van der Heijden. In his study, van der Heijden [1979] recognized that it was not the behavior in the vicinity of bifurcation, but the behavior close to the maximum load that controls the imperfection sensitivity. This led him to give an asymptotic estimate of the possible maximum loads close to the reduced modulus load thereby gaining knowledge about the approximate asymptotic behavior at maximum load. He then matched the asymptotic expansion established by Hutchinson with his own and ended up with an approximate expression for the equilibrium from bifurcation to maximum load. For maximum loads close to bifurcation this yields excellent predictions, but further away from bifurcation the accuracy decreases considerably, yet slightly less than Hutchinson's, as it appears from van der Heijden's comparison with numerical results [van der Heijden 1979]. The implementation of van der Heijden's method is lengthy in that three asymptotic expansions must be established, and the matching procedure is not straightforward and therefore hard to extend to higher degrees of asymptotic expansions as well as to generalize to other kinds of structures.

The hypoelastic imperfection sensitivity studies by Hutchinson and Budiansky and by Tvergaard and Needleman. The hypoelastic approach used by Hutchinson and Budiansky [1976] and by Needleman and Tvergaard [1976] suppresses the elastic unloading branch making it possible to analyze a nonlinear comparison version of plastic structures asymptotically in the spirit of Koiter's well-known linear elastic approach [Koiter 1945]. However, the similarity between the plastic structure and its associated comparison model in postbuckling strongly depends on the extent of the unloading zone and its added stiffness. This approximation will therefore only be satisfactory when elastic unloading is of minor importance.

Parameters of the solution. The postbuckling solution depends on the parameters of the material nonlinearity represented in the stress-strain relation and on the parameters of the kinematic nonlinearity concentrated in the nonlinear spring at the top of the column; see Figure 1(a). To fully understand the plastic behavior in postbuckling of the column, it is therefore crucial to investigate the influence the parameters of the model on the location of the maximum load point.

As presupposed in Section 1.2 the column unloads linearly elastic with a constant Young's modulus E . The larger E , the more elastic unloading dominates and makes the maximum load move away from bifurcation. The basic expressions (9) and (10) do not depend on the shape of the stress-strain relation before bifurcation, only on the values of E and E_t , where E_t denotes the tangent modulus, which, in general, depends on the strain.

As in most other buckling and postbuckling studies we assume that the tangent modulus E_t decreases with strain and approaches zero at infinite strain. The smaller the rate of decrease of E_t , the further from bifurcation the maximum load is.

The spring K (see Figure 1(a)) provides a *destabilizing* nonlinearity in order to make the structure *imperfection sensitive* and ensure the existence of a maximum load after bifurcation. The smaller the rate of increase of the kinematic nonlinearity the further from bifurcation the maximum load is going to be.

The stress-strain relation is mainly important close to bifurcation because, as E_t approaches zero, K will totally dominate the equilibrium equations. Since it is known that existing methods work well close to bifurcation it is particularly interesting to examine the behavior as the locus of maximum moves away from the point of bifurcation. This means that an investigation where K as well as the rate of decrease in E_t is small, while E is large, is particularly relevant to perform. For the sake of studying plastic effects on stability it is especially important that accurate results are obtained when E_t^c/E is small, where E_t^c designates the value of E_t at bifurcation.

We shall try not to exploit features that are particular to the Shanley–Hutchinson-model in our derivations in the hope that the method developed here is applicable to a broader variety of structures.

General idea. It is evident from the above that when examining plastic postbuckling behavior, one has to include elastic unloading. To keep it simple and straightforward, we would like to avoid the complications and limitations inherent in the reduced modulus approach, yet we would like to utilize the knowledge about the equilibrium when far from bifurcation in order to determine maxima in the advanced postbuckling regime. Hutchinson's general, simple and excellent concept of a Koiter-like asymptotic expansion [Hutchinson 1974] does not cover advanced postbuckling states due to the fact that the postbuckling fields were expanded in (fractional) powers of the buckling mode amplitude. Therefore, focus was centered on the immediate neighborhood of bifurcation. It is a well-known fact that the range over which an asymptotic expansion yields sufficiently accurate results is hard to predict, in fact, the range can be extremely small and may very well decrease with the number of terms in the asymptotic expansion, but choosing a set of more suitable trial functions, if available, may improve convergence. Below, we show that use of other trial functions that behave in a globally correct way may indeed extend the validity to cover advanced postbuckling states.

In order to improve the approximation of the correct equilibrium by the asymptotic expansion suggested by Hutchinson [1973b; 1974] and thereby obtain reliable results even when the maximum supported load does not appear close to bifurcation, we shall first examine carefully the general behavior of the Shanley–Hutchinson column in advanced postbuckling. Subsequently, we will use the acquired knowledge to choose suitable trial functions and make an asymptotic match at bifurcation between the new expansion and the original one by Hutchinson.

1.2. Basic equations. Throughout this paper a superscript c or a subscript c denotes a value taken at bifurcation. Superscript o or subscript o refers to Hutchinson’s original values with dimensions, while nondimensional quantities are left unmarked for convenience.

In order to isolate the kinematic nonlinearities in the top spring shown in Figure 1(a), Hutchinson used the approximation $\sin(\theta) \approx \theta$, and gave the top spring response as

$$K_o(\theta_o) = k_{io}\theta_o^{i+1}, \quad i \in \{1, 2, 3, \dots\} \tag{1}$$

where we note that *positive* values of k_{io} imply *destabilizing*. Since the lowest power of θ_o is 2, asymmetric postbifurcation of the kind experienced by the so-called Roorda Frame is not covered; see [Roorda 1965] and [Koiter 1966] for the elastic version, and [Byskov 1982–83] for the elastic-plastic version. In the purely elastic case, symmetric postbuckling like the one typical of many shell structures may be modeled by letting $k_{1o} > 0$. In the following examples we do not cover the case $k_{2o} \neq 0$ because it is rather trivial, but, as we shall see, for a special reason, address the one with $k_{3o} > 0$.

Together, Figure 1(a) and Figure 2 define the geometry. Note that the quantity E_{eff} , which is introduced below, designates the immediate effective tangent modulus, that is, it is E_t for loading and E for unloading, and that s is the stress. We keep as close to Hutchinson’s original notation as possible, but introduce the following nondimensional quantities:

$$\begin{aligned} x &= \frac{x_o}{L} & P &= \frac{P_o}{P_o^c} & s &= \frac{s_o}{2s_o^c} \\ \theta &= \frac{\tilde{L}}{L} \theta_o & u &= \frac{\tilde{L}}{L^2} u_o & \varepsilon &= \frac{\tilde{L}}{L^2} \varepsilon_o \\ E_{\text{eff}} &= \frac{3E_{\text{eff}}^o}{2E_{t_o}^c} & k_i &= \frac{L^{i+2}}{P_o^c \tilde{L}^i} k_{io} & \bar{\theta} &= \frac{\tilde{L}}{L} \bar{\theta}_o \end{aligned} \tag{2}$$

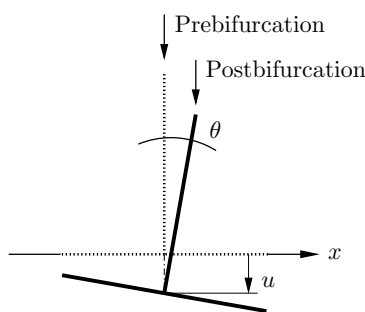


Figure 2. Definition of the kinematic variables u and θ .

where $\bar{\theta}$ signifies a geometric imperfection; see [Section 2.1, Figure 10](#).

The lowest bifurcation load is given by Hutchinson as

$$P_o^c = \frac{2E_{t_0}^c L^3}{3\tilde{L}},$$

which, by the way, is the same as the bifurcation load of the nonlinear elastic comparison model. The following nondimensional quantities evaluated at bifurcation are used extensively in the following:

$$P_c = 1, \quad s_c = \frac{1}{2}, \quad E_t^c = \frac{3}{2}. \tag{3}$$

Utilize the nondimensional quantities introduced in [Equation \(2\)](#) to obtain the nondimensional equilibrium equations of the geometrically perfect realization of the model column:

$$P = \int_{-1}^1 s dx, \quad P(\theta) + K(\theta) = \int_{-1}^1 s x dx, \tag{4}$$

where, in analogy with [Equation \(1\)](#), the nondimensional spring stiffness is

$$K(\theta) = k_i \theta^{i+1}, \quad i \in \{1, 2, 3, \dots\},$$

and the strain-displacement relation of the continuous spring support is

$$\varepsilon = u + \theta x. \tag{5}$$

When linear-elastic unloading is included, the stress increment \dot{s} is given as

$$\dot{s} = E_{\text{eff}} \dot{\varepsilon}, \tag{6}$$

where

$$E_{\text{eff}} = \begin{cases} E_t(\varepsilon), & \text{for } ((s = s_{\text{max}}) \wedge (\dot{s} \geq 0)), \\ E, & \text{for } ((s < s_{\text{max}}) \vee ((s = s_{\text{max}}) \wedge (\dot{s} < 0))), \end{cases} \tag{7}$$

and where a dot indicates an increment, and $s > 0$ implies compression.

The incremental equilibrium equations are readily obtained by differentiation of [Equation \(4\)](#) and the use of [Equation \(6\)](#).

The zone of elastic unloading spreads from the edge of the column support and extends to the point d , where no sign reversal of the strain rate has occurred, that is, $\partial\varepsilon/\partial\theta = \partial u/\partial\theta + d = 0$, and thus

$$d = -\frac{\partial u}{\partial\theta}. \tag{8}$$

When $d < -1$, there is no elastic unloading. Elastic unloading always initiates at the lowest bifurcation load of the perfect Shanley–Hutchinson column [[Hutchinson 1974](#)]. After introduction of the constitutive equation [\(7\)](#) the incremental equilibrium equations of the geometrically perfect model column may be written:

$$\frac{\partial P}{\partial\theta} = \int_{-1}^d E \left(\frac{\partial u}{\partial\theta} + x \right) dx + \int_d^1 E_t \left(\frac{\partial u}{\partial\theta} + x \right) dx \tag{9}$$

and

$$\frac{\partial P}{\partial \theta} \theta + P + \frac{\partial K}{\partial \theta} = \int_{-1}^d E \left(\frac{\partial u}{\partial \theta} + x \right) x dx + \int_d^1 E_t \left(\frac{\partial u}{\partial \theta} + x \right) x dx. \tag{10}$$

1.3. General behavior of the equilibrium. Before the postbuckling equations (9) and (10) can be solved, the constitutive relation, given by E and the expression for $E_t(\varepsilon)$ after buckling, as well as the kinematic nonlinearity in terms of $K(\theta)$ must be chosen. The study of plastic postbuckling mainly differs from the elastic in that, in the plastic case it is necessary to consider the effect of stiffening by unloading with the modulus E . In order to examine the influence of the stiffening, we therefore keep the postbuckling unloading stress-strain relationship and the kinematic nonlinearities fixed only allowing the initial Young’s modulus E to vary. An upper bound for the equilibrium is found when the unloading modulus approaches infinity, that is, when $E_t^c/E = 0$. When the initial slope of the postbuckling equilibrium is negative, that is, when $(\partial P/\partial \theta)_c \leq 0$, a lower bound with P_c as the maximum is characterized by $E_t^c/E = 1$. After the bounds have been established we are furnished with a firm frame for our further investigations: all other solutions are limited to this area and are furthermore not allowed to cross each other.

Upper bound. When $E \rightarrow \infty \Rightarrow E_t^c/E \rightarrow 0$ and it is assumed that $|P| < \infty$ and $|\partial P/\partial \theta| < \infty$, Equations (9) and (10) simplify substantially in that the introduction of $E_t^c/E = 0$ provides

$$0 = \int_{-1}^d \left(\frac{\partial u_\infty}{\partial \theta} + x \right) dx \quad \text{and} \quad 0 = \int_{-1}^d \left(\frac{\partial u_\infty}{\partial \theta} + x \right) x dx. \tag{11}$$

Superscript ∞ or subscript ∞ denotes the upper bound. Insert d given by Equation (8) to solve (11). The only possible solution is

$$\frac{\partial u_\infty}{\partial \theta} = 1 \quad \implies \quad u_\infty = \theta + u_c, \tag{12}$$

which means that the unloading zone does not progress into the cross-section, but is limited to one edge of the support. Express E by P and u in Equation (9) as

$$E = \frac{\frac{\partial P}{\partial \theta} - \int_d^1 E_t \left(\frac{\partial u}{\partial \theta} + x \right) dx}{\int_{-1}^d \left(\frac{\partial u}{\partial \theta} + x \right) dx},$$

and insert this expression and Equation (12) in Equation (10) to determine the load $P^\infty(\theta)$ associated with the upper bound

$$(1 + \theta) \frac{\partial P^\infty}{\partial \theta} + P^\infty = \int_{-1}^1 E_t(x + 1)^2 dx - \frac{\partial K}{\partial \theta},$$

identified as a first order linear differential equation, which, when the boundary condition $P^\infty(0) = 1$ is applied, has the solution

$$P^\infty(\theta) = \frac{1}{1 + \theta} \left(-K(\theta) + \int_{-1}^1 s_{\text{hypo}}(x + 1) dx \right). \tag{13}$$

Here, s_{hypo} is the nondimensional nonlinear hypoelastic postbuckling stress found independent of elastic unloading. For some choices of constitutive relations the integral may be computed explicitly when the stress-strain relationship is chosen.

The upper bound solution is particularly interesting because it covers the solutions where the maximum load appears as far from bifurcation as possible. This provides an ideal basis for the selection and fitting of asymptotic trial functions which provide reliable solutions far from bifurcation.

Lower bound. When E_t , as supposed, is a decreasing function of ε , the plastic model is able to carry higher loads than the related hypoelastic comparison model because of the stiffening of the elastically unloaded region. Thus, the comparison model provides an absolute lower bound for the plastic solutions. As mentioned above, in the plastic regime the maximum load usually does not occur at bifurcation. It is the case under the usual conditions that the stress-strain relation is continuous and that E is larger than E_t^c , otherwise the structure will not feel unloading as a stiffening. Furthermore, it is assumed that bifurcation does not take place at a sharp bend in the stress-strain relation. If, as an experiment, we choose $E_t^c/E \geq 1$ in the buckling model the usual conditions mentioned above are violated and it may be realized that the initial postbuckling stiffness will be smaller than that of the comparison model. The value of $\partial P_c/\partial \theta$ of the comparison model is always smaller than or equal to zero when no stabilizing kinematic nonlinearities are present and therefore the plastic model with $E_t^c/E = 1$ has a maximum at bifurcation. From this we deduce the important information that, as E_t^c/E decreases from 1 to 0, the maximum load will move from the bifurcation point to the maximum of P^∞ given by Equation (13). Since s is monotonically increasing from $x = -1$ to $x = 1$ for $\theta > 0$, the right side of Equation (4) will always be positive. This provides an absolute minimum for the solution of Equation (4) (right) and therefore a lower bound for any plastic solution with $E_t^c/E < 1$:

$$P \geq \frac{-K(\theta)}{\theta} = P_{\text{lower}}. \tag{14}$$

1.4. Hyperbolic asymptotic method. It may be shown that, as θ approaches infinity and E_t approaches zero, the integral in the upper bound solution Equation (13) loses significance compared to $K(\theta)$ yielding the far field solution

$$\lim_{\theta \rightarrow \infty} P^\infty \rightarrow \begin{cases} 0, & K(\theta) = 0, \\ -\frac{K(\theta)}{1 + \theta}, & K(\theta) \neq 0. \end{cases}$$

Compare the above equation to the absolute minimum solution Equation (14) and notice that they are approximately parallel to each other with a limited distance less than 1 when θ is large. Furthermore, we find that the solutions are asymptotically similar, that is, $P^\infty \sim P_{\text{lower}}$ for $\theta \rightarrow \infty$. Any arbitrary solution lies between the upper and lower bound and must therefore also behave asymptotically like the upper bound at infinity with a distance less than 1. In order to use the knowledge of the upper bound and the relative shape of other solutions it seems obvious to concentrate on an asymptotic expansion of the difference $\Delta P^\infty \leq 0$ between the upper bound P^∞ and the solution P ; see Figure 3.

$$\Delta P^\infty = P - P^\infty. \tag{15}$$

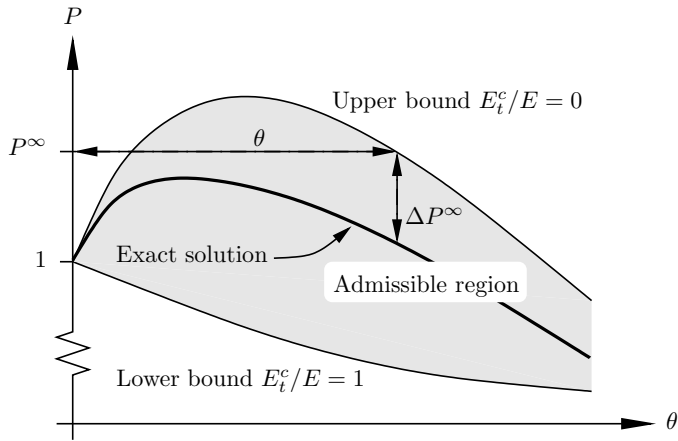


Figure 3. The hyperbolic asymptotic method and the admissible region.

This choice has the convenient feature that it predicts both the maximum load and its associated displacement well when the solution lies close to the upper bound, even when the maximum load occurs far from bifurcation. The usual polynomial asymptotic trial functions are, however, not suited for the expansion of ΔP^∞ because they do not in general fulfill the above-mentioned conditions of parallelism and negativity. Hyperbolic functions¹ not only satisfy these conditions, but have the property that their lowest order terms dominate the general behavior, that is, not only for small, but for all values of θ . The basic idea is to establish a hyperbolic approximation $\mathcal{H}(\theta)$ using the characteristics of ΔP^∞ and matching these terms with the first few nonvanishing asymptotic terms of the series of Hutchinson [1974]; see Appendices A and B. Since ΔP^∞ in general only vanishes *relative* to P^∞ at infinity, we choose the leading power of the denominator to be only fractionally higher than that of the numerator. The lowest order asymptotic term is then given by the numerator, while the next terms are used in the denominator to restrain the growth of the expression. In practice, applying the first two terms of the denominator proves to furnish a sufficiently accurate first approximation

$$\Delta P^\infty \approx \mathcal{H}(\theta) = a_1^\infty H(\theta) = a_1^\infty \frac{\theta^{\frac{3}{2}}}{(1 + h_1\theta^{\frac{1}{2}} + h_2\theta)^2}.$$

Notice that $\mathcal{H}(\theta)$ will always be negative because, according to Equation (B.3); see Appendix B, and the above equation, $a_1^\infty = a_2^\Delta < 0$. If further exploration is desired, $H(\theta)$ provides a basic trial function for a *hyperbolic* asymptotic method

$$\Delta P^\infty = a_1^\infty H(\theta) + a_\alpha^\infty H(\theta)^\alpha + a_\beta^\infty H(\theta)^\beta + O(H(\theta)^\gamma), \quad 1 < \alpha < \beta < \dots < \gamma. \quad (16)$$

When $H(\theta)$ is chosen to match the first three nonvanishing asymptotic terms, a_α^∞ and α may be determined from the fourth term and so forth. The general expansion Equation (16) still behaves globally correct. It approaches zero at infinity and higher order asymptotic terms of $H(\theta)$ become increasingly less significant compared to lower order terms for large values of θ .

¹Here, we use the term *hyperbolic* in a somewhat generalized sense.

Hyperbolic asymptotic expansion coefficients. In order to determine $a_1^\infty, h_1, h_2, a_\alpha^\infty, \alpha$, etc., we match the hyperbolic expansion Equation (16) with that of Hutchinson [1974]. An asymptotic expansion carried to a higher degree in θ than Hutchinson's is given in Appendix A; see Equations (A.1), (A.2), (A.6) and (A.7). The extension of the method is straightforward, but rather lengthy. The polynomial expansion of $H(\theta)$ is

$$H(\theta) = \theta^{\frac{3}{2}} - 2h_1\theta^2 - (2h_2 - 3h_1^2)\theta^{\frac{5}{2}} + (6h_1h_2 - 4h_1^3)\theta^3 + O(\theta^{\frac{7}{2}}).$$

Insert the above equation into (16) and compare with Equation (B.2) to obtain expressions for the hyperbolic coefficients

$$a_1^\infty = a_2^\Delta, \quad h_1 = \frac{a_3^\Delta}{-2a_2^\Delta}, \quad h_2 = \frac{a_4^\Delta}{-2a_2^\Delta} + \frac{3}{2}h_1^2,$$

where a_i^Δ are the polynomial asymptotic coefficients given in Equation (B.3). When a_1^∞, h_1 and h_2 are determined from the three initial asymptotic terms, α must be equal to 2 for the θ^3 -term to match. Thus,

$$\alpha = 2: \quad a_\alpha^\infty = a_2^\infty = a_5^\Delta - a_2^\Delta(6h_1h_2 - 4h_1^3).$$

Although we have found no case where it was necessary to determine the β -term of Equation (16), we mention that the value of β is $\frac{7}{3}$. Carrying out the expansion to cover this is, however, so lengthy and complicated that it may not be worth the while.

Finally, inserting Equation (16) into (15) provides the total solution for P .

The fact that we have chosen other trial functions than the usual polynomials does not change the asymptotic behavior of the initial postbuckling path, that is, for small values of θ . The new asymptotic expansion will therefore be no worse than the original one when E_t^c/E is increased and the maximum load approaches bifurcation as shown in the lower bound solution. This indicates that the use of our hyperbolic trial functions will produce accurate maximum loads for all $0 \leq E_t^c/E \leq 1$. When P is determined, the displacement u may be found after P has been inserted into Equations (9) and (10).

1.5. Constitutive relation. Traditionally, a Ramberg-Osgood type stress-strain relation has often been employed in elastic-plastic buckling studies, such as the important ones by Hutchinson [1974] and by van der Heijden [1979]. For our purpose, this constitutive model has the disadvantage of expressing the strain in terms of the stresses instead of the other way around implying numerical integrations. As far as possible, we prefer analytic manipulations and therefore propose another constitutive model, which provides an explicit formula for the tangent modulus E_t in terms of the added strain $\Delta\varepsilon$ after bifurcation and a shape parameter ρ :

$$E_t = \frac{E_t^c}{1 + \rho\Delta\varepsilon} = \frac{3}{2(1 + \rho\Delta\varepsilon)}. \tag{17}$$

When ρ and the ratio E_t^c/E are varied, this relation may cover a wide variety of constitutive behavior and may be considered as versatile and valid as the Ramberg-Osgood type formula [Hutchinson 1974]:

$$\frac{\varepsilon}{\varepsilon_y} = \frac{s}{s_y} + \psi \left(\frac{s}{s_y} \right)^n, \tag{18}$$

where ε_y and $s_y = E\varepsilon_y$ are effective initial yield values, n is the hardening parameter, and ψ is a shape parameter.

In [Example 1](#) below we wish to compare results obtained by our improved method with those found by [Hutchinson \[1974\]](#) and by [van der Heijden \[1979\]](#). Therefore, we need to examine the differences between the two constitutive relations for a certain set of parameters. Both [Hutchinson \[1974\]](#) and [van der Heijden \[1979\]](#) take $(n, \psi) = (3, 0.2)$. Numerical experiments show that the tangent modulus decrease rate $\rho = 3.0$ in [Equation \(17\)](#) produces a constitutive law very similar to the one used by Hutchinson and van der Heijden; see [Figure 4](#), where the relative difference between the values of the tangent modulus E_t found by the two constitutive relations is plotted over a very large interval of $\Delta\varepsilon$. It may be worthwhile noticing that for $n = 10$ the proper value of ρ is about 25.

Stress-strain relation and the upper bound. In [Equation \(13\)](#) the postbuckling stress-strain relation is represented by s_{hypo} . To avoid a numerical calculation of the integral, we therefore chose E_t as an explicit function of ε ; see [\(17\)](#). Now, [\(17\)](#) may yield the following expression for s_{hypo} :

$$s_{\text{hypo}} = \frac{E_t^c}{\rho} \ln(1 + \rho\Delta\varepsilon) + \frac{1}{2} = \frac{3}{2\rho} \ln(1 + \rho\Delta\varepsilon) + \frac{1}{2}. \tag{19}$$

At the upper bound, straightforward use of [Equation \(12\)](#) provides $\Delta\varepsilon = (1 + x)\theta$. Introduce this expression into [\(19\)](#) and exploit this in [Equation \(13\)](#) to get an explicit nondimensional expression for the upper bound:

$$P^\infty = 1 + \frac{1}{1 + \theta} \left[-\theta - K(\theta) + \frac{3}{2\rho} \left(\frac{1}{\rho\theta} - 1 + \left(2 - \frac{1}{2(\rho\theta)^2} \right) \ln(1 + 2\rho\theta) \right) \right]. \tag{20}$$

Example 1: comparison with previous results. As a demonstration of the improved accuracy of our new method, we compare the postbifurcation equilibrium with the asymptotic solution of [Hutchinson \[1974\]](#) and with the approximate solution by [van der Heijden \[1979\]](#) and utilize numerical results to judge the accuracy for a case which was found to be particularly demanding by [Hutchinson \[1974\]](#) and [van der Heijden \[1979\]](#), namely the case where $E_t^c/E = 0.459$. Furthermore, the example covers cases where the maximum load occurs close to bifurcation and where it lies close to the upper bound maximum.

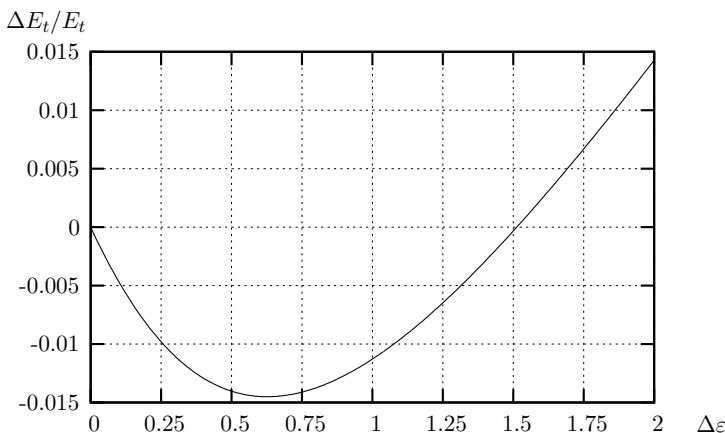


Figure 4. Relative difference between E_t found by the Ramberg–Osgood constitutive law [Equation \(18\)](#) with $(n, \psi) = (3, 0.2)$ and by [Equation \(17\)](#) with $\rho = 3$.

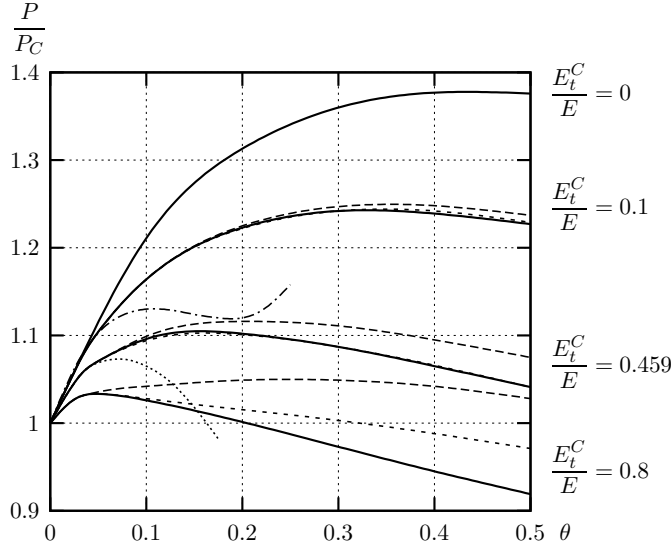


Figure 5. Postbuckling equilibria of the hyperbolic asymptotic method compared with numerical results, $(n, \psi) = (3, 0.2)$, $\rho = 3.0$, $k_i = 0$. Hutchinson’s and van der Heijden’s results are only plotted for $E_t^c/E = 0.459$. Here, the dotted line shows Hutchinson 1973, dot-dashed line, van der Heijden 1979, thin dashed line, 2 Hyperbolic terms, thick dashed line, 1 Hyperbolic term and solid line, Numerical.

Figure 5 contains plots of the postbuckling path determined by our hyperbolic asymptotic solution with 1 and 2 terms and by numerical computations, respectively. For purpose of comparison, the upper bound solution $E_t^c/E = 0$ is also indicated.

A good measure of the effect of some hyperbolic asymptotic term, $cH(\theta)^k$, on the solution is its maximum value. In each example, define \tilde{H} such that its maximum value is 1. Then, the hyperbolic asymptotic expressions (15) and (16) yield:

$$\begin{aligned}
 \frac{E_t^c}{E} = 0.1: \quad & P = P^\infty - 0.16\tilde{H} - 0.01\tilde{H}^2, \quad \tilde{H} \equiv \frac{17.2\theta^{\frac{3}{2}}}{(1 + 0.13\theta^{\frac{1}{2}} + 3.01\theta)^2}, \\
 \frac{E_t^c}{E} = 0.459: \quad & P = P^\infty - 0.33\tilde{H} - 0.04\tilde{H}^2, \quad \tilde{H} \equiv \frac{22.5\theta^{\frac{3}{2}}}{(1 + 0.35\theta^{\frac{1}{2}} + 3.39\theta)^2}, \\
 \frac{E_t^c}{E} = 0.8: \quad & P = P^\infty - 0.36\tilde{H} - 0.06\tilde{H}^2, \quad \tilde{H} \equiv \frac{45.0\theta^{\frac{3}{2}}}{(1 + 0.75\theta^{\frac{1}{2}} + 5.00\theta)^2}.
 \end{aligned} \tag{21}$$

Notice that the maximum (coefficient) value of the second asymptotic term is small compared to the maximum of the first asymptotic term even when E_t^c/E is much greater than 0 and the solution lies far from the upper bound. This indicates that the solution is relatively accurate even with only one asymptotic term. Still, the ratio between the first and the second asymptotic coefficient does not drop

significantly for increasing ratios of E_i^c/E , which indicates that more than one asymptotic term is needed for satisfactory results when the solution lies far from the upper bound.

From Figure 5, it is clear that the one-term hyperbolic solution provides excellent agreement with the numerical results when E_i^c/E is small. As E_i^c/E is increased and the solution moves away from the upper bound, the accuracy becomes less good. Employment of a second hyperbolic term makes the hyperbolic solution almost identical to the numerical one for $\theta \lesssim \theta_{\max}^{\infty} \approx 0.46$ both when $E_i^c/E = 0.1$ and $E_i^c/E = 0.459$. For $E_i^c/E = 0.8$ the maximum load and its neighborhood are determined accurately because of their proximity to bifurcation, but the solution is so far from the upper bound that the general hyperbolic asymptotic postbuckling path starts to deviate from the numerical one from $\theta \approx 0.1$. This is in agreement with what was deduced from Equation (21).

As expected, the two-term hyperbolic solution is considerably closer to the general numerical equilibrium than Hutchinson's and van der Heijden's solutions for $E_i^c/E = 0.459$ and the maximum load is more precise. Both Hutchinson's and van der Heijden's methods are basically polynomial asymptotics emanating from the ordinate axis, and therefore their solutions tend to deteriorate rapidly with increasing θ . Of the solutions investigated by Hutchinson and by van der Heijden, the case with $E_i^c/E = 0.459$, $k_i = 0$ exhibits the greatest ratio between the maximum load and the critical load and the largest θ -value at maximum load. From Figure 5 it is seen that other equilibria have maxima that occur significantly further from the bifurcation point and it is for such cases the hyperbolic method has its real *raison d'être*.

Even though the maximum load is determined with excellent accuracy by a two-term hyperbolic expansion, the value of θ at maximum may not be as precise.

Example 2: maximum loads. As stated earlier, our real interest lies in a precise determination of the maximum load. Previously, we have discussed the impact of the different parameters of the model on the location of maximum load relative to the critical load. The implementation of the postbuckling uploading stress-strain relation Equation (19) reduces the number of independent parameters in the determination of $P_{\infty}(\theta)$ to the kinematic nonlinearities, k_i , the rate of decrease in tangent modulus ρ and the level of plasticity E_i^c/E .

The parameters, k_i , control the fundamental *overall* shape of the equilibrium. Three basically different shapes may be distinguished:

- (i) $k_i = 0$: no destabilizing kinematic nonlinearity is present. The maximum load will be far from bifurcation.
- (ii) $k_1 \neq 0$: a rapid initial drop in load-carrying capacity will occur and the maximum load is close to bifurcation.
- (iii) $k_i \neq 0$, i large: if i is sufficiently large the k_i -term will not be felt at the present stage of Hutchinson's asymptotic expansion Equation (B.2). The third spring constant, k_3 , is the lowest level of kinematic nonlinearity not to appear in the terms of the Hutchinson asymptotic expansion used to determine the first 2 hyperbolic asymptotic terms. On the other hand, in the application of our method it enters through the expression (20) for P^{∞} . To have any noticeable influence on the maximum load, k_3 must be relatively large. When $\theta = 0.5$, the value $k_3 = 12$ furnishes a kinematic nonlinearity equal the nonlinearity associated with $k_1 = 3$.

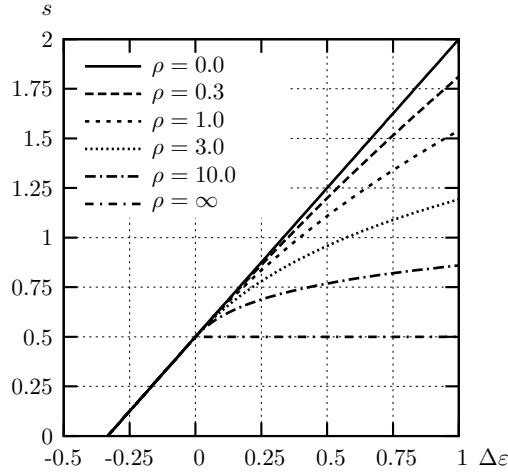


Figure 6. Stress-strain relations for ρ -values used in the maximum load plots. Unloading paths are not shown.

Figures 7, 8 and 9 show the maximum load for each of these cases as a function of the level of plasticity E_t^c/E for the tangent modulus decrease rate, ρ , varying between no decrease $\rho = 0$ and infinitely rapid decrease $\rho \rightarrow \infty$, as illustrated in Figure 6. As is clear from the figure, a wide spectrum of stress-strain relations are covered by the constitutive equation Equation (17).

Because of the different nature of each of the plots in Figures 7–9, we shall first examine each plot separately and then draw a more general conclusion. Note that, in order to make it possible to differentiate between the curves found by the hyperbolic method and by numerical computations, the plots in Figures 7–9 are scaled differently.

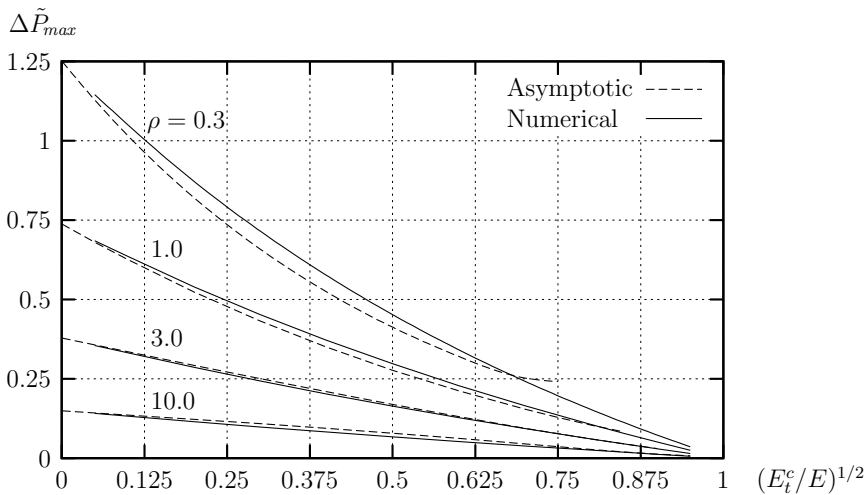


Figure 7. Maximum loads approximated with 2 asymptotic terms, $K(\theta) = 0$.

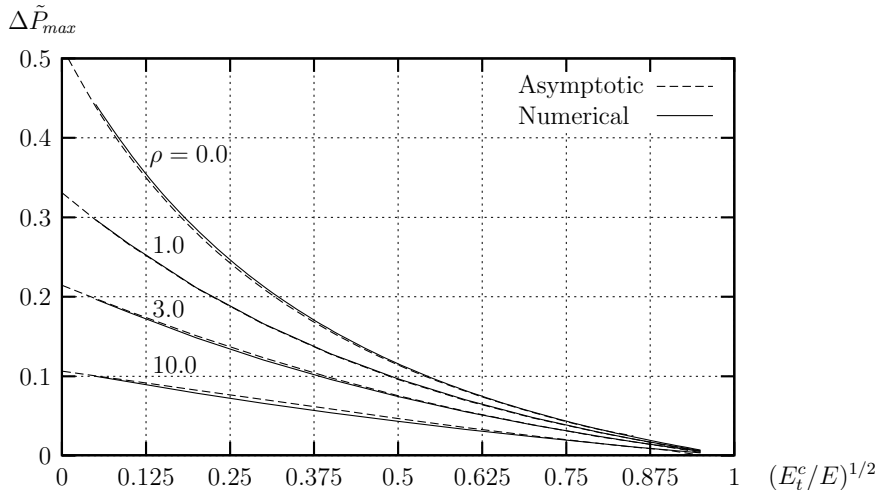


Figure 8. Maximum loads approximated with 2 asymptotic terms, $K(\theta) = 3\theta^2$.

- **Figure 7**, $k_i = 0$: In this case, the kinematic nonlinearity is as weak as possible in that the only kinematically nonlinear effect is the one which provides bifurcation. Therefore, the maximum load curve for $\rho = 0.0$ does not exist for finite θ . This means that when ρ is close to 0, the 2-term hyperbolic expansion does not provide a maximum because it is too far from both the upper bound and bifurcation.

Apart from the above-mentioned exception, the *added* load-carrying capacity in postbuckling, ΔP_{max} , is found with only a small relative error of less than $\approx 10\%$ everywhere.

The plot shows that ΔP_{max} is often significant compared to P_c as it for $\rho \leq 0.3$ becomes as large as 125% of P_c (recall that $P_c = 1$). For $\rho \rightarrow 0$ the upper bound solution yields a ΔP_{max} of 400% of P_c .

- **Figure 8**, $k_1 = 3$: Here, the kinematic nonlinearity is strong and, as a consequence of this, all maximum loads are extremely well approximated independently of the distance from the bifurcation point. This hinges on the fact that every solution is close to both the upper bound and the bifurcation point at maximum. Observe that, even when the first order kinematic nonlinearity, $k_1 = 3$, is large, the column has a considerable load-carrying reserve in postbuckling of up to $\approx 50\%$ of P_c when ρ and E_t^c/E are small.
- **Figure 9**, $k_3 = 12$: As mentioned above, this is a case where k_i only enters through the formula for ΔP^∞ . Therefore, the approximations by the hyperbolic expansion could be expected to be inaccurate.

However, except for fairly large values of E_t^c/E and small values of ρ , the difference between the predictions of the hyperbolic expansion and those obtained by numerical computations is small. Though not as precise as in the above cases, the hyperbolic expansion curves still yield satisfactory accuracy, generally under 15% relative error on the postbuckling load reserve, except very close to linear elastic, kinematically linear behavior.

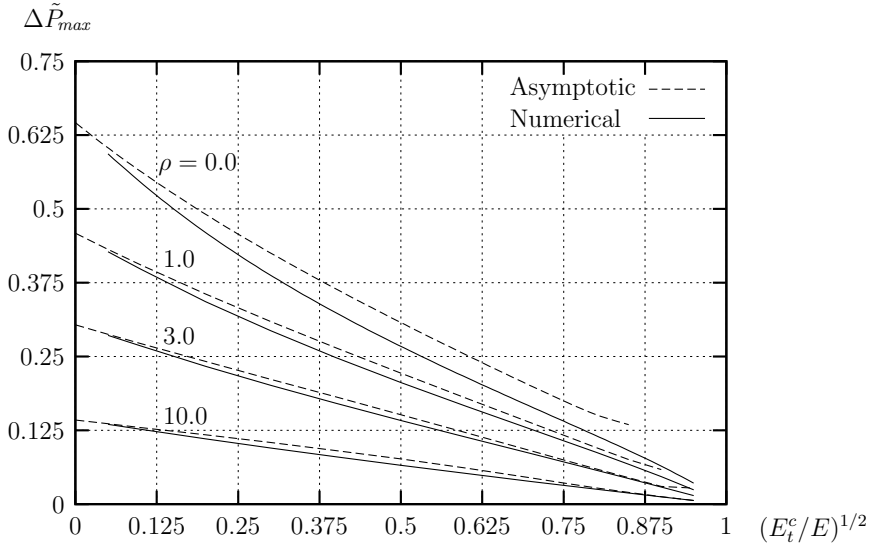


Figure 9. Maximum loads approximated with 2 asymptotic terms, $K(\theta)=12\theta^4$.

In this case, the Hutchinson asymptotic expansion is here identical to the expansion for $k_i = 0$. For ρ large the maximum loads are almost not influenced by the kinematic nonlinearity and they equal the loads for $k_i = 0$ in Figure 7.

Our method has thus proved to be capable of handling effects that are not included in the Hutchinson asymptotic expansion, simply because of the influence from ΔP^∞ .

We emphasize that the precision of the postbuckling load reserves determined by the hyperbolic asymptotic method is generally satisfactory when 2 terms are used. Only very close to linear elasticity combined with no dominating destabilizing kinematic nonlinearities (where the postbuckling load reserve is insignificant) may a third term be necessary to ensure sufficient accuracy.

From our plots we conclude that the model column is often able to carry loads which are much larger than the critical load, even without kinematically stabilizing effects in postbuckling. It is therefore important to have an accurate method for advanced postbuckling calculations, and the hyperbolic asymptotic method is found to fulfill this demand.

It may be argued that some of the large maximum loads are found at extreme values of the angle θ that would never be allowed in a design situation. Yet those loads are interesting because the maximum load-carrying capability will serve as an energy absorber of extreme unpredicted influences or imperfections and thereby prevent sudden collapse of stability. Also, since we are not studying a real structure, but a model column, the values of θ must not be taken too literally.

Conclusion. A hyperbolic asymptotic method for initial as well as advanced postbuckling analysis of Hutchinson’s plastic model column is derived. The simple explicit solution for $E_i^c/E = 0$ (the upper bound) is found and it is shown that any other solution must approach it asymptotically to lowest order at infinity. The difference between the upper bound and the actual solution is estimated by an asymptotic expansion with hyperbolic trial functions that vanish at infinity.

It is shown that maximum loads are often obtained far from bifurcation, which creates the need for a method which is precise also in the advanced postbuckling regime. Comprehensive comparison to numerical results proves our method accurate both close to and far from bifurcation.

We are confident that the principle of the hyperbolic asymptotic method will prove applicable to a wide range of structures. Though the upper bound may not always be as easily obtained, the correct global behavior of the asymptotic trial functions can still be investigated and used through knowledge of the postbuckling equilibrium between or close to bounds, for example, the upper bound, a simple expansion of the lower bound close to bifurcation, the elastic solution, an expansion at infinity, etc.

2. Geometrically imperfect model column

2.1. General concept. When the amplitude of the imperfection approaches zero, the equilibrium path of the imperfect structure approaches the postbuckling equilibrium path of the perfect one. Therefore, if the postbuckling equilibrium of the perfect model column has been determined, the equilibrium path of the imperfect structure may be found from an asymptotic expansion in a characteristic imperfection amplitude, which for the Shanley–Hutchinson column is the initial rotation $\bar{\theta}$ mentioned in Section 1.2; see Figure 10. A closer investigation of Hutchinson’s asymptotic expansion at the onset of elastic unloading may provide useful knowledge on which to base the expansion mentioned above.

2.1.1. Hutchinson’s asymptotic expansion at onset of elastic unloading. The equilibrium equations of the imperfect model exhibit singular behavior when elastic unloading initiates, and solutions including linear elastic unloading cannot be extended into the (hypo-)elastic zone. Asymptotic expressions for $\hat{\theta}$, \hat{P} and \hat{u} are given by Hutchinson [1973a]:

$$\hat{\theta} = \hat{\theta}_1 \bar{\theta}^{\frac{1}{2}} + O(\bar{\theta}), \quad \hat{P} = 1 + \hat{p}_1 \bar{\theta}^{\frac{1}{2}} + O(\bar{\theta}), \quad \hat{u} = u_c + \hat{u}_1 \bar{\theta}^{\frac{1}{2}} + O(\bar{\theta}) \quad (22)$$

where

$$\hat{\theta}_1 = \left(\frac{\omega}{a_1^{pla} - a_1^{ela}} \right)^{\frac{1}{2}}, \quad \hat{p}_1 = (2a_1^{ela} - a_1^{pla}) \left(\frac{\omega}{a_1^{pla} - a_1^{ela}} \right)^{\frac{1}{2}}, \quad \hat{u}_1 = \frac{L}{3L} p_1^e.$$

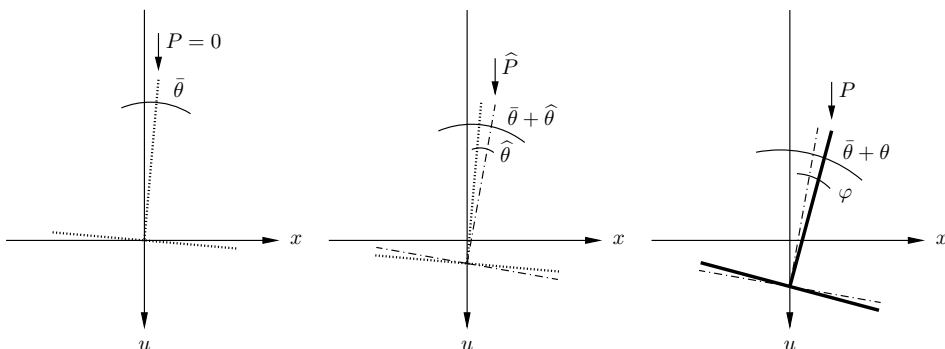


Figure 10. Definition of the kinematic variables θ , $\hat{\theta}$, φ and u as well as various values of the load. The hat $\hat{}$ indicates values at the onset of elastic unloading.

Here, a_1^{ela} and a_1^{pla} are the initial slopes of the elastic and plastic equilibrium paths of the geometrically perfect structure, respectively. The formula for ω is given by [Hutchinson 1974, Equation (2.52)]²

$$\omega = \left(1 - \frac{LE_t^{c'} L}{3E_t^c \tilde{L}}\right)^{-1}, \quad a_1^{pla} = \frac{3\tilde{L}}{L}, \quad a_1^{ela} = -\frac{3\omega k_1 \tilde{L}}{2L}.$$

Note that Equation (22) gives the onset of elastic unloading for the imperfect column as the onset of elastic unloading for the perfect column at bifurcation plus additional asymptotic terms in the imperfection $\bar{\theta}$.

2.1.2. Asymptotic expansion for the imperfect column in the plastic domain. In order to utilize Hutchinson’s asymptotic expansion of the onset of unloading as a bound, or boundary state, of an asymptotic expansion of the equilibrium of the imperfect column after unloading has initiated, our expansion must match Hutchinson’s expansion at the onset of unloading. Therefore, the fundamental form of the asymptotic expansion for the geometrically imperfect structure is taken to be

$$\begin{aligned} \theta_{\text{imp}}(\bar{\theta}) &= \theta_{\text{per}} + \Delta\theta_i = \theta_{\text{per}} + \theta_1 \bar{\theta}^{\frac{1}{2}} + O(\bar{\theta}), \\ P_{\text{imp}}(\bar{\theta}) &= P_{\text{per}} + \Delta P_i = P_{\text{per}} + p_1 \bar{\theta}^{\frac{1}{2}} + O(\bar{\theta}), \\ u_{\text{imp}}(\bar{\theta}) &= u_{\text{per}} + \Delta u_i = u_{\text{per}} + u_1 \bar{\theta}^{\frac{1}{2}} + O(\bar{\theta}). \end{aligned} \tag{23}$$

For brevity only the dependence on $\bar{\theta}$ is indicated. Subscripts $_{\text{per}}$ and $_{\text{imp}}$ refer to equilibrium of the perfect and the imperfect structure, respectively.

When the perfect column starts unloading θ increases from 0, and boundary conditions for the asymptotic functions θ_1 , p_1 and u_1 given by Equation (22) yield

$$\theta_1 \Big|_{\theta_{\text{per}}=0} = \widehat{\theta}_1, \quad p_1 \Big|_{\theta_{\text{per}}=0} = \widehat{p}_1, \quad u_1 \Big|_{\theta_{\text{per}}=0} = \widehat{u}_1.$$

One of the functions, θ_1 , p_1 or u_1 , in Equation (23) may be chosen independently as long as the boundary conditions given above are fulfilled, and all equilibrium states of the imperfect structure states may be reached. Since $\theta_{\text{per}} \in [0; \infty[$ and $\theta_{\text{imp}} \in [\widehat{\theta}_1 \bar{\theta}^{\frac{1}{2}} + O(\bar{\theta}); \infty[$ a valid, simple choice of independent variable is

$$\theta_{\text{imp}}(\bar{\theta}) = \theta_{\text{per}} + \widehat{\theta}_1 \bar{\theta}^{\frac{1}{2}} + O(\bar{\theta}), \tag{24}$$

which for a given imperfection is just a transformation of θ as demonstrated in Figure 11. Note that when $\theta_{\text{per}} \geq 0$ the solutions for the perfect and the imperfect column both lie in the plastic domain.

This asymptotic approach to the plastic imperfection analysis has some advantages which are not present in earlier expansions:

- (i) it proves to be fairly simple;
- (ii) the accuracy of the imperfection sensitivity analysis will be good even for large $\varphi \equiv \theta - \widehat{\theta}$ if the solution for the geometrically perfect structure is accurate;
- (iii) it allows utilization of either a numerical or an asymptotic solution to the geometrically perfect column, which can be of great advantage since a numerical solution that is accurate even for large values of θ may be obtained for most structures.

²Hutchinson [1974] uses ρ instead of ω , but for consistency with Section 1, where ρ is used for another purpose, we use ω .

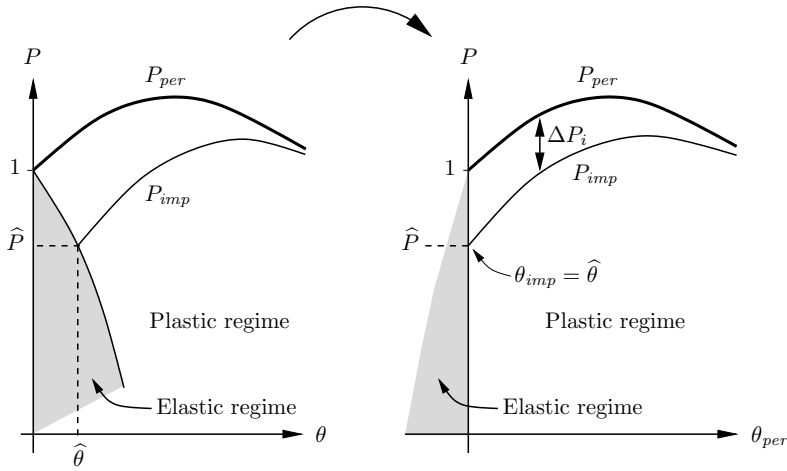


Figure 11. The asymptotic method for the imperfect structure.

2.2. Asymptotic solution for the imperfect structure. Equilibrium for the geometrically imperfect model column is controlled by Equations (9) and (10). These equations must be transformed in such a way that they depend only on θ_{per} and $\bar{\theta}$. Let a dot denote differentiation with respect to θ_{per} :

$$\dot{(\cdot)} \equiv \frac{\partial(\cdot)}{\partial\theta_{per}}.$$

Since, according to Equation (24), $\dot{\theta}_{imp} = 1$ holds everywhere, by insertion of Equations (23) and (24), Equations (9) and (10) are transformed into

$$\dot{P}_{imp} = \int_{-\dot{u}_{imp}}^1 E_t^{imp}(\dot{u}_{imp} + x) dx + \int_{-1}^{-\dot{u}_{imp}} E(\dot{u}_{imp} + x) dx \tag{25}$$

and

$$\begin{aligned} \dot{P}_{imp}(\theta_{per} + \hat{\theta}_1 \bar{\theta}^{\frac{1}{2}} + O(\bar{\theta})) + P_{imp} + (i + 1) k_i (\theta_{per} + \hat{\theta}_1 \bar{\theta}^{\frac{1}{2}} + O(\bar{\theta}))^i \\ = \int_{-\dot{u}_{imp}}^1 E_t^{imp}(\dot{u}_{imp} + x) x dx + \int_{-1}^{-\dot{u}_{imp}} E(\dot{u}_{imp} + x) x dx. \end{aligned} \tag{26}$$

2.2.1. Expansion of the tangent modulus. In the vicinity of the solution for the geometrically perfect column the tangent modulus E_t can be given in terms of a Taylor expansion in the strain ε_{imp} . For a given value of θ_{per} the expansion becomes:

$$E_t^{imp}(\bar{\theta}, \theta_{per}, x) = E_t^{per}(\theta_{per}, x) + (\varepsilon_{imp} - \varepsilon_{per}) E_t^{per'}(\theta_{per}, x) + O((\varepsilon_{imp} - \varepsilon_{per})^2).$$

where prime (') denotes differentiation with respect to ε , and the dependence of ε_{imp} and ε_{per} on the kinematic variables is not indicated. Insert ε as given by Equation (5) together with (23) and (24) and get:

$$E_t^{imp}(\bar{\theta}, \theta_{per}, x) = E_t^{per}(\theta_{per}, x) + \bar{\theta}^{\frac{1}{2}} (u_1(\theta_{per}) + \hat{\theta}_1 x) E_t^{per'}(\theta_{per}, x) + O(\bar{\theta}). \tag{27}$$

Notice that $E_t^{\text{per}}(\theta_{\text{per}}, x)$ and $E_t^{\text{per}'}(\theta_{\text{per}}, x)$ are known from the solution to the problem for the geometrically perfect structure alone.

2.2.2. The governing equations. Introduce E_t^{imp} given by Equation (27) and P_{imp} and u_{imp} given by Equation (23) in the equilibrium equations (25) and (26) for the imperfect column and obtain the equations of the asymptotic expansion in $\bar{\theta}$

$$\begin{aligned} \dot{P}_{\text{per}} + \dot{p}_1 \bar{\theta}^{\frac{1}{2}} &= \int_{d_{\text{per}}}^1 (E_t^{\text{per}} + \bar{\theta}^{\frac{1}{2}}(u_1 + \widehat{\theta}_1 x) E_t^{\text{per}'}) (\dot{u}_{\text{per}} + \dot{u}_1 \bar{\theta}^{\frac{1}{2}} + x) dx + \int_{-1}^{d_{\text{per}}} E (\dot{u}_{\text{per}} + \dot{u}_1 \bar{\theta}^{\frac{1}{2}} + x) dx \\ &+ \int_{d_{\text{per}} - \dot{u}_1 \bar{\theta}^{\frac{1}{2}}}^{d_{\text{per}}} (E_t^{\text{per}} + \bar{\theta}^{\frac{1}{2}}(u_1 + \widehat{\theta}_1 x) E_t^{\text{per}'}) (\dot{u}_{\text{per}} + \dot{u}_1 \bar{\theta}^{\frac{1}{2}} + x) dx \\ &+ \int_{d_{\text{per}}}^{d_{\text{per}} - \dot{u}_1 \bar{\theta}^{\frac{1}{2}}} E (\dot{u}_{\text{per}} + \dot{u}_1 \bar{\theta}^{\frac{1}{2}} + x) dx + O(\bar{\theta}) \end{aligned} \quad (28)$$

and

$$\begin{aligned} (\dot{P}_{\text{per}} + \dot{p}_1 \bar{\theta}^{\frac{1}{2}}) (\theta_{\text{per}} + \widehat{\theta}_1 \bar{\theta}^{\frac{1}{2}}) + P_{\text{per}} + p_1 \bar{\theta}^{\frac{1}{2}} + (i+1) k_i (\theta_{\text{per}}^i + i \theta_{\text{per}}^{i-1} \widehat{\theta}_1 \bar{\theta}^{\frac{1}{2}}) \\ = \int_{d_{\text{per}}}^1 (E_t^{\text{per}} + \bar{\theta}^{\frac{1}{2}}(u_1 + \widehat{\theta}_1 x) E_t^{\text{per}'}) (\dot{u}_{\text{per}} + \dot{u}_1 \bar{\theta}^{\frac{1}{2}} + x) x dx \\ + \int_{-1}^{d_{\text{per}}} E (\dot{u}_{\text{per}} + \dot{u}_1 \bar{\theta}^{\frac{1}{2}} + x) x dx \\ + \int_{d_{\text{per}} - \dot{u}_1 \bar{\theta}^{\frac{1}{2}}}^{d_{\text{per}}} (E_t^{\text{per}} + \bar{\theta}^{\frac{1}{2}}(u_1 + \widehat{\theta}_1 x) E_t^{\text{per}'}) (\dot{u}_{\text{per}} + \dot{u}_1 \bar{\theta}^{\frac{1}{2}} + x) x dx \\ + \int_{d_{\text{per}}}^{d_{\text{per}} - \dot{u}_1 \bar{\theta}^{\frac{1}{2}}} E (\dot{u}_{\text{per}} + \dot{u}_1 \bar{\theta}^{\frac{1}{2}} + x) x dx + O(\bar{\theta}). \end{aligned} \quad (29)$$

Eliminate the solution for the perfect structure, which is given by the terms of order zero in $\bar{\theta}$, and utilize that

$$\int_c^{c+\Delta} f(x) ((x-c) - \Delta) dx = -\frac{1}{2} f(c) \Delta^2 + O(\Delta^3),$$

which proves that the last two integrals of both Equation (28) and Equation (29) are of order $O(\bar{\theta})$. The asymptotic equilibrium equations (28) and (29) therefore simplify to

$$\begin{aligned} \bar{\theta}^{\frac{1}{2}} \dot{p}_1 &= \bar{\theta}^{\frac{1}{2}} (\dot{u}_1 f_1 + u_1 f_2 + \widehat{\theta}_1 f_3) + O(\bar{\theta}), \\ \bar{\theta}^{\frac{1}{2}} (\dot{p}_1 \theta_{\text{per}} + p_1) &= \bar{\theta}^{\frac{1}{2}} (\dot{u}_1 f_4 + u_1 f_3 + \widehat{\theta}_1 f_5) + O(\bar{\theta}), \end{aligned} \quad (30)$$

where the functions f_1, \dots, f_5 are associated with the solution for the geometrically perfect column and are:

$$\begin{aligned}
 f_1(\theta_{\text{per}}) &= E(1 - \dot{u}_{\text{per}}(\theta_{\text{per}})) + \int_{d_{\text{per}}}^1 E_t^{\text{per}}(\theta_{\text{per}}, x) dx, \\
 f_2(\theta_{\text{per}}) &= \int_{d_{\text{per}}}^1 E_t^{\text{per}'}(\theta_{\text{per}}, x)(\dot{u}_{\text{per}}(\theta_{\text{per}}) + x) dx, \\
 f_3(\theta_{\text{per}}) &= \int_{d_{\text{per}}}^1 E_t^{\text{per}'}(\theta_{\text{per}}, x)(\dot{u}_{\text{per}}(\theta_{\text{per}}) + x)x dx, \\
 f_4(\theta_{\text{per}}) &= \frac{1}{2}E(\dot{u}_{\text{per}}^2(\theta_{\text{per}}) - 1) + \int_{d_{\text{per}}}^1 E_t^{\text{per}}(\theta_{\text{per}}, x)x dx, \\
 f_5(\theta_{\text{per}}) &= \int_{d_{\text{per}}}^1 E_t^{\text{per}'}(\theta_{\text{per}}, x)(\dot{u}_{\text{per}}(\theta_{\text{per}}) + x)x^2 dx - \left(\dot{P}_{\text{per}} + (i + 1)ik_i\theta_{\text{per}}^{i-1}\right).
 \end{aligned}
 \tag{31}$$

In [Appendix C](#), expressions for f_i , [\(C.5\)](#), which do not contain integrals, are computed but f_i may also be computed directly by inserting the stress-strain relation and the solution for the geometrically perfect structure.

2.2.3. The first order imperfection sensitivity problem. To establish the lowest order problem for the imperfect column gather terms of order $\bar{\theta}^{\frac{1}{2}}$ in the perturbed problems [Equation \(30\)](#) to get

$$\dot{p}_1 = \dot{u}_1 f_1 + u_1 f_2 + \hat{\theta}_1 f_3, \quad \dot{p}_1 \theta_{\text{per}} + p_1 = \dot{u}_1 f_4 + u_1 f_3 + \hat{\theta}_1 f_5.
 \tag{32}$$

The asymptotic procedure has reduced the problem of the equilibrium of the imperfect structure to be linear in that [Equation \(32\)](#) consists of two linear first order differential equations, which are easily solved by a numerical method using the boundary conditions at $\theta_{\text{per}} = 0$. A solution to [Equation \(32\)](#) yields the exact asymptotic equilibrium of the geometrically imperfect structure for *all* values of θ_{per} , including the particularly interesting exact asymptotic maximum load of the imperfect structure.

2.3. Approximate determination of asymptotic functions. To simplify the solution for the first order imperfection sensitivity problem [Equation \(32\)](#), we exploit the fact that p_1 and u_1 vary slowly with θ after the onset of elastic unloading to construct an approximate solution required to provide accurate estimates of the exact asymptotic maximum load. It was shown by [van der Heijden \[1979\]](#) that although the second derivatives of u and P are infinite only at initiating elastic unloading for the perfect structure, they become extremely large for small imperfections. This implies rapid variation of the derivatives of u and P which makes them unfit for asymptotic expansion close to initiating elastic unloading.

It will be shown in [Section 2.4](#) that the exact asymptotic maximum load of the geometrically imperfect structure is found at $\theta_{\text{per}} = \theta_{\text{per}}^m$ where the maximum load of the perfect structure occurs. Here, superscript m indicates a quantity calculated at the maximum load. Expand p_1 and u_1 asymptotically around $\theta_{\text{per}} = \theta_{\text{per}}^m$ to determine the asymptotic behavior of the first order imperfection problem at maximum load of the imperfect structure.

Because the asymptotic equation [\(32\)](#) consists of two first order differential equations two boundary conditions are needed to fix our solution. The only directly accessible asymptotic boundary conditions for p_1 and u_1 are found at initiating elastic unloading where $p_1 = \hat{p}_1$ and $u_1 = \hat{u}_1$.

2.3.1. Asymptotic expansion of the first order imperfection problem around maximum load. Approximating polynomials for p_1 and u_1 around θ_{per}^m may be written as:

$$\begin{aligned} p_1 &= p_1^1 + p_1^2 \Delta\theta + \frac{1}{2} p_1^3 (\Delta\theta)^2 + \dots, \\ u_1 &= u_1^1 + u_1^2 \Delta\theta + \frac{1}{2} u_1^3 (\Delta\theta)^2 + \dots, \end{aligned} \tag{33}$$

where $\Delta\theta = \theta_{\text{per}} - \theta_{\text{per}}^m$, $\Delta\theta \in [-\theta_{\text{per}}^m; 0]$ and the total asymptotic solution for the imperfect structure is

$$\begin{aligned} P_{\text{imp}} &= P_{\text{per}} + \bar{\theta}^{\frac{1}{2}} \left(p_1^1 + p_1^2 \Delta\theta + \frac{1}{2} p_1^3 (\Delta\theta)^2 + \dots \right) + O(\bar{\theta}), \\ u_{\text{imp}} &= u_{\text{per}} + \bar{\theta}^{\frac{1}{2}} \left(u_1^1 + u_1^2 \Delta\theta + \frac{1}{2} u_1^3 (\Delta\theta)^2 + \dots \right) + O(\bar{\theta}). \end{aligned}$$

The lowest order imperfection problem is linear in both p_1 and u_1 and their derivatives. Hence, it follows that p_1^i and u_1^i may be given as linear functions of p_1^1 and u_1^1 when Equation (32) is expanded asymptotically around θ_{per}^m

$$f_i(\Delta\theta) = f_i^m + \Delta\theta \dot{f}_i^m + O(\Delta\theta^2). \tag{34}$$

The functions, f_i and \dot{f}_i , are given in Appendices C and D, respectively. The functions f_i^m and \dot{f}_i^m are then found by inserting θ_{per}^m in Equation (31). Assume that f_i^m and \dot{f}_i^m have been determined and insert Equations (33) and (34) in Equation (32) to get the asymptotic equations at the maximum load by gathering terms of the same order in $\Delta\theta$.

Zeroth order in $\Delta\theta$:

$$\begin{aligned} p_1^2 &= u_1^2 f_1^m + u_1^1 f_2^m + \hat{\theta}_1 f_3^m, \\ p_1^3 \theta_{\text{per}}^m + p_1^1 &= u_1^2 f_4^m + u_1^1 f_3^m + \hat{\theta}_1 f_5^m. \end{aligned} \tag{35}$$

First order in $\Delta\theta$:

$$\begin{aligned} p_1^3 &= u_1^3 f_1^m + u_1^2 (f_2^m + \dot{f}_1^m) + u_1^1 \dot{f}_2^m + \hat{\theta}_1 \dot{f}_3^m, \\ p_1^3 \theta_{\text{per}}^m + 2p_1^2 &= u_1^3 f_4^m + u_1^2 (f_3^m + \dot{f}_4^m) + u_1^1 \dot{f}_3^m + \hat{\theta}_1 \dot{f}_5^m. \end{aligned} \tag{36}$$

This procedure may be extended to any order in $\Delta\theta$, but our experience shows that it is not necessary to go beyond the order used here, see below. Because the first order imperfection sensitivity problem Equation (32) is linear in p_1 and u_1 , the above asymptotic equations of any order, Equations (35), (36), etc., are linear in the asymptotic coefficients p_1^i and u_1^i . As mentioned earlier the problem always entails two unknowns more than the number of equations because the first order imperfection sensitivity problem consists of two first order differential equations. To obtain the two additional equations required to determine p_1^i and u_1^i , assume that the asymptotic expansions of p_1 and u_1 around maximum furnish accurate results at initiating elastic unloading. This provides two boundary conditions at $\Delta\theta = -\theta_{\text{per}}^m$,

that is, $\theta_{\text{per}} = 0$:

$$\begin{aligned} \widehat{p}_1 &= p_1^1 + p_1^2(-\theta_{\text{per}}^m) + \dots + \frac{1}{n} p_1^{n+1}(-\theta_{\text{per}}^m)^n, \\ \widehat{u}_1 &= u_1^1 + u_1^2(-\theta_{\text{per}}^m) + \dots + \frac{1}{n} u_1^{n+1}(-\theta_{\text{per}}^m)^n. \end{aligned}$$

The asymptotic equations of order 0 to n , Equations (35), (36), etc., plus the general boundary conditions given above constitute $2(n + 1)$ linear equations with $2(n + 1)$ unknown asymptotic coefficients to determine the approximate asymptotic polynomials of degree n .

In practice it turns out that linear approximations yield good results, while parabolic approximations provide excellent accuracy for the maximum load because of the slow variation of p_1 and u_1 . Thus, the problem of investigating imperfection sensitivity is reduced to solving 4 (linear approximation) or 6 (parabolic approximation) linear equations with 4 or 6 unknowns, respectively.

2.4. The maximum load. Only if the solution $p_1(\Delta\theta)$ is found exactly are we able to determine the maximum load asymptotically correct. On the other hand, if we have a good approximation of $p_1(\Delta\theta)$ near the maximum load of the perfect column, a good estimate of the asymptotic maximum load may be obtained. Close to the maximum load of the perfect structure, P_{per} may asymptotically be given as

$$P_{\text{per}}(\Delta\theta) = P_{\text{per}}^m + \frac{1}{2} \Delta\theta^2 \ddot{P}_{\text{per}}^m + O(\Delta\theta^3),$$

because the first derivative \dot{P}_{per}^m of the load equilibrium for the perfect structure vanishes.

Expand P_{imp} in Equation (23) as

$$P_{\text{imp}}(\Delta\theta) \approx P_{\text{per}}^m + \frac{1}{2} \Delta\theta^2 \ddot{P}_{\text{per}}^m + \bar{\theta}^{\frac{1}{2}} (p_1^1 + p_1^2 \Delta\theta + \frac{1}{2} p_1^3 \Delta\theta^2) + O(\bar{\theta}, \Delta\theta^3). \tag{37}$$

When the first order imperfection sensitivity problem Equation (32) is solved approximately by (33) p_1^i in (37) coincides with p_1^i in (33). In order for P_{imp} to attain a maximum (or minimum)

$$\Delta\theta_{\text{imp}}^m = - \frac{p_1^2 \bar{\theta}^{\frac{1}{2}}}{\ddot{P}_{\text{per}}^m} + O(\bar{\theta}),$$

which after insertion in Equation (37) furnishes the following approximate expression for the maximum load of the imperfect column

$$P_{\text{imp}}^m = P_{\text{per}}^m + p_1^1 \bar{\theta}^{\frac{1}{2}} + O(\bar{\theta}).$$

Note that, like in the elastic case, the maximum load-carrying capacity of the elastic-plastic imperfect structure compared to that of the perfect structure is controlled by only one parameter, namely p_1^1 , the lowest order term in the approximation to p_1 .

2.5. Asymptotic results and comparison. In Figures 12 and 13 the applicability of the approximate asymptotic method developed above is demonstrated by comparison with numerical results for two column geometries and two constitutive relations which entailed the least accurate asymptotic predictions in the studies by Hutchinson [1974] and by van der Heijden [1979] for the structures of Figures 13 and 12, respectively. The results of these studies were obtained by use of a Ramberg-Osgood type constitutive

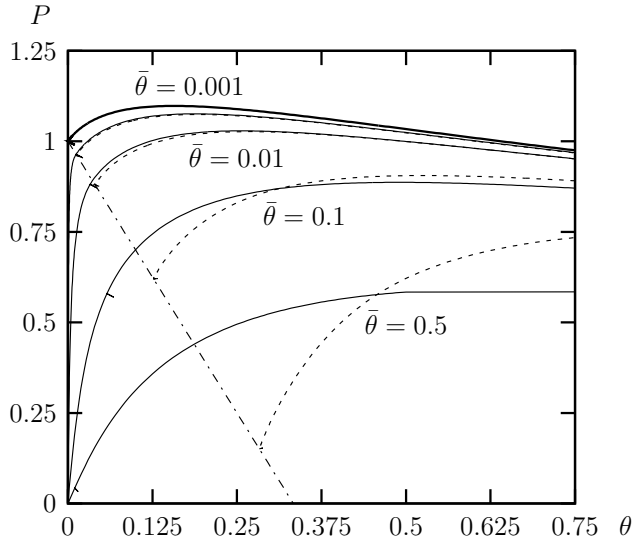


Figure 12. Comparison between numerical results and the approximate asymptotic method for $(n, \psi, s_c/s_y) = (3, 0.2, 1.4)$, $\rho = 3.0$. No kinematic nonlinearities, that is, $k_i = 0$. The dash-dot straight line indicates lowest order asymptotic prediction of initiation of linear elastic unloading. Here, the thick solid line represents perfect numerical, the thin solid line, imperfect numerical and the dashed line, asymptotic.

relation Equation (18). As shown in Section 1 the constitutive model Equation (17), which is better suited for our derivations, may predict a constitutive behavior very close to that of Equation (18) for the postbifurcation regime of the geometrically perfect column provided that the value of ρ is chosen appropriately. Both plots support the idea that our approximate asymptotic expansion for the imperfect column developed above does indeed approximate the exact solution very well in that our asymptotic curve almost coincides with both the shape and the values of the numerical curve for small imperfection amplitudes, that is, $\bar{\theta} \lesssim 0.001$.

In Figure 12 the maximum load-carrying capacity of the imperfect structure is approximated well even at the large imperfection $\bar{\theta} = 0.1$. However, for larger imperfection amplitudes our asymptotic expansion fails to predict the point of initial unloading accurately. For cases where the maximum load is located very close to initial unloading the maximum load is therefore not as well approximated for larger imperfections as it was in Figure 12. This is demonstrated by Figure 13 where for imperfections above approximately $\bar{\theta} = 0.1$ the numerical maximum load is obtained before the asymptotic method predicts initial unloading. Thus, for large imperfection amplitudes and maximum load close to initial unloading, our asymptotic method fails to predict the maximum load accurately because the point of initial unloading is poorly predicted by the nonlinear elastic asymptotic imperfection theory of the comparison model, as it was also pointed out by van der Heijden [1979].

In general, our asymptotic expansion to the lowest order of the equilibrium for the elastic-plastic imperfect column provides better estimates of maximum loads than its elastic counterpart. This is due to the fact that, in contrast to an elastic structure, a geometrically perfect plastic structure obtains its

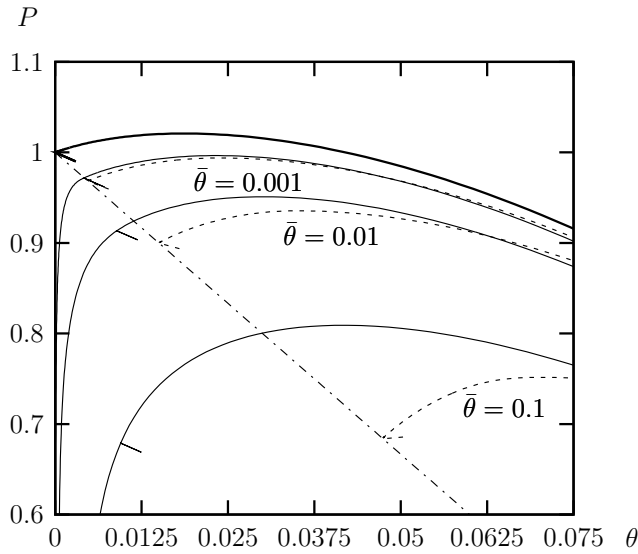


Figure 13. Comparison between numerical results and the approximate asymptotic method for $(n, \psi, s_c/s_y) = (10, 0.2, 1.2)$, $\rho = 25$. Kinematic nonlinearity given by $k_1/E = 1$. The dash-dot straight line indicates lowest order asymptotic prediction of initiation of linear elastic unloading. Here, the thick solid line represents Perfect numerical, the thin solid line, Imperfect numerical and the dashed line, Asymptotic.

maximum load at some finite distance from its lowest bifurcation load, where the asymptotic method provides better load estimates for an imperfect structure since it is further from the singular point of bifurcation. However, in order to obtain more accurate maximum load predictions for large imperfection amplitudes we need a better approximation by the nonlinear elastic asymptotic method of the point of initial unloading.

2.6. Enhancement of the asymptotic solution. Christensen and Byskov [2007a] establish a new expression, which is valid for the kinematically nonlinear equilibrium of an *elastic*, geometrically imperfect structure. It matches the traditional asymptotic expansion for an imperfect structure for buckling amplitudes $\theta \neq 0$, and for all imperfection amplitudes $\bar{\theta}$ it fulfills the boundary condition that $\theta = 0$ when the load $P = 0$. Christensen and Byskov [2007b] provide an example of the accuracy of this expression for the Euler column.

By comparison with numerical results it may be shown that, for relatively small θ , the kinematically nonlinear *elastic* equilibrium of an imperfect realization of the column shown in Figure 12 may be approximated in the following way

$$P = 1 - \frac{\rho\bar{\theta}}{\theta + \rho\bar{\theta}}, \quad \frac{\partial P}{\partial \theta} = \frac{\rho\bar{\theta}}{(\theta + \rho\bar{\theta})^2}, \tag{38}$$

where the value of ρ depends on the parameters constitutive relation.

Because of extremely large derivatives of the elastic-plastic stress-strain relation relatively close to the critical stress, the preunloading path of the elastic-plastic imperfect column of Figure 13 is only approximated well when a higher order asymptotic expression for imperfection sensitivity is employed. Such an expansion has been developed by Christensen and Byskov [2007a].

To construct a simple enhancement of the solution for the imperfect structure, adopt the assumption that the nonlinear *elastic* path of the imperfect structure given by Equation (38) also describes the entire path of the *elastic-plastic* imperfect column well up till the asymptotic straight line emanating from the bifurcation point and separating the unloading and the nonunloading zone; see Figure 12. Let the enhanced asymptotic solution, which is in no way asymptotically more exact than the original one, be given as a higher order term of $\bar{\theta}$ added to the original solution

$$P_{\text{imp}}^e = P_{\text{per}} + p_1(\theta_{\text{per}})\bar{\theta}^{\frac{1}{2}} + \Delta p(\bar{\theta}), \quad \theta_{\text{imp}}^e = \theta_{\text{per}} + \hat{\theta}_1\bar{\theta}^{\frac{1}{2}} + \Delta\theta(\bar{\theta}),$$

where superscript e indicates the enhanced asymptotic solution, and $\Delta p(\bar{\theta})$ and $\Delta\theta(\bar{\theta})$ are additions to the original asymptotic expansion which do not depend on θ_{per} and are both functions of order θ , leaving this expression asymptotically equivalent to the original asymptotic expansion. Note that

$$(\Delta p(\bar{\theta}), \Delta\theta(\bar{\theta})) \sim O(\bar{\theta}).$$

To fully fix Δp and $\Delta\theta$, use the boundary conditions such that

- (i) the asymptotic solution passes through the point of initiating unloading as determined by the crossing between the straight boundary and the enhanced preunloading expression (38);
- (ii) at the asymptotic straight boundary between no unloading and unloading, the derivative of the load P is continuous with respect to θ , as shown by van der Heijden [1979].

In Figure 14 the added precision of the enhanced approximate asymptotic method is demonstrated for the column of Figure 12, for which the previous asymptotic methods failed to provide reliable results for moderate and large imperfection levels. The asymptotic solution enhanced by better approximation of preunloading and the use of slope boundary conditions at initial asymptotic unloading for the column in question provides very close approximations to the numerical results both at maximum load and at initial unloading even at the large imperfection of $\bar{\theta} = 0.5$, which corresponds to an angle of 27° .³ Also, comparison with the original asymptotic expansion shows that the equilibrium prediction has been enhanced considerably, especially for the larger values of $\bar{\theta}$.

Conclusion. An asymptotic expression for the equilibrium of the imperfect realization of the Shanley–Hutchinson continuous model column is derived in the main body of this paper. The method hinges on the fact that for decreasing imperfections the equilibrium path of the imperfect structure approaches that of the perfect one, and that the expression for the path of the geometrically imperfect structure may be written as the postbuckling path of the perfect structure plus a small contribution which is expanded asymptotically to the lowest degree in the imperfection amplitude. The asymptotic coefficient associated with the lowest order imperfection amplitude is given by a linear, second order differential equation, which may be solved numerically. A simple polynomial approximation of the asymptotic coefficient function is derived based on its slow variation.

³For a model structure, such as the present one, the concept of large or small rotations is somewhat uncertain.

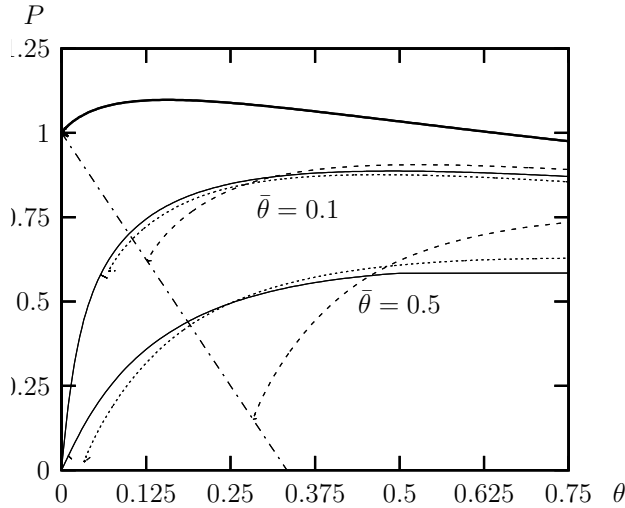


Figure 14. Comparison between numerical results, the approximate asymptotic method, and the enhanced approximate method applied to the column of Figure 12. The dash-dot straight line indicates lowest order asymptotic prediction of initiation of linear elastic unloading. The thick solid line represents the perfect, numerical, the thin solid line, imperfect, numerical, the dotted line, enhanced asymptotic and the dashed line, asymptotic results.

For a numerically determined postbuckling path, the approximate asymptotic equilibrium is determined for the column which in the study by van der Heijden [1979] proved to yield the most inaccurate estimates with his method. By our method, the approximation of the maximum load of the imperfect model column is excellent for small imperfections, and an asymptotic expansion which utilizes an enhanced approximation of initial unloading, provides very precise estimates of the entire equilibrium of the imperfect structure, even for large imperfections.

Appendix A: a study of Hutchinson’s asymptotic method

Hutchinson [1973b; 1974] showed that $P_{\text{per}}(\theta)$ and $u_{\text{per}}(\theta)$ can be developed asymptotically in the spirit of Koiter’s elastic theory [Koiter 1945] when extra terms containing fractional powers of θ are added. Hutchinson determined the form of the perturbation expansion for the Shanley–Hutchinson column to be

$$P = 1 + \Delta P = 1 + a_1\theta + a_2\theta^{\frac{3}{2}} + a_3\theta^2 + a_4\theta^{\frac{5}{2}} + a_5\theta^3 + a_6\theta^{\frac{7}{2}} + O(\theta^4), \tag{A.1}$$

$$u = u_c + \Delta u = u_c + b_1\theta + b_2\theta^{\frac{3}{2}} + b_3\theta^2 + b_4\theta^{\frac{5}{2}} + b_5\theta^3 + b_6\theta^{\frac{7}{2}} + O(\theta^4), \tag{A.2}$$

and calculated the first three constants of each expression. Here we determine two additional constants for both P and u . Knowing that elastic unloading starts at bifurcation we get

$$-d(\theta = 0) = \frac{\partial u}{\partial \theta}(\theta = 0) \Rightarrow b_1 = 1. \tag{A.3}$$

Expansion of the tangent modulus. In order to be able to carry out the integrations in Equation (9) and Equation (10) we expand E_t in Taylor series around $x = 0$. Use of ε given by Equation (5) provides $E_t = E_t(u) + (\theta x)E_t'(u) + \frac{1}{2}(\theta x)^2 E_t''(u) + \dots$ where

$$(\)' \equiv \frac{\partial(\)}{\partial \varepsilon}.$$

Compute the integrals of the equilibrium equations (9) and (10) to transform them into ordinary differential equations:

$$\begin{aligned} \frac{\partial P}{\partial \theta} = & \left(-\frac{1}{2} \left(\frac{\partial u}{\partial \theta} \right)^2 + \frac{\partial u}{\partial \theta} - \frac{1}{2} \right) E + \left(+\frac{1}{2} \left(\frac{\partial u}{\partial \theta} \right)^2 + \frac{\partial u}{\partial \theta} + \frac{1}{2} \right) E_t(u) + \left(-\frac{1}{6} \left(\frac{\partial u}{\partial \theta} \right)^3 + \frac{1}{2} \frac{\partial u}{\partial \theta} + \frac{1}{3} \right) \theta E_t'(u) \\ & + \left(+\frac{1}{12} \left(\frac{\partial u}{\partial \theta} \right)^4 + \frac{1}{3} \frac{\partial u}{\partial \theta} + \frac{1}{4} \right) \frac{\theta^2}{2} E_t''(u) + O(\theta^3), \end{aligned}$$

and

$$\begin{aligned} \frac{\partial P}{\partial \theta} \theta + P + \frac{\partial K}{\partial \theta} = & \left(+\frac{1}{6} \left(\frac{\partial u}{\partial \theta} \right)^3 - \frac{1}{2} \frac{\partial u}{\partial \theta} + \frac{1}{3} \right) E + \left(-\frac{1}{6} \left(\frac{\partial u}{\partial \theta} \right)^3 + \frac{1}{2} \frac{\partial u}{\partial \theta} + \frac{1}{3} \right) E_t(u) \\ & + \left(+\frac{1}{12} \left(\frac{\partial u}{\partial \theta} \right)^4 + \frac{1}{3} \frac{\partial u}{\partial \theta} + \frac{1}{4} \right) \theta E_t'(u) \\ & + \left(-\frac{1}{20} \left(\frac{\partial u}{\partial \theta} \right)^5 + \frac{1}{4} \frac{\partial u}{\partial \theta} + \frac{1}{5} \right) \frac{\theta^2}{2} E_t''(u) + O(\theta^3), \end{aligned}$$

where

$$E_t^{(i)}(u) = E_t^{c(i)} + \Delta u E_t^{c(i+1)} + \frac{\Delta u^2}{2} E_t^{c(i+2)} + O(\theta^3),$$

with (i) , $(i + 1)$ and $(i + 2)$ indicate the order of differentiation.

A.0.1. The governing equations. Employ the perturbation series for P and u given by Equations (A.1) and (A.2), respectively, and exploit the fact that $b_1 = 1$ (see Equation (A.3)) in order to establish the asymptotic equations:

$$\begin{aligned} 0 = & -a_1 - \frac{3}{2} a_2 \theta^{\frac{1}{2}} - 2a_3 \theta^1 - \frac{5}{2} a_4 \theta^{\frac{3}{2}} - 3a_5 \theta^2 + E \left(-\frac{9}{8} b_2^2 \theta^1 - 3b_2 b_3 \theta^{\frac{3}{2}} - \left(\frac{15}{4} b_2 b_4 + 2b_3^2 \right) \theta^2 \right) \\ & + E_t^c \left(2 + 3b_2 \theta^{\frac{1}{2}} + \left(\frac{9}{8} b_2^2 + 4b_3 \right) \theta^1 + (3b_2 b_3 + 5b_4) \theta^{\frac{3}{2}} + \left(\frac{15}{4} b_2 b_4 + 2b_3^2 + 6b_5 \right) \theta^2 \right) \\ & + \left(\theta E_t^{c'} + \theta^{\frac{3}{2}} b_2 E_t^{c'} + \theta^2 (b_3 E_t^{c'} + \frac{1}{2} E_t^{c''}) \right) \left(2 + 3b_2 \theta^{\frac{1}{2}} + \left(\frac{9}{8} b_2^2 + 4b_3 \right) \theta^1 \right) \\ & + \left(\theta E_t^{c'} + \theta^2 E_t^{c''} \right) \left(\frac{2}{3} - \frac{3}{8} b_2^2 \theta^1 \right) + \theta^2 \frac{1}{3} E_t^{c''} + O(\theta^{\frac{5}{2}}), \quad (\text{A.4}) \end{aligned}$$

and

$$\begin{aligned}
 0 = & +1 - 1 - 2a_1\theta - \frac{5}{2}a_2\theta^{\frac{3}{2}} - 3a_3\theta^2 - \frac{7}{2}a_4\theta^{\frac{5}{2}} - 2k_1\theta - 3k_2\theta^2 \\
 & + (E - E_t^c) \left(\frac{9}{8}b_2^2\theta^1 + (3b_2b_3 + \frac{9}{16}b_2^3)\theta^{\frac{3}{2}} + (\frac{15}{4}b_2b_4 + \frac{9}{4}b_2^2b_3 + 2b_3^2)\theta^2 \right. \\
 & \quad \left. + (\frac{9}{2}b_2b_5 + 5b_3b_4 + \frac{45}{16}b_2^2b_4 + 3b_2b_3^2)\theta^{\frac{5}{2}} \right) \\
 & + (\theta E_t^{c'} + \theta^{\frac{3}{2}}b_2E_t^{c'} + \theta^2(b_3E_t^{c'} + \frac{1}{2}E_t^{c''}) + \theta^{\frac{5}{2}}(b_4E_t^{c'} + b_2E_t^{c''})) \\
 & \quad \left(\frac{2}{3} - \frac{9}{8}b_2^2\theta^1 - (3b_2b_3 + \frac{9}{16}b_2^3)\theta^{\frac{3}{2}} \right) \\
 & + (\theta E_t^{c'} + \theta^2E_t^{c''} + \theta^{\frac{5}{2}}b_2E_t^{c''}) \left(\frac{2}{3} + b_2\theta^{\frac{1}{2}} + (\frac{4}{3}b_3 + \frac{9}{8}b_2^2)\theta^1 + (\frac{5}{3}b_4 + \frac{9}{8}b_2^3 + 3b_2b_3)\theta^{\frac{3}{2}} \right) \\
 & \quad + \theta^2 \frac{1}{5}E_t^{c''} + O(\theta^3). \tag{A.5}
 \end{aligned}$$

Gather terms containing θ of the same order in Equations (A.4) and (A.5) and introduce the assumption that Equations (A.1) and (A.2) fulfill the equilibrium equations in a small area around $\theta = 0$. The polynomial identification theorem then gives us two sets of equations to determine the constants a_i and b_i . The first 5 terms in Equations (A.4) and (A.5) furnish

$$\begin{aligned}
 \theta^0: & \quad a_1 = 3, \\
 \theta^{\frac{1}{2}}: & \quad a_2 = 3b_2, \\
 \theta^1: & \quad a_3 = \frac{1}{E - E_t^c} \left(2 - k_1 - E_t^{c'} \right) - 3 - k_1 + 2E_t^{c'}, \\
 \theta^{\frac{3}{2}}: & \quad a_4 = 3b_4 - \frac{6}{5}(E - E_t^c)b_2b_3 + 2E_t^{c'}b_2, \\
 \theta^2: & \quad a_5 = 3b_5 - (E - E_t^c) \left(\frac{5}{4}b_2b_4 + \frac{2}{3}b_3^2 \right) + E_t^{c'}(2b_3 + b_2^2) + \frac{2}{3}E_t^{c''},
 \end{aligned} \tag{A.6}$$

and

$$\begin{aligned}
 \theta^0: & \quad 0 = 0, \\
 \theta^{\frac{1}{2}}: & \quad 0 = 0, \\
 \theta^1: & \quad b_2^2 = \frac{16}{9(E - E_t^c)} \left(3 + k_1 - \frac{2}{3}E_t^{c'} \right), \\
 \theta^{\frac{3}{2}}: & \quad b_3 = \frac{1}{3(E - E_t^c)} \left(2 - k_1 - E_t^{c'} \right), \\
 \theta^2: & \quad b_4 = \frac{4(a_3 + k_2)}{5(E - E_t^c)b_2} - \frac{8b_3^2}{15b_2} - \frac{3}{5}b_2b_3 - \frac{8E_t^{c'}b_3}{15(E - E_t^c)b_2} - \frac{8E_t^{c''}}{25(E - E_t^c)b_2}, \\
 \theta^{\frac{5}{2}}: & \quad b_5 = \frac{7a_4}{9(E - E_t^c)b_2} - \frac{10b_3b_4}{9b_2} - \frac{5}{8}b_2b_4 - \frac{2}{3}b_3^2 - \frac{E_t^{c'}(-\frac{1}{8}b_2^3 + \frac{14}{27}b_4)}{(E - E_t^c)b_2} - \frac{14E_t^{c''}}{27(E - E_t^c)}.
 \end{aligned} \tag{A.7}$$

These equations give us a_1 explicitly. The remaining constants a_i and b_i are found by alternately inserting the known quantities into Equations (A.6) and (A.7).

Appendix B: asymptotic expansion of ΔP^∞

In order to determine the coefficients for the new hyperbolic solution [Equation \(16\)](#), the ordinary polynomial expansion of ΔP^∞ is needed. Subtracting the asymptotic polynomial of P^∞ from that of the enhanced Hutchinson solution [Equation \(A.1\)](#) provides the desired polynomial.

The regular expansion of P^∞ (see [Equation \(20\)](#)) may be found as

$$P^\infty = 1 + 3\theta - (k_1 + 3\rho + 3)\theta^2 + \left(\frac{16}{5}\rho^2 + 3\rho + k_1 - k_2 + 3\right)\theta^3 + O(t^4).$$

Recall [Equation \(3\)](#) and realize that from [Equation \(17\)](#) we may find $\rho = -\frac{E_t^{c'}}{E_t^c}$, $\rho^2 = \frac{E_t^{c''}}{2E_t^c}$, then

$$P^\infty = 1 + 3\theta - (3 + k_1 - 2E_t^{c'})\theta^2 + \left(3 + k_1 - k_2 - 2E_t^{c'} + \frac{16}{15}E_t^{c''}\right)\theta^3 + O(t^4). \quad (\text{B.1})$$

Introduce an asymptotic expansion of ΔP^∞ :

$$\Delta P^\infty = a_1^\Delta \theta + a_2^\Delta \theta^{\frac{3}{2}} + a_3^\Delta \theta^2 + a_4^\Delta \theta^{\frac{5}{2}} + a_5^\Delta \theta^3 + O(\theta^{\frac{7}{2}}). \quad (\text{B.2})$$

Recall the definition of ΔP^∞ ([Equation \(15\)](#)), the expansion for the total load P (see [Equation \(A.1\)](#)), utilize the results for a_j obtained in [Equation \(A.6\)](#), and compare the two ensuing expansions for ΔP^∞ to get the following expansions for a_j^Δ :

$$\begin{aligned} a_1^\Delta &= 0, & a_2^\Delta &= a_2, \\ a_3^\Delta &= a_3 + 3 + k_1 - 2E_t^{c'}, & a_4^\Delta &= a_4, \\ a_5^\Delta &= a_5 - 3 - k_1 + k_2 + 2E_t^{c'} - \frac{16}{15}E_t^{c''}. \end{aligned} \quad (\text{B.3})$$

Appendix C: determination of f_i

We exploit the fact that the integrals of f_1 and f_2 can be computed directly when the solution for the geometrically perfect column is established

$$\begin{aligned} \int_{d_{\text{per}}}^1 E_t^{\text{per}} dx &= \frac{1}{\theta_{\text{per}}} \int_{x=d_{\text{per}}}^{x=1} E_t^{\text{per}} d\varepsilon_{\text{per}} = \frac{s_{\text{per}}|_{x=1} - s_{\text{per}}|_{x=d}}{\theta_{\text{per}}}, \\ \int_{d_{\text{per}}}^1 E_t^{\text{per}'} (\dot{u}_{\text{per}} + x) dx &= \frac{1}{\theta_{\text{per}}} \left([E_t^{\text{per}'} (\dot{u}_{\text{per}} + x)]_{d_{\text{per}}}^1 - \int_{d_{\text{per}}}^1 E_t^{\text{per}} dx \right) \\ &= \frac{E_t^{\text{per}'}|_{x=1} (\dot{u}_{\text{per}} + 1)}{\theta_{\text{per}}} - \frac{s_{\text{per}}|_{x=1} - s_{\text{per}}|_{x=d}}{\theta_{\text{per}}^2}, \end{aligned} \quad (\text{C.1})$$

which by insertion in [Equation \(31\)](#) gives us f_1 and f_2 . The remaining functions are given as functions of f_1 and f_2 when we use the perfect equilibrium and its derivatives with respect to θ_{per}

$$P_{\text{per}} = \int_{-1}^{d_{\text{per}}} E (\dot{u}_{\text{per}} + x) dx + \int_{d_{\text{per}}}^1 E_t^{\text{per}'} (\dot{u}_{\text{per}} + x) dx = \dot{u}_{\text{per}} f_1 + f_4 \quad (\text{C.2})$$

and

$$\ddot{P}_{\text{per}} = \int_{-1}^{d_{\text{per}}} E \ddot{u}_{\text{per}} dx + \int_{d_{\text{per}}}^1 (E_t^{\text{per}} \ddot{u}_{\text{per}} + E_t^{\text{per}'} (\dot{u}_{\text{per}} + x)^2) dx = \ddot{u}_{\text{per}} f_1 + \dot{u}_{\text{per}} f_2 + f_3 \quad (\text{C.3})$$

and

$$\begin{aligned} \ddot{P}_{\text{per}} \theta_{\text{per}} + 2 \dot{P}_{\text{per}} + (i+1) i k_i \theta_{\text{per}}^{i-1} &= \int_{-1}^{d_{\text{per}}} E \ddot{u}_{\text{per}} x dx + \int_{d_{\text{per}}}^1 (E_t^{\text{per}} \ddot{u}_{\text{per}} + E_t^{\text{per}'} (\dot{u}_{\text{per}} + x)^2) x dx \\ &= \ddot{u}_{\text{per}} f_4 + \dot{u}_{\text{per}} f_3 + f_5 + \dot{P}_{\text{per}} + (i+1) i k_i \theta_{\text{per}}^{i-1}. \end{aligned} \quad (\text{C.4})$$

The expressions for f_i can now be determined directly as functions of θ_{per} alone given by the solution for the geometrically perfect column problem. From Equations (C.1)–(C.4) and Equation (31), we get:

$$\begin{aligned} f_1 &= E(L - \dot{u}_{\text{per}}) + \frac{s_{\text{per}}|_{x=1} - s_{\text{per}}|_{x=d}}{\theta_{\text{per}}}, & f_2 &= \frac{E_t^{\text{per}}|_{x=1} (\dot{u}_{\text{per}} + 1)}{\theta_{\text{per}}} - \frac{s_{\text{per}}|_{x=1} - s_{\text{per}}|_{x=d}}{\theta_{\text{per}}^2}, \\ f_3 &= \ddot{P}_{\text{per}} - \ddot{u}_{\text{per}} f_1 - \dot{u}_{\text{per}} f_2, & f_4 &= \dot{P}_{\text{per}} - \dot{u}_{\text{per}} f_1, \\ f_5 &= \ddot{P}_{\text{per}} \theta_{\text{per}} + \dot{P}_{\text{per}} - \ddot{u}_{\text{per}} f_4 - \dot{u}_{\text{per}} f_3. \end{aligned} \quad (\text{C.5})$$

Appendix D: determination of \dot{f}_i

While f_3, f_4 and f_5 are straight forward to differentiate given Equation (C.5), the derivatives of f_i with respect to θ_{per} , that is, \dot{f}_1 and \dot{f}_2 are slightly more difficult to calculate:

$$\dot{f}_1 = -\ddot{u}_{\text{per}} (E - E_t^{\text{per}}|_{x=d}) + \int_{d_{\text{per}}}^1 E_t^{\text{per}'} (\dot{u}_{\text{per}} + x) dx = -\ddot{u}_{\text{per}} (E - E_t^{\text{per}}|_{x=d}) + f_2,$$

and

$$\begin{aligned} \dot{f}_2 &= \int_{d_{\text{per}}}^1 (E_t^{\text{per}'} (\dot{u}_{\text{per}} + x)^2 + \ddot{u}_{\text{per}} E_t^{\text{per}'}) dx \\ &= \frac{1}{\theta_{\text{per}}} \left(\left[E_t^{\text{per}'} (\dot{u}_{\text{per}} + x)^2 \right]_{d_{\text{per}}}^1 - \ddot{u}_{\text{per}} \left(\int_{d_{\text{per}}}^1 E_t^{\text{per}'} 2(\dot{u}_{\text{per}} + x) dx + E_t^{\text{per}}|_{x=d} - E_t^{\text{per}}|_{x=1} \right) \right) \\ &= \frac{1}{\theta_{\text{per}}} \left(\ddot{u}_{\text{per}} (E_t^{\text{per}}|_{x=1} - E_t^{\text{per}}|_{x=d} - 2f_2) + E_t^{\text{per}'}|_{x=1} (\dot{u}_{\text{per}} + 1)^2 \right). \end{aligned}$$

Finally, differentiation provides the remaining \dot{f}_i

$$\begin{aligned} \dot{f}_3 &= \ddot{P}_{\text{per}} - \ddot{u}_{\text{per}} f_1 - \ddot{u}_{\text{per}} (\dot{f}_1 + f_2) - \dot{u}_{\text{per}} \dot{f}_2, \\ \dot{f}_4 &= \dot{P}_{\text{per}} - \dot{u}_{\text{per}} f_1 - \dot{u}_{\text{per}} \dot{f}_1, \\ \dot{f}_5 &= \ddot{P}_{\text{per}} \theta_{\text{per}} + 2 \dot{P}_{\text{per}} - \ddot{u}_{\text{per}} f_4 - \ddot{u}_{\text{per}} (\dot{f}_4 + f_3) - \dot{u}_{\text{per}} \dot{f}_3. \end{aligned}$$

References

- [Byskov 1982–83] E. Byskov, “Plastic symmetry of Roorda’s frame”, *J. Struct. Mech.* **10**:3 (1982–83), 311–328.
- [Christensen and Byskov 2007a] C. D. Christensen and E. Byskov, “Nonlinear elastic and kinematic asymptotic postbuckling and imperfection sensitivity”, 2007. To be submitted.
- [Christensen and Byskov 2007b] C. D. Christensen and E. Byskov, “Plastic stability and imperfection sensitivity of the Euler column”, 2007. To be submitted.
- [Duberg and Wilder 1952] J. E. Duberg and T. W. Wilder, “Inelastic column behavior”, NACA Report NACA-TR-1072, 1952, Available at <http://hdl.handle.net/2060/19930092117>.
- [Engesser 1889] F. Engesser, “Die knickfestigkeit gerader Stäbe”, *Z. Arch. Ing. Vereins Hannover* **17** (1889), 35–455.
- [van der Heijden 1979] A. van der Heijden, “A study of Hutchinson’s plastic buckling model”, *J. Mech. Phys. Solids* **27**:5–6 (1979), 441–464.
- [Hill 1957] R. Hill, “Stability of rigid-plastic solids”, *J. Mech. Phys. Solids* **6**:1 (1957), 1–8.
- [Hutchinson 1972] J. W. Hutchinson, “On the postbuckling behavior of imperfection-sensitive structures in the plastic range”, *J. Appl. Mech. (Trans. ASME)* **39** (1972), 155–162.
- [Hutchinson 1973a] J. W. Hutchinson, “Imperfection-sensitivity in the plastic range”, *J. Mech. Phys. Solids* **21**:3 (1973), 191–204.
- [Hutchinson 1973b] J. W. Hutchinson, “Post-bifurcation behavior in the plastic range”, *J. Mech. Phys. Solids* **21**:3 (1973), 163–190.
- [Hutchinson 1974] J. W. Hutchinson, “Plastic buckling”, *Advances in Applied Mechanics* **14** (1974), 67–144.
- [Hutchinson and Budiansky 1976] J. W. Hutchinson and B. Budiansky, “Analytical and numerical study of the effects of initial imperfections on the inelastic buckling of a cruciform column”, pp. 98–105 in *Buckling of structures: symposium* (Cambridge, MA), edited by B. Budiansky, Springer-Verlag, Berlin, 1976.
- [Koiter 1945] W. T. Koiter, *The stability of elastic equilibrium (Dissertation, Delft University)*, H.J. Paris, Amsterdam, 1945. (in Dutch); also NASA TT-F10,833, (1967); also Air Force Flight Dynamics Laboratory, AFFDL-TR-70-25, (1970).
- [Koiter 1966] W. Koiter, “Post-buckling analysis of a simple two-bar frame”, in *Recent progress in applied mechanics: the Folke Odqvist volume*, edited by B. Broberg et al., Almqvist and Wiksell, Stockholm, 1966.
- [Ming and Wenda 1990] S. X. Ming and L. Wenda, “Postbuckling and imperfection sensitivity analysis of structures in the plastic range, I: model analysis”, *Thin Wall. Struct.* **10**:4 (1990), 263–275.
- [Needleman and Tvergaard 1976] A. Needleman and V. Tvergaard, “An analysis of the imperfection sensitivity of square elastic-plastic plates under axial compression”, *Int. J. Solids Struct.* **12**:3 (1976), 185–201.
- [Roorda 1965] J. Roorda, “Stability of structures with small imperfections”, *J. Eng. Mech. Div ASCE* **91** (1965), 87–95.
- [Scherzinger and Triantafyllidis 1998] W. Scherzinger and N. Triantafyllidis, “Asymptotic analysis of stability for prismatic solids under axial loads”, *J. Mech. Phys. Solids* **46**:6 (1998), 955–1007.
- [Shanley 1947] F. R. Shanley, “Inelastic column theory”, *J. Aeronaut. Sci.* **14** (1947), 261–267.

Received 10 Oct 2006. Accepted 12 Nov 2007.

CLAUS DENCKER CHRISTENSEN: Claus.DenckerChristensen@nktflexibles.com
 NKT Flexibles I/S, Priorparken 510, 2605 Brøndby, Denmark

ESBEN BYSKOV: eb@civil.aau.dk
 Department of Civil Engineering, Aalborg University, Sohngaardsholmsvej 57, DK-9000 Aalborg, Denmark

ROLLING CONTACT WITH SLIP ON A THERMOELASTIC HALF-SPACE: COMPARISON WITH PERFECT ROLLING CONTACT

LOUIS MILTON BROCK

A rigid cylinder rolls at constant speed on a thermoelastic half-space under a compressive load. Heat flow across the contact zone is neglected, and the zone has a central region of perfect contact and two edge regions of frictionless slip. A robust asymptotic inversion of the exact transform solution to a related unmixed boundary value problem allows the mixed-mixed problem of rolling contact to be solved analytically. The solution is compared with that for perfect rolling contact. Both show variations in contact zone size and temperature change with rolling speed and load. Distinctions exist however: slip zones preclude oscillatory solution behavior and are much smaller than zones of oscillation. Moreover, perfect rolling contact may exaggerate the difference between imposed and effective angular velocity due to surface deformation.

Introduction

Models for rolling contact that involve elastic bodies have been developed within the framework of contact mechanics [Muskhelishvili 1975; Gladwell 1980; Johnson 1987; Hills and Barber 1993; Hills et al. 1993] and empirical observation [Bayer 1994; Blau 1996]. The more basic models are generally quasi-static, assume Hertzian contact, and are isothermal. However, more recent studies consider, variously, thermoelastic contact and inertial effects [Hills and Barber 1986; Georgiadis and Barber 1993; Pauk and Yevtushenko 1997; Barber 1999; Jang 2000; Pauk and Zastrau 2002; Andersson et al. 2005; Jang 2005]. In addition, studies of the mathematically-similar problem of the interface crack [Hills and Barber 1993; Hills et al. 1993] address issues that also arise in contact. Two key issues are the oscillatory solution behavior that occurs when perfect contact is modeled and a Hertzian contact zone stress distribution is not assumed, and the role of critical speed in contact zone formation.

In light of these issues, Brock [2004a; 2004b] considered a rigid cylinder of infinite length rolling at constant speed over a thermoelastic half-space. A dynamic steady state of plane strain was assumed, and robust asymptotic solutions to the mixed-mixed problem were obtained analytically. These exhibited clear variations with rolling speed and increases in contact zone temperature. The increase was prominent when the compressive force on the cylinder was large enough to produce contact zone compressive stress that neared values critical for yield.

The solutions also exhibited the aforementioned oscillation near contact zone edges. This is, of course, typical of mixed-mixed problems [Muskhelishvili 1975], but the behavior violates the assumption of nontensile contact zone stress. On the other hand, violation is confined to edge zones that are orders

Keywords: rolling contact, slip zones, perfect contact, effective angular velocity, coupled thermoelasticity, mixed-mixed problem.

of magnitude smaller than the zone itself. These microzones can be interpreted to mean that slip must occur at the contact zone edges.

For additional insight into their effects, this article imposes slip zones in the mixed-mixed problem for rolling contact. For simplicity, friction is ignored, and the resultant force that keeps the cylinder in contact with the surface acts through the cylinder axis. Jang [2000; 2005] has presented results for the basic problem of transient thermoelastic contact. However, to allow comparison with [Brock 2004a], coupled thermoelasticity governs here, but a dynamic steady state of plain strain is considered. Similarly, while it will be seen that a thermoelastic Rayleigh speed produces critical solution behavior, rolling speed is subcritical. Insight into behavior at supercritical speed can be found in work by Georgiadis and Barber [1993] and Brock and Georgiadis [2000].

The study begins in the next section with the problem formulation. Subsequently, exact expressions for the integral transform solution to a related unmixed problem are presented, and robust approximate inversions extracted. An analytical result for coupled singular integral equations provides a candidate solution. The solution itself follows by enforcing auxiliary conditions for rolling contact. Numerical calculations of contact zone parameters are then compared with those presented in [Brock 2004a]. Although similar, the two calculation sets illustrate distinctive behaviors. In particular, slip zones are orders of magnitude smaller than zones of oscillation seen in the no-slip model.

Problem formulation

Consider a linear isotropic thermoelastic half-space defined by the Cartesian coordinates (x, y, z) as the region $y > 0$. It is initially at rest at uniform (absolute) temperature T_0 when a rigid cylinder of infinite length and radius r is pressed into the surface with constant force (per unit of cylinder length) F and rolled in the positive x -direction with constant subcritical speed v . It will be shown that this speed corresponds to a thermoelastic Rayleigh speed. The process creates a zone of perfect contact between the cylinder and the half-space that is bordered by two zones of slip (frictionless sliding contact). The cylinder geometry is independent of coordinate z , so that the process is one of plane strain. Because (r, F, v) are constant, it is also assumed that a dynamic steady state is achieved in which the perfect contact and slip zones maintain constant widths.

It is convenient, then, to locate the Cartesian system origin below the cylinder axis ($x = 0$) and translate it with the same speed v . The boundary conditions governing the half-space surface $y = 0$ can then be written as [Brock 2004a]

$$\partial_y \theta = 0 \quad (\text{all } x), \quad (\sigma_{xy}, \sigma_y) = 0 \quad (x \notin C), \quad (1a)$$

$$\sigma_{xy} = 0, \quad \partial_x u_y = -\frac{x}{r} \quad (x \in C_{\pm}), \quad (1b)$$

$$\partial_x u_x = -\frac{\dot{U}_0}{v_r} - \frac{x^2}{2r^2}, \quad \partial_x u_y = -\frac{x}{r} \quad (x \in C_0). \quad (1c)$$

Here (u_x, u_y, θ) are the (x, y) -displacements and change in temperature from T_0 , and $(\sigma_x, \sigma_y, \sigma_z, \sigma_{xy})$ are the tractions in plane strain. These quantities depend only on (x, y) , and (∂_x, ∂_y) signify (x, y) -differentiation. Constant \dot{U}_0 is the unknown tangential velocity of the contact zone directly below the cylinder axis ($x = 0$). This is the point of maximum depression and has no normal velocity. Region C

is the contact zone defined by $L_- < x < L_+$. Region C_0 , defined by $l_- < x < l_+$, is the zone of perfect contact in C . Regions C_{\pm} are slip zones defined by $l_+ < x < L_+$ and $L_- < x < l_-$. Lengths (L_{\pm}, l_{\pm}) are unknown, but one can assume that

$$L_- < l_- < 0 < l_+ < L_+, \quad l < L \ll r, \tag{2}$$

$$L = L_+ - L_-, \quad l = l_+ - l_-. \tag{3}$$

The first condition in Equation (1a) imposes an assumption that heat flux through C is negligible. For a half-space that obeys the Fourier model of coupled thermoelasticity, governing equations for $y > 0$ can be written as [Brock and Georgiadis 2000; Brock 2004a]

$$\partial_x \sigma_x + \partial_y \sigma_{yx} = c^2 \partial_x^2 u_x, \quad \partial_x \sigma_{xy} + \partial_y \sigma_y = c^2 \partial_x^2 u_y, \tag{4a}$$

$$h \nabla^2 \theta + c \partial_x \left(\frac{\varepsilon}{\alpha_v} \Delta + \theta \right) = 0, \tag{4b}$$

$$\begin{bmatrix} \sigma_x \\ \sigma_y \\ \sigma_z \end{bmatrix} = \mu \begin{bmatrix} m+1 & m-1 & 1 \\ m-1 & m+1 & 1 \\ m-1 & m-1 & 1 \end{bmatrix} \begin{bmatrix} \partial_x u_x \\ \partial_y u_y \\ -\alpha_v \theta \end{bmatrix}, \tag{4c}$$

$$(\sigma_{xy}, \sigma_{yx}) = \mu (\partial_y u_x + \partial_x u_y). \tag{4d}$$

Equations (4b) and (4c) can be used to rewrite Equation (4a) in partly coupled form

$$(a \nabla^2 - c^2 \partial_x^2) \Delta - \alpha_v \nabla^2 \theta = 0, \quad (\nabla^2 - c^2 \partial_x^2) \varpi_z = 0. \tag{5}$$

Here (Δ, ϖ_z) is the dilatation and rotation. Constants $(m, a, h, \varepsilon, c)$ are given by

$$m = \frac{1}{1-2\nu}, \quad a = m+1, \quad h = \frac{k}{c_v \sqrt{\mu \rho}}, \quad \varepsilon = \frac{\mu T_0}{\rho c_v} \alpha_v^2, \tag{6a}$$

$$c = \frac{v}{v_r}, \quad v_r = \sqrt{\frac{\mu}{\rho}}. \tag{6b}$$

Quantities (h, ε, v_r) are the thermoelastic characteristic length, dimensionless coupling constant and rotational wave speed; $(\mu, \rho, \nu, k, \alpha_v, c_v)$ are, respectively, shear modulus, mass density, Poisson’s ratio, conductivity, volumetric thermal expansion coefficient, and specific heat at constant strain. Various sources [Sokolnikoff 1956; Chadwick 1960; Achenbach 1973; Davis 1998; Brock 1999] indicate that Equation (6a) gives

$$\varepsilon \approx O(10^{-2}), \quad h \approx O(10^{-8}) \text{ m}. \tag{7}$$

In addition to satisfying Equations (1)–(7), field quantities $(u_x, u_y, \nabla u_x, \nabla u_y, \theta)$ should be continuous for $y \geq 0$ and bounded above as $\sqrt{x^2 + y^2} \rightarrow \infty$. Smooth separation of the rolling cylinder and half-space surface requires, in particular, that $(\nabla u_x, \nabla u_y)$ are finite at the zone edge $x = (L_{\pm}, l_{\pm})$. Contact is also governed by the constraints

$$\sigma_y \leq 0 \quad (x \in C), \tag{8a}$$

$$\int_C \sigma_y dx = -F, \quad \int_C x \sigma_y dx = 0, \quad \int_{C_0} \sigma_{xy} dx = 0. \tag{8b}$$

The unilateral constraint, Equation (8a), guarantees a nontensile contact zone stress. The first two conditions in Equation (8b) specify that F is the resultant force on the cylinder and that its line of action is through the cylinder axis. The last condition specifies that the cylinder axis does not accelerate. The boundedness-continuity requirements, Equation (8a) and Equation (8b) give additional formulas necessary to find the contact zone parameters (U'_0, L_{\pm}, l_{\pm}).

Related problem: unmixed boundary conditions

The rolling contact problem is addressed by first considering the related problem of a half-space governed by Equations –(7) and the same boundedness-continuity conditions. The constraint, Equation (8), is relaxed, however, and Equation (1) for $y = 0$ is replaced by the unmixed conditions

$$\partial_y \theta = 0, \quad \sigma_y = \sigma(x), \quad \sigma_{xy} = \tau(x), \tag{9a}$$

$$\sigma(x) \equiv 0 \quad (x \notin C), \quad \tau(x) \equiv 0 \quad (x \notin C_0). \tag{9b}$$

The traction σ is continuous for $x \in C$ and vanishes at $x = L_{\pm}$, while the traction τ is continuous for $x \in C_0$ and vanishes at $x = l_{\pm}$. By following [Brock 2004a], an exact solution for the bilateral Laplace transform in x for this related problem can be obtained, and analytical expressions for the inverse can be derived that are valid for $\sqrt{x^2 + y^2} \gg h$. In view of Equation (7), these expressions are robust and are given for all $y \geq 0$ by

$$\begin{aligned} \partial_x u_x &= -\frac{Ay}{\pi R} \int_C \frac{\sigma}{\mu} \left[\frac{T}{(t-x)^2 + A^2 y^2} + \frac{2B^2}{(t-x)^2 + B^2 y^2} \right] dt \\ &\quad - \frac{B}{\pi R} \int_{C_0} \frac{\tau}{\mu} \left[\frac{2(t-x)}{(t-x)^2 + A^2 y^2} + \frac{T(t-x)}{(t-x)^2 + B^2 y^2} \right] dt, \\ \partial_x u_y &= \frac{By}{\pi R} \int_{C_0} \frac{\tau}{\mu} \left[\frac{2A^2}{(t-x)^2 + A^2 y^2} + \frac{T}{(t-x)^2 + B^2 y^2} \right] dt \\ &\quad - \frac{A}{\pi R} \int_C \frac{\sigma}{\mu} \left[\frac{T(t-x)}{(t-x)^2 + A^2 y^2} + \frac{2(t-x)}{(t-x)^2 + B^2 y^2} \right] dt, \\ \theta &= \frac{\varepsilon c^2}{\alpha_v a_\varepsilon} \frac{1}{\pi R} \left[T \int_C \frac{\sigma}{\mu} \frac{Ay}{(t-x)^2 + A^2 y^2} dt + 2B \int_{C_0} \frac{\tau}{\mu} \frac{t-x}{(t-x)^2 + B^2 y^2} dt \right]. \end{aligned} \tag{10}$$

In Equation (10), the quantities (A, B, T, R) are defined as

$$A = \sqrt{1 - \frac{c^2}{a_\varepsilon}}, \quad B = \sqrt{1 - c^2}, \quad T = c^2 - 2, \quad R = 4AB - T^2, \tag{11a}$$

$$a_\varepsilon = a + \varepsilon. \tag{11b}$$

The quantity R is a form of the classical [Achenbach 1973] Rayleigh function in the dimensionless rolling speed c . It has roots $c = \pm c_R$ ($0 < c_R < 1$) and these correspond to the Rayleigh speed $v_R = c_R v_f$. Equation (10) exhibits critical behavior as $R \rightarrow 0$, so rolling speed in this study is restricted to

$$0 < v < v_R \quad (0 < c < c_R). \tag{12}$$

The critical nature of the Rayleigh speed is well-established in isothermal elastodynamic contact [Craggs and Roberts 1967; Robinson and Thompson 1974; Georgiadis and Barber 1993]. Results for thermoelastic sliding contact with friction for any constant sliding speed are found in [Brock and Georgiadis 2000].

Candidate solution

In view of Equation (9), (σ, τ) correspond to the contact zone traction, and Equation (1a) and the first condition in Equation (1b) are automatically satisfied by Equation (10). Enforcing Equation (1c) and the second condition in Equation (1b), and using Equation (10), give integral equations for (σ, τ) :

$$-\frac{c^2 A}{\pi R} (vp) \int_C \frac{\sigma}{\mu} \frac{dt}{t-x} = -\frac{x}{r} \quad (x \in C_{\pm}), \quad (13a)$$

$$\frac{N}{R} \frac{\tau}{\mu} - \frac{c^2 A}{\pi R} (vp) \int_C \frac{\sigma}{\mu} \frac{dt}{t-x} = -\frac{x}{r} \quad (x \in C_0), \quad N = T + 2AB, \quad (13b)$$

$$-\frac{N}{R} \frac{\sigma}{\mu} - \frac{c^2 B}{\pi R} (vp) \int_{C_0} \frac{\tau}{\mu} \frac{dt}{t-x} = -\frac{\dot{U}_0}{v_r} - \frac{x^2}{2r^2} \quad (x \in C_0). \quad (13c)$$

Here, (vp) signifies the Cauchy principal value, and use is made of the Dirac relation [Carrier and Pearson 1988],

$$\frac{\eta}{\xi^2 + \eta^2} \rightarrow \pi \delta(\xi) \quad (\eta \rightarrow 0+). \quad (14)$$

To address Equation (13), we introduce the trial functions

$$\frac{\sigma}{\mu} = G_{\pm} \cos \pi v_{\pm} + \frac{Q_{\pm}}{\pi} \Sigma_{\pm} \sin \pi v_{\pm}, \quad (x \in C_{\pm}), \quad (15a)$$

$$\frac{\sigma}{\mu} = G_0 \cos \pi v_0 + \frac{Q_0}{\pi} \Sigma_0 \sin \pi v_0, \quad (x \in C_0), \quad (15b)$$

$$\Sigma_{\pm} = S_0 + S_{\mp} + (vp) S_{\pm}, \quad (x \in C_{\pm}), \quad (15c)$$

$$\Sigma_0 = S_- + S_+ + (vp) S_0, \quad (x \in C_0). \quad (15d)$$

Here, (v_0, v_{\pm}) are real-valued constants of magnitude $|v_0, v_{\pm}| < 1$, (G_0, G_{\pm}) are unknown functions, and

$$\begin{aligned} S_- &= \int_{C_-} \frac{G_-}{Q_-} \frac{dt}{t-x}, & Q_- &= \left(\frac{l_- - x}{x - L_-} \right)^{\nu_-} \left(\frac{l_+ - x}{l_- - x} \right)^{\nu_0} \left(\frac{L_+ - x}{l_+ - x} \right)^{\nu_+}, \\ S_0 &= \int_{C_0} \frac{G_0}{Q_0} \frac{dt}{t-x}, & Q_0 &= \left(\frac{x - l_-}{x - L_-} \right)^{\nu_-} \left(\frac{l_+ - x}{x - l_-} \right)^{\nu_0} \left(\frac{L_+ - x}{l_+ - x} \right)^{\nu_+}, \\ S_+ &= \int_{C_+} \frac{G_+}{Q_+} \frac{dt}{t-x}, & Q_+ &= \left(\frac{x - l_-}{x - L_-} \right)^{\nu_-} \left(\frac{x - l_+}{x - l_-} \right)^{\nu_0} \left(\frac{L_+ - x}{x - l_+} \right)^{\nu_+}. \end{aligned} \quad (16)$$

The trial functions have the property that

$$\frac{1}{\pi}(vp) \int_C \frac{\sigma}{\mu} \frac{dt}{t-x} = -G_{\pm} \sin \pi v_{\pm} + \frac{Q_{\pm}}{\pi} \Sigma_{\pm} \cos \pi v_{\pm} \quad (x \in C_{\pm}), \tag{17a}$$

$$\frac{1}{\pi}(vp) \int_C \frac{\sigma}{\mu} \frac{dt}{t-x} = -G_0 \sin \pi_0 + \frac{Q_0}{\pi} \Sigma_0 \cos \pi v_0 \quad (x \in C_0). \tag{17b}$$

Substitution of Equation (15a) and Equation (15c) into Equation (13a), in view of Equation (17a), leads to the result

$$G_{\pm} = \pm \frac{R}{c^2 A} \frac{x}{r}, \quad v_{\pm} = \mp \frac{1}{2} \quad (x \in C_{\pm}). \tag{18}$$

In a similar manner, substitution of Equation (15b) into (13b) and (13c), in view of (17b), produces coupled equations for (G_0, τ) that can be solved to give

$$\frac{\tau}{\mu} = \frac{R}{c^2 B} \frac{Q}{\pi} (vp) \int_{C_0} \left(U'_0 - \frac{t^2}{2r^2} \right) \frac{dt}{Q(t-x)} \quad (x \in C_0), \tag{19a}$$

$$G_0 = Q_0 \frac{Q}{\pi} (vp) \int_{C_0} \frac{P_0}{Q} \frac{dt}{t-x}, \quad v_0 = 0 \quad (x \in C_0). \tag{19b}$$

Equation (19) defines the quantities

$$Q = \sqrt{\frac{l_+ - x}{x - l_-}}, \quad P_0 = \frac{1}{c^2 A Q_0} \left(-R \frac{x}{r} - \frac{N}{2} \frac{\tau}{\mu} \right) + \frac{1}{\pi} (S_+ + S_-). \tag{20}$$

Obtaining Equation (10) and Equations (18)–(20) completes construction of a candidate solution for the rolling problem. The solution itself must be bounded and continuous for $x \in C$ and satisfy auxiliary condition (8).

Rolling contact solution

Equation (19a) is bounded at $x = l_-$, and the last two conditions in (8b) are satisfied if

$$L_{\pm} = \pm \frac{L}{2}, \quad l_{\pm} = \pm \frac{l}{2}, \quad \dot{U}_0 = -\frac{l^2 v_r}{16r^2}. \tag{21}$$

In view of Equations (18) and (19b), Equations (15a) and (15b) are bounded for all $x \in C$, and the first condition in (8b) is satisfied when

$$\pi + \frac{N}{2c^2 B} \frac{L}{2r} [K(\lambda) - E(\lambda)] = 0, \quad \lambda = \frac{l}{L}, \tag{22a}$$

$$\frac{\pi R}{c^2 A r^2} \left[\frac{Ll}{2} + \frac{5}{32} (3L+l)(L-l) \right] = \frac{F}{\mu r}. \tag{22b}$$

Here (K, E) are complete elliptic integrals of the first and second kind of modulus λ . The solution to Equation (22) will give the contact zone length parameters (l, L) , whereupon $(L_{\pm}, l_{\pm}, \dot{U}_0)$ can be obtained from Equation (21).

Contact zone fields

Use of Equations (19b), (22), and a standard table [Gradshteyn and Ryzhik 1980] in Equations (15a), (15b), and (19a), gives the contact zone traction

$$\frac{\tau}{\mu} = \frac{-R}{4c^2 B} \frac{x}{r^2} \sqrt{l^2 - 4x^2} \quad (x \in C_0), \quad (23a)$$

$$\frac{\sigma}{\mu} = \frac{RN}{8\pi c^4 AB} \frac{1}{r^2 L} |4x^2 - l^2| \sqrt{L^2 - 4x^2} \left[K(\lambda) - \Pi\left(\frac{l^2}{4x^2}, \lambda\right) \right] \quad (x \in C). \quad (23b)$$

In a similar manner, the temperature change θ_C in the contact zone is

$$\theta_C = \frac{\varepsilon}{\alpha_v a_\varepsilon} \left[\frac{1}{8r^2} (8x^2 - l^2) - \frac{\sigma}{\mu} \right] \quad (x \in C_0), \quad (24a)$$

$$\theta_C = \frac{\varepsilon}{\alpha_v a_\varepsilon} \left[\frac{1}{8r^2} (2x - \sqrt{4x^2 - 1})^2 + \frac{c^2 T}{R} \frac{\sigma}{\mu} \right] \quad (c \in C_\pm). \quad (24b)$$

Here Π is the complete elliptic integral of the third kind of modulus λ and parameter $l^2/4x^2$. In light of the property that $N \leq 0$, $T < 0$, $R \geq 0$ for Equation (12), Equation (23b) satisfies the unilateral constraint Equation (8a), and Equation (24) gives positive values. It can be shown that the maximum (compressive) normal traction σ^* occurs at $x = 0$ and is given by

$$\frac{\sigma^*}{\mu} = -\frac{R}{c^2 A} \frac{l^2}{2Lr} \frac{K(\lambda)}{K(\lambda) - E(\lambda)}. \quad (25)$$

A useful measure of the thermal response of the contact zone is the average temperature change $\tilde{\theta}_C$. Integration of Equation (24) gives this quantity as

$$\tilde{\theta}_C = \frac{\varepsilon}{2\alpha_v a_\varepsilon r^2} \left[\frac{1}{B} \left(\frac{L^2}{3} - \frac{l^2}{2} \right) - \frac{\pi T r}{AL} \left(Ll + \frac{5}{16} (3L + l)(L - l) \right) \right]. \quad (26)$$

Calculations: comparison with no-slip rolling contact results

Insight into the solution behavior can be gained by providing calculations for key results and comparing them with those for the model of rolling contact with no slip. Expressions that correspond to Equations (21)–(26) for that model can be found in [Brock 2004a] and are presented in the Appendix. The symbols are altered to match those employed here. The properties for what was referred to as 4340 steel were used for calculations. Under the updated classification schemes [Davis 1998], the properties are close to those for ASTM-A36 structural steel and, in any event, are also used here for purposes of comparison:

$$\begin{aligned} \nu &= \frac{1}{3}, & \rho &= 7834 \text{ kg/m}^3, \\ \mu &= 75 \text{ GPa}, & v_r &= 3094 \text{ m/s}, \\ v_R &= 2887 \text{ m/s}, & k &= 34.6 \text{ W/m} \cdot ^\circ\text{K}, \\ \alpha_v &= 89.6(10^{-6})1/^\circ\text{K}, & c_v &= 448 \text{ J/kg} \cdot ^\circ\text{K}. \end{aligned}$$

For rolling contact with no slip, infinitely rapid oscillations in contact zone traction occur in regions at zone edges defined by Equation (A.6) in the Appendix. Their existence may imply [Johnson 1987] that slip should in fact occur. Thus $|x|$ defined by Equation (A.6) plays the role of $l/2$, and a parameter corresponding to that in Equation (22a) can be obtained:

$$\lambda = \tanh \frac{\pi}{4\omega}. \tag{27}$$

Calculations in [Brock 2004a] show that Equation (27) behaves as $\lambda \approx 1 -$, and so λ in both Equation (22a) and Equation (27) is written in terms of a dimensionless exponent χ :

$$\lambda = 1 - 10^{-\chi}. \tag{28}$$

Thus χ and the dimensionless contact zone width, L/r , for the two models can be obtained from Equations (A.1), (A.6), and (22). These, in turn, give (l, L) . Values of $(\chi, L/r)$ are given in Table 1 for the dimensionless subcritical rolling speed c . Similarly, values for the tangential velocity \dot{U}_0 of the contact zone at its maximum depression point, maximum normal stress σ^* , and average change in contact zone temperature $\tilde{\theta}_C$, are given in Table 2. The dimensionless normal force used in both tables is

$$\frac{F}{\mu r} = 10^{-6}.$$

Values of χ in Table 1 indicate that the ratio $\frac{1}{2}(1 - l/L)$ of oscillation zone to contact zone widths are orders of magnitude smaller than unity, but that the ratio of slip zone to contact zone widths is orders of magnitude smaller yet. In the latter case, Equation (2) and a computer algorithm [Abramowitz and Stegun 1972] for (K, E) allow Equations (22) to be treated essentially as polynomials in $(\chi, L/r)$. Table 1 also shows that the ratios increase (χ decreases) markedly with dimensionless rolling speed c . Values of L/r

$\frac{F}{\mu r} = 10^{-6}$				
	Rolling contact with slip		Rolling contact (no slip)	
c	χ	L/r	χ	L/r
0.1	63,444	0.000653	8.121	0.000128
0.2	61,784	0.00066	7.811	0.00013
0.3	58,557	0.0006732	7.442	0.000133
0.4	54,115	0.000694	6.926	0.000136
0.5	48,456	0.000725	6.246	0.000142
0.6	41,575	0.000774	5.408	0.000151
0.7	33,424	0.000857	4.407	0.000165
0.8	23,734	0.00103	3.203	0.000192
0.9	10,745	0.001793	1.594	0.000291

Table 1. Dimensionless exponent χ and contact zone width L/r .

for the two cases in Table 1 are more comparable in magnitude, but those for perfect contact with slip are larger.

Table 2 indicates that the magnitude of σ^* for rolling contact (no slip) is greater than that for rolling contact with slip. Similarly, \dot{U}_0 can be orders of magnitude larger when slip does not occur, and the difference grows with increasing c . Both velocities are in the direction opposite to that of cylinder travel. Both models exhibit nominal increases in $\tilde{\theta}_C$. The increase for rolling contact with no slip is greater at low ($c \rightarrow 0$) rolling speed; that for rolling contact with slip is greater as rolling speed becomes critical ($c \rightarrow c_R$).

In ideal (rigid-rigid) rolling contact by a cylinder of radius r over a stationary plane surface, the single contact point (line parallel to the cylinder axis) has no velocity, so that the angular velocity is v/r , where again v is the translational speed of the cylinder axis. In this study, the corresponding point translates parallel to the deformable surface with velocity \dot{U}_0 . Thus, the effective angular velocity $\dot{\Theta}$ and its percentage difference $\delta\dot{\Theta}$ with v/r are, respectively,

$$\dot{\Theta} = \frac{1}{r}(v - \dot{U}_0), \quad \delta\dot{\Theta} = -\frac{\dot{U}_0}{v} (100\%). \quad (29)$$

The percentage difference is given in Table 3 for the data used in Tables 1 and 2. The values are all positive and small. However, it is well-known [Johnson 1987; Hills and Barber 1993; Hills et al. 1993] that this effective angular velocity behavior produces measured travel distances for rolling bodies that are less than the distance predicted from the number revolutions performed. Although both are small, the percentage changes for rolling contact with perfect contact in Table 3 are orders of magnitude larger than those for the slip case. That is, the more artificial no-slip rolling contact model may serve to exaggerate the difference between imposed and effective angular velocity.

$\frac{F}{\mu r} = 10^{-6}$						
	Rolling contact with slip			Rolling contact (no slip)		
c	\dot{U}_0 (m/s)	σ^* (GPa)	$\tilde{\theta}_C$ ($^{\circ}\text{K}$)	\dot{U}_0 (m/s)	σ^* (GPa)	$\tilde{\theta}_C$ ($^{\circ}\text{K}$)
0.1	-8.24-E4	-0.03657	0.284	-3.20-E3	-0.07460	1.0858
0.2	-8.42-E4	-0.03618	0.2837	-6.71-E3	-0.07374	1.0691
0.3	-8.76-E4	-0.03547	0.2839	-0.01068	-0.07274	1.0450
0.4	-9.31-E4	-0.03431	0.2844	-0.01537	-0.07040	1.0291
0.5	-1.017-E3	-0.03291	0.2861	-0.02164	-0.06790	0.9788
0.6	-1.159-E3	-0.03083	0.2904	-0.03067	-0.06441	0.9204
0.7	-1.421-E3	-0.02785	0.3014	-0.04519	-0.05483	0.8423
0.8	-2.050-E3	-0.02319	0.3333	-0.07482	-0.05157	0.7239
0.9	-6.220-E3	-0.01331	0.5209	-0.20368	-0.03694	0.4776

Table 2. Tangential speed \dot{U}_0 , maximum normal traction σ^* , average temperature change $\tilde{\theta}_C$. Note: $\pm M - EN \equiv \pm M(10^{-N})$.

$\frac{F}{\mu r} = 10^{-6}$				
	Rolling contact with slip		Rolling contact (no slip)	
c	\dot{U}_0 (m/s)	$\delta\dot{\Theta}$ (%)	\dot{U}_0 (m/s)	$\delta\dot{\Theta}$ (%)
0.1	-8.24-E4	0.000266	-3.20-E3	0.001035
0.2	-8.42-E4	0.000136	-6.71-E3	0.001084
0.3	-8.76-E4	0.000094	-0.01068	0.001151
0.4	-9.31-E4	0.000075	-0.01537	0.001242
0.5	-1.117-E3	0.000066	-0.02164	0.001399
0.6	-1.159-E3	0.000062	-0.03067	0.001652
0.7	-1.421-E3	0.000066	-0.4519	0.002087
0.8	-2.050-E3	0.000083	-0.07482	0.003023
0.9	-6.220-E3	0.000223	-0.20368	0.007315

Table 3. Tangential speed \dot{U}_0 , difference $\delta\dot{\Theta}$ between effective and imposed angular velocity. Note: $\pm M - EN \equiv \pm M(10^{-N})$.

Calculations for rolling contact with slip

Tables 4 and 5 give values of $(\chi, L/r, \dot{U}_0, \sigma^*, \tilde{\theta}_C)$ for rolling contact with slip when the dimensionless applied normal forces are, respectively,

$$\frac{F}{\mu r} = 10^{-5}, \quad \frac{F}{\mu r} = 5(10^{-5}).$$

These values show that increasing F decreases χ but increases the magnitudes of contact zone parameters $(L/r, \dot{U}_0, \sigma^*, \tilde{\theta}_C)$. The increase involving \dot{U}_0 is essentially linear, those involving $(L/r, \sigma^*, \tilde{\theta}_C)$ are less than linear, and the decrease in χ is greater than linear. Tables 1, 2, 4 and 5 also indicate that parameters $(L/r, \dot{U}_0)$ increase in magnitude with increasing c while parameter χ decreases. Parameter $\tilde{\theta}_C$ however, decreases for small c , reaches a minimum and then increases with increasing c . The variation with c for σ^* is itself sensitive to F : Tables 2 and 4 exhibit decreases in the magnitude with increasing c , but Table 5 shows that the magnitude of σ^* actually increases for small c , reaches a peak, and then decreases. That is, for small c , $(\sigma^*, \tilde{\theta}_C)$ vary inversely with each other. It should be noted that the maximum magnitude of σ^* displayed in Table 5 is close to that for plastic yield under uniaxial loading [Davis 1998], and that changes in $\tilde{\theta}_C$ exhibited in Table 5 are nominal but not trivial.

General comments

The observations above are based on a two-dimensional dynamic steady-state analysis of two idealized models for rolling contact. The one presented here allows slip zones at a contact zone edge, the one considered in [Brock 2004a] involved only perfect contact. In both models, the rolling cylinder is rigid, the resultant force on it is purely compressive and is directed through the cylinder axis, and heat flow

$\frac{F}{\mu r} = 10^{-5}$					
c	χ	L/r	\dot{U}_0 (m/s)	σ^* (GPa)	$\tilde{\theta}_C$ (°K)
0.1	20,063	2.0644-E3	-8.24-E4	-0.11565	0.8980
0.2	19,538	2.0866-E3	-8.42-E4	-0.11442	0.8973
0.3	18,518	2.1286-E3	-8.76-E4	-0.11216	0.8976
0.4	17,113	2.1942-E3	-9.31-E4	-0.10881	0.8994
0.5	15,323	2.2938-E3	-1.017-E3	-0.10409	0.9047
0.6	13,147	2.4484-E3	-1.159-E3	-0.09751	0.9184
0.7	10,570	2.7104-E3	-1.421-E3	-0.08809	0.9530
0.8	7506	3.2560-E3	-2.050-E3	-0.07332	1.0536
0.9	3398	5.6712-E3	-6.219-E3	-0.04211	1.6472

Table 4. Dimensionless exponent χ and contact zone width L/r , tangential speed \dot{U}_0 , maximum normal traction σ^* , average temperature change $\tilde{\theta}_C$. Note: $\pm M - EN \equiv \pm M(10^{-N})$.

across the contact zone is neglected. In the model treated here, slip is frictionless and occurs only in two edge zones.

Nevertheless, the observations are based on solutions that are generated from the mixed-mixed problems that arise in rolling contact. The solutions and calculations based on them exhibit four basic features. The first is, of course, that solution oscillation does not occur when slip zones exist at the contact zone edges. The second feature is that variation in size, average temperature change and maximum compressive traction of the contact zone with parameters rolling speed and resultant compressive force is

$\frac{F}{\mu r} = 5(10^{-5})$					
c	χ	L/r	\dot{U}_0 (m/s)	σ^* (GPa)	$\tilde{\theta}_C$ (°K)
0.1	8973	4.616-E3	-4.120-E3	-0.23311	2.0079
0.2	8738	4.666-E3	-4.210-E3	-0.25588	2.0064
0.3	8282	4.760-E3	-4.381-E3	-0.25082	2.0072
0.4	7653	4.907-E3	-4.655-E3	-0.24332	2.0111
0.5	6853	5.129-E3	-5.087-E3	-0.23277	2.0230
0.6	5880	5.475-E3	-5.797-E3	-0.21807	2.0536
0.7	4727	6.061-E3	-7.103-E3	-0.19700	2.1310
0.8	3357	7.281-E3	-0.01026	-0.16401	2.3558
0.9	1520	0.012681	-0.03110	-0.09421	3.6833

Table 5. Dimensionless exponent χ and contact zone width L/r , tangential speed \dot{U}_0 , maximum normal traction σ^* , average temperature change $\tilde{\theta}_C$. Note: $\pm M - EN \equiv \pm M(10^{-N})$.

important for both models. The third feature is that slip zones form essentially where the separation of the cylinder and elastic body occurs. Their widths are orders of magnitude smaller even than the extremely small slip zone widths implied by the oscillation zones in rolling contact without slip. This phenomenon may well arise from the continuity of traction required everywhere in the contact zone. As seen in Equation (23), this requirement enforces zero traction at points $|x| = L/2$ of the cylinder/half-space separation but also gives zero traction at points $|x| = l/2$ of the perfect contact-slip transition. Finally, the perfect rolling contact model may overstate the increase in effective angular velocity of rolling above the rigid-rigid limit.

It is hoped that the results of this article, while limited in various aspects in comparison to the newer contact analyses listed at the outset, does allow insight into aspects of rapid contact behavior. These results are now forming the basis of dynamic studies that include thermal relaxation effects, heat conduction across a contact zone, and both dry and viscous friction.

Appendix

For the case of perfect contact over all C [Brock 2004a], the contact zone parameters (L, L_{\pm}, \dot{U}_0) are given by

$$\begin{aligned} L_{\pm} &= \pm \frac{L}{2}, & \dot{U}_0 &= \frac{L}{4} \left[\sqrt{\frac{B}{A}} \omega + (4\omega^2 - 1) \frac{L}{16r} \right] v_r, \\ \left(\frac{L}{\kappa r}\right)^3 + 3\left(\frac{L}{\kappa r}\right)^2 - 4\frac{F}{F_0} &= 0, & \frac{F_0}{\mu r} &= \frac{\pi B R}{6c^2 A^2} \left(4 + \frac{1}{\omega^2}\right). \end{aligned} \quad (\text{A.1})$$

The contact zone traction is

$$\frac{\tau}{\mu} = -\frac{P(x)}{4Br^2} \sqrt{L^2 - 4x^2} \sin\left(\phi - \omega \ln \frac{L - 2x}{L + 2x}\right) \quad (x \in C), \quad (\text{A.2a})$$

$$\frac{\sigma}{\mu} = -\frac{P(x)}{4\sqrt{AB}r^2} \sqrt{L^2 - 4x^2} \cos\left(\phi - \omega \ln \frac{L - 2x}{L + 2x}\right) \quad (x \in C). \quad (\text{A.2b})$$

In Equations (A.1) and (A.2), the terms $(P, \phi, \omega, \kappa)$ are given by

$$\begin{aligned} P(x) &= \sqrt{\frac{R}{1-AB}} \sqrt{(2Br + \omega AL)^2 + 4ABx^2}, & \tan \phi &= \frac{2\sqrt{AB}x}{2Br + \omega AL}, \\ \omega &= \frac{1}{2\pi} \ln \frac{c^2\sqrt{AB} + N}{c^2\sqrt{AB} - N}, & \kappa &= \frac{\sqrt{B}}{\omega\sqrt{A}}. \end{aligned}$$

Here, (R, N, A, B) are defined by Equations (11a) and (13b), and for the parameter $\omega > 0$ in Equation (12). The contact zone temperature change θ_C can be extracted from [Brock 2004a] as

$$\theta_C = \frac{\varepsilon}{\alpha_v a_\varepsilon} \left[\frac{x^2}{r^2} + \omega \sqrt{\frac{B}{A}} \frac{L}{2r} - \frac{1}{8} (1 - 4\omega^2) \frac{L^2}{r^2} - \frac{\sigma}{\mu} \right] \quad (x \in C). \quad (\text{A.3})$$

The maximum value of (A.2b) occurs at $x = 0$ and is given by

$$\frac{\sigma^*}{\mu} = -\sqrt{\frac{R}{1-AB}} \left(\sqrt{\frac{B}{A}} + \frac{\omega L}{2r} \right) \frac{L}{2r}. \quad (\text{A.4})$$

The average of (A.3) is obtained as

$$\tilde{\theta}_C = \frac{\varepsilon}{\alpha_v a_\varepsilon} \left[\frac{F}{\mu L} + 2 \frac{\omega \sqrt{B} L}{\sqrt{A} r} + \frac{1}{24} (12\omega^2 - 1) \frac{L^2}{r^2} \right]. \quad (\text{A.5})$$

The oscillatory behavior exhibited by (A.2) as $|x| \rightarrow 0$ implies that the condition of nontensile contact stress does not hold everywhere in regions at the edges of C defined by

$$\tanh \frac{\pi}{4\omega} < \left| \frac{2x}{L} \right| < 1. \quad (\text{A.6})$$

References

- [Abramowitz and Stegun 1972] M. Abramowitz and I. A. Stegun, *Handbook of mathematical functions, with formulas, graphs, and mathematical tables*, Dover, New York, 1972.
- [Achenbach 1973] J. D. Achenbach, *Wave propagation in elastic solids*, North-Holland, Amsterdam, Netherlands, 1973.
- [Andersson et al. 2005] L.-E. Andersson, A. Klarbring, J. R. Barber, and M. Ciavarella, “On the existence and uniqueness of steady state solutions in thermoelastic contact with frictional heating”, *P. Roy. Soc. Lond. A Mat.* **461**:2057 (2005), 1261–1282.
- [Barber 1999] J. R. Barber, “Thermoelasticity and contact”, *J. Therm. Stresses* **22**:4-5 (1999), 513–525.
- [Bayer 1994] R. G. Bayer, *Mechanical wear prediction and prevention*, Marcel Dekker, New York, 1994.
- [Blau 1996] P. J. Blau, *Friction science and technology*, Marcel Dekker, New York, 1996.
- [Brock 1999] L. M. Brock, “Process-altered surface convection effects in a coupled thermoelastic analysis of rapid sliding indentation with friction”, *J. Therm. Stresses* **22**:8 (1999), 737–756.
- [Brock 2004a] L. M. Brock, “Coupled thermoelastic analysis of perfect rolling contact: solution behavior near yield initiation”, *J. Therm. Stresses* **27**:5 (2004), 383–403.
- [Brock 2004b] L. M. Brock, “Rolling without slip on a transversely isotropic thermoelastic half-space”, *J. Elasticity* **77**:2 (2004), 139–162.
- [Brock and Georgiadis 2000] L. M. Brock and H. G. Georgiadis, “Sliding contact with friction of a thermoelastic solid at subsonic, transonic and supersonic speeds”, *J. Therm. Stresses* **23**:7 (2000), 629–656.
- [Carrier and Pearson 1988] G. F. Carrier and C. E. Pearson, *Partial differential equations: theory and technique*, 2nd ed., Academic Press, Boston, 1988.
- [Chadwick 1960] P. Chadwick, “Thermoelasticity, the dynamical theory”, pp. 263–328 in *Progress in solid mechanics*, vol. 1, edited by I. N. Sneddon and R. Hill, North-Holland, Amsterdam, Netherlands, 1960.
- [Craggs and Roberts 1967] J. W. Craggs and A. M. Roberts, “On the motion of a heavy cylinder over the surface of an elastic half-space”, *J. Appl. Mech. (Trans. ASME)* **34** (1967), 207–209.
- [Davis 1998] J. R. Davis (editor), *Metals handbook desk edition*, American Society for Metals, Metals Park, OH, 1998.
- [Georgiadis and Barber 1993] H. G. Georgiadis and J. R. Barber, “On the super-Rayleigh/subseismic elastodynamic indentation problem”, *J. Elasticity* **31**:3 (1993), 141–161.
- [Gladwell 1980] G. M. L. Gladwell, *Contact problems in the classical theory of elasticity*, Sijthoff and Noordhoff, Alphen aan den Rijn, Netherlands, 1980.
- [Gradshteyn and Ryzhik 1980] I. S. Gradshteyn and I. M. Ryzhik, *Table of integrals, series, and products*, Academic Press, New York, 1980.

- [Hills and Barber 1986] D. A. Hills and J. R. Barber, “Steady sliding of a circular cylinder over a dissimilar thermally conducting half-plane”, *Int. J. Mech. Sci.* **28**:9 (1986), 613–622.
- [Hills and Barber 1993] D. A. Hills and J. R. Barber, “Interface cracks”, *Int. J. Mech. Sci.* **35**:1 (1993), 27–37.
- [Hills et al. 1993] D. A. Hills, D. Nowell, and A. Sackfield, *Mechanics of elastic contacts*, Butterworth-Heinemann, Oxford, 1993.
- [Jang 2000] Y. H. Jang, “Transient thermoelastic contact problems for an elastic foundation”, *Int. J. Solids Struct.* **37**:14 (2000), 1997–2004.
- [Jang 2005] Y. H. Jang, “Effects of thermal contact resistance on transient thermoelastic contacts for an elastic foundation”, *J. Appl. Mech. (Trans. ASME)* **72**:6 (2005), 972–977.
- [Johnson 1987] K. L. Johnson, *Contact mechanics*, Cambridge University Press, Cambridge, 1987.
- [Muskhelishvili 1975] N. I. Muskhelishvili, *Some basic problems of the mathematical theory of elasticity: fundamental equations, plane theory of elasticity, torsion and bending*, Noordhoff International, Leyden, 1975.
- [Pauk and Yevtushenko 1997] V. J. Pauk and A. A. Yevtushenko, “Frictional heating in sliding contact of two thermoelastic bodies”, *Int. J. Solids Struct.* **34**:12 (1997), 1505–1516.
- [Pauk and Zastrau 2002] V. Pauk and B. Zastrau, “2D rolling contact problem involving frictional heating”, *Int. J. Mech. Sci.* **44**:12 (2002), 2573–2584.
- [Robinson and Thompson 1974] A. R. Robinson and J. C. Thompson, “Transient stresses in an elastic half-space resulting from the frictionless indentation of a rigid wedge-shaped die”, *Z. Angew. Math. Mech.* **54**:3 (1974), 139–144.
- [Sokolnikoff 1956] I. S. Sokolnikoff, *Mathematical theory of elasticity*, 2nd ed., McGraw-Hill, New York, 1956.

Received 29 Sep 2007. Accepted 6 Dec 2007.

LOUIS MILTON BROCK: brock@engr.uky.edu

265 RGAN, Mechanical Engineering, University of Kentucky, Lexington, KY 40506-0503, United States

A VARIATIONAL DEDUCTION OF SECOND GRADIENT POROELASTICITY PART I: GENERAL THEORY

GIULIO SCIARRA, FRANCESCO DELL'ISOLA, NICOLETTA IANIRO AND ANGELA MADEO

Second gradient theories have to be used to capture how local micro heterogeneities macroscopically affect the behavior of a continuum. In this paper a configurational space for a solid matrix filled by an unknown amount of fluid is introduced. The Euler–Lagrange equations valid for second gradient poromechanics, generalizing those due to Biot, are deduced by means of a Lagrangian variational formulation. Starting from a generalized Clausius–Duhem inequality, valid in the framework of second gradient theories, the existence of a macroscopic solid skeleton Lagrangian deformation energy, depending on the solid strain and the Lagrangian fluid mass density as well as on their Lagrangian gradients, is proven.

1. Introduction

Poroelasticity stems from Biot's pioneering contributions on consolidating fluid saturated porous materials [Biot 1941] and now spans a lot of different interrelated topics, from geo- to biomechanics, wave propagation, transport, unsaturated media, etc. Many of these topics are related to modeling coupled phenomena (for example, chemomechanical swelling of shales [Dormieux et al. 2003; Coussy 2004], or biomechanical models of cartilaginous tissues), and nonstandard constitutive features (for instance, in freezing materials [Coussy 2005]). In all these cases, complexity generally remains in rendering how heterogeneities affect the macroscopic mechanical behavior of the overall material.

It is well known from the literature how microscopically heterogeneous materials can be described in the framework of statistically homogeneous media [Torquato 2002] considering suitable generalizations of the dilute approximation due to Eshelby [Nemat-Nasser and Hori 1993; Dormieux et al. 2006]; however, some lack in the general description of the homogenization procedure arises when dealing with heterogeneous materials, the characteristic length of which can be compared with the thickness of the region where high deformation gradients occur. This could be due, for example, to external periodic loading, the wavelength of which is comparable with the characteristic length of the material, or to phase transition, etc.

From the macroscopic point of view the quoted modeling difficulties, arising when high gradients occur, are discussed in the framework of so called high gradient theories [Germain 1973], where the assumption of locality in the characterization of the material response is relaxed. In these theories, the momentum balance equation reads in a more complex way than the classical one used for Cauchy continua. As a matter of fact, it is the divergence of the difference between the stress tensor and the divergence of so-called hyperstresses that balance the external bulk forces. Stress and hyperstress are introduced by a straightforward application of the principle of virtual power, as those quantities working on the gradient of velocity and the second gradient of velocity, respectively [Casal 1972; Casal and

Keywords: poromechanics, second gradient materials, lagrangian variational principle.

Gouin 1988]. Even the classical Cauchy theorem is, in this context, revised by introducing dependence of tractions not only on the outward normal unit vector but also on the local curvature of the boundary [dell'Isola and Seppecher 1997]; moreover symmetric and skew-symmetric couples (the actions called “double-forces” by Germain) must be prescribed on the boundary in terms of the hyperstress tensor together with contact edge forces along the lines where discontinuities of the normal vector occur.

Following the early papers on fluid capillarity [Casal 1972; Casal and Gouin 1988], the second gradient model can indeed be introduced by means of a variational formulation where the considered Helmholtz free energy depends both on the strain and the strain gradient tensors.

In the case of fluids, second gradient theories are typically applied for modeling phase transition phenomena [de Gennes 1985] or for modeling wetting phenomena [de Gennes 1985], when a characteristic length, say the thickness of a liquid film on a wall, becomes comparable with the thickness of the liquid/vapor interface [Seppecher 1993], annihilation (nucleation) of spherical droplets, when the radius of curvature is of the same order of the thickness of the interface [dell'Isola et al. 1996], or topological transition [Lowengrub and Truskinovsky 1998].

In the case of solids, second gradient theories are applied, for instance, when modeling the failure process associated with strain localization [Elhers 1992; Vardoulakis and Aifantis 1995; Chambon et al. 2004]. To the best of our knowledge, second gradient theories are very seldom applied in the mechanics of porous materials [dell'Isola et al. 2003] and no second gradient poromechanical model, consistent with the classical Biot theory, is available except the one presented in [Sciarra et al. 2007]. As gradient fluid models, second gradient poromechanics will be capable of providing significant corrections to the classical Biot model when considering porous media with characteristic length comparable to the thickness of the region where high fluid density (deformation) gradients occur. We refer, for instance, to crack/pore opening phenomena triggered by strain gradients or fluid percolation, the characteristic length being in this case the average length of the space between grains (pores).

Several authors have focused their attention on the development of homogenization procedures capable of rendering the heterogeneous response of the material at the microlevel by means of a second gradient macroscopic constitutive relation [Pideri and Seppecher 1997; Camar-Eddine and Seppecher 2003]; however, very few contributions seem to address this problem in the framework of averaging techniques [Drugan and Willis 1996; Gologanu and Leblond 1997; Koutetzova et al. 2002]. The present work does not investigate the microscopic interpretation of second gradient poromechanics, but directly discusses its macroscopic formulation. It is divided into two papers: in the first paper the basics of kinematics, Section 2; the physical principles, Section 3; the thermodynamical restrictions, Section 4; and in Section 5 the variational deduction of the governing equations for a second gradient fluid filled porous material are presented.

In particular, in Section 2 a purely macroscopic Lagrangian description of motion is addressed by introducing two placement maps in χ_s and ϕ_f (Equation (1)). We do not explicitly distinguish which part of the current configuration of the fluid filled porous material is occupied at any time t by the solid and fluid constituents, this information being partially included by the solid and fluid apparent density fields, which provide the density of solid/fluid mass with respect to the volume of the porous system (Equation (5)).

The deformation power, or stress working (Equation (12)), following Truesdell [1977] is deduced in Section 3 starting from the second gradient expression of power of external forces (Equation (9)) Cauchy theorem (Equation (10)) and balance of global momentum (see (11)).

In the spirit of Coussy et al. [1998] and Coussy [2004] thermodynamical restrictions on admissible constitutive relations are stated in Section 4, finding out a suitable overall potential, defined on the reference configuration of the solid skeleton. This last depends on the skeleton strain tensor and the fluid mass content, measured in the reference configuration of the solid, as well as on their Lagrangian gradients, in Equation (18).

Finally a deduction of the governing equations is presented in Section 5, based on the principle of virtual works, by requiring the variation of the internal energy to be equal to the virtual work of external and dissipative forces (see (19)). A second gradient extension of the two classical Biot equations of motion [Coussy 2004; Sciarra et al. 2007], endowed with the corresponding transversality conditions on the boundary, is therefore formulated (see Equations (30)–(33)). Generalizing the treatment developed, for example, by Baek and Srinivasa [2004] for first gradient theories, one of the equations of motion found by means of a variational principle is interpreted as the balance law for total momentum, when suitable definitions of the global stress and hyperstress tensors are introduced (see (34)).

In a subsequent paper (Part II, to be published in a forthcoming issue of this journal), an application of the second gradient model to the classical consolidation problem will be discussed. Our aim is to show how the present model enriches the description of a well-known phenomenon, typical of geomechanics, curing some of the weaknesses of the classical Terzaghi equation [von Terzaghi 1943]. In particular we will figure out the behavior of the fluid pressure during the consolidation process when varying the initial pressures of the solid skeleton and/or the saturating fluid. From the mathematical point of view, the initial boundary value problem will be discussed according with the theory of linear pencils.

2. Kinematics of fluid filled porous media and mass balances

The behavior of a fluid filled porous material is described, in the framework of a macroscopic model, adopting a Lagrangian description of motion with respect to the reference configuration of the solid skeleton. At any current time t the configuration of the system is determined by the maps χ_s and ϕ_f , defined as

$$\chi_s : \mathcal{B}_s \times \mathcal{I} \rightarrow \mathcal{E}, \quad \phi_f : \mathcal{B}_s \times \mathcal{I} \rightarrow \mathcal{B}_f, \quad (1)$$

where \mathcal{B}_α ($\alpha = s, f$) is the reference configuration of the α -th constituent, while \mathcal{E} is the Euclidean place manifold, and \mathcal{I} indicates a time interval. The map $\chi_s(\cdot, t)$ prescribes the current (time t) placement \mathbf{x} of the skeleton material particle \mathbf{X}_s in \mathcal{B}_s . The map $\phi_f(\cdot, t)$, on the other hand, identifies the fluid material particle \mathbf{X}_f in \mathcal{B}_f which, at time t , occupies the same current place \mathbf{x} as the solid particle \mathbf{X}_s . Therefore the set of fluid material particles filling the solid skeleton is unknown, to be determined by means of evolution equations. Both these maps are assumed to be at least diffeomorphisms on \mathcal{E} . The current configuration \mathcal{B}_t of the porous material is the image of \mathcal{B}_s under $\chi_s(\cdot, t)$. In accordance with the properties of χ_s and ϕ_f it is straightforward to introduce the fluid placement map as

$$\chi_f : \mathcal{B}_f \times \mathcal{I} \rightarrow \mathcal{E}, \quad \text{such that } \chi_f(\cdot, t) = \chi_s(\cdot, t) \circ \phi_f(\cdot, t)^{-1},$$

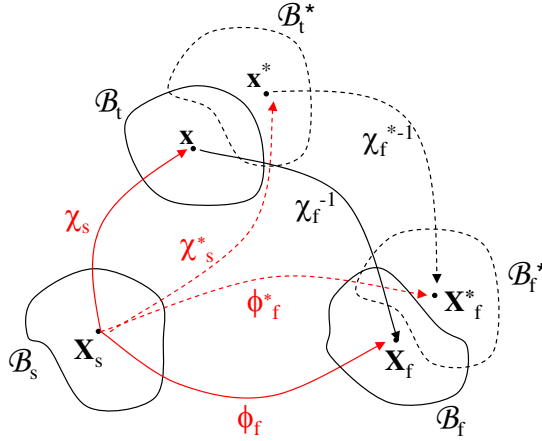


Figure 1. Lagrangian variations of the placement maps χ_s , ϕ_f , and χ_f .

where $\chi_f(\cdot, t)$ is still a diffeomorphism on \mathcal{E} . **Figure 1** shows how the introduced maps operate on the skeleton particle $X_s \in \mathcal{B}_s$; admissible variations of the two maps $\chi_s(\cdot, t)$ and $\phi_f(\cdot, t)$ are also depicted, in **Section 5**. In this way the space of configurations we will use has been introduced.

Independently of $t \in \mathcal{I}$, the Lagrangian gradients of χ_s and ϕ_f are introduced as

$$\begin{aligned} F_s(\cdot, t) : \mathcal{B}_s &\rightarrow \text{Lin}(V\mathcal{E}), & \Phi_f(\cdot, t) : \mathcal{B}_s &\rightarrow \text{Lin}(V\mathcal{E}), \\ X_s &\mapsto \nabla_s \chi_s(X_s, t), & X_s &\mapsto \nabla_s \phi_f(X_s, t), \end{aligned} \tag{2}$$

with $V\mathcal{E}$ being the space of translations associated to the Euclidean place manifold. In **Equation (2)** ∇_s indicates the Lagrangian gradient in the reference configuration of the solid skeleton; analogously, the gradient of χ_f is given by $F_f(X_f, t) = F_s(X_s, t) \cdot \Phi_f(X_s, t)^{-1}$, where $X_f = \phi_f(X_s, t)$.¹

In the following the fluid Lagrangian gradient of χ_f will be indicated both by F_f or $\nabla_f \chi_f$ when confusion can arise. Moreover, the time derivatives of χ_s and χ_f , say the Lagrangian velocities of the solid skeleton and the fluid, can be introduced as

$$\text{for all } X_\alpha \in \mathcal{B}_\alpha, \quad \mathcal{V}_\alpha(X_\alpha, \cdot) : \mathcal{I} \rightarrow V\mathcal{E}, \quad t \mapsto \left. \frac{d\chi_\alpha}{dt} \right|_{(X_\alpha, t)}.$$

We also introduce the Eulerian velocities v_α as the push-forward of \mathcal{V}_α into the current domain

$$v_\alpha(\cdot, t) = \mathcal{V}_\alpha(\cdot, t) \circ \chi_\alpha(\cdot, t)^{-1}.$$

In the following we do not explicitly distinguish the map χ_s from its section $\chi_s(\cdot, t)$ if no ambiguity can arise. Moreover we will distinguish between the Lagrangian gradient (∇_s) in the reference configuration of the solid skeleton and the Eulerian gradient (∇) with respect to the current position x . Analogously, the solid Lagrangian and the Eulerian divergence operations will be noted by div_s and div , respectively. All the classical transport formulas can be derived both for the solid and the fluid quantities; in particular,

¹From now on we will indicate single, double and triple contraction between two tensors with \cdot , \cdot , and $\dot{\cdot}$ respectively.

those ones for an image volume and oriented surface element turn to be

$$d\mathcal{B}_t = J_\alpha d\mathcal{B}_\alpha, \quad \mathbf{n} dS_t = J_\alpha \mathbf{F}_\alpha^{-T} \cdot \mathbf{n}_\alpha dS_\alpha,$$

where $d\mathcal{B}_t$ and dS_t represent the current elementary volume and elementary oriented surface corresponding to $d\mathcal{B}_\alpha$ and dS_α , respectively, where $J_\alpha = \det \mathbf{F}_\alpha$, and where \mathbf{n} and \mathbf{n}_α are the outward unit normal vectors to dS_t and dS_α . As far as only the solid constituent is concerned, we can understand that deformation induces changes in both the lengths of the material vectors and the angles between them. As it is well known, the Green–Lagrange strain tensor $\boldsymbol{\varepsilon}$ measures these changes, and is defined as

$$\boldsymbol{\varepsilon} := \frac{1}{2} (\mathbf{F}_s^T \cdot \mathbf{F}_s - \mathbf{I}), \tag{3}$$

where \mathbf{I} clearly represents the second order identity tensor.

The balance of mass both for the solid and the fluid constituent are introduced as

$$\mathbb{M}_\alpha = \int_{\mathcal{B}_t} \rho_\alpha d\mathcal{B}_t = \text{const} = \int_{\mathcal{B}_\alpha} \rho_\alpha^0 d\mathcal{B}_\alpha, \quad (\alpha = s, f), \tag{4}$$

where \mathbb{M}_α is the total mass of the α -th constituent, ρ_α is the current apparent density of mass of the α -th constituent per unit volume of the porous material, while ρ_α^0 is the corresponding density in the reference configuration of the α -th constituent. When localizing, Equation (4) reads

$$\rho_\alpha J_\alpha = \rho_\alpha^0, \quad (\alpha = s, f),$$

or, in differential form,

$$\frac{d^\alpha \rho_\alpha}{dt} + \rho_\alpha \operatorname{div} (\mathbf{v}_\alpha) = 0, \quad (\alpha = s, f), \tag{5}$$

where $d^\alpha \rho_\alpha / dt$ represents the material time derivative relative to the motion of the α -th constituent. In other words,

$$\frac{d^\alpha}{dt} := \frac{d}{dt} \Big|_{X_\alpha = \text{const}}.$$

The macroscopic conservation laws could also be deduced in the framework of micromechanics [Dormieux and Ulm 2005; Dormieux et al. 2006] starting from a refined model, where the solid and the fluid material particles occupy two disjoint subsets of the current configuration, and considering an average of the solid and fluid microscopic mass balances. The macroscopic laws do involve the so called apparent density of the constituents and suitable macroscopic velocity fields. For a detailed description of the procedure which leads to averaged conservation laws we refer to the literature [Coussy 2004].

2.1. Pull back of continuity equations. It is clear that Equation (5) consists of Eulerian equations, meaning that they are defined on the current configuration of the porous medium. Following Wilmanski [1996] and Coussy [2004] we want to write both these equations in the reference configuration of the solid skeleton. With this purpose in mind let us define the relative fluid mass flow \mathbf{w} as $\mathbf{w} := \rho_f (\mathbf{v}_f - \mathbf{v}_s)$. The use of this definition allows us to rearrange the fluid continuity (5) in the form

$$\frac{d^s \rho_f}{dt} + \rho_f \operatorname{div} \mathbf{v}_s + \operatorname{div} \mathbf{w} = 0. \tag{6}$$

We want now to rewrite the continuity equation for the fluid constituent in the reference configuration of the solid skeleton. The Lagrangian approach to the fluid mass balance can be carried out by introducing the current Lagrangian fluid mass content m_f , defined as

$$m_f := J_s (\rho_f \circ \chi_s). \quad (7)$$

Furthermore, let \mathbf{M} be the Lagrangian vector referred to the reference configuration of the solid and related to the flow \mathbf{w} through the relations

$$\mathbf{M} := J_s \mathbf{F}_s^{-1} \cdot (\mathbf{w} \circ \chi_s), \quad J_s (\operatorname{div} \mathbf{w} \circ \chi_s) = (\operatorname{div}_s \mathbf{M}). \quad (8)$$

By using the definitions from Equations (7) and (8) in (6) the fluid Lagrangian mass balance takes the form

$$\frac{dm_f}{dt} + \operatorname{div}_s \mathbf{M} = 0.$$

3. Power of external forces

In this section, starting from the statement of the power of external forces for a second gradient solid-fluid mixture, we deduce its corresponding reduced form, accounting for the extended Cauchy theorem valid for second gradient continua [Casal 1972; Germain 1973; dell'Isola and Seppecher 1997], and the balance of global momentum. The external power $\mathcal{P}^{\text{ext}}(\mathbf{v}_s, \mathbf{v}_f)$ for a second gradient porous medium can be defined as a continuous linear functional of the velocity fields \mathbf{v}_α ; in particular

$$\begin{aligned} \mathcal{P}^{\text{ext}}(\mathbf{v}_s, \mathbf{v}_f) := & \int_{\mathcal{B}_t} (\mathbf{b}_s \cdot \mathbf{v}_s + \mathbf{b}_f \cdot \mathbf{v}_f) d\mathcal{B}_t + \int_{\partial\mathcal{B}_t} (\mathbf{t}_s \cdot \mathbf{v}_s + \mathbf{t}_f \cdot \mathbf{v}_f) d\mathcal{S}_t \\ & + \int_{\partial\mathcal{B}_t} \left(\boldsymbol{\tau}_s \cdot \frac{\partial \mathbf{v}_s}{\partial \mathbf{n}} + \boldsymbol{\tau}_f \cdot \frac{\partial \mathbf{v}_f}{\partial \mathbf{n}} \right) d\mathcal{S}_t + \sum_{k=1}^m \int_{\mathcal{E}_k} (\mathbf{f}_s^k \cdot \mathbf{v}_s + \mathbf{f}_f^k \cdot \mathbf{v}_f) dl, \quad (9) \end{aligned}$$

where \mathcal{B}_t is the current volume occupied by the porous medium, $\partial\mathcal{B}_t$ its boundary, and m is the number of edges \mathcal{E}_k (if any) of the boundary. In addition, \mathbf{b}_α , \mathbf{t}_α , $\boldsymbol{\tau}_\alpha$, and \mathbf{f}_α^k represent the body force density, the generalized traction force (Cauchy stress vector), the double force vector, and the force per unit line acting on the k -th edge of the boundary, respectively.

The physical meaning of the double force $\boldsymbol{\tau}_\alpha$ can be described in a way similar to that used in different contexts in [Germain 1973] and [dell'Isola and Seppecher 1997]. It can be regarded as the sum of two different contributions, the first of which works on the rate of dilatancy along the outward unit normal \mathbf{n} ($\nabla \mathbf{v}_\alpha : (\mathbf{n} \otimes \mathbf{n})$), and the second being a tangential couple working on the vorticity; this nomenclature is due to Germain [1973].

Let $\boldsymbol{\sigma}_\alpha$ and \mathbb{C}_α be the apparent Cauchy stress and hyperstress tensors per unit volume of the porous material relative to the α -th constituent [Germain 1973; dell'Isola and Seppecher 1997]. The Cauchy theorem can be extended for a second gradient continuum, and in particular for a second gradient porous continuum, in order to specify how the generalized external tractions appearing in (9) can be balanced

by the internal forces when considering any subdomain of the current volume. In particular we have²

$$\mathbf{t}_\alpha = (\boldsymbol{\sigma}_\alpha - \operatorname{div} \mathbb{C}_\alpha) \cdot \mathbf{n} - \operatorname{div}^S (\mathbb{C}_\alpha \cdot \mathbf{n}), \quad \boldsymbol{\tau}_\alpha = (\mathbb{C}_\alpha \cdot \mathbf{n}) \cdot \mathbf{n}, \quad \mathbf{f}_\alpha^k = \llbracket (\mathbb{C}_\alpha \cdot \mathbf{n}) \cdot \mathbf{v} \rrbracket_k, \quad (10)$$

where \mathbf{v} is the binormal unit vector which form a left-handed frame with the unit normal \mathbf{n} and the unit vector being tangent to the k -th edge. We note that, since \mathbf{n} is not continuous through the edge k , the vector \mathbf{v} is also discontinuous when passing from one side of the edge k to the other. It is for this reason that the edge force \mathbf{f}_α^k is balanced by the jump of the internal force $(\mathbb{C}_\alpha \cdot \mathbf{n}) \cdot \mathbf{v}$ through the edge k . Extending classical poromechanics [Biot 1941; Coussy 2004] we now define the overall stress and hyperstress tensors as $\boldsymbol{\sigma} := \boldsymbol{\sigma}_f + \boldsymbol{\sigma}_s$ and $\mathbb{C} := \mathbb{C}_f + \mathbb{C}_s$, so that the momentum balance for the porous medium as a whole reads

$$\operatorname{div} (\boldsymbol{\sigma} - \operatorname{div} \mathbb{C}) + \mathbf{b} = 0, \quad (11)$$

where $\mathbf{b} = \mathbf{b}_s + \mathbf{b}_f$ is the overall body force. Bearing in mind both the extended Cauchy theorem, Equation (10), and the overall balance of momentum, (11), together with the principle of virtual powers ($\mathcal{P}^{\text{ext}} = \mathcal{P}^{\text{def.}}$), (9) leads to the expression for the deformation power

$$\mathcal{P}^{\text{def.}}(\mathbf{v}, \boldsymbol{\omega}) = \int_{\mathcal{B}_t} \left[\boldsymbol{\sigma} : \nabla \mathbf{v} + \operatorname{div} (\boldsymbol{\sigma}_f^T \cdot \boldsymbol{\omega}) + \mathbb{C} : \nabla \nabla \mathbf{v} + \mathbb{C}_f : \nabla \nabla \boldsymbol{\omega} - \operatorname{div} (\operatorname{div} \mathbb{C}_f) \cdot \boldsymbol{\omega} \right] d\mathcal{B}_t. \quad (12)$$

Here and later on $\mathbf{v} := \mathbf{v}_s$ and $\boldsymbol{\omega} := \mathbf{v}_f - \mathbf{v}_s$. Moreover, it must be remarked that (12) is obtained under the hypothesis of absence of volume forces ($\mathbf{b}_\alpha = 0$) so that no inertia is taken into account in our model. We refer to [Coussy 2004] for the complete form of the deformation power in the case of first gradient porous continua. From now on, we also assume that the structure of the hyperstress tensors \mathbb{C}_α ($\alpha = f, s$) takes the particular form

$$\mathbb{C}_\alpha = \mathbf{I} \otimes \mathbf{c}_\alpha, \quad \alpha = f, s, \quad (13)$$

where \mathbf{I} is the second order identity tensor and \mathbf{c}_α is a kind of hyperstress vector related to the α -th constituent. The use of this assumption restricts second gradient external forces just to vector fields $\boldsymbol{\tau}_\alpha$, which only work on the stretching velocity of the α -th constituent; in other words, no contribution to the vorticity on the boundary of \mathcal{B}_t comes from $\boldsymbol{\tau}_\alpha$. The aforementioned hypotheses indeed restrict the second gradient model; however, solid microdilataancies and capillarity effects can be still described by this second gradient model. According to (13) the external power due to second gradient effects, Equations (9) and (10), reduces to

$$\boldsymbol{\tau}_\alpha \cdot \frac{\partial \mathbf{v}_\alpha}{\partial \mathbf{n}} = \{[(\mathbf{I} \otimes \mathbf{c}_\alpha) \cdot \mathbf{n}] \cdot \mathbf{n}\} \cdot \frac{\partial \mathbf{v}_\alpha}{\partial \mathbf{n}} = (\mathbf{c}_\alpha \cdot \mathbf{n}) \mathbf{n} \cdot \frac{\partial \mathbf{v}_\alpha}{\partial \mathbf{n}} = (\mathbf{c}_\alpha \cdot \mathbf{n}) [\nabla \mathbf{v}_\alpha : (\mathbf{n} \otimes \mathbf{n})].$$

3.1. Pull-back operations. Let us now consider the solid reference configuration pull-back of the deformation power; in order to do so, we will introduce the Piola–Kirchhoff like stress and hyperstress tensors for the overall body and for the fluid constituent. Thus, Piola–Kirchhoff stress (\mathbf{S}) and hyperstress ($\boldsymbol{\gamma}$) are defined so that

$$J_s \boldsymbol{\sigma} : \nabla \mathbf{v} =: \mathbf{S} : \frac{d\boldsymbol{\epsilon}}{dt} \implies \mathbf{S} = J_s \mathbf{F}_s^{-1} \cdot \boldsymbol{\sigma} \cdot \mathbf{F}_s^{-T}, \quad (14)$$

²Fixed a basis $(\mathbf{e}_1, \mathbf{e}_2, \mathbf{e}_3)$, where \mathbf{e}_1 and \mathbf{e}_2 span the plane tangent to the surface $\partial \mathcal{B}_t$ at \mathbf{x} , and the surface divergence of a second order tensor field \mathbf{A} is defined as $\operatorname{div}^S \mathbf{A} := \sum_{\alpha=1}^2 (\partial \mathbf{A} / \partial x_\alpha) \mathbf{e}_\alpha$.

$$J_s \mathbb{C} : \nabla \nabla \mathbf{v} =: \boldsymbol{\gamma} \cdot \left[\left(\nabla_s \frac{d\boldsymbol{\varepsilon}}{dt} \right)^T : \mathbf{C}^{-1} - (\nabla_s \mathbf{C})^T : \left(\mathbf{C}^{-1} \cdot \frac{d\boldsymbol{\varepsilon}}{dt} \cdot \mathbf{C}^{-1} \right) \right] \implies \boldsymbol{\gamma} = J_s \mathbf{F}_s^{-1} \cdot \mathbf{c},$$

where $\mathbf{C} = \mathbf{F}_s^T \cdot \mathbf{F}_s$ is the Cauchy–Green strain tensor and \mathbf{c} is the total hyperstress vector defined by $\mathbf{c} = \mathbf{c}_s + \mathbf{c}_f$. Moreover, the fluid ones are $\mathbf{S}_f =: J_s \mathbf{F}_s^{-1} \cdot \boldsymbol{\sigma}_f \cdot \mathbf{F}_s^{-T}$, and $\boldsymbol{\gamma}_f =: J_s \mathbf{F}_s^{-1} \cdot \mathbf{c}_f$. The deformation power $\mathcal{P}^{\text{def.}}$ can be finally written in the Lagrangian form

$$\mathcal{P}_{\mathcal{E}}^{\text{def.}} = \int_{\mathcal{B}_s} \hat{\mathcal{P}}_{\mathcal{E}}^{\text{def.}} d\mathcal{B}_s,$$

where

$$\begin{aligned} \hat{\mathcal{P}}_{\mathcal{E}}^{\text{def.}} = & \left\{ \left[\mathbf{S} - \mathbf{C}^{-1} \cdot ((\nabla_s \mathbf{C}) \cdot \boldsymbol{\gamma}) \cdot \mathbf{C}^{-1} \right] : \frac{d\boldsymbol{\varepsilon}}{dt} + (\mathbf{C}^{-1} \otimes \boldsymbol{\gamma}) : \left(\nabla_s \frac{d\boldsymbol{\varepsilon}}{dt} \right) + \text{div}_s \left(\frac{1}{m_f} \mathbf{S}_f^T \cdot \mathbf{M} \right) \right. \\ & \left. + \nabla_s \left[\text{div}_s \left(\frac{\mathbf{M}}{m_f} \right) \right] \cdot \boldsymbol{\gamma}_f - \frac{\mathbf{M}}{m_f} \cdot \nabla_s (\text{div}_s \boldsymbol{\gamma}_f) + \text{div}_s \left[\left(J_s^{-1} \frac{\mathbf{M}}{m_f} \cdot \nabla_s J_s \right) \boldsymbol{\gamma}_f \right] \right\}. \end{aligned}$$

4. Thermodynamics: deduction of a macroscopic second gradient strain energy potential

In this section, starting from the first and second principles of thermodynamics, we will prove that a suitable macroscopic strain potential can be identified depending both on the solid strain and on the fluid mass density as well as on their Lagrangian gradients. Let e_α be the Eulerian density of internal energy relative to the α -th constituent, and the corresponding energy density of the porous medium is defined as $e := \rho_s e_s + \rho_f e_f$. The first principle of thermodynamics can be written as [Coussy 2004]

$$\frac{d^s}{dt} \int_{\mathcal{B}_t} \rho_s e_s d\mathcal{B}_t + \frac{d^f}{dt} \int_{\mathcal{B}_t} \rho_f e_f d\mathcal{B}_t = \mathcal{P}^{\text{ext}} + \dot{\mathcal{Q}},$$

where $\dot{\mathcal{Q}} := - \int_{\mathcal{B}_t} \mathbf{q} \cdot \mathbf{n} d\mathcal{B}_t$ is the rate of heat externally supplied, and where \mathbf{q} is the heat flow vector. In the Lagrangian form the first principle reads

$$\frac{d}{dt} \int_{\mathcal{B}_s} E d\mathcal{B}_s = \mathcal{P}_{\mathcal{E}}^{\text{def.}} - \int_{\mathcal{B}_s} \text{div}_s (e_f \mathbf{M} + \mathbf{Q}) d\mathcal{B}_s. \quad (15)$$

where we recall that d/dt is the material time derivative associated with the motion of the solid, $E := J_s e$ represents the Lagrangian density of internal energy, and \mathbf{Q} is the Lagrangian heat flux defined by $\mathbf{Q} := J_s \mathbf{F}_s^{-1} \cdot \mathbf{q}$. Starting from Equation (15), the local Lagrangian form of the first principle is naturally given by

$$\frac{dE}{dt} = \hat{\mathcal{P}}_{\mathcal{E}}^{\text{def.}} - \text{div}_s (e_f \mathbf{M} + \mathbf{Q}).$$

Let us now consider the second principle of thermodynamics and introduce the overall Eulerian density of entropy s as $s := \rho_s s_s + \rho_f s_f$. The corresponding Lagrangian entropy is $S := J_s s$, and the Lagrangian form of the second principle can be written as [Coussy 2004]

$$\frac{d}{dt} \int_{\mathcal{B}_s} S d\mathcal{B}_s \geq - \int_{\mathcal{B}_s} \text{div}_s \left(s_f \mathbf{M} + \frac{\mathbf{Q}}{T} \right) d\mathcal{B}_s. \quad (16)$$

If we now introduce the Helmholtz free energy Ψ as $\Psi := E - TS$, Equation (16) can be rewritten in the local form as

$$\frac{dE}{dt} - S \frac{dT}{dt} - \frac{d\Psi}{dt} \geq -T \operatorname{div}_s \left(s_f \mathbf{M} + \frac{\mathbf{Q}}{T} \right).$$

Merging the local form of the first and the second principles, the extended Clausius–Duhem inequality (dissipation inequality) can be deduced. In particular, following Sciarra et al. [2007], we will distinguish different contributions to the dissipation function due to the solid and fluid motion and to thermal effects, respectively (Φ_s , Φ_f , and Φ_{th}).

We now constitutively restrict [Coleman and Noll 1963] the admissible processes only to those ones which guarantee the dissipation inequality to be satisfied, because Φ_s , Φ_f and Φ_{th} are separately non-negative. In particular, the solid dissipation Φ_s reads

$$\begin{aligned} \Phi_s = & \left\{ \mathbf{S} - \mathbf{C}^{-1} \cdot [(\nabla_s \mathbf{C}) \cdot \boldsymbol{\gamma}] \cdot \mathbf{C}^{-1} - [J_s \mathbf{C}^{-1} \cdot \nabla_s (J_s^{-1} m_f)] \otimes \frac{\boldsymbol{\gamma}_f}{m_f} \right\} : \frac{d\boldsymbol{\epsilon}}{dt} + (\mathbf{C}^{-1} \otimes \boldsymbol{\gamma}) : \frac{d}{dt} (\nabla_s \boldsymbol{\epsilon}) \\ & + \left[g_f - \left(1 + \frac{1}{\operatorname{tr} \mathbf{I}} \right) \boldsymbol{\gamma}_f \cdot \nabla_s \left(\frac{1}{m_f} \right) - \frac{J_s^{-1} \boldsymbol{\gamma}_f \cdot \nabla_s J_s}{\operatorname{tr} \mathbf{I} m_f} \right] \cdot \frac{dm_f}{dt} - \frac{\boldsymbol{\gamma}_f}{m_f} \cdot \frac{d}{dt} (\nabla_s m_f) - S \frac{dT}{dt} - \frac{d\Psi}{dt}. \end{aligned} \quad (17)$$

Assuming nondissipative processes occurring in the solid skeleton ($\Phi_s = 0$), Equation (17) allows for regarding the internal energy Ψ as a state function

$$\Psi = \Psi (\boldsymbol{\epsilon}, m_f, \nabla_s \boldsymbol{\epsilon}, \nabla_s m_f, T). \quad (18)$$

From now on we will treat an isothermal problem and therefore assume the energy Ψ does not depend on the temperature field T .

5. Variational deduction of second gradient poroelastic equations

5.1. Basic concepts and first variation of the internal energy. In this section we deduce the governing equations for a second gradient poroelastic continuum by means of a variational procedure. Variational approaches to first gradient mixture models are available in the literature [Bedford and Drumheller 1978; Gavriluk et al. 1998; Gouin and Ruggeri 2003].

In our case, we introduce the varied placement maps χ_s^* and ϕ_f^* for all $\mathbf{X}_s \in \mathcal{B}_s$ as

$$\chi_s^* (\mathbf{X}_s, t) = \chi_s (\mathbf{X}_s, t) + \delta \chi_s (\mathbf{X}_s, t), \quad \phi_f^* (\mathbf{X}_s, t) = \phi_f (\mathbf{X}_s, t) + \delta \phi_f (\mathbf{X}_s, t),$$

where $\delta \chi_s$ and $\delta \phi_f$ represent arbitrary variations of the functions χ_s and ϕ_f , respectively. The physical meaning of the variation $\delta \chi_s$ is well known in continuum mechanics, and stands for the virtual displacement (deformation) of the solid skeleton. The variation $\delta \phi_f$, instead, accounts for the virtual relative displacement of a fluid material particle with respect to a solid one (see Figure 1). Since these variations keep fixed $\mathbf{X}_s \in \mathcal{B}_s$ we label them Lagrangian variations and we note that the symbol δ commutes with the integral over \mathcal{B}_s and with the Lagrangian gradient operator ∇_s .

Following the statements of classical mechanics [Gantmacher 1970; Arnold 1989], the principle of virtual works reads

$$\delta \mathcal{A} = \delta \mathcal{L}^{\text{ext}} + \delta \mathcal{L}^{\text{diss}}, \quad (19)$$

where $\delta\mathcal{A}$ represents the Lagrangian variation of the internal energy of the porous material, defined as

$$\mathcal{A} := \int_{\mathbb{B}_s} \Psi d\mathbb{B}_s,$$

while $\delta\mathcal{L}^{\text{ext}}$ and $\delta\mathcal{L}^{\text{diss}}$ are the virtual works due to the external and dissipative forces acting on the porous system. Because of the aforementioned properties of the Lagrangian variations we can write

$$\delta\mathcal{A} = \delta \int_{\mathbb{B}_s} \Psi d\mathbb{B}_s = \int_{\mathbb{B}_s} \delta\Psi d\mathbb{B}_s. \quad (20)$$

Recalling now [Equation \(18\)](#), [\(20\)](#) implies

$$\delta\mathcal{A} = \int_{\mathbb{B}_s} \left(\frac{\partial\Psi}{\partial\boldsymbol{\epsilon}} : \delta\boldsymbol{\epsilon} + \frac{\partial\Psi}{\partial m_f} \delta m_f + \frac{\partial\Psi}{\partial(\nabla_s\boldsymbol{\epsilon})} : \delta(\nabla_s\boldsymbol{\epsilon}) + \frac{\partial\Psi}{\partial(\nabla_s m_f)} \cdot \delta(\nabla_s m_f) \right) d\mathbb{B}_s. \quad (21)$$

The variations $\delta\boldsymbol{\epsilon}$, δm_f , $\delta(\nabla_s\boldsymbol{\epsilon})$, and $\delta(\nabla_s m_f)$ must now be rewritten in terms of the variations of the primitive kinematical fields χ_s and ϕ_f , bearing in mind that the Lagrangian variation commutes with the operator ∇_s . We show here directly the results obtained in [Appendix A](#), to which we refer for detailed calculations,

$$\delta\boldsymbol{\epsilon} = \frac{1}{2} \left\{ (\nabla_s(\delta\chi_s))^T \cdot \mathbf{F}_s + \mathbf{F}_s^T \cdot \nabla_s(\delta\chi_s) \right\}, \quad (22)$$

and

$$\delta m_f = m_f (\nabla_s \phi_f)^{-T} : \nabla_s(\delta\phi_f). \quad (23)$$

Substituting [\(22\)](#) and [\(23\)](#) into [\(21\)](#), integration by parts (see [Appendix B](#) for details), allows us to write the variation of the second gradient potential \mathcal{A} as

$$\delta\mathcal{A} = \int_{\mathbb{B}_s} A d\mathbb{B}_s + \int_{\partial\mathbb{B}_s} a d\mathcal{S}_s + \sum_{k=1}^m \int_{\mathfrak{C}_k} \alpha dl, \quad (24)$$

where m is the number of edges \mathfrak{C}_k of the body in the reference configuration of the solid and

$$\begin{aligned} A &:= -\operatorname{div}_s \left[\mathbf{F}_s \cdot \left(\frac{\partial\Psi}{\partial\boldsymbol{\epsilon}} - \operatorname{div}_s \left(\frac{\partial\Psi}{\partial(\nabla_s\boldsymbol{\epsilon})} \right) \right) \right] \cdot \delta\chi_s + \left\{ (\nabla_s \phi_f)^{-T} \cdot \left[-m_f \nabla_s \left(\frac{\partial\Psi}{\partial m_f} - \operatorname{div}_s \left(\frac{\partial\Psi}{\partial(\nabla_s m_f)} \right) \right) \right] \right\} \cdot \delta\phi_f, \\ a &:= \left\{ \left[\mathbf{F}_s \cdot \left(\frac{\partial\Psi}{\partial\boldsymbol{\epsilon}} - \operatorname{div}_s \left(\frac{\partial\Psi}{\partial(\nabla_s\boldsymbol{\epsilon})} \right) \right) \right] \cdot \mathbf{n}_s - \operatorname{div}_s^S \left[\mathbf{F}_s \cdot \left(\frac{\partial\Psi}{\partial(\nabla_s\boldsymbol{\epsilon})} \cdot \mathbf{n}_s \right) \right] \right\} \cdot \delta\chi_s \\ &\quad + \left\{ \left[\mathbf{F}_s \cdot \left(\frac{\partial\Psi}{\partial(\nabla_s\boldsymbol{\epsilon})} \cdot \mathbf{n}_s \right) \right] \cdot \mathbf{n}_s \right\} \cdot \frac{\partial(\delta\chi_s)}{\partial\mathbf{n}_s} \\ &\quad + \left\{ (\nabla_s \phi_f)^{-T} \cdot \left[m_f \left(\frac{\partial\Psi}{\partial m_f} - \operatorname{div}_s \left(\frac{\partial\Psi}{\partial(\nabla_s m_f)} \right) \right) \mathbf{n}_s - m_f \nabla_s^S \left(\frac{\partial\Psi}{\partial(\nabla_s m_f)} \cdot \mathbf{n}_s \right) \right] \right\} \cdot \delta\phi_f \\ &\quad + \left[(\nabla_s \phi_f)^{-T} \cdot \left(m_f \frac{\partial\Psi}{\partial(\nabla_s m_f)} \cdot \mathbf{n}_s \right) \mathbf{n}_s \right] \cdot \frac{\partial(\delta\phi_f)}{\partial\mathbf{n}_s}, \\ \alpha &:= \left\{ \left[\mathbf{F}_s \cdot \left(\frac{\partial\Psi}{\partial(\nabla_s\boldsymbol{\epsilon})} \cdot \mathbf{n}_s \right) \right] \cdot \mathbf{v} \right\} \cdot \delta\chi_s + \left[(\nabla_s \phi_f)^{-T} \cdot \left(m_f \frac{\partial\Psi}{\partial(\nabla_s m_f)} \cdot \mathbf{n}_s \right) \mathbf{v} \right] \cdot \delta\phi_f. \end{aligned}$$

5.2. Dissipative governing equations. In order to obtain the equations of motion for a second gradient poroelastic continuum, the form of the external and dissipation virtual works, $\delta\mathcal{L}^{\text{ext}}$ and $\delta\mathcal{L}^{\text{diss}}$, formally introduced in Equation (19), must be stated. The virtual dissipation $\delta\mathcal{L}^{\text{diss}}$ will account for the classical Darcy effects and for the so called Brinkman-like contributions [Brinkman 1947]. We define the dissipation $\delta\mathcal{L}^{\text{diss}}$ in the Eulerian configuration as

$$\begin{aligned} \delta\mathcal{L}^{\text{diss}} := & - \int_{\mathbb{B}_t} \left\{ \mathbb{D} (\mathbf{v}_f - \mathbf{v}_s) \cdot [(\delta\chi_f \circ \phi_f - \delta\chi_s) \circ \chi_s^{-1}] \right\} d\mathbb{B}_t \\ & - \int_{\mathbb{B}_t} \left\{ [\mathbb{A} \cdot \nabla (\mathbf{v}_f - \mathbf{v}_s)] : \nabla [(\delta\chi_f \circ \phi_f - \delta\chi_s) \circ \chi_s^{-1}] \right\} d\mathbb{B}_t, \end{aligned} \quad (25)$$

where \mathbb{D} is the symmetric, definite positive Darcy tensor and \mathbb{A} is a suitably defined symmetric, definite positive second gradient Darcy-like tensor.

Moreover, from now on, we assume the following Eulerian expression for the external work $\delta\mathcal{L}^{\text{ext}}$,

$$\delta\mathcal{L}^{\text{ext}} := - \int_{\partial\mathbb{B}_t} \left\{ \mathbf{t} \cdot (\delta\chi_s \circ \chi_s^{-1}) + \mathbf{t}_f \cdot [(\delta\chi_f \circ \phi_f - \delta\chi_s) \circ \chi_s^{-1}] \right\} d\mathcal{S}_t. \quad (26)$$

We restrict our attention to \mathbf{t} and \mathbf{t}_f , defined as

$$\mathbf{t} := p^{\text{ext}} \mathbf{n}, \quad \mathbf{t}_f := \rho_f \mu^{\text{ext}} \mathbf{n}, \quad (27)$$

where p^{ext} is the overall external pressure applied on $\partial\mathbb{B}_t$, and μ^{ext} is the chemical potential of the fluid outside the porous system. By comparison of Equation (26) with (9), we are assuming vanishing double forces and edge forces on the external boundary, as well as vanishing bulk actions. Equation (26), the expression for the external work, states that the external force \mathbf{t} works only on the displacement of the solid skeleton ($\delta\chi_s$), while μ^{ext} works on the fluid mass virtual relative displacement $\rho_f (\delta\chi_f - \delta\chi_s)$. We note that if μ^{ext} is spatially constant then

$$\int_{\partial\mathbb{B}_t} \rho_f \mu^{\text{ext}} [(\delta\chi_f \circ \phi_f - \delta\chi_s) \circ \chi_s^{-1}] d\mathcal{S}_t = \int_{\partial\mathbb{B}_s} (\mu^{\text{ext}} \circ \chi_s) \delta m_f d\mathcal{S}_s,$$

that is, μ^{ext} works on the fluid mass which leaves (or enters) the solid skeleton (see Appendix C for details). Equation (26) for $\delta\mathcal{L}^{\text{ext}}$ can be rewritten (see Appendix C) on the reference configuration of the solid as

$$\delta\mathcal{L}^{\text{ext}} = \int_{\partial\mathbb{B}_s} \left\{ - (p^{\text{ext}} J_s \mathbf{F}_s^{-T} \cdot \mathbf{n}_s) \cdot \delta\chi_s + \left[\mu^{\text{ext}} m_f (\nabla_s \phi_f)^{-T} \cdot \mathbf{n}_s \right] \cdot \delta\phi_f \right\} d\mathcal{S}_s. \quad (28)$$

Finally, (25) for $\delta\mathcal{L}^{\text{diss}}$ (see Appendix C) assumes the Lagrangian form

$$\begin{aligned} \delta\mathcal{L}^{\text{diss}} = & \int_{\mathbb{B}_s} \left\{ [(\nabla_s \phi_f)^{-T} \cdot (J_s D\mathbf{F}_s^T \cdot (\mathcal{V}_f \circ \phi_f - \mathcal{V}_s))] \cdot \delta\phi_f \right\} d\mathbb{B}_s \\ & - \int_{\mathbb{B}_s} \left\{ (\nabla_s \phi_f)^{-T} \cdot [\mathbf{F}_s^T \cdot \text{div}_s (J_s \mathbb{A} \cdot \nabla_s (\mathcal{V}_f \circ \phi_f - \mathcal{V}_s) \cdot (\mathbf{F}_s^T \cdot \mathbf{F}_s)^{-1})] \right\} \cdot \delta\phi_f d\mathbb{B}_s \\ & + \int_{\partial\mathbb{B}_s} \left\{ [(\nabla_s \phi_f)^{-T} \cdot (J_s \mathbf{F}_s^T \cdot \mathbb{A} \cdot \nabla_s (\mathcal{V}_f \circ \phi_f - \mathcal{V}_s) \cdot (\mathbf{F}_s^T \cdot \mathbf{F}_s)^{-1})] \cdot \mathbf{n}_s \right\} \cdot \delta\phi_f d\mathcal{S}_s. \end{aligned} \quad (29)$$

Starting from the principle of virtual works, (19), and using (24), (29), and (28) for $\delta\mathcal{A}$, $\delta\mathcal{L}^{\text{diss}}$, and $\delta\mathcal{L}^{\text{ext}}$, respectively, we can write the local equations of motion on \mathcal{B}_s as

$$-\operatorname{div}_s \left[\mathbf{F}_s \cdot \left(\frac{\partial \Psi}{\partial \boldsymbol{\varepsilon}} - \operatorname{div}_s \left(\frac{\partial \Psi}{\partial (\nabla_s \boldsymbol{\varepsilon})} \right) \right) \right] = 0, \quad (30)$$

and

$$\begin{aligned} (\nabla_s \phi_f)^{-T} \cdot \left[-m_f \nabla_s \left(\frac{\partial \Psi}{\partial m_f} - \operatorname{div}_s \left(\frac{\partial \Psi}{\partial (\nabla_s m_f)} \right) \right) - J_s D \mathbf{F}_s^T \cdot (\mathcal{V}_f \circ \phi_f - \mathcal{V}_s) \right] \\ + (\nabla_s \phi_f)^{-T} \cdot \left[\mathbf{F}_s^T \cdot \operatorname{div}_s (J_s \mathbb{A} \cdot \nabla_s (\mathcal{V}_f \circ \phi_f - \mathcal{V}_s) \cdot (\mathbf{F}_s^T \cdot \mathbf{F}_s)^{-1}) \right] = 0. \end{aligned} \quad (31)$$

Analogously the boundary conditions on $\partial \mathcal{B}_s$ read

$$\left[\mathbf{F}_s \cdot \left(\frac{\partial \Psi}{\partial \boldsymbol{\varepsilon}} - \operatorname{div}_s \left(\frac{\partial \Psi}{\partial (\nabla_s \boldsymbol{\varepsilon})} \right) \right) \right] \cdot \mathbf{n}_s - \operatorname{div}_s^S \left[\mathbf{F}_s \cdot \left(\frac{\partial \Psi}{\partial (\nabla_s \boldsymbol{\varepsilon})} \cdot \mathbf{n}_s \right) \right] = -J_s \rho^{\text{ext}} \mathbf{F}_s^{-T} \cdot \mathbf{n}_s$$

$$\begin{aligned} (\nabla_s \phi_f)^{-T} \cdot \left[m_f \left(\frac{\partial \Psi}{\partial m_f} - \operatorname{div}_s \left(\frac{\partial \Psi}{\partial (\nabla_s m_f)} \right) \right) \mathbf{n}_s - m_f \nabla_s^S \left(\frac{\partial \Psi}{\partial (\nabla_s m_f)} \cdot \mathbf{n}_s \right) \right] + \\ - (\nabla_s \phi_f)^{-T} \cdot \left\{ \left[J_s \mathbf{F}_s^T \cdot \mathbb{A} \cdot \nabla_s (\mathcal{V}_f \circ \phi_f - \mathcal{V}_s) \cdot (\mathbf{F}_s^T \cdot \mathbf{F}_s)^{-1} \right] \cdot \mathbf{n}_s \right\} = (\nabla_s \phi_f)^{-T} \cdot (m_f \mu^{\text{ext}} \mathbf{n}_s), \end{aligned} \quad (32)$$

$$\left[\mathbf{F}_s \cdot \left(\frac{\partial \Psi}{\partial (\nabla_s \boldsymbol{\varepsilon})} \cdot \mathbf{n}_s \right) \right] \cdot \mathbf{n}_s = 0,$$

$$(\nabla_s \phi_f)^{-T} \cdot \left[\left(m_f \frac{\partial \Psi}{\partial (\nabla_s m_f)} \cdot \mathbf{n}_s \right) \mathbf{n}_s \right] = 0.$$

Finally, on the edges \mathfrak{E}_k of the boundary (if any) the following conditions hold true:

$$\left[\mathbf{F}_s \cdot \left(\frac{\partial \Psi}{\partial (\nabla_s \boldsymbol{\varepsilon})} \cdot \mathbf{n}_s \right) \right] \cdot \mathbf{v} = \mathbf{0}, \quad (\nabla_s \phi_f)^{-T} \cdot \left[\left(m_f \frac{\partial \Psi}{\partial (\nabla_s m_f)} \cdot \mathbf{n}_s \right) \mathbf{v} \right] = \mathbf{0}. \quad (33)$$

The Darcy and Brinkman dissipations appearing in Equations (31) and (32) can be rewritten in terms of the Lagrangian vector \mathbf{M} , previously defined as $\mathbf{M} = m_f \mathbf{F}_s^{-1} \cdot (\mathbf{v}_f - \mathbf{v}_s)$. In fact, after some straightforward calculations, it can be proven that

$$\nabla (\mathbf{v}_f - \mathbf{v}_s) = \frac{1}{m_f} \left\{ [(\nabla_s \mathbf{F}_s)^T \cdot \mathbf{M}]^T + \mathbf{F}_s \cdot \nabla_s \mathbf{M} \right\} + \mathbf{F}_s \cdot \left[\mathbf{M} \otimes \nabla_s \left(\frac{1}{m_f} \right) \right].$$

We now show that (30) is in agreement with the classical second gradient balance law for the total momentum [Germain 1973; dell'Isola and Seppecher 1997]. In order to do so, considering assumption (13), it can be proven that the constitutive relations for \mathbf{S} and $\boldsymbol{\gamma}$ (see Equations (14))

$$\frac{\partial \Psi}{\partial \boldsymbol{\varepsilon}} = \mathbf{S} - \mathbf{C}^{-1} \cdot ((\nabla_s \mathbf{C}) \cdot \boldsymbol{\gamma}) \cdot \mathbf{C}^{-1}, \quad \frac{\partial \Psi}{\partial (\nabla_s \boldsymbol{\varepsilon})} = \mathbf{C}^{-1} \otimes \boldsymbol{\gamma}, \quad (34)$$

imply that (30) can be regarded as the solid-Lagrangian pull-back of (11). In other words,

$$J_s \operatorname{div} (\boldsymbol{\sigma} - \operatorname{div} \mathbb{C}) = \operatorname{div}_s \left\{ \mathbf{F}_s \cdot [\mathbf{S} - \mathbf{C}^{-1} \cdot ((\nabla_s \mathbf{C}) \cdot \boldsymbol{\gamma}) \cdot \mathbf{C}^{-1} - \mathbf{F}_s \cdot \operatorname{div}_s (\mathbf{C}^{-1} \otimes \boldsymbol{\gamma})] \right\} = 0.$$

6. Concluding remarks

In this paper a purely macroscopic second gradient theory of poromechanics is presented, extending classical Biot poromechanics [Biot 1941; Coussy 2004]. Following a standard procedure, sketched in [Coussy et al. 1998], we determine a suitable representation formula of the deformation power, (12), for a second gradient porous medium, assuming the forces acting on solid skeleton to be balanced (using the generalized second gradient balance of momentum in the current domain and the generalized second gradient Cauchy theorem on its boundary) and the power of external forces to be that of two superposed second gradient continua [Germain 1973]. The principles of thermodynamics, together with the aforementioned representation of the deformation power, allow for deducing the existence of a suitable overall strain energy potential Ψ depending on the solid strain tensor $\boldsymbol{\epsilon}$ and the solid Lagrangian fluid mass density m_f , as well as on their Lagrangian gradients.

The Euler–Lagrange equations associated with the energy density Ψ are the governing equations of the problem. In particular, Lagrangian variations of the placement maps χ_s and ϕ_f are considered. It is worth noting that the governing equations associated with the solid Lagrangian displacement $\delta\chi_s$ (when $\delta\phi_f = 0$) represents the balance of total momentum and therefore allows for the constitutive characterization of the overall stress and hyperstress tensors. This is a characteristic feature of the classical Biot model [Baek and Srinivasa 2004], which is completely recovered in this more general framework. On the other hand, the governing equation associated with the fluid placement map $\delta\phi_f$ represents the balance of momentum relative to the pure fluid, which, in this case, is a generalization of the classical Darcy law.

In part II, an application to the classical consolidation problem will show how the present model improve the classical ones. It is well known that second gradient theories are capable to detect boundary layer effects in the vicinity of interfaces; this is indeed what we will observe in the case of consolidation. In particular, a kind of fluid mass density increment in the neighborhood of the impermeable wall will be observed for the first time in a one dimensional problem [Mandel 1953; Cryer 1963].

Appendix A: Basic variations

We show here how to derive the variations $\delta\boldsymbol{\epsilon}$ and δm_f in terms of the kinematical variations $\delta\chi_s$ and $\delta\phi_f$. Equation (3) for the Green–Lagrange strain tensor implies

$$\delta\boldsymbol{\epsilon} = \frac{1}{2} \left[(\delta_s \mathbf{F}_s^T) \cdot \mathbf{F}_s + \mathbf{F}_s^T \cdot \delta_s \mathbf{F}_s \right],$$

where by definition $\mathbf{F}_s := \nabla_s \chi_s$; the expression (22) for $\delta\boldsymbol{\epsilon}$ is easily derived. As far as the variation δm_f is concerned, recalling definition (7) for m_f we can write

$$m_f = J_s J_f^{-1} \rho_f^0, \tag{A.1}$$

where ρ_f^0 is the fluid density in the reference configuration of the fluid. Since by definition

$$J_f := \det(\nabla_f \chi_f) \quad \text{and} \quad \phi_f := \chi_f^{-1} \circ \chi_s,$$

we have

$$J_f = \det \left[\nabla_f \left(\chi_s \circ \phi_f^{-1} \right) \right] = \det \left(\nabla_s \chi_s \cdot \nabla_f \phi_f^{-1} \right) = J_s \det \left(\nabla_s \phi_f \right)^{-1},$$

where for the sake of simplicity we neglect the dependence of the considered fields on the reference places. Equation (A.1) thus reads

$$m_f = \rho_f^0 \det \left(\nabla_s \phi_f \right). \quad (\text{A.2})$$

By derivation rule of the determinant and assuming $\rho_f^0 = \text{constant}$, we get

$$\delta m_f = \rho_f^0 \delta \left[\det \left(\nabla_s \phi_f \right) \right] = \rho_f^0 \det \left(\nabla_s \phi_f \right) \text{tr} \left[\left(\nabla_s \phi_f \right)^{-1} \cdot \delta \left(\nabla_s \phi_f \right) \right] = m_f \left[\left(\nabla_s \phi_f \right)^{-T} : \nabla_s \left(\delta \phi_f \right) \right].$$

Appendix B: Variation of the internal energy

The procedure to calculate the variation $\delta \mathcal{A}$ of the internal energy will be here shown in detail.

According to Equations (21)–(23) and recalling that $\partial \Psi / \partial \boldsymbol{\varepsilon}$ is a symmetric second order tensor, while $\partial \Psi / \partial (\nabla_s \boldsymbol{\varepsilon})$ is a third order tensor symmetric with respect to its first two indices, we can write

$$\delta \mathcal{A} = \int_{\mathcal{B}_s} \left(A^1 + A_s^2 + A_f^2 \right) d\mathcal{B}_s, \quad (\text{B.1})$$

where

$$\begin{aligned} A^1 &:= \frac{\partial \Psi}{\partial \boldsymbol{\varepsilon}} : \left(\mathbf{F}_s^T \cdot \nabla_s \left(\delta \chi_s \right) \right) + m_f \frac{\partial \Psi}{\partial m_f} \left(\nabla_s \phi_f \right)^{-T} : \nabla_s \left(\delta \phi_f \right), \\ A_s^2 &:= \frac{\partial \Psi}{\partial (\nabla_s \boldsymbol{\varepsilon})} : \nabla_s \left(\mathbf{F}_s^T \cdot \nabla_s \left(\delta \chi_s \right) \right), \\ A_f^2 &:= \frac{\partial \Psi}{\partial (\nabla_s m_f)} \cdot \nabla_s \left(m_f \left(\nabla_s \phi_f \right)^{-T} : \nabla_s \left(\delta \phi_f \right) \right), \end{aligned}$$

account for the first gradient contribution to $\delta \mathcal{A}$ and for the solid and fluid second gradient contributions respectively.

The following identities are recalled in order to perform integrations by parts in (B.1); let λ , \mathbf{a} , \mathbf{A} , and \mathbb{A} be scalar, first, second, and third order tensor fields respectively. (Here $\nabla^S \mathbf{a}$ indicates the surface gradient operator of a vector field \mathbf{a} defined— analogously to div_s^S — as $\nabla^S \mathbf{a} = \partial \mathbf{a} / \partial x_\alpha \otimes \mathbf{e}_\alpha$, $\alpha = 1, 2$, where \mathbf{e}_α belong to the tangent plane.) Then,

$$\begin{aligned} \text{div} \left(\mathbf{A}^T \cdot \mathbf{a} \right) &= \mathbf{A} : \nabla \mathbf{a} + \mathbf{a} \cdot \text{div} \mathbf{A}, \quad \text{div} \left(\lambda \mathbf{A} \right) = \mathbf{A} \cdot \nabla \lambda + \lambda \text{div} \mathbf{A}, \quad \text{div} \left(\lambda \mathbf{a} \right) = \mathbf{a} \cdot \nabla \lambda + \lambda \text{div} \mathbf{a}, \\ \text{div} \left(\mathbb{A}^T : \mathbf{A} \right) &= \mathbf{A} : \text{div} \mathbb{A} + \left(\nabla \mathbf{A} \right) : \mathbb{A}, \quad \nabla \mathbf{a} = \nabla^S \mathbf{a} + \frac{\partial \mathbf{a}}{\partial \mathbf{n}} \otimes \mathbf{n}, \end{aligned}$$

where transposition for third order tensors is defined so as $\mathbb{A}^T := a_{ijk} \mathbf{e}_k \otimes \mathbf{e}_i \otimes \mathbf{e}_j$ if $\mathbb{A} = a_{ijk} \mathbf{e}_i \otimes \mathbf{e}_j \otimes \mathbf{e}_k$. Moreover, given second order tensors \mathbf{A} , \mathbf{B} , \mathbf{C} , third and first order tensors \mathbb{A} and \mathbf{a} the following identities are satisfied:

$$\mathbf{A} : (\mathbf{B} \cdot \mathbf{C}) = (\mathbf{B}^T \cdot \mathbf{A}) : \mathbf{C} = (\mathbf{A} \cdot \mathbf{C}^T) : \mathbf{B}, \quad (\mathbb{A}^T : \mathbf{A}) \cdot \mathbf{a} = \mathbf{A} : (\mathbb{A} \cdot \mathbf{a}).$$

Finally, if $\varphi = \chi_s$ or $\varphi = \phi_f$, the identity holds true that

$$0 = \operatorname{div}_s [\det(\nabla_s \varphi) (\nabla_s \varphi)^{-T}] = \det(\nabla_s \varphi) \operatorname{div}_s [(\nabla_s \varphi)^{-T}] + (\nabla_s \varphi)^{-T} \cdot \nabla_s [\det(\nabla_s \varphi)]. \quad (\text{B.2})$$

We underline that this equality holds unchanged for the surface divergence operator div_s^S . For the sake of simplicity, we will perform integration by parts for the first and second gradient terms appearing in (B.1) separately. Integration by parts of the first gradient term, recalling Equation (A.2) for m_f and using Equation (B.2) for ϕ_f , leads to

$$\begin{aligned} \int_{\mathcal{B}_s} A^1 d\mathcal{B}_s &= - \int_{\mathcal{B}_s} \operatorname{div}_s \left(\mathbf{F}_s \cdot \frac{\partial \Psi}{\partial \boldsymbol{\varepsilon}} \right) \cdot \delta \chi_s d\mathcal{B}_s + \int_{\partial \mathcal{B}_s} \left[\left(\mathbf{F}_s \cdot \frac{\partial \Psi}{\partial \boldsymbol{\varepsilon}} \right) \cdot \mathbf{n}_s \right] \cdot \delta \chi_s d\mathcal{G}_s \\ &- \int_{\mathcal{B}_s} \left\{ (\nabla_s \phi_f)^{-T} \cdot \left[m_f \nabla_s \left(\frac{\partial \Psi}{\partial m_f} \right) \right] \right\} \cdot \delta \phi_f d\mathcal{B}_s + \int_{\partial \mathcal{B}_s} \left[(\nabla_s \phi_f)^{-T} \cdot \left(m_f \frac{\partial \Psi}{\partial m_f} \mathbf{n}_s \right) \right] \cdot \delta \phi_f d\mathcal{G}_s. \end{aligned} \quad (\text{B.3})$$

Integrating by parts the solid second gradient term we get

$$\begin{aligned} \int_{\mathcal{B}_s} A_s^2 d\mathcal{B}_s &= - \int_{\mathcal{B}_s} \nabla_s (\delta \chi_s) : \left[\mathbf{F}_s \cdot \operatorname{div}_s \left(\frac{\partial \Psi}{\partial (\nabla_s \boldsymbol{\varepsilon})} \right) \right] d\mathcal{B}_s + \int_{\partial \mathcal{B}_s} \nabla_s (\delta \chi_s) : \left[\mathbf{F}_s \cdot \left(\frac{\partial \Psi}{\partial (\nabla_s \boldsymbol{\varepsilon})} \cdot \mathbf{n}_s \right) \right] d\mathcal{G}_s \\ &= - \int_{\partial \mathcal{B}_s} \left[\left(\mathbf{F}_s \cdot \operatorname{div}_s \left(\frac{\partial \Psi}{\partial (\nabla_s \boldsymbol{\varepsilon})} \right) \right) \cdot \mathbf{n}_s \right] \cdot \delta \chi_s d\mathcal{G}_s + \int_{\mathcal{B}_s} \operatorname{div}_s \left[\mathbf{F}_s \cdot \operatorname{div}_s \left(\frac{\partial \Psi}{\partial (\nabla_s \boldsymbol{\varepsilon})} \right) \right] \cdot \delta \chi_s d\mathcal{B}_s \\ &\quad + \int_{\partial \mathcal{B}_s} \left(\nabla_s^S (\delta \chi_s) + \frac{\partial (\delta \chi_s)}{\partial \mathbf{n}_s} \otimes \mathbf{n}_s \right) : \left[\mathbf{F}_s \cdot \left(\frac{\partial \Psi}{\partial (\nabla_s \boldsymbol{\varepsilon})} \cdot \mathbf{n}_s \right) \right] d\mathcal{G}_s. \end{aligned}$$

Performing a further surface integration by parts we finally get

$$\begin{aligned} \int_{\mathcal{B}_s} A_s^2 d\mathcal{B}_s &= - \int_{\partial \mathcal{B}_s} \left[\left(\mathbf{F}_s \cdot \operatorname{div}_s \left(\frac{\partial \Psi}{\partial (\nabla_s \boldsymbol{\varepsilon})} \right) \right) \cdot \mathbf{n}_s \right] \cdot \delta \chi_s d\mathcal{G}_s + \int_{\mathcal{B}_s} \operatorname{div}_s \left[\mathbf{F}_s \cdot \operatorname{div}_s \left(\frac{\partial \Psi}{\partial (\nabla_s \boldsymbol{\varepsilon})} \right) \right] \cdot \delta \chi_s d\mathcal{B}_s \\ &- \int_{\partial \mathcal{B}_s} \operatorname{div}_s^S \left(\mathbf{F}_s \cdot \left(\frac{\partial \Psi}{\partial (\nabla_s \boldsymbol{\varepsilon})} \cdot \mathbf{n}_s \right) \right) \cdot \delta \chi_s d\mathcal{G}_s + \int_{\partial \mathcal{B}_s} \left[\left(\mathbf{F}_s \cdot \left(\frac{\partial \Psi}{\partial (\nabla_s \boldsymbol{\varepsilon})} \cdot \mathbf{n}_s \right) \right) \cdot \mathbf{n}_s \right] \cdot \frac{\partial (\delta \chi_s)}{\partial \mathbf{n}_s} d\mathcal{G}_s \\ &\quad + \sum_{k=1}^n \int_{\mathfrak{E}_k} \left[\left(\mathbf{F}_s \cdot \left(\frac{\partial \Psi}{\partial (\nabla_s \boldsymbol{\varepsilon})} \cdot \mathbf{n}_s \right) \right) \cdot \mathbf{v} \right] \cdot \delta \chi_s dl. \end{aligned} \quad (\text{B.4})$$

We finally rewrite the fluid second gradient term as

$$\begin{aligned} \int_{\mathcal{B}_s} A_f^2 d\mathcal{B}_s &= \int_{\mathcal{B}_s} \frac{\partial \Psi}{\partial (\nabla_s m_f)} \cdot \nabla_s \left[m_f \operatorname{div}_s \left((\nabla_s \phi_f)^{-1} \cdot \delta \phi_f \right) \right] d\mathcal{B}_s \\ &- \int_{\mathcal{B}_s} \frac{\partial \Psi}{\partial (\nabla_s m_f)} \cdot \nabla_s \left[m_f \operatorname{div}_s \left((\nabla_s \phi_f)^{-T} \right) \cdot \delta \phi_f \right] d\mathcal{B}_s; \end{aligned}$$

recalling Equation (A.2) for m_f , using Equation (B.2) for ϕ_f and rearranging, we have

$$\begin{aligned} \int_{\mathcal{B}_s} A_f^2 d\mathcal{B}_s &= \int_{\mathcal{B}_s} \frac{\partial \Psi}{\partial (\nabla_s m_f)} \cdot \nabla_s \left[m_f \operatorname{div}_s \left((\nabla_s \phi_f)^{-1} \cdot \delta \phi_f \right) \right] d\mathcal{B}_s \\ + \int_{\mathcal{B}_s} \frac{\partial \Psi}{\partial (\nabla_s m_f)} \cdot \nabla_s \left[\left((\nabla_s \phi_f)^{-1} \cdot \delta \phi_f \right) \cdot \nabla_s m_f \right] d\mathcal{B}_s &= \int_{\mathcal{B}_s} \frac{\partial \Psi}{\partial (\nabla_s m_f)} \cdot \nabla_s \left[\operatorname{div}_s \left(m_f (\nabla_s \phi_f)^{-1} \cdot \delta \phi_f \right) \right] d\mathcal{B}_s. \end{aligned}$$

Integrating by parts we get

$$\int_{\mathcal{B}_s} A_f^2 d\mathcal{B}_s = \int_{\partial \mathcal{B}_s} \operatorname{div}_s \left(m_f (\nabla_s \phi_f)^{-1} \delta \phi_f \right) \frac{\partial \Psi}{\partial (\nabla_s m_f)} \cdot \mathbf{n}_s d\mathcal{G}_s - \int_{\mathcal{B}_s} \operatorname{div}_s \left(m_f (\nabla_s \phi_f)^{-1} \delta \phi_f \right) \operatorname{div}_s \left(\frac{\partial \Psi}{\partial (\nabla_s m_f)} \right) d\mathcal{B}_s,$$

and, integrating again,

$$\begin{aligned} \int_{\mathcal{B}_s} A_f^2 d\mathcal{B}_s &= \int_{\partial \mathcal{B}_s} m_f \operatorname{div}_s \left((\nabla_s \phi_f)^{-1} \cdot \delta \phi_f \right) \left(\frac{\partial \Psi}{\partial (\nabla_s m_f)} \cdot \mathbf{n}_s \right) d\mathcal{G}_s \\ + \int_{\partial \mathcal{B}_s} \left(\nabla_s m_f \cdot \left((\nabla_s \phi_f)^{-1} \cdot \delta \phi_f \right) \right) \left(\frac{\partial \Psi}{\partial (\nabla_s m_f)} \cdot \mathbf{n}_s \right) d\mathcal{G}_s &- \int_{\partial \mathcal{B}_s} \left[m_f \operatorname{div}_s \left(\frac{\partial \Psi}{\partial (\nabla_s m_f)} \right) (\nabla_s \phi_f)^{-T} \cdot \mathbf{n}_s \right] \cdot \delta \phi_f d\mathcal{G}_s \\ &+ \int_{\mathcal{B}_s} m_f \left[(\nabla_s \phi_f)^{-T} \cdot \nabla_s \left(\operatorname{div}_s \left(\frac{\partial \Psi}{\partial (\nabla_s m_f)} \right) \right) \right] \cdot \delta \phi_f d\mathcal{B}_s. \end{aligned}$$

Recalling again Equation (A.2) for m_f , using (B.2) for ϕ_f and rearranging we get

$$\begin{aligned} \int_{\mathcal{B}_s} A_f^2 d\mathcal{B}_s &= \int_{\partial \mathcal{B}_s} \nabla_s (\delta \phi_f) : \left[m_f \left(\frac{\partial \Psi}{\partial (\nabla_s m_f)} \cdot \mathbf{n}_s \right) (\nabla_s \phi_f)^{-T} \right] d\mathcal{G}_s \\ &- \int_{\partial \mathcal{B}_s} \left[m_f \operatorname{div}_s \left(\frac{\partial \Psi}{\partial (\nabla_s m_f)} \right) (\nabla_s \phi_f)^{-T} \cdot \mathbf{n}_s \right] \cdot \delta \phi_f d\mathcal{G}_s \\ &+ \int_{\mathcal{B}_s} m_f \left[(\nabla_s \phi_f)^{-T} \cdot \nabla_s \left(\operatorname{div}_s \left(\frac{\partial \Psi}{\partial (\nabla_s m_f)} \right) \right) \right] \cdot \delta \phi_f d\mathcal{B}_s. \end{aligned}$$

Decomposing $\nabla_s (\delta\phi_f)$ as $\nabla_s (\delta\phi_f) = \nabla_s^S (\delta\phi_f) + (\partial (\delta\phi_f) / \partial \mathbf{n}_s) \otimes \mathbf{n}_s$, performing a last surface integration by parts and using (B.2) for the surface divergence operator we finally get

$$\begin{aligned} \int_{\mathcal{B}_s} A_f^2 d\mathcal{B}_s &= \int_{\partial\mathcal{B}_s} \left\{ (\nabla_s \phi_f)^{-T} \cdot \left[m_f \left(\frac{\partial \Psi}{\partial (\nabla_s m_f)} \cdot \mathbf{n}_s \right) \mathbf{n}_s \right] \right\} \cdot \frac{\partial (\delta\phi_f)}{\partial \mathbf{n}_s} d\mathcal{G}_s + \\ &- \int_{\partial\mathcal{B}_s} \left\{ (\nabla_s \phi_f)^{-T} \cdot \left[m_f \nabla_s^S \left(\frac{\partial \Psi}{\partial (\nabla_s m_f)} \cdot \mathbf{n}_s \right) \right] \right\} \cdot \delta\phi_f d\mathcal{G}_s + \sum_{k=1}^n \int_{\mathcal{C}_k} \left\{ (\nabla_s \phi_f)^{-T} \cdot \left[m_f \left(\frac{\partial \Psi}{\partial (\nabla_s m_f)} \cdot \mathbf{n}_s \right) \mathbf{v} \right] \right\} \cdot \delta\phi_f dl \\ &\quad - \int_{\partial\mathcal{B}_s} \left\{ (\nabla_s \phi_f)^{-T} \cdot \left[m_f \operatorname{div}_s \left(\frac{\partial \Psi}{\partial (\nabla_s m_f)} \right) \mathbf{n}_s \right] \right\} \cdot \delta\phi_f d\mathcal{G}_s \\ &\quad + \int_{\mathcal{B}_s} \left\{ (\nabla_s \phi_f)^{-T} \cdot \left[m_f \nabla_s \left(\operatorname{div}_s \left(\frac{\partial \Psi}{\partial (\nabla_s m_f)} \right) \right) \right] \right\} \cdot \delta\phi_f d\mathcal{B}_s. \quad (\text{B.5}) \end{aligned}$$

Substituting (B.3), (B.4), and (B.5) into (B.1), the variation of the internal energy given in (24) has been recovered.

Appendix C: External and dissipation works

The dissipation and external works have been defined in (25) and (26) on the Eulerian configuration of the system in terms of $\delta\chi_s$ and $\delta\chi_f \circ \phi_f$. These works must then be rewritten in terms of the independent variations $\delta\chi_s$ and $\delta\phi_f$. In order to do so, the relationship between $(\delta\chi_f \circ \phi_f - \delta\chi_s)$ and $\delta\phi_f$ must be established. We know by definition that $\chi_f \circ \phi_f = \chi_s$, so that $\delta(\chi_f \circ \phi_f) = \delta\chi_s$. Moreover, by differentiation rule for composite functions we have $\delta\chi_s = \delta(\chi_f \circ \phi_f) = \delta\chi_f \circ \phi_f + [(\nabla_f \chi_f) \circ \phi_f] \cdot \delta\phi_f$. But since $\chi_f = \chi_s \circ \phi_f^{-1}$, we get

$$\nabla_f \chi_f \circ \phi_f = \nabla_s \chi_s \cdot \left[\nabla_f (\phi_f^{-1}) \circ \phi_f \right] = \nabla_s \chi_s \cdot (\nabla_s \phi_f)^{-1},$$

so that $\delta\chi_s = \delta\chi_f \circ \phi_f + \nabla_s \chi_s \cdot (\nabla_s \phi_f)^{-1} \cdot \delta\phi_f$, or,

$$\delta\chi_f \circ \phi_f - \delta\chi_s = -\mathbf{F}_s \cdot (\nabla_s \phi_f)^{-1} \cdot \delta\phi_f. \quad (\text{C.1})$$

We now prove that the external work due to the force \mathbf{t}_f appearing in Equation (26) and prescribed by (27) represents the external work $\mathcal{L}_f^{\text{ext}}$ done to change the fluid mass inside the porous system when the external chemical potential μ^{ext} is assumed to be constant. We define this work as

$$\mathcal{L}_f^{\text{ext}} = \int_{\mathcal{B}_s} (\mu^{\text{ext}} \circ \chi_s) \delta m_f d\mathcal{B}_s;$$

according to (23) and neglecting composition operations we can write

$$\mathcal{L}_f^{\text{ext}} = \int_{\mathcal{B}_s} \mu^{\text{ext}} m_f (\nabla_s \phi_f)^{-T} : \nabla_s (\delta\phi_f) d\mathcal{B}_s,$$

which, integrating by parts, recalling (A.2) for m_f , and assuming μ^{ext} constant, gives

$$\mathcal{L}_f^{\text{ext}} = \int_{\partial\mathcal{B}_s} \left\{ \left[\mu^{\text{ext}} m_f (\nabla_s \phi_f)^{-T} \cdot \mathbf{n}_s \right] \cdot \delta \phi_f \right\} d\mathcal{G}_s - \int_{\mathcal{B}_s} \mu^{\text{ext}} \rho_f^0 \operatorname{div}_s \left[\det(\nabla_s \phi_f) (\nabla_s \phi_f)^{-T} \right] d\mathcal{B}_s.$$

It is known from (B.2) that the divergence appearing in the second integral is vanishing, so that $\mathcal{L}_f^{\text{ext}}$ can be rewritten on the Eulerian configuration as

$$\mathcal{L}_f^{\text{ext}} = \int_{\partial\mathcal{B}_t} \left\{ \left[\mu^{\text{ext}} \rho_f \left((\nabla_s \phi_f)^{-T} \cdot \mathbf{F}_s^T \right) \cdot \mathbf{n} \right] \cdot \delta \phi_f \right\} \circ \chi_s^{-1} d\mathcal{G}_t,$$

or, using (C.1),

$$\mathcal{L}_f^{\text{ext}} = - \int_{\partial\mathcal{B}_t} \left[\rho_f \mu^{\text{ext}} \mathbf{n} \cdot (\delta \chi_f \circ \phi_f - \delta \chi_s) \right] \circ \chi_s^{-1} d\mathcal{G}_t,$$

which is the expression of the fluid external work used in (26).

The final expressions for $\delta \mathcal{L}^{\text{diss}}$ and $\delta \mathcal{L}^{\text{ext}}$ can now be determined. We first consider the solid Lagrangian pull-back of (25), which, recalling that $\nabla \mathbf{v}_\alpha = \nabla_s \mathcal{V}_\alpha \cdot \mathbf{F}_s^{-1}$, reads

$$\begin{aligned} \delta \mathcal{L}^{\text{diss}} := & - \int_{\mathcal{B}_s} \left\{ J_s D(\mathcal{V}_f \circ \phi_f - \mathcal{V}_s) \cdot [(\delta \chi_f \circ \phi_f - \delta \chi_s)] \right\} d\mathcal{B}_s \\ & - \int_{\mathcal{B}_s} \left\{ J_s [\mathbb{A} \cdot \nabla_s (\mathcal{V}_f \circ \phi_f - \mathcal{V}_s) \cdot \mathbf{F}_s^{-1}] : \nabla [(\delta \chi_f \circ \phi_f - \delta \chi_s)] \right\} d\mathcal{B}_s. \end{aligned}$$

Recalling Equation (C.1), the dissipation work can be rewritten as

$$\begin{aligned} \delta \mathcal{L}^{\text{diss}} = & \int_{\mathcal{B}_s} \left[(\nabla_s \phi_f)^{-T} \cdot (J_s D \mathbf{F}_s^T \cdot (\mathcal{V}_f \circ \phi_f - \mathcal{V}_s)) \right] \cdot \delta \phi_f d\mathcal{B}_s \\ & + \int_{\mathcal{B}_s} \left\{ J_s [\mathbb{A} \cdot \nabla_s (\mathcal{V}_f \circ \phi_f - \mathcal{V}_s) \cdot \mathbf{F}_s^{-1} \cdot \mathbf{F}_s^{-T}] : \nabla_s \left[\mathbf{F}_s \cdot (\nabla_s \phi_f)^{-1} \cdot \delta \phi_f \right] \right\} d\mathcal{B}_s; \end{aligned}$$

integrating the second term by parts, Equation (29) for the dissipation work is easily recovered.

References

- [Arnold 1989] V. I. Arnold, *Mathematical methods of classical mechanics*, Springer Verlag, New York, 1989.
- [Baek and Srinivasa 2004] S. Baek and A. R. Srinivasa, “Diffusion of a fluid through an elastic solid undergoing large deformation”, *Int. J. Non-Linear Mech.* **39** (2004), 201–218.
- [Bedford and Drumheller 1978] A. Bedford and D. S. Drumheller, “A variational theory of immiscible mixtures”, *Arch. Rational Mech. Anal.* **68** (1978), 37–51.
- [Biot 1941] M. A. Biot, “General theory of three-dimensional consolidation”, *J. Appl. Phys.* **12** (1941), 155–164.
- [Brinkman 1947] H. C. Brinkman, “A calculation of the viscous force exerted by a flowing fluid on a dense swarm of particles”, *Appl. Sci. Res. A* **1** (1947), 27–34.
- [Camar-Eddine and Seppecher 2003] M. Camar-Eddine and P. Seppecher, “Determination of the closure of the set of elasticity functionals”, *Arch. Rational Mech. Anal.* **170** (2003), 211–245.
- [Casal 1972] P. Casal, “La théorie du second gradient et la capillarité”, *C. R. Acad. Sc. Paris Série A* **274** (1972), 1571–1574.

- [Casal and Gouin 1988] P. Casal and H. Gouin, “Equations du mouvement des fluides thermocapillaires”, *C. R. Acad. Sci. Paris Série II* **306** (1988), 99–104.
- [Chambon et al. 2004] R. Chambon, D. Cailleire, and C. Tamagnini, “A strain space gradient plasticity theory for finite strain”, *Comput. Methods Appl. Mech. Eng.* **193** (2004), 2797–2826.
- [Coleman and Noll 1963] B. D. Coleman and W. Noll, “The thermodynamics of elastic material with heat conduction and viscosity”, *Arch. Rational Mech. Anal.* **13** (1963), 167–178.
- [Coussy 2004] O. Coussy, *Poromechanics*, J. Wiley & Sons, Chichester, 2004.
- [Coussy 2005] O. Coussy, “Poromechanics of freezing materials”, *J. Mech. Phys. Solids* **53** (2005), 1689–1718.
- [Coussy et al. 1998] O. Coussy, L. Dormieux, and E. Detournay, “From mixture theory to Biot’s approach for porous media”, *Int. J. Solids Struct.* **35**:34–35 (1998), 4619–4635.
- [Cryer 1963] C. W. Cryer, “A comparison of the three-dimensional consolidation theories of Biot and Terzaghi”, *Q. J. Mech. Appl. Math.* **16**:4 (1963), 401–412.
- [dell’Isola and Seppecher 1997] F. dell’Isola and P. Seppecher, “Edge contact forces and quasi balanced power”, *Meccanica* **32** (1997), 33–52.
- [dell’Isola et al. 1996] F. dell’Isola, H. Gouin, and G. Rotoli, “Nucleation of spherical shell-like interfaces by second gradient theory: numerical simulation”, *Eur. J. Mech. B: Fluids* **15** (1996), 545–568.
- [dell’Isola et al. 2003] F. dell’Isola, G. Sciarra, and R. C. Batra, “Static deformations of a linear elastic porous body filled with an inviscid fluid”, *J. Elasticity* **72** (2003), 99–120.
- [Dormieux and Ulm 2005] L. Dormieux and F. J. Ulm, *Applied micromechanics of porous materials series CISM n. 480*, Springer-Verlag, Wien New York, 2005.
- [Dormieux et al. 2003] L. Dormieux, E. Lemarchand, and O. Coussy, “Macroscopic and micromechanical approaches to the modeling of the osmotic swelling in clays”, *Transp. Porous Media* **50** (2003), 75–91.
- [Dormieux et al. 2006] L. Dormieux, D. Kondo, and F. J. Ulm, *Microporomechanics*, Wiley, Chichester, 2006.
- [Drugan and Willis 1996] W. J. Drugan and J. R. Willis, “A micromechanics-based nonlocal constitutive equation and estimates of representative volume element size for elastic component”, *J. Mech. Phys. Solids* **44**:4 (1996), 497–524.
- [Elhers 1992] W. Elhers, “An elastoplasticity model in porous media theories”, *Transp. Porous Media* **9**:1–2 (1992), 49–59.
- [Gantmacher 1970] F. R. Gantmacher, *Lectures in analytical mechanics*, MIR, Moscow, 1970.
- [Gavrilyuk et al. 1998] S. Gavrilyuk, H. Gouin, and Y. V. Perepechko, “Hyperbolic models of homogeneous two-fluid mixtures”, *Meccanica* **33** (1998), 161–175.
- [de Gennes 1985] P. G. de Gennes, “Wetting: statics and dynamics”, *Rev. Mod. Phys.* **57**:3 (1985), 827–863.
- [Germain 1973] P. Germain, “La méthode des puissances virtuelles en mécanique des milieux continus”, *J. Mécanique* **12**:2 (1973), 235–274.
- [Gologanu and Leblond 1997] M. Gologanu and J. B. Leblond, *Recent extensions of Gurson’s model for porous ductile materials in continuum micromechanics*, vol. 377, CISM Courses and Lectures, Springer, New York, 1997.
- [Gouin and Ruggeri 2003] H. Gouin and T. Ruggeri, “Hamiltonian principle in the binary mixtures of Euler fluids with applications to second sound phenomena”, *Rend. Mat. Acc. Lincei* **14**:9 (2003), 69–83.
- [Koutetzova et al. 2002] V. Koutetzova, M. G. D. Geers, and W. A. M. Brekelmans, “Multi-scale constitutive modelling of heterogeneous materials with a gradient-enhanced computational homogenization scheme”, *Int. J. Numer. Methods Eng.* **54** (2002), 1235–1260.
- [Lowengrub and Truskinovsky 1998] J. Lowengrub and L. Truskinovsky, “Quasi-incompressible Cahn-Hilliard fluids and topological transitions”, *Proc. R. Soc. Lond. A* **454** (1998), 2617–2654.
- [Mandel 1953] J. Mandel, “Consolidation des sols (étude mathématique)”, *Géotechnique* **3** (1953), 287–299.

- [Nemat-Nasser and Hori 1993] S. Nemat-Nasser and M. Hori, *Micromechanics: Overall properties of heterogeneous materials*, North-Holland, Amsterdam, 1993.
- [Pideri and Seppecher 1997] C. Pideri and P. Seppecher, "A second gradient material resulting from the homogenization of a heterogeneous linear elastic medium", *Continuum. Mech. Therm.* **9** (1997), 241–257.
- [Sciarra et al. 2007] G. Sciarra, F. dell'Isola, and O. Coussy, "Second gradient poromechanics", *International Journal of Solids and Structures* **44** (2007), 6607–6629.
- [Seppecher 1993] P. Seppecher, "Equilibrium of a Cahn-Hilliard fluid on a wall: influence of the wetting properties of the fluid upon the stability of a thin liquid film", *Eur. J. Mech. B:Fluids* **12** (1993), 169–184.
- [von Terzaghi 1943] K. von Terzaghi, *Theoretical soil mechanics*, John Wiley & Sons, Chichester, 1943.
- [Torquato 2002] S. Torquato, *Random heterogeneous materials*, Springer, New York, 2002.
- [Truesdell 1977] C. A. Truesdell, *A first course in rational continuum mechanics*, Academic Press, New York, 1977.
- [Vardoulakis and Aifantis 1995] I. Vardoulakis and E. C. Aifantis, "Heterogeneities and size effects in geo materials", *AMD - Am. Soc. Mech. Eng., Appl. Mech. Div. Newsl.* **201** (1995), 27–30.
- [Wilmanski 1996] K. Wilmanski, "Porous media at finite strains. The new model with the balance equilibrium for porosity", *Arch. Mech.* **48**:4 (1996), 591–628.

Received 8 Mar 2007. Revised 27 Jul 2007. Accepted 25 Nov 2007.

GIULIO SCIARRA: giulio.sciarra@uniroma1.it

Dipartimento di Ingegneria Chimica Materiali Ambiente, Università di Roma "La Sapienza", Via Eudossiana 18, 00184 Rome, Italy

FRANCESCO DELL'ISOLA: francesco.dellisola@uniroma1.it

Dipartimento di Ingegneria Strutturale e Geotecnica, Università di Roma "La Sapienza", Via Eudossiana 18, 00184 Rome, Italy

and

Laboratorio di Strutture e Materiali Intelligenti, Palazzo Caetani (Ala Nord), 04012 Cisterna di Latina (Lt), Italy

NICOLETTA IANIRO: ianiro@dmmm.uniroma1.it

Dipartimento di Metodi e Modelli Matematici per le Scienze Applicate, Università di Roma "La Sapienza", Via Scarpa 16, 00161 Rome, Italy

ANGELA MADEO: angela.madeo@uniroma1.it

Dipartimento di Metodi e Modelli Matematici per le Scienze Applicate, Università di Roma "La Sapienza", Via Scarpa 16, 00161 Rome, Italy

ESTIMATION OF PARAMETERS OF A THREE-LAYERED SANDWICH BEAM

NILSON BARBIERI, RENATO BARBIERI, LUIZ CARLOS WINIKES AND LUIS FERNANDO ORESTEN

In this work the physical parameters of a sandwich beam made with the association of hot rolled steel, polyurethane rigid foam, and high impact polystyrene, used for the assembly of household refrigerators and food freezers, are estimated using measured and numeric frequency response functions. The mathematical models are obtained using the finite element method and the Timoshenko beam theory. The physical parameters are estimated using the amplitude correlation coefficient and genetic algorithm methods. Initially, the experimental procedure to determine the material's mechanical properties, Young and shear moduli, and the density of the components of the sandwich beam is described. The elastic properties were obtained through tension and torsion tests. The shear modulus G_c of the polyurethane rigid foam core was determined using a rectangular specimen and the Young's moduli of the steel and high impact polystyrene were determined using a conventional tension test. To estimate the dynamical values of the parameters in the frequency range from 10 to 400 Hz, separated dynamic sweeping tests were conducted using cantilevered beams of polyurethane rigid foam and high impact polystyrene. The experimental data from a three layered sandwich beam were obtained using an impact hammer and four accelerometers, displaced along the cantilevered beam sample. The parameters estimated are the Shear modulus and the loss factor of the polyurethane rigid foam, and the Young's modulus and the loss factor of the high impact polystyrene.

1. Introduction

Modern engineering requires the use of sophisticated and optimized structural designs. One way to achieve this goal is to use materials in a way that will optimize their inherent properties. An engineering application known as sandwich structure is very suitable for this purpose. Sandwich materials are frequently used wherever high strength and low weight are important criteria. The most important applications are found in the transport industry — such as in the aerospace, automobile, railroad, and marine industries — where high stiffness/weight and strength/weight ratios provide increased payload capacity, improved performance, and lower energy consumption. These applications are often subjected to vibrations. It is therefore important to know the particular dynamic and vibroacoustic properties, such as the natural frequencies, of these constructions for design purposes [Tavallaey 2001].

For household refrigerators and food freezers, one of the main complaints to customer care centers is related to noise generation, related most of the time to vibration of the cabinet, which radiates sound from internal components like shelves and containers, leaking to the outside of the unit.

The modeling of sandwich structures has been studied extensively, but less attention has been paid to their material identification [Shi et al. 2006]. Material parameter identification by inverse methods

Keywords: sandwich beam, genetic algorithm, amplitude correlation coefficient, parameter updating.

using measured resonance frequencies is a recent type of nondestructive evaluation method. The principle of inverse methods for material identification is to update iteratively the engineering constants in a finite element model of the test specimens in such a way that the computed frequencies match the measured frequencies. The engineering constants that minimize an output residual are considered as the solution of the procedure. The minimization of the output residual is realized by optimization methods, which minimize a scalar value called the objective function. A typical objective function is the sum of the squared residual components. The underlying idea of inverse methods based on measurement of resonance frequencies originates from the observation that all constructions made with elastic materials have a characteristic set of resonance frequencies. The values of these frequencies are determined by the geometry, boundary conditions, the elastic moduli, and the density of the materials.

Caracciolo et al. [2004] presented an experimental technique for completely characterizing a viscoelastic material, by determining the Poisson's ratio and the complex dynamic Young's modulus of a small beam-like specimen subject to seismic excitation, together with the theoretical background. The same experimental device is used basically for both kinds of tests; the specimen is instrumented, placed into a temperature controlled chamber and excited by means of an electrodynamic shaker. The longitudinal and the transversal deformations are measured by strain gauges to get the Poisson's ratio, whereas the vertical displacement of the specimen and the acceleration of the support are measured to get Young's modulus of the tested material. The experimental curves of the Poisson's ratio and of the Young's modulus, obtained at different temperatures, are then gathered into a unique master curve by using the reduced variables method. The two master curves, respectively, represent the Poisson's ratio and Young's modulus for the tested material in a very broad frequency range.

Park [2005] used experimental methods to measure frequency-dependant dynamic properties of complex structures. Flexural wave propagations are analyzed using the Timoshenko beam, the classical beam, and the shear beam theories. Wave speeds, bending, and shear stiffnesses of the structures are measured through the transfer function method, requiring small number of vibration measurements. Sensitivity analysis is performed to investigate the effects of experimental variables on the measured properties and to study optimal sensor locations of the vibration measurements. Using the developed methods, the complex bending and shear stiffnesses of sandwich beams of different core materials and a polymer beam are measured. Continuous variations of the measured bending and shear stiffnesses and their loss factors with frequency were obtained. To further illustrate the measurements of frequency-dependent variation of dynamic properties of complex structures, the damping of structural vibration using porous and granular materials is investigated.

Kim and Kreider [2006] studied the parameter identification in nonlinear elastic and viscoelastic plates by solving an inverse problem numerically. The material properties of the plate, which appear in the constitutive relations, are recovered by optimizing an objective function constructed from reference strain data. The resulting inverse algorithm consists of an optimization algorithm coupled with a corresponding direct algorithm that computes the strain fields given a set of material properties. Numerical results are presented for a variety of constitutive models; they indicate that the methodology works well, even with noisy data.

Pintelon et al. [2004] analyzed the stress-strain relationship of linear viscoelastic materials characterized by a complex valued, frequency-dependent elastic modulus (Young's modulus). Using system identification techniques it is shown the elastic modulus can be measured accurately in a broad frequency

band from forced flexural (transverse) and longitudinal vibration experiments on a beam under free-free boundary conditions. The approach is illustrated on brass, copper, plexiglass, and PVC beams.

Yang et al. [2005] analyzed the vibration and dynamic stability of a traveling sandwich beam using the finite element method. The damping layer is assumed to be linear viscoelastic and almost incompressible. The extensional and shear moduli of the viscoelastic material are characterized by complex quantities. Complex eigenvalue problems are solved by the state-space method, and the natural frequencies and modal loss factors of the composite beam are extracted. The effects of stiffness and thickness ratios of the viscoelastic and constrained layers on natural frequencies and modal loss factors are reported. Tension fluctuations are the dominant source of excitation in a traveling sandwich material, and the regions of dynamic instability are determined by a modified Bolotin's method. Numerical results show that the constrained damping layer stabilizes the traveling sandwich beam.

Singh et al. [2003] formulated a system identification procedure for estimation of parameters associated with a dynamic model of a single degree of freedom foam-mass system. Ohkami and Swoboda [1999] presented two parameter identification procedures for linear viscoelastic materials. Chang [2006] used the genetic algorithm for parameter estimation of nonlinear systems.

Backström and Nilsson [2007] indicate the need for simple methods describing the dynamics of these complex structures. By implementing frequency dependent parameters, the vibration of sandwich composite beams can be approximated using simple fourth order beam theory. A higher order sandwich beam model is utilized in order to obtain estimates of the frequency-dependent bending stiffness and shear modulus of the equivalent Euler–Bernoulli and Timoshenko models. The resulting predicted eigenfrequencies and transfer acceleration functions are compared to the data obtained from the higher order model and from measurements. It can be noticed that for lower order wavenumbers the ordinary Timoshenko theory and the higher order theory show satisfactory agreement.

In this work the physical parameters of a sandwich beam made with the association of hot rolled steel, polyurethane rigid foam, and high impact polystyrene, used for the assembly of household refrigerators and food freezers, are estimated using measured and numeric frequency response functions (FRFs). The mathematical models are obtained using the finite element method (FEM) and Timoshenko beam theory. The physical parameters are estimated using the amplitude correlation coefficient [Grafe 1998] and genetic algorithm (GA) [Chang 2006] methods. The experimental data are obtained using an impact hammer and four accelerometers displaced along the cantilevered beam sample. The parameters estimated are the shear modulus and the loss factor of the polyurethane rigid foam and the Young's modulus and the loss factor of the high impact polystyrene. The frequency range is chosen for the test in which the FRF curve presents a good signal to noise ratio. To estimate the initial values of the parameters, separated static and dynamic tests were conducted using cantilevered beams of polyurethane rigid foam and high impact polystyrene. The static values are used as the initial reference values for the dynamic estimation.

2. Mathematical model

A lot of research has been done on finite element models of cantilever beams based on Euler–Bernoulli beam theory. In Euler–Bernoulli beam theory the assumption is made that the plane cross section before bending remains plane and normal to the neutral axis after bending. This assumption is valid if the

length to thickness ratio is large, and for small deflection of beam. However if the length to thickness ratio is small, plane deflection before bending will not remain normal to the neutral axis after bending. In practical situations a large number of modes of vibrations contribute to the structure's performance. Euler–Bernoulli beam theory gives inaccurate results for higher modes of vibration. Timoshenko beam theory corrects the simplifying assumptions made in Euler–Bernoulli beam theory. In this theory cross sections remain plane and rotate about the same neutral axis as the Euler–Bernoulli model, but do not remain normal to the deformed longitudinal axis. The deviation from normality is produced by a transverse shear that is assumed to be constant over the cross section. Thus the Timoshenko beam model is superior to the Euler–Bernoulli model in precisely predicting the beam response [Backström and Nilsson 2007] for a lower number of vibration modes.

The equation of motion for the vibration of a sandwich beam according to the Timoshenko beam theory [Zenkert 1997] is

$$D \frac{\partial^4 w}{\partial x^4} + \rho^* \frac{\partial^2 w}{\partial t^2} - \frac{\rho^*}{S} \left(D \frac{\partial^4 w}{\partial x^2 \partial t^2} - \mathfrak{R} \frac{\partial^4 w}{\partial t^4} \right) - \mathfrak{R} \frac{\partial^4 w}{\partial x^2 \partial t^2} = f(x) e^{i\omega t}, \quad (1)$$

where $w(x, t)$ is the transverse displacement, D is the bending stiffness, ρ^* is the mass per unit of surface, S is the shear stiffness, \mathfrak{R} is the rotational inertia, x is the coordinate along the beam axis, t is the time, $f(x)$ is the amplitude of the external force applied along the beam span, ω is the excitation frequency, and $i = \sqrt{-1}$.

The dimensions and parameters of the sandwich beam shown in Figure 1 are as follows: E_1 , E_2 , and E_c are the Young's moduli, ρ_1 , ρ_2 , and ρ_c are the densities, G_c is the shear modulus, t_1 , t_2 , and t_c are the thicknesses, e is the position of the neutral line, d is the distance between the center line of the steel and the high impact polystyrene beam, and z is the position of the reference axis.

According to Figure 1 and the theory of sandwich beams [Zenkert 1997]

$$\begin{aligned} e &= \frac{E_1 t_1 \left(\frac{t_1}{2} + t_c + \frac{t_2}{2} \right) + E_c t_c \left(\frac{t_c}{2} + \frac{t_2}{2} \right)}{E_1 t_1 + E_c t_c + E_2 t_2}, & d &= t_c + \frac{t_1}{2} + \frac{t_2}{2}, \\ D &= \frac{E_1 t_1^3}{12} + \frac{E_2 t_2^3}{12} + \frac{E_c t_c^3}{12} + E_1 t_1 (d - e)^2 + E_2 t_2 e^2 + E_c t_c \left(\frac{t_c + t_2}{2} - e \right)^2, & \rho^* &= \rho_1 t_1 + \rho_2 t_2 + \rho_c t_c, \\ \mathfrak{R} &= \frac{\rho_1 t_1^3}{12} + \frac{\rho_2 t_2^3}{12} + \frac{\rho_c t_c^3}{12} + \rho_1 t_1 (d - e)^2 + \rho_2 t_2 e^2 + \rho_c t_c \left(\frac{t_c + t_2}{2} - e \right)^2, & S &= \frac{G_c d^2}{t_c}. \end{aligned}$$

Making $w = w(x, t)$ a harmonic function, it is possible to admit that $w(x, t) = W(x) e^{i\omega t}$. Substituting this $w(x, t)$ into Equation (1) we obtain

$$D \frac{\partial^4 W}{\partial x^4} - \rho^* \omega^2 W(x) - \frac{\rho^*}{S} \left(-D \omega^2 \frac{\partial^2 W}{\partial x^2} - \mathfrak{R} \omega^4 W(x) \right) + \mathfrak{R} \omega^2 \frac{\partial^2 W}{\partial x^2} = f(x). \quad (2)$$

The exact solution $W(x)$ needs to satisfy Equation (2) at every point x , and in general is unknown. To overcome this problem the approximate solution $\tilde{W}(x)$ is used. This approximate solution is interpolated over a finite element, see Figure 1, with 2 nodes, according to the expression $W(x) \cong \tilde{W}(x) = [\phi] \{q\}$, where $[\phi(x)]$ is the shape function matrix (1×4) and the four $\phi_j(x)$ are the well known Hermitian interpolation functions [Cook et al. 1989] with C^1 continuity. The vector $\{q\}$ is the generalized displacement

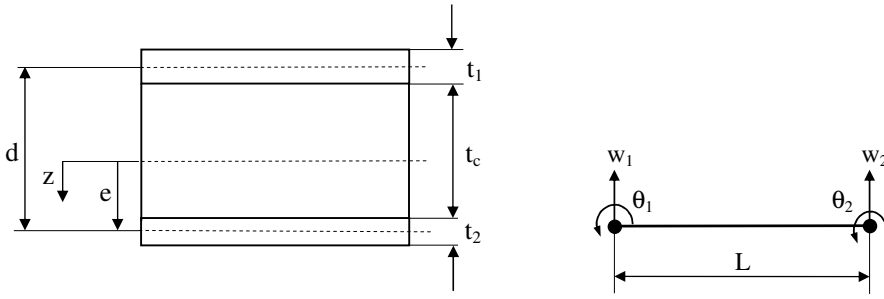


Figure 1. Sandwich beam geometric parameters (left) and finite element degrees of freedom (right).

vector, $\{q\} = \{w_1, \theta_1, w_2, \theta_2\}^t$ where w_i denotes the nodal displacement and θ_i is the rotation at element node i .

Substituting the approximate solution into Equation (2) introduces a residual error, $E(x, \omega)$, which is minimized using the Galerkin weighted residual method. In mathematical terms, the residual error is made orthogonal to the weight functions

$$\int_0^L [\phi]^t \left(D \frac{\partial^4 \tilde{W}}{\partial x^4} - \rho^* \omega^2 \tilde{W}(x) - \frac{\rho^*}{S} \left(-D \omega^2 \frac{\partial^2 \tilde{W}}{\partial x^2} - \Re \omega^4 \tilde{W}(x) \right) + \Re \omega^2 \frac{\partial^2 \tilde{W}}{\partial x^2} - f(x) \right) dx = 0, \quad (3)$$

where L is the element length.

Substituting the shape functions into Equation (3) obtains the standard finite element equation

$$[K_e(\omega)] \{q\} = \{F\},$$

where

$$[K_e(\omega)] = D [K] + \omega^2 \left[-\rho^* [M] + \left(\frac{\rho^* D}{S} + \Re \right) [K_\sigma] \right] + \omega^4 \frac{\rho^* \Re}{S} [M],$$

$$[K] = \frac{1}{L^3} \begin{bmatrix} 12 & 6L & -12 & 6L \\ 6L & 4L^2 & -6L & 2L^2 \\ -12 & -6L & 12 & -6L \\ 6L & 2L^2 & -6L & 4L^2 \end{bmatrix}, \quad [K_\sigma] = \frac{1}{30L} \begin{bmatrix} 36 & 3L & -36 & 3L \\ 3L & 4L^2 & -3L & -L^2 \\ -36 & -3L & 36 & -3L \\ 3L & -L^2 & -3L & 4L^2 \end{bmatrix},$$

$$[M] = \frac{l}{420} \begin{bmatrix} 156 & 22L & 54 & -13L \\ 22L & 4L^2 & 13L & -3L \\ 54 & 13L & 156 & -22L \\ -13L & -3L & -22L & 4L^2 \end{bmatrix}, \quad \{F\} = \int_0^L [\phi]^T f(x) dx.$$

3. Numerical estimation methods

To approximate the experimental and numeric FRF data, the predictor-corrector updating technique [Grafe 1998] based on two correlation coefficients (shape and amplitude) and their sensitivities can

be used. In this work, only the amplitude correlation coefficient is used. This coefficient is defined as

$$\chi_a(\omega_k) = \frac{2|\{H_X(\omega_k)\}^T\{H_A(\omega_k)\}|}{(\{H_X(\omega_k)\}^T\{H_X(\omega_k)\}) + (\{H_A(\omega_k)\}^T\{H_A(\omega_k)\})},$$

where $H_X(\omega_k)$ and $H_A(\omega_k)$ are the measured and predicted response vectors at matching excitation-response locations.

The corresponding sensitivity is

$$\frac{\partial \chi_a(\omega_k)}{\partial \varphi} = 2 \frac{\partial |\{H_x\}^T\{H_A\}|}{\partial \varphi} \frac{(\{H_X\}^T\{H_X\}) + (\{H_A\}^T\{H_A\})}{(\{H_X\}^T\{H_X\}) + (\{H_A\}^T\{H_A\})^2} - 2 \frac{\partial (\{H_A\}^T\{H_A\})}{\partial \varphi} \frac{|\{H_x\}^T\{H_A\}|}{(\{H_X\}^T\{H_X\}) + (\{H_A\}^T\{H_A\})^2}.$$

It is therefore proposed to make use of $\chi_a(\omega_k)$ and its sensitivity in a combined manner to improve the overall level of correlation. Based on a truncated Taylor series expansion, one can therefore write one equation for frequency point ω_k as

$$\{1 - \chi_a(\omega_k)\} = \left[\frac{\partial \chi_a(\omega_k)}{\partial \varphi_1} \quad \frac{\partial \chi_a(\omega_k)}{\partial \varphi_2} \quad \dots \quad \frac{\partial \chi_a(\omega_k)}{\partial \varphi_{N_\varphi}} \right]_{1 \times N_\varphi} \{\Delta \varphi\}, \quad (4)$$

where N_φ is the number of updating parameters $\{\varphi_1, \varphi_2, \dots, \varphi_{N_\varphi}\}$ and Equation (4) is recognized to be in the standard form of sensitivity based model updating formulations $\{\varepsilon\} = [S] \{\Delta \varphi\}$, where $\{\Delta \varphi\}$ is the change in design parameters of the finite element model.

An extended weighted least square approach is proposed which minimizes

$$J(\{\varphi\}) = \{\varepsilon\}^T [W_f] \{\varepsilon\} + \{\Delta \varphi\}^T [W_\varphi] \{\Delta \varphi\}, \quad (5)$$

where $[W_f]$ and $[W_\varphi]$ are diagonal weighting matrices for the frequency points and updating parameters respectively (see [Grafe 1998] for more details).

Another update method used in this work is the GA method. This method is widely used and is based on the evolutionary biological process [Chang 2006]; the GA parameters used in this application are: mutation rate = 0.02, population size = 50, and number of generations = 5000. The objective function is defined by

$$f = \sum_{i=1}^{np} |\text{FRF}_{\text{exp}} - \text{FRF}_{\text{FEM}}|, \quad (6)$$

where FRF_{exp} is the experimental FRF obtained with laser transducer or accelerometer, FRF_{FEM} is the numeric FRF and np is the number of experimental points (np varies according the system and frequency range). Equation (6) is used as a fitness function. The impulsive data were collected using a frequency range varying from 0 to 400 Hz and a frequency increment $\Delta \omega = 0.25$ Hz.

The numeric FRF is obtained using frequency sweeping in the range of interest with the same increment as the measurements. The final finite elements system of equations is solved for each frequency, and two procedures are used to specify the boundary condition and the force vector:

- (a) When the FRF is obtained using the impact hammer, the force vector is calculated using unitary force applied in the excitation node, and the clamped boundary condition is prescribed for the fixed base node.
- (b) When the FRF is obtained using base excitation (a shaker) and the measurements are made with a laser transducer, the force vector is null and the boundary conditions for the fixed base node are the measured displacement with null rotation.

4. Static characterization

This section shows the experimental procedure used to determine the material's mechanical properties, Young and shear moduli, and the density of the components of the sandwich beam. The elastic properties were obtained through tension and torsion tests. The shear modulus G_c of the polyurethane rigid foam core was determined with a torsion test using a prismatic specimen with a rectangular section, and the Young's moduli of the steel and high impact polystyrene were determined using conventional tension tests.

4.1. Polyurethane rigid foam core. Due to the difficulty of adapting the specimen for use in the conventional testing machines (for torsion and/or tension tests) a special pure torsion device test was projected to evaluate the shear modulus G of the core.

For pure torsion the relative angle of twist for a prismatic bar is

$$\theta = \frac{TL}{GJ},$$

where T is the torque, L is the length (as a relative position) and J is the polar area moment of inertia.

For a rectangular section with dimensions d and t with $d \geq t$ the polar area moment of inertia J is given by [Boresi and Chong 1999]

$$J = K_1 \frac{d \times t^3}{3},$$

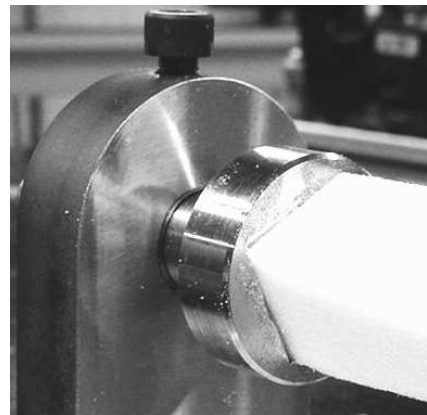
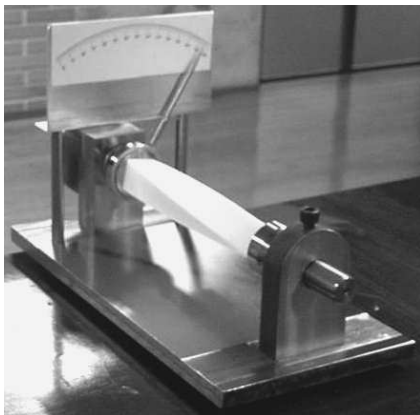


Figure 2. Special device for torsion test of the polyurethane rigid foam core (left) and the sample inserted in fixed extremity (right).

where

$$K_1 = 1 - \frac{192}{\pi^5} \frac{t}{d} \sum_{n=0,1,2,\dots} \frac{1}{(2n+1)^5} \tanh\left(\frac{2n+1}{2} \frac{d}{t} \pi\right).$$

For $d = t$, using 10 terms in the series, $K_1 \cong 0.422$ and the expression for the angle of twist reduces to

$$\theta = \frac{T \times L}{G \times d \times t^3 \times 0.14066}.$$

The specimen with dimensions of 30 mm × 30 mm × 250 mm is inserted with low interference at the fixed extremity (see Figure 2), and the external torque is applied on the other extremity (which is free to rotate) using a pulley and dead weight (see Figure 3).

A cursor was inserted as shown in Figures 2 and 3 to measure the twist angle using a calibrated disc in steps with 0.5 degree resolution. The external torque is applied using calibrated weights (see Figure 3) and the test is carried out varying the torque and making direct measurement of the twist angle.

The polyurethane rigid foam samples were extracted from the same cabinet to avoid variations due to different production conditions. The samples were obtained from the lateral refrigerator wall (a straight region, with less foaming faults and voids) and it was classified according to the quantity of superficial faults (see Figure 4). The goal of this classification was to evaluate the variation of the G value obtained with perfect samples and with superficial faults.

The tests were performed on 12 samples with torque increments of 0.02375 Nm in such a manner to produce an adequate twist angle variation. Table 1 shows the values of G , as well the average value and the variance. The average values of the shear modulus G of samples with superficial faults are greater than that of samples without faults. Usually the stiffness will be reduced if there are defects in the specimen. However, the variance is also greater for the samples with faults.

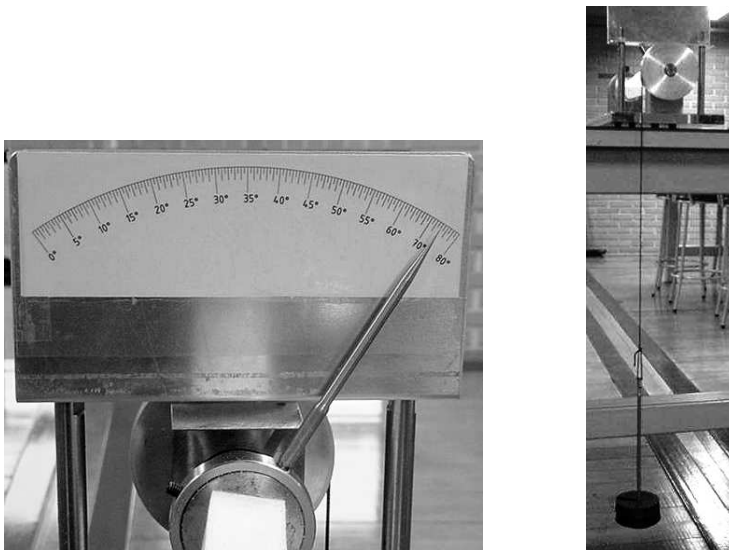


Figure 3. Free rotating end with calibrated disc (left) and torque application through calibrated weights (right).

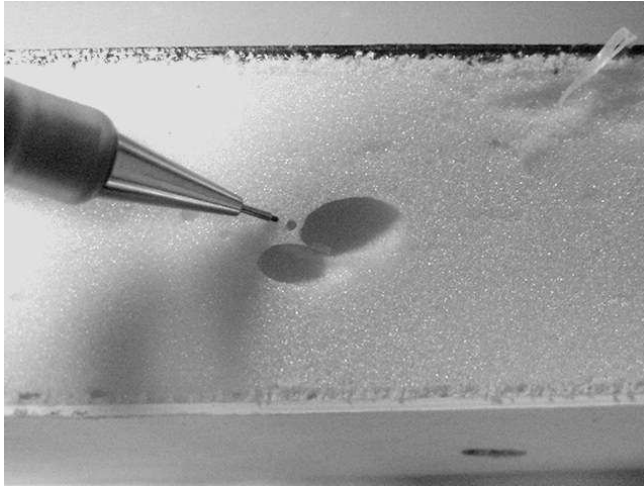


Figure 4. A sample with superficial faults.

Figure 5 shows a typical curve of the torque as a function of twist angle; it can be noticed that this relation is linear, with lower residue, as found in [Branner 1995]. Apparently the curve presents linear behavior. In the torsion test used to obtain the shear modulus G of the polyurethane rigid foam core, the twist angle can reach nearly 30 degrees. For such large rotation, the nonlinear effect may be dominant. The nonlinearity reduces the stiffness and lower G may be obtained.

Branner [1995] shows the dependence of the shear modulus G , as well as the elastic modulus E , on the specific material density. A precision weighing balance Scientech model SA210 was used, with resolution of 0.001 g. Table 2 shows the density values obtained for 12 samples (6 with and 6 without superficial faults).

4.2. Steel beam. The Young's modulus of the steel beam was determined using the procedures described in the technical norm [ASTM 2004].

Sample (without superficial faults)	G (MPa)	Sample (with superficial faults)	G (MPa)
1	1.977	1	2.423
2	2.015	2	1.896
3	2.215	3	1.935
4	2.045	4	2.205
5	2.091	5	2.496
6	2.054	6	2.152
Average value = 2.066 MPa		Average value = 2.184 MPa	
Variance = 0.082 MPa		Variance = 0.245 MPa	

Table 1. Experimental shear modulus.

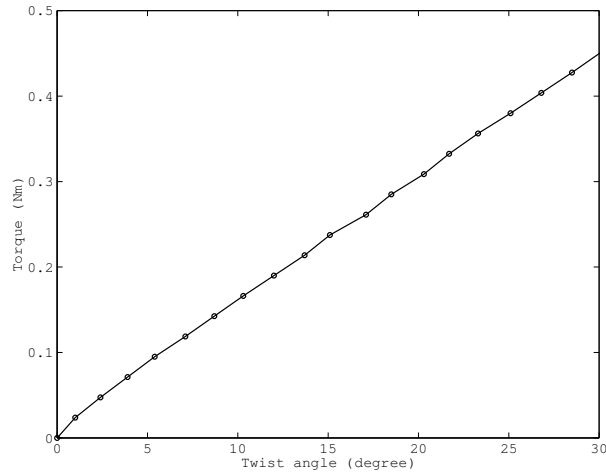


Figure 5. Twist angle versus applied torque.

As a result of the stress-strain test of the steel sample, a correlation between applied force and resultant deformations was obtained. The Young's modulus can be obtained from

$$E = \frac{P}{\varepsilon A},$$

where P is the applied load (in N), A is the transversal section area (in m^2), and ε is the longitudinal deformation (nondimensional).

The value of the Young's modulus obtained was 209.6 GPa, and [Figure 6](#) shows the variation of the applied force and the strain.

4.3. High impact polystyrene. The characterization of the high impact polystyrene is performed using the procedures described in the technical norm [\[ASTM 2003\]](#) for plastics tensile testing.

Sample (without superficial faults)	Density (kg/m^3)	Sample (with superficial faults)	Density(kg/m^3)
1	28.400	1	29.111
2	28.876	2	28.573
3	28.769	3	28.262
4	28.751	4	29.280
5	28.369	5	29.111
6	28.329	6	29.671
Average value	28.582 kg/m^3	Average value	29.002 kg/m^3
Variance	0.242 kg/m^3	Variance	0.506 kg/m^3

Table 2. Polyurethane rigid foam core density.

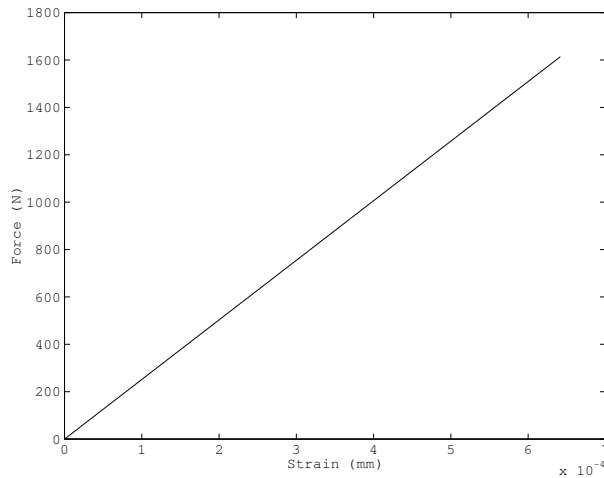


Figure 6. Strain versus applied force.

Five tests were carried out using a universal tensile testing machine EMIC with load cell capacity of 2000 N and test speed of 5 mm/min. The Young's modulus was obtained through the angular coefficient of the linear range of the stress-strain curve (see [Figure 7](#)).

[Table 3](#) shows the Young's modulus values obtained from the five samples, the average value, and the variance.

The technical norm [\[ASTM 2000\]](#) describes the standard test methods for density and specific gravity (or relative density) of plastics by displacement. The body mass is first measured in the atmosphere. After this step the body is immersed in a liquid and the apparent mass is measured. After few manipulations the plastic density is obtained. Six samples were tested and the results are shown in [Table 4](#).

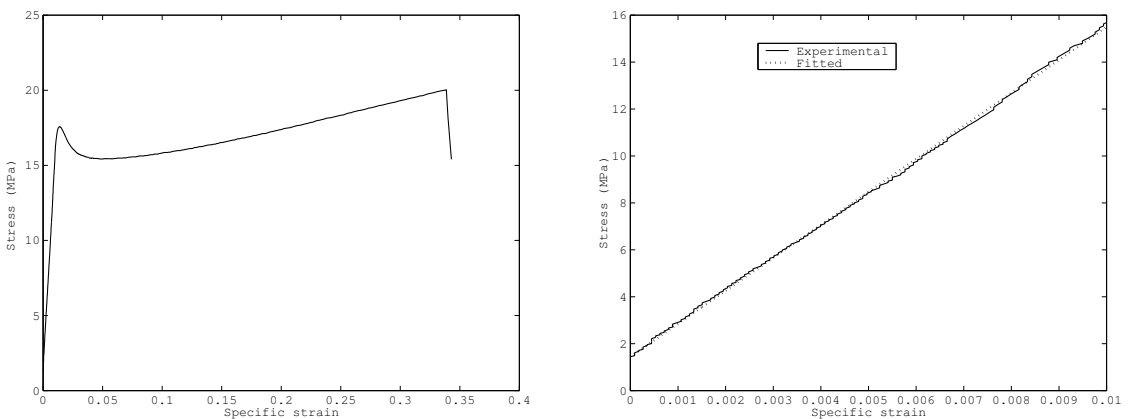


Figure 7. Specific strain versus stress (left) and adjusted curve of specific strain versus stress (right).

Sample	Young's modulus (GPa)
1	1.392
2	1.388
3	1.439
4	1.399
5	1.409
Average value 1.405 GPa	
Variance 0.018 GPa	

Table 3. Young's modulus of the PSAL.

5. Dynamic characterization

The experimental sample of the sandwich beam made with the association of hot rolled steel, polyurethane rigid foam, and high impact polystyrene is shown in [Figure 8](#). The thicknesses of the steel, polyurethane, and polystyrene are 0.6 mm, 38.25 mm, and 1.25 mm, respectively, and the beam width is 39.18 mm.

The experimental data are obtained using the impact hammer and the four accelerometers displaced along the sample ($A1$, $A2$, $A3$, and $A4$). [Figure 9](#) shows the FRF curves of the four accelerometers. The impact force was applied in the position of the accelerometer $A2$ on the steel side.

The rational fraction polynomial [[Maia et al. 1997](#)] method was used to estimate the damping ratio, ξ , and the natural frequencies, ω , of the first three mode shapes. The fourth mode was not considered due to poor signal to noise ratio.

[Table 5](#) shows the values of these parameters for the four accelerometers. The position of the accelerometer $A3$ is near the nodal point of the second mode shape. This justifies the results suppressed in [Table 5](#).

To validate the mathematical model of the sandwich beam it was attempted to estimate separately some physical parameters of the system, namely the shear modulus and the loss factor of the polyurethane rigid foam, and the Young's modulus and the loss factor of the high impact polystyrene.

Sample	Density (kg/m^3)
1	1059.6
2	1069.1
3	1060.1
4	1059.1
5	1060.3
6	1062.8
Average value 1061.9 kg/m^3	
Variance 3.8 kg/m^3	

Table 4. Density of the PSAL.

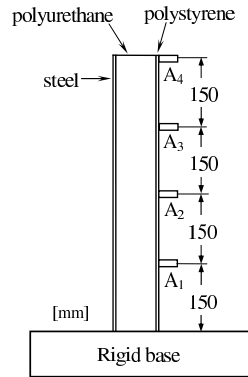


Figure 8. Sandwich beam.

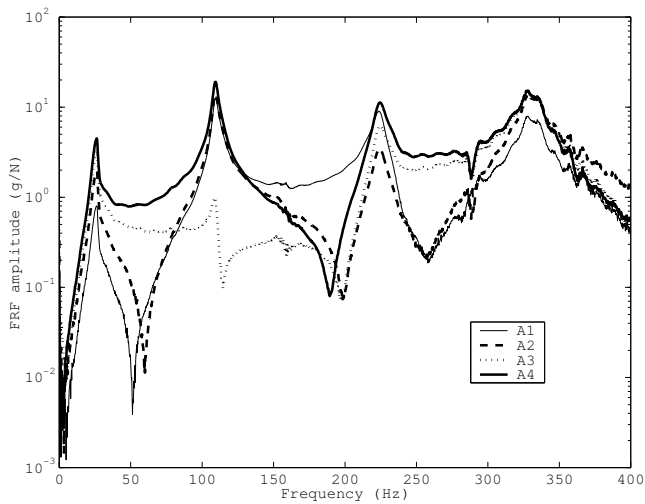


Figure 9. FRF curves of the four accelerometers.

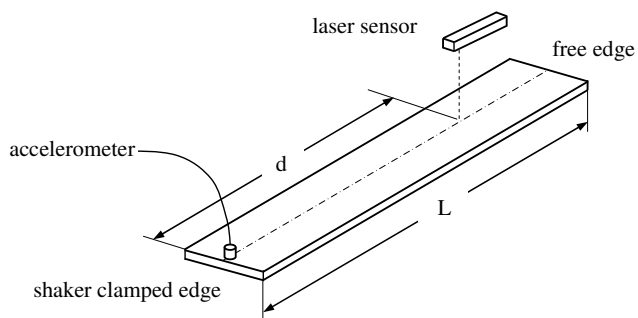


Figure 10. Experimental specimen of cantilever beam with position sensor.

Mode shape	Accelerometers							
	A1		A2		A3		A4	
	ω (Hz)	ξ	ω (Hz)	ξ	ω (Hz)	ξ	ω (Hz)	ξ
1	25.42	0.050	25.39	0.050	25.33	0.052	25.32	0.053
2	109.41	0.0171	109.45	0.0165	—	—	109.39	0.0167
3	223.97	0.0154	224.00	0.0152	224.05	0.0159	224.18	0.0157

Table 5. Experimental damping ratio and natural frequencies.

The loss factor η was estimated considering the complex Young's modulus $E^* = E(1 + j\eta)$. To obtain initial values of these parameters separate studies were conducted on the polyurethane rigid foam and the high impact polystyrene. The first approximation of the loss factor was $\eta = \xi \cong 0.05$ (the damping ratio of the first mode according Table 5).

Figure 10 shows the experimental specimen for the high impact polystyrene and polyurethane rigid foam cantilever beam. The high impact polystyrene beam dimensions and material property are length, $L = 0.145$ m, width = 0.02 m, thickness = 0.0018 m, and density $\rho = 1060$ kg/m³. The mini shaker (B&K model 4810) was used in the sweep sine test with the frequency range varied from 10 to 400 Hz with an increment of 2.5 Hz (157 points). One accelerometer (PCB model 353B18) and one laser velocity transducer (B&K model 3544) were used to collect the vibration data. The accelerometer was placed at the base excitation point (the shaker) and the laser sensor at the position $d = 0.135$ m. Figure 11 shows the experimental and estimated curves of the velocity/acceleration ratio PVA (velocity/base acceleration). The parameters were estimated using the genetic algorithm, and the objective function was defined using the difference between the values of the experimental and numeric PVA. The parameters updated are the Young's modulus and the loss factor of the high impact polystyrene. The optimal values found are shown in Table 6.

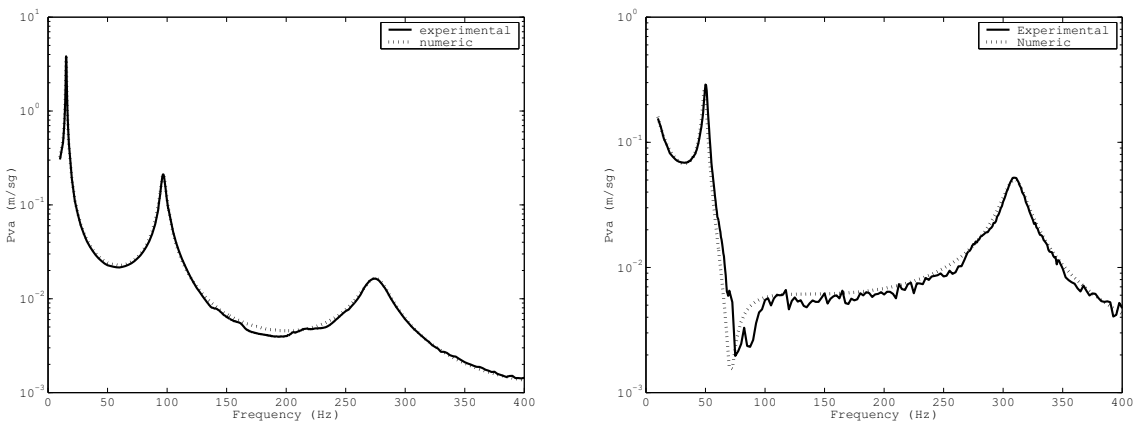


Figure 11. PVA curves of the high impact polystyrene cantilever beam (left) and the polyurethane rigid foam cantilever beam right.

Frequency range (Hz)	E (GPa)	η
10.0 – 57.5	1.3350	0.0385
57.5 – 177.5	1.3725	0.0450
177.5 – 400.0	1.4150	0.0805

Table 6. Optimal parameters.

Frequency range (Hz)	G (MPa)	η
10.0 – 150.0	2.6497	0.0575
150.0 – 400.0	2.5498	0.0625

Table 7. Optimal parameters.

The polyurethane rigid foam cantilever beam dimensions and material property are length, $L = 0.225$ m, width = 0.03 m, thickness = 0.03 m, and density $\rho = 29$ kg/m³. The laser sensor position is $d = 0.1125$ m. The mini shaker was used in the sweep sine test, with the frequency range varying from 10 to 400 Hz with an increment of 2.5 Hz (157 points). [Figure 11](#) shows the experimental and the estimated curves of the velocity/acceleration ratio PVA. The parameters updated are the shear modulus and the loss factor of the polyurethane rigid foam. The optimal values found for these parameters are shown in [Table 7](#). As mentioned by [Backström \[2006\]](#), the elasticity modulus of the core does not have significant influence on the dynamics of typical beams, and is assumed to be related to the core shear modulus by the isotropic relation $E_c = 2(1 + \nu)G_c$, where ν is Poisson's ratio. Since the eigenfrequencies of the beam are not sensitive the value of ν , and as G_c is known directly, ν is set to a default value of $\nu = 0.3$. Thus, by defining an error function describing the proximity of the calculated curve of PVA to the measured, the optimal values of G_c are found by minimization.

[Figure 11](#) shows good agreement between the estimated and experimental curves, even near the resonances.

The physical parameters of the cantilevered sandwich beam shown in [Figure 8](#) were estimated using the amplitude correlation coefficient (ACC) and GA. The frequency range was varied from 10 to 250 Hz (961 points, $\Delta\omega = 0.25$ Hz), chosen for the good signal to noise ratio. [Figure 12](#) shows the experimental and numeric (estimated) FRF curves for the sandwich beam. The curves obtained using ACC and GA methods are practically superposed, and the optimal parameter values found with these methods are shown in [Table 8](#).

Method	Frequency range (Hz)	High impact polystyrene		Polyurethane rigid foam	
		E (GPa)	η	G (MPa)	η
GA	10 – 250	1.5830	0.0446	3.2874	0.0645
ACC	10 – 250	1.5800	0.0471	3.2917	0.0635

Table 8. Optimal parameters.

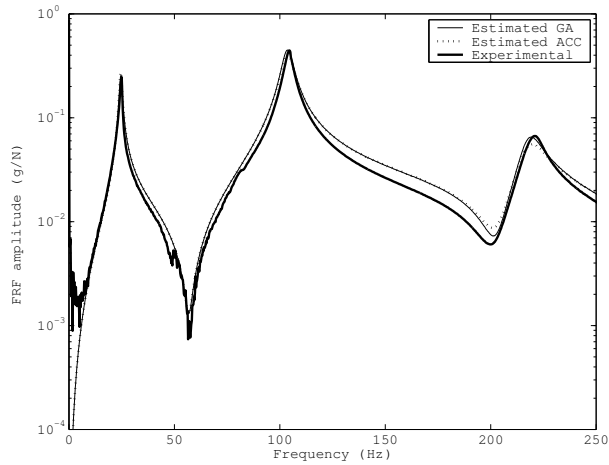


Figure 12. Experimental and estimated FRF curves.

6. Conclusions

Two methods, the genetic algorithm and the amplitude correlation coefficient methods, were used to update the values of physical parameters of mathematical models of a sandwich beam made with the association of hot rolled steel, polyurethane rigid foam, and high impact polystyrene as used for the assembly of household refrigerators and food freezers.

The physical parameters estimated were the shear modulus and the loss factor of the polyurethane rigid foam, and the Young's modulus and loss factor of the high impact polystyrene.

Both methods, the genetic algorithm and the amplitude correlation coefficient, presented good results when it compared to the estimated and the experimental FRF curves.

The genetic algorithm method does not use derivatives, thus it is a good estimated method even for the resonance region.

The amplitude correlation coefficient method uses derivatives, but even so it was possible to obtain good estimation of the parameters near the resonance region.

It was verified that the parameters are frequency dependent. The values found with a conventional, static, test are good approximations for the initial updated methods' starting point.

The static and dynamic tests yielded about the same, 1.4 GPa, for the elastic modulus of the high impact polystyrene. There is some discrepancy for the polyurethane rigid foam; the static test value is about 2.1 MPa, while the dynamic test value is about 2.5 MPa. Pritz [2004] demonstrated mathematically and verified experimentally that the modulus of elasticity of polyurethane rigid foam increases with the increase of the frequency. Therefore the results of this work are in accordance with the data of the literature.

The estimated parameters for the sandwich beam components are greater than the values estimated and measured for the individual (separated) samples. For sandwich beam samples the estimated Young's modulus of the high impact polystyrene was 1.58 GPa, and the estimated shear modulus of the polyurethane rigid foam was 3.29 MPa. The loss factor of the materials varied from 0.04 to 0.06. Some reasons for

the variations of the values between the static and dynamic tests can be associated with the compacting pressure, the glue between the layers, and imperfections in the foam core layer.

References

- [ASTM 2000] “Standard test methods for density and specific gravity (relative density) of plastics by displacement”, Technical report ASTM D792-00, 2000, Available at http://www.techstreet.com/cgi-bin/basket?action=add&item_id=3343161. 6 pages.
- [ASTM 2003] “Standard test method for tensile properties of plastics”, Technical report ASTM D638-03, 2003, Available at http://www.techstreet.com/cgi-bin/detail?product_id=1149803. 15 pages.
- [ASTM 2004] “Standard test methods for tension testing of metallic materials [metric]”, Technical report ASTM E8M-04, ASTM International, 2004, Available at http://www.techstreet.com/cgi-bin/basket?action=add&item_id=3644558. 24 pages.
- [Backström 2006] D. Backström, *Vibration of sandwich beams*, Doctoral Thesis, Kungliga Tekniska Högskolan, Stockholm, 2006, Available at http://www.diva-portal.org/diva/getDocument?urn_nbn_se_kth_diva-4030-2_._ful%ltext.pdf.
- [Backström and Nilsson 2007] D. Backström and A. C. Nilsson, “Modelling the vibration of sandwich beams using frequency-dependent parameters”, *J. Sound Vib.* **300**:3-5 (2007), 589–611.
- [Boresi and Chong 1999] A. P. Boresi and K. P. Chong, *Elasticity in engineering mechanics*, 2nd ed., Wiley-Interscience, New York, 1999.
- [Branner 1995] K. Branner, *Capacity and lifetime of foam core sandwich structures*, Doctoral Dissertation, Technical University of Denmark, Lyngby, Denmark, 1995.
- [Caracciolo et al. 2004] R. Caracciolo, A. Gasparetto, and M. Giovagnoni, “An experimental technique for complete dynamic characterization of a viscoelastic material”, *J. Sound Vib.* **272**:3-5 (2004), 1013–1032.
- [Chang 2006] W.-D. Chang, “An improved real-coded genetic algorithm for parameters estimation of nonlinear systems”, *Mech. Syst. Signal Process.* **20**:1 (2006), 236–246.
- [Cook et al. 1989] R. D. Cook, D. S. Malkus, and M. E. Plesha, *Concepts and applications of finite element analysis*, 3rd ed., John Wiley & Sons, New York, 1989.
- [Grafe 1998] H. Grafe, *Model updating structural dynamics models using measured response functions*, Ph.D. Thesis, Imperial College of Science, Technology & Medicine, Department of Mechanical Engineering, London, 1998.
- [Kim and Kreider 2006] S. Kim and K. L. Kreider, “Parameter identification for nonlinear elastic and viscoelastic plates”, *Appl. Numer. Math.* **56**:12 (2006), 1538–1544.
- [Maia et al. 1997] N. M. M. Maia and J. M. M. Silva (editors), *Theoretical and experimental modal analysis*, John Wiley & Sons Inc., New York, 1997.
- [Ohkami and Swoboda 1999] T. Ohkami and G. Swoboda, “Parameter identification of viscoelastic materials”, *Comput. Geotech.* **24**:4 (1999), 279–295.
- [Park 2005] J. Park, “Transfer function methods to measure dynamic mechanical properties of complex structures”, *J. Sound Vib.* **288**:1-2 (2005), 57–79.
- [Pintelon et al. 2004] R. Pintelon, P. Guillaume, S. Vanlanduit, K. Belder, and Y. Rolain, “Identification of Young’s modulus from broadband modal analysis experiments”, *Mech. Syst. Signal Process.* **18**:4 (2004), 699–726.
- [Pritz 2004] T. Pritz, “Frequency power law of material damping”, *Appl. Acoust.* **65**:11 (2004), 1027–1036.
- [Shi et al. 2006] Y. Shi, H. Sol, and H. Hua, “Material parameter identification of sandwich beams by an inverse method”, *J. Sound Vib.* **290**:3-5 (2006), 1234–1255.
- [Singh et al. 2003] R. Singh, P. Davies, and A. K. Bajaj, “Estimation of the dynamical properties of polyurethane foam through use of Prony series”, *J. Sound Vib.* **264**:5 (2003), 1005–1043.
- [Tavallaey 2001] S. S. Tavallaey, *Wave propagation in sandwich structures*, Doctoral Dissertation, Marcus Wallenberg Laboratory, Stockholm, 2001, Available at www.diva-portal.org/diva/getDocument?urn_nbn_se_kth_diva-3088-2_._fulltext.pdf.

[Yang et al. 2005] W.-P. Yang, L.-W. Chen, and C.-C. Wang, “Vibration and dynamic stability of a traveling sandwich beam”, *J. Sound Vib.* **285**:3 (2005), 597–614.

[Zenkert 1997] D. Zenkert, *Introduction to sandwich construction*, Engineering Materials Advisory Services, Cradley Heath, UK, 1997.

Received 18 Jun 2007. Revised 4 Sep 2007. Accepted 18 Sep 2007.

NILSON BARBIERI: nilson.barbieri@pucpr.br

Pontifícia Universidade Católica do Paraná, Programa de Pós-Graduação em Engenharia Mecânica, Rua Imaculada Conceição, 1155, Prado Velho, 80215-901 Curitiba, Paraná, Brazil

RENATO BARBIERI: renato.barbieri@pucpr.br

Pontifícia Universidade Católica do Paraná, Programa de Pós-Graduação em Engenharia Mecânica, Rua Imaculada Conceição, 1155, Prado Velho, 80215-901, Curitiba, Paraná, Brazil

LUIZ CARLOS WINIKES: l Luiz.winikes@ig.com.br

Pontifícia Universidade Católica do Paraná, Programa de Pós-Graduação em Engenharia Mecânica, Rua Imaculada Conceição, 1155, Prado Velho, 80215-901 Curitiba, Paraná, Brazil

LUIS FERNANDO ORESTEN: luis-fernando.oresten@electrolux.com.br

Pontifícia Universidade Católica do Paraná, Programa de Pós-Graduação em Engenharia Mecânica, Rua Imaculada Conceição, 1155, Prado Velho, 80215-901 Curitiba, Paraná, Brazil

EXTENDED DISPLACEMENT DISCONTINUITY METHOD FOR CRACK ANALYSIS IN THREE-DIMENSIONAL TWO-PHASE TRANSVERSELY ISOTROPIC MAGNETOELECTROELASTIC MEDIA

MINGHAO ZHAO, NA LI, CUIYING FAN AND TONG LIU

Green's functions for extended displacement discontinuity in a three-dimensional two-phase transversely isotropic magnetoelastoelectric medium are obtained by using the integral equation method. Based on the obtained Green's functions, an extended displacement discontinuity method is developed for analysis of planar cracks of arbitrary shape in three-dimensional two-phase magnetoelastoelectric media. A rectangular interior crack parallel to the interface under the electrically and magnetically impermeable boundary condition is analyzed, and the extended intensity factors are calculated by the proposed method. The magnetoelastoelectric medium is made with BaTiO_3 as the inclusion and CoFe_2O_4 as the matrix. The influences of the interface and the material properties on the extended intensity factors are studied. Numerical results show that the three normalized extended intensity factors, that is, the stress intensity factor, the electric displacement intensity factor, and the magnetic induction intensity factor, are different both from each other and from the case of a crack in a homogeneous medium.

1. Introduction

Because of the coupling effect among the mechanical, electrical and magnetic properties, magnetoelastoelectric materials are finding more and more applications in many areas such as electronics, lasers, supersonics, infrared, and microwave sources. Laminated composite structures of these materials are often used to enhance the coupling effects. The integrity and reliability of the structures depend greatly on the defects, such as inclusion, void, crack, etc., in the materials and structures. So the study of cracks in magnetoelastoelectric materials and structures has been attracting more and more efforts [Huang and Kuo 1997; Wang and Shen 2003; Wang and Mai 2003; Gao and Noda 2004; Zhou et al. 2004; Tian and Rajapakse 2005; Zhao et al. 2006a; Zhao et al. 2006b].

It is difficult to find the analytical solution of a problem in a general case. Numerical approaches have to be used such as the finite element method (FEM) and the boundary element method (BEM). BEM is one of the preferred techniques for dealing with field concentration and singularity problems in fracture mechanics. In this method, the Green's function or a fundamental solution plays an important role. A lot of work has been done in this field. In two-dimensional problems, for example, Chung and Ting [1995] gave the two-dimensional Green's functions for anisotropic magnetoelastoelectric media with an

Keywords: Green's functions, two-phase, three-dimensional, magnetoelastoelectric medium, displacement discontinuity method, crack, intensity factor.

The work was supported by the National Natural Science Foundation of China (No.10572131) and the Program for New Century Excellent Talents in University of Henan Province (HANCET).

elliptic hole or rigid inclusion. Based on the Stroh formalism, [Jiang and Pan \[2004\]](#) obtained the two-dimensional Green's functions in an exact closed form for general inclusion problems of anisotropic and fully coupled magneto-electroelastic full, half, and bimaterial planes. [Liu and Liu \[2001\]](#) derived the Green's functions for an infinite two-dimensional anisotropic magneto-electroelastic medium including an elliptical cavity by use of the technique of conformal mapping and the Laurent series expansions. [Qin \[2004\]](#) derived the Green's function for magneto-electroelastic solids with an arbitrarily oriented half-plane or bimaterial interface. [Ding et al. \[2005\]](#) obtained the Green's functions for two-phase transversely isotropic magneto-electroelastic media, including the two-dimensional Green's functions of an infinite plane and an infinite half-plane as well as the three-dimensional counterparts.

In three-dimensional problems, [Pan \[2002\]](#) obtained the three-dimensional Green's functions in anisotropic infinite, semiinfinite, and two-phase magneto-electroelastic media based on extended Stroh formalism. [Hou et al. \[2005\]](#) presented the three-dimensional Green's functions of infinite, two-phase, and semiinfinite transversely isotropic magneto-electroelastic media under point forces, point charge, and magnetic monopole in terms of elementary functions for all cases of distinct eigenvalues and multiple eigenvalues. [Wang and Shen \[2002\]](#) gave the general solutions and the fundamental solutions or Green's functions for magneto-electroelastic media through five potential functions.

Parallel to the Green's functions for point force, the displacement discontinuity fundamental solutions [\[Crouch 1976\]](#) are other important kinds of Green's functions, which are of special use in displacement discontinuity boundary integral equation methods in fracture mechanics. This method is commonly called displacement discontinuity method (DDM). It has been proved to be one of the most powerful methods in fracture mechanics of purely elastic media [\[Wen 1996; Pan and Amadei 1996; Zhao et al. 1998\]](#), poroelastic media [\[Pan 1991\]](#), as well as for piezoelectric media [\[Zhao et al. 1997a; Zhao et al. 1997b; Zhao et al. 2004\]](#). In the present paper, the Green's functions for the extended displacement discontinuity in three-dimensional two-phase transversely isotropic magneto-electroelastic media will be derived. Based on the obtained Green's function, the extended Crouch fundamental solutions for uniformly distributed extended displacement discontinuity on a rectangular segment are obtained and the extended displacement discontinuity method is proposed. A rectangular crack is analyzed by the proposed method as an application.

2. Basic equation

In the absence of body force, electric charge, and electric current, the basic equations for a three-dimensional two-phase transversely isotropic magneto-electroelastic medium with the poling direction being along the z -direction in the $oxyz$ Cartesian coordinate system are given by

$$\sigma_{ij,j} = 0, \quad D_{i,i} = 0, \quad B_{i,i} = 0, \quad (1a)$$

$$\begin{aligned} \sigma_{ij} &= c_{ijkl}(u_{k,l} + u_{l,k})/2 + e_{kij}\varphi_{,k} + f_{kij}\psi_{,k}, \\ D_i &= e_{ikl}(u_{k,l} + u_{l,k})/2 - \varepsilon_{ik}\varphi_{,k} - g_{ik}\psi_{,k}, \\ B_i &= f_{ikl}(u_{k,l} + u_{l,k})/2 - g_{ik}\varphi_{,k} - \mu_{ik}\psi_{,k}, \end{aligned} \quad (1b)$$

where $i, j = 1, 2, 3(x, y, z)$, and σ_{ij} , D_i , and B_i are the stress, electric displacement, and magnetic induction components, respectively. u_i is the displacement component, and φ and ψ are respectively

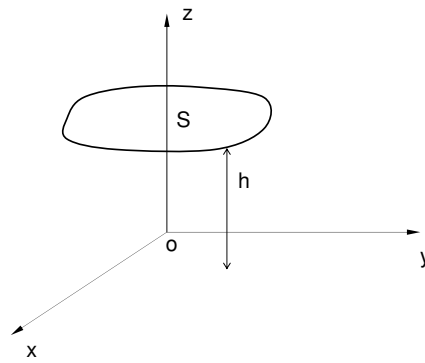


Figure 1. An arbitrarily shaped planar crack S in the $z = h (h > 0)$ plane in a magneto-electroelastic bimaterial.

the electric potential and magnetic potential. c_{ij} , e_{kij} , f_{kij} , ϵ_{ij} , g_{ij} and μ_{ij} are the elastic constant, piezo-electric constant, piezomagnetic constant, dielectric permittivity, electromagnetic constant, and magnetic permeability, respectively. A subscript comma denotes the partial differentiation with respect to the coordinate.

3. Boundary integral expressions of extended displacement discontinuity

Consider a three-dimensional two-phase transversely isotropic magneto-electroelastic medium with the interface being parallel to the plane of isotropy. A Cartesian coordinate system is set up such that the xoy -plane lies in the interface. A planar crack S of arbitrary shape lies in the plane $z = h (h > 0)$ as shown in Figure 1. The upper and lower surfaces of S are denoted by S^+ and S^- , respectively. The outer normal vectors of S^+ and S^- are respectively given by

$$\{n_i\}^+ = \{0, 0, -1\}, \quad \{n_i\}^- = \{0, 0, 1\}. \tag{2}$$

The prescribed tractions, the electric displacement boundary value, and the magnetic induction boundary value on the crack faces are denoted respectively by p_i ($i = 1, 2, 3$, or x, y, z), ω , and γ , which hereafter are called extended tractions. By using the extended point force fundamental solutions given in Appendix A and the Somigliana identity for magneto-electroelastic media, the displacements u_i , the electric potential φ , and the magnetic potential ψ at any internal point (x, y, z) can be expressed in the following forms

$$u_i(x, y, z) = - \int_{S^+} [P_{ij}^F u_j + \Omega_i^F \varphi + \Gamma_i^F \psi] dS - \int_{S^-} [P_{ij}^F u_j + \Omega_i^F \varphi + \Gamma_i^F \psi] dS + \int_{S^+} [p_j U_{ij}^F + \omega \Phi_i^F + \gamma \Psi_i^F] dS + \int_{S^-} [p_j U_{ij}^F + \omega \Phi_i^F + \gamma \Psi_i^F] dS, \tag{3}$$

$$\begin{aligned}
 -\varphi(x, y, z) = & -\int_{S^+} [P_j^D u_j + \Omega^D \varphi + \Gamma^D \psi] dS - \int_{S^-} [P_j^D u_j + \Omega^D \varphi + \Gamma^D \psi] dS \\
 & + \int_{S^+} [p_j U_j^D + \omega \Phi^D + \gamma \Psi^D] dS + \int_{S^-} [p_j U_j^D + \omega \Phi^D + \gamma \Psi^D] dS, \quad (4)
 \end{aligned}$$

$$\begin{aligned}
 -\psi(x, y, z) = & -\int_{S^+} [P_j^B u_j + \Omega^B \varphi + \Gamma^B \psi] dS - \int_{S^-} [P_j^B u_j + \Omega^B \varphi + \Gamma^B \psi] dS \\
 & + \int_{S^+} [p_j U_j^B + \omega \Phi^B + \gamma \Psi^B] dS + \int_{S^-} [p_j U_j^B + \omega \Phi^B + \gamma \Psi^B] dS, \quad (5)
 \end{aligned}$$

where $P_{ij}^F, \Omega_i^F, \Gamma_i^F, U_{ij}^F, \Phi_i^F,$ and Ψ_i^F are the tractions, the electric displacement boundary value, the magnetic induction boundary value, the displacements, the electric potential, and the magnetic potential of the fundamental solutions corresponding to the unit point force in the i th direction, respectively, $P_j^D, \Omega^D, \Gamma^D, U_j^D, \Phi^D,$ and Ψ^D corresponding to the unit point electric charge and $P_j^B, \Omega^B, \Gamma^B, U_j^B, \Phi^B,$ and Ψ^B corresponding to the unit point electric current

$$\begin{aligned}
 P_{ij}^F &= \sigma_{ijk}^F n_k, & \Omega_i^F &= D_{ik}^F n_k, & \Gamma_i^F &= B_{ik}^F n_k, \\
 P_j^D &= \sigma_{jk}^D n_k, & \Omega^D &= D_k^D n_k, & \Gamma^D &= B_k^D n_k, \\
 P_j^B &= \sigma_{jk}^B n_k, & \Omega^B &= D_k^B n_k, & \Gamma^B &= B_k^B n_k,
 \end{aligned} \quad (6)$$

where the upper index $F, D,$ and B refer to the variables corresponding to point forces, point electric charge, and point electric current, respectively. Based on the fundamental solutions, we easily obtain the following relationship on the crack faces

$$\begin{aligned}
 P_{ij}^F|_{S^+} &= -P_{ij}^F|_{S^-}, & U_{ij}^F|_{S^+} &= U_{ij}^F|_{S^-}, & \Omega_i^F|_{S^+} &= -\Omega_i^F|_{S^-}, \\
 \Phi_i^F|_{S^+} &= \Phi_i^F|_{S^-}, & \Gamma_i^F|_{S^+} &= -\Gamma_i^F|_{S^-}, & \Psi_i^F|_{S^+} &= \Psi_i^F|_{S^-} \\
 P_j^D|_{S^+} &= -P_j^D|_{S^-}, & U_j^D|_{S^+} &= U_j^D|_{S^-}, & \Omega^D|_{S^+} &= -\Omega^D|_{S^-}, \\
 \Phi^D|_{S^+} &= \Phi^D|_{S^-}, & \Gamma^D|_{S^+} &= -\Gamma^D|_{S^-}, & \Psi^D|_{S^+} &= \Psi^D|_{S^-}, \\
 P_j^B|_{S^+} &= -P_j^B|_{S^-}, & U_j^B|_{S^+} &= U_j^B|_{S^-}, & \Omega^B|_{S^+} &= -\Omega^B|_{S^-}, \\
 \Phi^B|_{S^+} &= \Phi^B|_{S^-}, & \Gamma^B|_{S^+} &= -\Gamma^B|_{S^-}, & \Psi^B|_{S^+} &= \Psi^B|_{S^-}.
 \end{aligned}$$

On assuming that the extended tractions on the upper and lower crack faces satisfy the conditions

$$p_i|_{S^+} = -p_i|_{S^-}, \quad \omega|_{S^+} = -\omega|_{S^-}, \quad \gamma|_{S^+} = -\gamma|_{S^-}, \quad (7)$$

and considering Equations (2) and (6)–(7), Equations (3)–(5) are reduced to

$$\begin{aligned}
 u_i(x, y, z) &= -\int_{S^+} [P_{ij}^F \|u_j\| + \Omega_i^F \|\varphi\| + \Gamma_i^F \|\psi\|] dS(\xi, \eta), \\
 -\varphi(x, y, z) &= -\int_{S^+} [P_j^D \|u_j\| + \Omega^D \|\varphi\| + \Gamma^D \|\psi\|] dS(\xi, \eta), \\
 -\psi(x, y, z) &= -\int_{S^+} [P_j^B \|u_j\| + \Omega^B \|\varphi\| + \Gamma^B \|\psi\|] dS(\xi, \eta).
 \end{aligned} \quad (8)$$

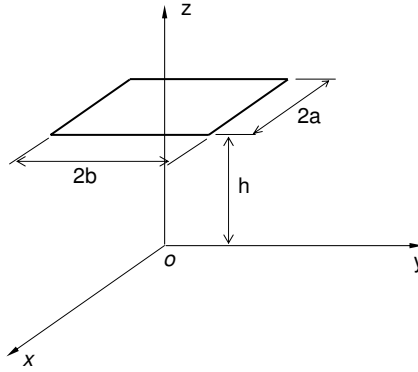


Figure 2. A rectangular crack in the plane $z = h (h > 0)$ in a magneto-electroelastic bimaterial.

In Equation (8), $\|u_i\|$, $\|\varphi\|$, and $\|\psi\|$ are respectively the displacement discontinuities, the electric potential discontinuity, and the magnetic potential discontinuity across the crack faces, which are called the extended displacement discontinuities and given by:

$$\begin{aligned} \|u_i(\xi, \eta)\| &= u_i(\xi, \eta, h^+) - u_i(\xi, \eta, h^-), & \|\varphi(\xi, \eta)\| &= \varphi(\xi, \eta, h^+) - \varphi(\xi, \eta, h^-), \\ \|\psi(\xi, \eta)\| &= \psi(\xi, \eta, h^+) - \psi(\xi, \eta, h^-). \end{aligned}$$

In the following derivations, the displacement components are also denoted by $u = u_x, v = u_y, w = u_z$, and the following symbols will be used

$$\begin{aligned} z_i &= s_i z, & \zeta_i &= s_i h, & z_{ij} &= h_i + z_j, \\ R_{ij} &= \sqrt{(\xi - x)^2 + (\eta - y)^2 + z_{ij}^2}, & \bar{z}_{ij} &= h_i - z_j, \\ \bar{R}_{ij} &= \sqrt{(\xi - x)^2 + (\eta - y)^2 + \bar{z}_{ij}^2}, & \tilde{R}_{ij} &= R_{ij} + z_{ij}, \\ \hat{R}_{ij} &= \bar{R}_{ij} - \bar{z}_{ij}, & (i, j &= 1, 2, 3, 4, \text{ and } i = j = 5), \end{aligned}$$

where s_i are material constants, which are given in Appendix A.

4. Green's functions for unit extended point displacement discontinuities

Assume that the planar crack S is a rectangle of length $2a = 2b$ with the center being at point $(0, 0, h)$, as shown in Figure 2.

The fundamental solutions corresponding to extended displacement discontinuities should satisfy the governing equations of magneto-electroelastic media subject, respectively, to the following conditions:

$$\lim_{a \rightarrow 0} \int_S \{ \|u\|, \|v\|, \|w\|, \|\varphi\|, \|\psi\| \} dS = \{1, 0, 0, 0, 0\}, \tag{9a}$$

$$\lim_{a \rightarrow 0} \int_S \{ \|u\|, \|v\|, \|w\|, \|\varphi\|, \|\psi\| \} dS = \{0, 1, 0, 0, 0\}, \tag{9b}$$

$$\lim_{a \rightarrow 0} \int_S \{ \|u\|, \|v\|, \|w\|, \|\varphi\|, \|\psi\| \} dS = \{0, 0, 1, 0, 0\}, \tag{9c}$$

$$\lim_{a \rightarrow 0} \int_S \{ \|u\|, \|v\|, \|w\|, \|\varphi\|, \|\psi\| \} dS = \{0, 0, 0, 1, 0\}, \tag{9d}$$

$$\lim_{a \rightarrow 0} \int_S \{ \|u\|, \|v\|, \|w\|, \|\varphi\|, \|\psi\| \} dS = \{0, 0, 0, 0, 1\}. \tag{9e}$$

4.1. Green’s function satisfying Equation (9a). On the plane $z = h (h > 0)$, the discontinuity boundary condition in the x -axis direction is indeed the Dirac δ -function

$$\|u(\xi, \eta)\| = \delta(\xi, \eta). \tag{10}$$

Inserting Equations (9a) and (10) and the fundamental solutions for extended point force in Appendix A into Equation (8) yields

$$u = -\omega_{51} \left[D_5 \left(\frac{1}{\bar{R}_{55} \hat{R}_{55}} - \frac{y^2}{\bar{R}_{55}^3 \hat{R}_{55}} - \frac{y^2}{\bar{R}_{55}^2 \hat{R}_{55}^2} \right) - D_{55} \left(\frac{1}{R_{55} \tilde{R}_{55}} - \frac{y^2}{R_{55}^3 \tilde{R}_{55}} - \frac{y^2}{R_{55}^2 \tilde{R}_{55}^2} \right) \right] + \sum_{i=1}^4 \omega_{i1} \left[D_i \left(\frac{1}{\bar{R}_{ii} \hat{R}_{ii}} - \frac{x^2}{\bar{R}_{ii}^3 \hat{R}_{ii}} - \frac{x^2}{\bar{R}_{ii}^2 \hat{R}_{ii}^2} \right) - \sum_{j=1}^4 D_{ij} \left(\frac{1}{R_{ij} \tilde{R}_{ij}} - \frac{x^2}{R_{ij}^3 \tilde{R}_{ij}} - \frac{x^2}{R_{ij}^2 \tilde{R}_{ij}^2} \right) \right], \tag{11}$$

$$v = -xy\omega_{51} \left[D_5 \left(\frac{1}{\bar{R}_{55}^3 \hat{R}_{55}} + \frac{1}{\bar{R}_{55}^2 \hat{R}_{55}^2} \right) - D_{55} \left(\frac{1}{R_{55}^3 \tilde{R}_{55}} + \frac{1}{R_{55}^2 \tilde{R}_{55}^2} \right) \right] - xy \sum_{i=1}^4 \omega_{i1} \left[D_i \left(\frac{1}{\bar{R}_{ii}^3 \hat{R}_{ii}} + \frac{1}{\bar{R}_{ii}^2 \hat{R}_{ii}^2} \right) - \sum_{j=1}^4 D_{ij} \left(\frac{1}{R_{ij}^3 \tilde{R}_{ij}} + \frac{1}{R_{ij}^2 \tilde{R}_{ij}^2} \right) \right], \tag{12}$$

$$w = -x \sum_{i=1}^4 \omega_{i1} \left(\frac{A_i}{\bar{R}_{ii}^3} - \sum_{j=1}^4 \frac{A_{ij}}{R_{ij}^3} \right), \quad \varphi = x \sum_{i=1}^4 \omega_{i1} \left(\frac{B_i}{\bar{R}_{ii}^3} - \sum_{j=1}^4 \frac{B_{ij}}{R_{ij}^3} \right), \tag{13}$$

$$\psi = x \sum_{i=1}^4 \omega_{i1} \left(\frac{C_i}{\bar{R}_{ii}^3} - \sum_{j=1}^4 \frac{C_{ij}}{R_{ij}^3} \right). \tag{14}$$

Substituting Equations (11)–(14) into the constitutive Equation (1b) yields the stress, electric displacement, and magnetic induction

$$\sigma_{yz} = 3xy \left\{ c_{44}\omega_{51} \left(D_5 \frac{s_5}{\bar{R}_{55}^5} - D_{55} \frac{s_5}{R_{55}^5} \right) + c_{44} \sum_{i=1}^4 \omega_{i1} \left(D_i \frac{s_i}{\bar{R}_{ii}^5} - \sum_{j=1}^4 D_{ij} \frac{s_j}{R_{ij}^5} \right) + \sum_{i=1}^4 \omega_{i1} \left[(c_{44}A_i - e_{15}B_i - f_{15}C_i) \frac{1}{\bar{R}_{ii}^5} - \sum_{j=1}^4 (c_{44}A_{ij} - e_{15}B_{ij} - f_{15}C_{ij}) \frac{1}{R_{ij}^5} \right] \right\}, \quad (15)$$

$$\sigma_{xz} = c_{44} \left\{ \omega_{51}s_5 \left[D_5 \left(\frac{1}{\bar{R}_{55}^3} - y^2 \frac{3}{\bar{R}_{55}^5} \right) - D_{55} \left(\frac{1}{R_{55}^3} - y^2 \frac{3}{R_{55}^5} \right) \right] + \sum_{i=1}^4 \omega_{i1} \left[-D_i s_i \left(\frac{1}{\bar{R}_{ii}^3} - x^2 \frac{3}{\bar{R}_{ii}^5} \right) + \sum_{j=1}^4 D_{ij} s_j \left(\frac{1}{R_{ij}^3} - x^2 \frac{3}{R_{ij}^5} \right) \right] - \sum_{i=1}^4 \omega_{i1} \left[(c_{44}A_i - e_{15}B_i - f_{15}C_i) \left(\frac{1}{\bar{R}_{ii}^3} - \frac{3x^2}{\bar{R}_{ii}^5} \right) - \sum_{j=1}^4 (c_{44}A_{ij} - e_{15}B_{ij} - f_{15}C_{ij}) \left(\frac{1}{R_{ij}^3} - \frac{3x^2}{R_{ij}^5} \right) \right] \right\}, \quad (16)$$

$$\sigma_{zz} = -4c_{13}x \sum_{i=1}^4 \omega_{i1} \left[D_i \left(\frac{1}{\bar{R}_{ii}^3 \hat{R}_{ii}} + \frac{1}{\bar{R}_{ii}^2 \hat{R}_{ii}^2} \right) - \sum_{j=1}^4 D_{ij} \left(\frac{1}{R_{ij}^3 \tilde{R}_{ij}} + \frac{1}{R_{ij}^2 \tilde{R}_{ij}^2} \right) \right] + (x^2 + y^2)xc_{13} \sum_{i=1}^4 \omega_{i1} \left[D_i \left(\frac{3}{\bar{R}_{ii}^5 \hat{R}_{ii}} + \frac{3}{\bar{R}_{ii}^4 \hat{R}_{ii}^2} + \frac{2}{\bar{R}_{ii}^3 \hat{R}_{ii}^3} \right) - \sum_{j=1}^4 D_{ij} \left(\frac{3}{R_{ij}^5 \tilde{R}_{ij}} + \frac{3}{R_{ij}^4 \tilde{R}_{ij}^2} + \frac{2}{R_{ij}^3 \tilde{R}_{ij}^3} \right) \right] - x \sum_{i=1}^4 3\omega_{i1} \left[\frac{s_i z_{ii}}{\bar{R}_{ii}^5} (c_{33}A_i - e_{33}B_i - f_{33}C_i) + \sum_{j=1}^4 \frac{s_j z_{ij}}{R_{ij}^5} (c_{33}A_{ij} - e_{33}B_{ij} - f_{33}C_{ij}) \right], \quad (17)$$

$$D_z = -4e_{31}x \sum_{i=1}^4 \omega_{i1} \left[D_i \left(\frac{1}{\bar{R}_{ii}^3 \hat{R}_{ii}} + \frac{1}{\bar{R}_{ii}^2 \hat{R}_{ii}^2} \right) - \sum_{j=1}^4 D_{ij} \left(\frac{1}{R_{ij}^3 \tilde{R}_{ij}} + \frac{1}{R_{ij}^2 \tilde{R}_{ij}^2} \right) \right] + (x^2 + y^2)xe_{31} \sum_{i=1}^4 \omega_{i1} \left[D_i \left(\frac{3}{\bar{R}_{ii}^5 \hat{R}_{ii}} + \frac{3}{\bar{R}_{ii}^4 \hat{R}_{ii}^2} + \frac{2}{\bar{R}_{ii}^3 \hat{R}_{ii}^3} \right) - \sum_{j=1}^4 D_{ij} \left(\frac{3}{R_{ij}^5 \tilde{R}_{ij}} + \frac{3}{R_{ij}^4 \tilde{R}_{ij}^2} + \frac{2}{R_{ij}^3 \tilde{R}_{ij}^3} \right) \right] - x \sum_{i=1}^4 3\omega_{i1} \left[\frac{s_i z_{ii}}{\bar{R}_{ii}^5} (e_{33}A_i + \varepsilon_{33}B_i + g_{33}C_i) + \sum_{j=1}^4 \frac{s_j z_{ij}}{R_{ij}^5} (e_{33}A_{ij} + \varepsilon_{33}B_{ij} + g_{33}C_{ij}) \right], \quad (18)$$

$$\begin{aligned}
 B_z = & -4f_{31}x \sum_{i=1}^4 \omega_{i1} \left[D_i \left(\frac{1}{\bar{R}_{ii}^3 \hat{R}_{ii}} + \frac{1}{\bar{R}_{ii}^2 \hat{R}_{ii}^2} \right) - \sum_{j=1}^4 D_{ij} \left(\frac{1}{R_{ij}^3 \tilde{R}_{ij}} + \frac{1}{R_{ij}^2 \tilde{R}_{ij}^2} \right) \right] \\
 & + (x^2 + y^2)x f_{31} \sum_{i=1}^4 \omega_{i1} \left[D_i \left(\frac{3}{\bar{R}_{ii}^5 \hat{R}_{ii}} + \frac{3}{\bar{R}_{ii}^4 \hat{R}_{ii}^2} + \frac{2}{\bar{R}_{ii}^3 \hat{R}_{ii}^3} \right) - \sum_{j=1}^4 D_{ij} \left(\frac{3}{R_{ij}^5 \tilde{R}_{ij}} + \frac{3}{R_{ij}^4 \tilde{R}_{ij}^2} + \frac{2}{R_{ij}^3 \tilde{R}_{ij}^3} \right) \right] \\
 & - x \sum_{i=1}^4 3\omega_{i1} \left[\frac{z_{ii} s_i}{\bar{R}_{ii}^5} (f_{33} A_i + g_{33} B_i + \mu_{33} C_i) + \sum_{j=1}^4 \frac{z_{ij} s_j}{R_{ij}^5} (f_{33} A_{ij} + g_{33} B_{ij} + \mu_{33} C_{ij}) \right]. \quad (19)
 \end{aligned}$$

From above solutions, the Green’s function corresponding to Equation (9b) can be easily obtained by coordinate transformation.

4.2. Green’s function satisfying Equation (9c). On the crack face, the displacement discontinuity condition in the z-axis direction is

$$\|w(\xi, \eta)\| = \delta(\xi, \eta). \quad (20)$$

Inserting Equations (9c) and (20) and the fundamental solutions for extended point force in Appendix A into Equation (8) yields the extended displacements

$$\begin{aligned}
 u &= -x \sum_{i=1}^4 \vartheta_{i1} \left[\frac{D_i}{\bar{R}_{ii}^3} + \sum_{j=1}^4 \frac{D_{ij}}{R_{ij}^3} \right], \\
 v &= -y \sum_{i=1}^4 \vartheta_{i1} \left[\frac{D_i}{\bar{R}_{ii}^3} + \sum_{j=1}^4 \frac{D_{ij}}{R_{ij}^3} \right], \\
 w &= \sum_{i=1}^4 \vartheta_{i1} \left[\frac{A_i(h_i - z_i)}{\bar{R}_{ii}^3} - \sum_{j=1}^4 \frac{A_{ij}(h_i + z_j)}{R_{ij}^3} \right], \\
 \varphi &= -\sum_{i=1}^4 \vartheta_{i1} \left[\frac{B_i(h_i - z_i)}{\bar{R}_{ii}^3} - \sum_{j=1}^4 \frac{B_{ij}(h_i + z_j)}{R_{ij}^3} \right], \\
 \psi &= -\sum_{i=1}^4 \vartheta_{i1} \left[\frac{C_i(h_i - z_i)}{\bar{R}_{ii}^3} - \sum_{j=1}^4 \frac{C_{ij}(h_i + z_j)}{R_{ij}^3} \right]. \quad (21)
 \end{aligned}$$

Similarly, the corresponding stress, electric displacement and magnetic induction are derived

$$\begin{aligned}
 \sigma_{yz} = & 3y \left\{ c_{44} \sum_{i=1}^4 \vartheta_{i1} \left(-D_i \frac{s_i z_{ii}}{\bar{R}_{ii}^5} + \sum_{j=1}^4 D_{ij} \frac{s_j z_{ij}}{R_{ij}^5} \right) - \sum_{i=1}^4 \vartheta_{i1} \left[(c_{44} A_i - e_{15} B_i - f_{15} C_i) \frac{(h_i - z_i)}{\bar{R}_{ii}^5} \right. \right. \\
 & \left. \left. - \sum_{j=1}^4 (c_{44} A_{ij} - e_{15} B_{ij} - f_{15} C_{ij}) \frac{(h_j + z_j)}{R_{ij}^5} \right] \right\}, \quad (22)
 \end{aligned}$$

$$\sigma_{xz} = 3x \left\{ c_{44} \sum_{i=1}^4 \vartheta_{i1} \left(-D_i \frac{s_i z_{ii}}{\bar{R}_{ii}^5} + \sum_{j=1}^4 D_{ij} \frac{s_j z_{ij}}{R_{ij}^5} \right) - \sum_{i=1}^4 \vartheta_{i1} \left[(c_{44} A_i - e_{15} B_i - f_{15} C_i) \frac{(h_i - z_i)}{\bar{R}_{ii}^5} - \sum_{j=1}^4 (c_{44} A_{ij} - e_{15} B_{ij} - f_{15} C_{ij}) \frac{(h_j + z_j)}{R_{ij}^5} \right] \right\}, \quad (23)$$

$$\sigma_{zz} = \sum_{i=1}^4 \vartheta_{i1} \left\{ c_{13} \left[D_i \left(-\frac{2}{\bar{R}_{ii}^3} + \frac{3(x^2 + y^2)}{\bar{R}_{ii}^5} \right) + \sum_{j=1}^4 D_{ij} \left(-\frac{2}{R_{ij}^3} + \frac{3(x^2 + y^2)}{R_{ij}^5} \right) \right] - s_i (c_{33} A_i - e_{33} B_i - f_{33} C_i) \left(\frac{1}{\bar{R}_{ii}^3} - \frac{3z_i (h_i - z_i)}{\bar{R}_{ii}^5} \right) - \sum_{j=1}^4 D_{ij} s_j (c_{33} A_{ij} - e_{33} B_{ij} - f_{33} C_{ij}) \left(\frac{1}{R_{ij}^3} - \frac{3z_j (h_i + z_j)}{R_{ij}^5} \right) \right\}, \quad (24)$$

$$D_z = \sum_{i=1}^4 \vartheta_{i1} \left\{ e_{31} \left[D_i \left(-\frac{2}{\bar{R}_{ii}^3} + \frac{3(x^2 + y^2)}{\bar{R}_{ii}^5} \right) + \sum_{j=1}^4 D_{ij} \left(-\frac{2}{R_{ij}^3} + \frac{3(x^2 + y^2)}{R_{ij}^5} \right) \right] - s_i (e_{33} A_i + \varepsilon_{33} B_i + g_{33} C_i) \left(\frac{1}{\bar{R}_{ii}^3} - \frac{3z_i (h_i - z_i)}{\bar{R}_{ii}^5} \right) - \sum_{j=1}^4 D_{ij} s_j (e_{33} A_{ij} + \varepsilon_{33} B_{ij} + g_{33} C_{ij}) \left(\frac{1}{R_{ij}^3} - \frac{3z_j (h_i + z_j)}{R_{ij}^5} \right) \right\}, \quad (25)$$

$$B_z = \sum_{i=1}^4 \vartheta_{i1} \left\{ f_{31} \left[D_i \left(-\frac{2}{\bar{R}_{ii}^3} + \frac{3(x^2 + y^2)}{\bar{R}_{ii}^5} \right) + \sum_{j=1}^4 D_{ij} \left(-\frac{2}{R_{ij}^3} + \frac{3(x^2 + y^2)}{R_{ij}^5} \right) \right] - s_i (f_{33} A_i + g_{33} B_i + \mu_{33} C_i) \left(\frac{1}{\bar{R}_{ii}^3} - \frac{3z_i (h_i - z_i)}{\bar{R}_{ii}^5} \right) - \sum_{j=1}^4 D_{ij} s_j (f_{33} A_{ij} + g_{33} B_{ij} + \mu_{33} C_{ij}) \left(\frac{1}{R_{ij}^3} - \frac{3z_j (h_i + z_j)}{R_{ij}^5} \right) \right\}. \quad (26)$$

The fundamental solutions corresponding to Equation (9d) and Equation (9e) can be obtained by taking ϑ_{i2} and ϑ_{i3} instead of ϑ_{i1} , respectively.

5. Extended crouch fundamental solution

In this section, the extended Crouch fundamental solutions are derived for a three-dimensional two-phase magneto-electroelastic medium.

Consider a rectangular crack of length $2a$ and width $2b$ in the plane $z = h$. Uniformly distributed extended displacement discontinuities $\|u^e\|$, $\|v^e\|$, $\|w^e\|$, $\|\varphi^e\|$, and $\|\psi^e\|$ are applied on the crack faces. Integrating the extended displacement discontinuity Green's functions derived in last section on the rectangular crack with lengthy manipulations yields the extended stress fields

$$\begin{aligned} \sigma_{xz}^e = & (L_{X1}\bar{G}_{55}^{(1)} - L_{X2}G_{55}^{(1)})\|u^e\| - (L_{X1}\bar{G}_{55}^{(3)} - L_{X2}G_{55}^{(3)})\|v^e\| \\ & + \sum_{i=1}^4 \left[\left(-L_{11}^i\bar{G}_{ii}^{(2)} + \sum_{j=1}^4 L_{12}^{ij}G_{ij}^{(2)} \right) \|u^e\| - \left(L_{11}^i\bar{G}_{ii}^{(3)} - \sum_{j=1}^4 L_{12}^{ij}G_{ij}^{(3)} \right) \|v^e\| \right. \\ & \quad - \bar{G}_{ii}^{(4)}(L_{211}^i\|w^e\| + L_{212}^i\|\varphi^e\| + L_{213}^i\|\psi^e\|) \\ & \quad \left. + \sum_{j=1}^4 G_{ij}^{(4)}(L_{221}^{ij}\|w^e\| + L_{222}^{ij}\|\varphi^e\| + L_{223}^{ij}\|\psi^e\|) \right], \quad (27) \end{aligned}$$

$$\begin{aligned} \sigma_{yz}^e = & (L_{X1}\bar{G}_{55}^{(3)} - L_{X2}G_{55}^{(3)})\|u^e\| - (L_{X1}\bar{G}_{55}^{(2)} - L_{X2}G_{55}^{(2)})\|v^e\| \\ & + \sum_{i=1}^4 \left[\left(L_{11}^i\bar{G}_{ii}^{(3)} - \sum_{j=1}^4 L_{12}^{ij}G_{ij}^{(3)} \right) \|u^e\| + \left(L_{11}^i\bar{G}_{ii}^{(1)} - \sum_{j=1}^4 L_{12}^{ij}G_{ij}^{(1)} \right) \|v^e\| \right. \\ & \quad - \bar{G}_{ii}^{(5)}(L_{211}^i\|w^e\| + L_{212}^i\|\varphi^e\| + L_{213}^i\|\psi^e\|) \\ & \quad \left. + \sum_{j=1}^4 G_{ij}^{(5)}(L_{221}^{ij}\|w^e\| + L_{222}^{ij}\|\varphi^e\| + L_{223}^{ij}\|\psi^e\|) \right], \quad (28) \end{aligned}$$

$$\begin{aligned} \sigma_{zz}^e = & \sum_{i=1}^4 \left[\left(-L_{Z1}^i\bar{G}_{ii}^{(4)} + \sum_{j=1}^4 L_{Z2}^{ij}G_{ij}^{(4)} \right) \|u^e\| + \left(L_{Z1}^i\bar{G}_{ii}^{(5)} + \sum_{j=1}^4 L_{Z2}^{ij}G_{ij}^{(5)} \right) \|v^e\| \right. \\ & \quad + \bar{G}_{ii}^{(6)}(L_{Z11}^i\|w^e\| + L_{Z12}^i\|\varphi^e\| + L_{Z13}^i\|\psi^e\|) \\ & \quad \left. + \sum_{j=1}^4 G_{ij}^{(6)}(L_{Z21}^{ij}\|w^e\| + L_{Z22}^{ij}\|\varphi^e\| + L_{Z23}^{ij}\|\psi^e\|) \right], \quad (29) \end{aligned}$$

$$\begin{aligned} D_z^e = & \sum_{i=1}^4 \left[\left(-L_{D1}^i\bar{G}_{ii}^{(4)} + \sum_{j=1}^4 L_{D2}^{ij}G_{ij}^{(4)} \right) \|u^e\| + \left(L_{D1}^i\bar{G}_{ii}^{(5)} + \sum_{j=1}^4 L_{D2}^{ij}G_{ij}^{(5)} \right) \|v^e\| \right. \\ & \quad + \bar{G}_{ii}^{(6)}(L_{D11}^i\|w^e\| + L_{D12}^i\|\varphi^e\| + L_{D13}^i\|\psi^e\|) \\ & \quad \left. + \sum_{j=1}^4 G_{ij}^{(6)}(L_{D21}^{ij}\|w^e\| + L_{D22}^{ij}\|\varphi^e\| + L_{D23}^{ij}\|\psi^e\|) \right], \quad (30) \end{aligned}$$

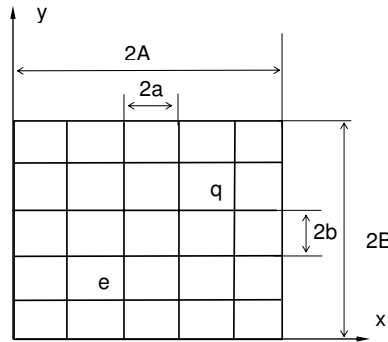


Figure 3. Boundary element mesh for a rectangular crack.

$$\begin{aligned}
 B_z^e = \sum_{i=1}^4 \left[\left(-L_{B1}^i \bar{G}_{ii}^{(4)} + \sum_{j=1}^4 L_{B2}^{ij} G_{ij}^{(4)} \right) \|u^e\| + \left(L_{B1}^i \bar{G}_{ii}^{(5)} + \sum_{j=1}^4 L_{B2}^{ij} G_{ij}^{(5)} \right) \|v^e\| \right. \\
 \left. + \bar{G}_{ii}^{(6)} (L_{B11}^i \|w^e\| + L_{B12}^i \|\varphi^e\| + L_{B13}^i \|\psi^e\|) \right. \\
 \left. + \sum_{j=1}^4 G_{ij}^{(6)} \left(L_{B21}^{ij} \|w^e\| + L_{B22}^{ij} \|\varphi^e\| + L_{B23}^{ij} \|\psi^e\| \right) \right], \quad (31)
 \end{aligned}$$

where the material related constants Ls and the functions Gs and $\bar{G}s$ with different superscripts and subscripts are given in [Appendix B](#). These solutions are called extended Crouch fundamental solutions.

Equations (27)–(31) can be written in a compact form

$$\sigma_i^e = \sum_{j=1}^5 F_{ij}^e \|u_j^e\|, \quad i, j = 1, 2, 3, 4, 5, \quad (32)$$

where $\sigma_1^e = \sigma_{xz}^e$, $\sigma_2^e = \sigma_{yz}^e$, $\sigma_3^e = \sigma_{zz}^e$, $\sigma_4^e = D_z^e$, $\sigma_5^e = B_z^e$, $\|u_1^e\| = \|u^e\|$, $\|u_2^e\| = \|v^e\|$, $\|u_3^e\| = \|w^e\|$, $\|u_4^e\| = \|\varphi^e\|$, $\|u_5^e\| = \|\psi^e\|$, and F_{ij}^e are called the influence functions of the rectangular element.

6. Extended displacement discontinuity method

If the domain of a crack is divided into N rectangular elements as shown in [Figure 3](#) by using the extended Crouch fundamental solutions, the extended stress at the centroid of element q can be obtained by superposing the contribution of all the elements. Then, introducing the boundary conditions on the crack faces, one has

$$\sum_{e=1}^N \sum_{j=1}^5 F_{ij}^e (x_q - x_e, y_q - y_e, z_q - z_e) \|u_j^e\| = \sigma_i^0(q), \quad q = 1, 2, 3, \dots, N, \quad (33)$$

where σ_i^0 is related to the applied extended loading on the crack faces

$$\begin{aligned} p_x(x, y) &= -\sigma_1^0(x, y), & p_y(x, y) &= -\sigma_2^0(x, y), \\ p_z(x, y) &= -\sigma_3^0(x, y), & \omega(x, y) &= -\sigma_4^0(x, y), \\ \gamma(x, y) &= -\sigma_5^0(x, y). \end{aligned} \quad (34)$$

Solving Equation (33), one obtains the extended displacement discontinuities on the crack faces. Furthermore, the extended stresses at any point in the crack plane can be calculated by

$$\sigma_i(x, y, h) = \sum_{e=1}^N \sum_{j=1}^5 F_{ij}^e(x - x_e, y - y_e, 0) \|u_j^e\|. \quad (35)$$

Finally, the extended stress intensity factors are calculated in [Zhao et al. 1997b; Zhao et al. 1998]:

$$K_I^F = \lim_{\rho \rightarrow 0} \sqrt{2\pi\rho} \sigma_{zz}, \quad K_I^D = \lim_{\rho \rightarrow 0} \sqrt{2\pi\rho} D_z, \quad K_I^B = \lim_{\rho \rightarrow 0} \sqrt{2\pi\rho} B_z, \quad (36)$$

where ρ is the distance from the crack tip.

7. Numerical examples and discussions

Consider a rectangular crack of sides $2A \times 2B$ at plane $z = h$ centered at point $(0, 0, h)$, with the sides parallel to the x - or y -axis. The magnetoelastic medium is made of BaTiO₃ as the inclusion with CoFe₂O₄ as the matrix. The piezoelectric volume fraction of the inclusion is denoted by V_i . The material constants are given as follows [Huang et al. 1998]:

BaTiO₃ :

$$\begin{aligned} c_{11} &= 166 \text{ GPa}, & c_{33} &= 162 \text{ GPa}, \\ c_{44} &= 43 \text{ GPa}, & c_{12} &= 77 \text{ GPa}, \\ c_{13} &= 78 \text{ GPa}, & e_{31} &= -4.4 \text{ C/m}^2, \\ e_{33} &= 18.6 \text{ C/m}^2, & e_{15} &= 11.6 \text{ C/m}^2, \\ \varepsilon_{11} &= 11.2 \times 10^{-9} \text{ C}^2/(\text{Nm}^2), & \varepsilon_{33} &= 12.6 \times 10^{-9} \text{ C}^2/(\text{Nm}^2), \\ \mu_{11} &= 5.0 \times 10^{-6} \text{ N s}^2/\text{C}^2, & \mu_{33} &= 10.0 \times 10^{-6} \text{ N s}^2/\text{C}^2. \end{aligned} \quad (37)$$

CoFe₂O₄ :

$$\begin{aligned} c_{11} &= 286 \text{ GPa}, & c_{33} &= 269.5 \text{ GPa}, \\ c_{44} &= 45.3 \text{ GPa}, & c_{12} &= 173.0 \text{ GPa}, \\ c_{13} &= 170.5 \text{ GPa}, & f_{31} &= 580.3 \text{ N/(Am)}, \\ f_{33} &= 699.7 \text{ N/(Am)}, & f_{15} &= 550. \text{ N/(Am)}, \\ \varepsilon_{11} &= 0.08 \times 10^{-9} \text{ C}^2/(\text{Nm}^2), & \varepsilon_{33} &= 0.093 \times 10^{-9} \text{ C}^2/(\text{Nm}^2), \\ \mu_{11} &= 590 \times 10^{-6} \text{ N s}^2/\text{C}^2, & \mu_{33} &= 157 \times 10^{-6} \text{ N s}^2/\text{C}^2. \end{aligned} \quad (38)$$

The following mixture rule is used to determine the composite material constants corresponding to the inclusion and matrix [Song and Sih 2003]

$$\Lambda^c = \Lambda^i V_i + \Lambda^m (1 - V_i), \quad (39)$$

where the superscripts “*c*”, “*i*”, and “*m*” represent the composite, inclusion, and matrix respectively. The two-phase transversely isotropic magnetoelastic medium is obtained by assigning two different values of V_i in the upper and lower half-space, which are denoted by V_i^+ and V_i^- , respectively.

It should be pointed out that the value of μ_{11} used in [Huang et al. 1998] was negative. However, the negative value is questionable because it causes a negative internal energy and the Stroh formalism cannot be applied [Pan 2002]. The handbook, [Neelakanta 1995], indicates that the magnetic permeability of ferromagnetic materials, such as CoFe_2O_4 , should be positive. Therefore, positive values were used in recent research [Sih et al. 2003]. Recently, this issue was discussed by [Chue and Liu 2005]. For these reasons, a positive value is also assigned to μ_{11} in the numerical calculations in the present paper.

Under the electrically and magnetically impermeable boundary condition, the uniformly distributed extended loadings on the crack faces are

$$p_x = 0, \quad p_y = 0, \quad p_z = 100 \text{ MPa}, \quad \omega = 0.1 \text{ C/m}^2, \quad \gamma = 10/\text{Am}. \quad (40)$$

The extended displacement discontinuity method is used to analyze the problem. The rectangular crack is divided into N rectangular elements of the same size. In order to decide the appropriate value of the element number N , we first consider a square crack far away from the interface, that is, the crack is in a homogeneous medium. The numerical calculations demonstrate that the maximum normalized intensity factors are the same and equal to 0.8072 when the element number $N = 81$. When $N = 225$ and $N = 625$, the values of maximum normalized intensity factors are 0.7928 and 0.7914, respectively. The normalized extended intensity factors F are given by

$$F_F = K_I^F / (\sqrt{\pi B} \sigma_z^0), \quad F_D = K_I^D / (\sqrt{\pi B} D_z^0), \quad F_B = K_I^F / (\sqrt{\pi B} B_z^0). \quad (41)$$

Though the convergence is not very fast, the difference of the maximum normalized intensity factors is less than 4% compared with that of purely elastic material in [Murkami 1992]. So the value $N = 225$ is used in the present paper for numerical analysis.

Figure 4 shows the normalized intensity factors along the crack front $\{0 < x < A, y = 0, z = h\}$ for different ratio of A/B . The larger the ratio of A/B is, the larger the normalized intensity factors are. The numerical results show that the extended intensity factors take the maximum value at the middle point $(A, 0, h)$. The most important finding is that the three normalized intensity factors become different due to the interface, which is unlike the case of a crack in a homogeneous medium [Zhao et al. 2006b].

Plotted in Figure 5 are the maximum normalized intensity factors versus $h/(2A)$ for different ratios of A/B . The three normalized intensity factors increase with the increase of A/B . When the ratio of $h/(2A)$ is larger than 1.0, the three maximum normalized extended stress intensity factors approach the same value for a given ratio of A/B . It shows the influence of the interface can be neglected and the crack can be considered in a homogeneous medium.

Figure 6 displays the normalized intensity factors versus x/A for different volume fractions V_i^- and $A/B = 1$. It can be seen that the stress and the magnetic induction intensity factors increase as x/A and

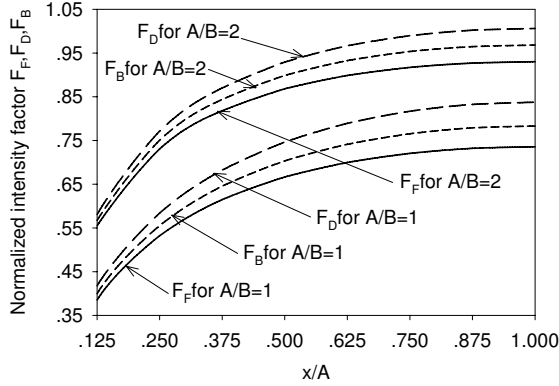


Figure 4. Normalized intensity factor F versus x/A with A/B for $V_i^+ = 0.5$, $V_i^- = 0.3$ and $h/(2A) = 0.2$.

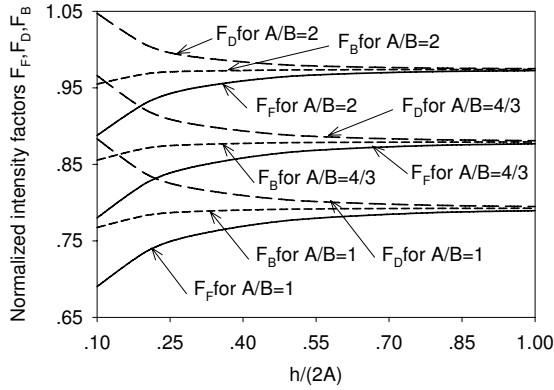


Figure 5. The maximum normalized intensity factor F versus $h/(2A)$ for $V_i^+ = 0.5$, $V_i^- = 0.3$ and different value of A/B .

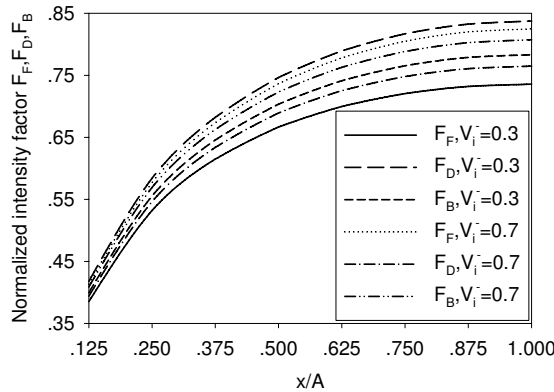


Figure 6. Normalized intensity factors F versus x/A with V_i^- for $V_i^+ = 0.5$, $h/(2A) = 0.2$ and $A/B = 1$.

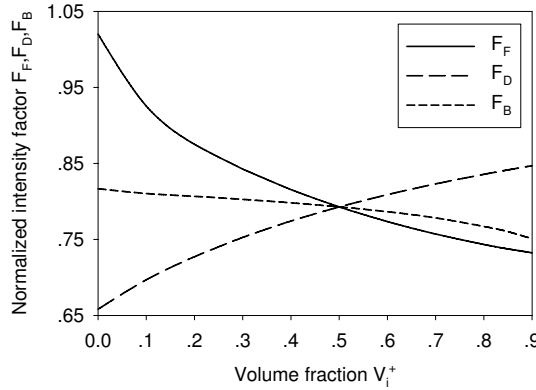


Figure 7. The maximum normalized intensity factors F versus V_i^+ for $h/(2A) = 0.2$, $V_i^- = 0.5$ and $A/B = 1$.

V_i^- increase, but the electric displacement intensity factors decrease as V_i^- increase. The normalized intensity factors take the maximum value at the middle point $(A, 0, h)$ independent of the volume fraction.

The maximum normalized intensity factors versus V_i^+ are depicted in Figure 7. It shows that the maximum stress and magnetic induction intensity factors decrease, while the maximum electric displacement intensity factors increase with the volume fraction V_i^+ increasing. The opposite trends are shown in Figure 8 for variation of V_i^- . It is interesting to note that the three maximum normalized intensity factors are the same when V_i^+ is equal to V_i^- , in which case the medium becomes homogeneous.

8. Concluding remarks

The displacement discontinuity method proposed by Crouch is extended to analyze cracks in three-dimensional two-phase transversely isotropic magneto-electroelastic media. The numerical results of rectangular cracks show that the extended method is very efficient.

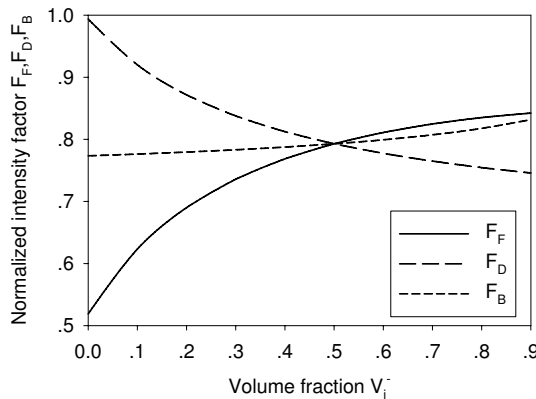


Figure 8. The maximum normalized intensity factors F versus V_i^- for $h/(2A) = 0.2$, $V_i^+ = 0.5$ and $A/B = 1$.

The three normalized intensity factors are equal for a crack in a homogeneous medium under the electrically and magnetically impermeable crack condition. For a crack in a two-phase medium, however, the three normalized intensity factors are unequal and greatly influenced by the size and the location of the crack and the material properties. This demonstrates that the crack behavior in an inhomogeneous magneto-electroelastic material is very complicated under combined mechanical-electrical-magnetic loadings.

Although various models, such as the strip polarization saturation model, charge-free zone model, etc., were proposed [Zhang et al. 2002], a linear analysis is the first and most fundamental step toward understanding the fracture behaviors of piezoelectric materials, and the intensity factors are the fundamental parameters in these nonlinear models. Until now, the problem hasn't been solved completely. The fracture behavior of magneto-electroelastic materials under combined mechanical-electrical-magnetic loading is more complicated than that of piezoelectric materials under combined mechanical-electrical loading. There is a long way yet to go to completely solve this problem.

Appendix A: Fundamental solutions

With regard to the problem of a point force, point charge, and point electric current applied at the point $(0, 0, h)$ in the interior of a two-phase transversely isotropic magneto-electroelastic media with the interface being parallel to the plane of isotropy, a Cartesian coordinate system is chosen such that the xoy -plane lies in the interface.

The following material related constants will be used in the fundamental solutions:

$$\begin{aligned}
 \alpha_{im} &= k_{mi}s_i, \quad i = 1, 2, 3, 4, \quad m = 1, 2, 3, \\
 \xi_i &= (c_{13}\alpha_{i1} + e_{31}\alpha_{i2} + f_{31}\alpha_{i3})s_i - c_{12}, \\
 \omega_{51} &= c_{44}s_5, \\
 \omega_{52} &= e_{15}s_5, \\
 \omega_{53} &= f_{15}s_5, \\
 \vartheta_{i1} &= (c_{33}\alpha_{i1} + e_{33}\alpha_{i2} + f_{33}\alpha_{i3})s_i - c_{13}, \\
 \vartheta_{i2} &= (e_{33}\alpha_{i1} - \varepsilon_{33}\alpha_{i2} - g_{33}\alpha_{i3})s_i - e_{31}, \\
 \vartheta_{i3} &= (f_{33}\alpha_{i1} - g_{33}\alpha_{i2} - \mu_{33}\alpha_{i3})s_i - f_{31}, \\
 \omega_{i1} &= c_{44}(s_i + \alpha_{i1}) + e_{15}\alpha_{i2} + f_{15}\alpha_{i3}, \\
 \omega_{i2} &= e_{15}(s_i + \alpha_{i1}) - \varepsilon_{11}\alpha_{i2} - g_{11}\alpha_{i3}, \\
 \omega_{i3} &= f_{15}(s_i + \alpha_{i1}) - g_{11}\alpha_{i2} - \mu_{11}\alpha_{i3},
 \end{aligned} \tag{A.1}$$

where s_i are the roots of the material characteristic equation and k_{mi} are the material related constants given in [Zhao et al. 2006b].

A.1. Fundamental solutions corresponding to unit point force P_3 in the z -direction. Using the derivation procedures of [Ding et al. 2005], the fundamental solutions are obtained.

When $z \geq 0$, we have

$$\begin{aligned} \tau_{xm} &= P_3 x \sum_{i=1}^4 \omega_{im} \left(\frac{A_i}{\bar{R}_{ii}^3} - \sum_{j=1}^4 \frac{A_{ij}}{R_{ij}^3} \right), & \tau_{ym} &= P_3 y \sum_{i=1}^4 \omega_{im} \left(\frac{A_i}{\bar{R}_{ii}^3} - \sum_{j=1}^4 \frac{A_{ij}}{R_{ij}^3} \right), \\ \sigma_m &= P_3 \sum_{i=1}^4 \vartheta_{im} \left(\frac{A_i \bar{z}_{ii}}{\bar{R}_{ii}^3} - \sum_{j=1}^4 \frac{A_{ij} z_{ij}}{R_{ij}^3} \right), \end{aligned} \tag{A.2}$$

and when $z \leq 0$,

$$\tau'_{xm} = P_3 x \sum_{i=1}^4 \sum_{j=1}^4 \omega'_{im} \frac{A'_{ij}}{R'_{ij}}, \quad \tau'_{ym} = P_3 y \sum_{i=1}^4 \sum_{j=1}^4 \omega'_{im} \frac{A'_{ij}}{R'_{ij}}, \quad \sigma'_m = P_3 \sum_{i=1}^4 \sum_{j=1}^4 \vartheta'_{im} \frac{A'_{ij} z'_{ij}}{R'_{ij}}, \tag{A.3}$$

where variables with a prime refer to the half-space $z \leq 0$ and those without a prime correspond to the half-space $z \geq 0$. The related coefficients are determined by

$$\begin{aligned} \sum_{i=1}^4 A_i &= 0, & 4\pi \sum_{i=1}^4 \vartheta_{i1} A_i &= -1, \\ 4\pi \sum_{i=1}^4 \vartheta_{i2} A_i &= 0, & 4\pi \sum_{i=1}^4 \vartheta_{i3} A_i &= 0, \\ A_i + \sum_{j=1}^4 A_{ji} &= \sum_{j=1}^4 A'_{ji}, & A_i \alpha_{im} - \sum_{j=1}^4 A_{ji} \alpha_{jm} &= \sum_{j=1}^4 A'_{ji} \alpha'_{jm}, \\ A_i \vartheta_{im} + \sum_{j=1}^4 A_{ji} \vartheta_{jm} &= \sum_{j=1}^4 A'_{ji} \vartheta'_{jm}, & A_i \omega_{i1} - \sum_{j=1}^4 A_{ji} \omega_{j1} &= \sum_{j=1}^4 A'_{ji} \omega'_{j1}. \end{aligned} \tag{A.4}$$

Solutions corresponding to the unit point charge P_4 and point current P_5 are in the same form as Equations (A.2)–(A.4), but P_3 and A_i should be replaced respectively by P_4 and B_i and P_5 and C_i . The coefficients B_i and C_i are determined by

$$\begin{aligned} \sum_{i=1}^4 B_i &= 0, & 4\pi \sum_{i=1}^4 \vartheta_{i1} B_i &= 0, \\ 4\pi \sum_{i=1}^4 \vartheta_{i2} B_i &= 1, & 4\pi \sum_{i=1}^4 \vartheta_{i3} B_i &= 0, \\ B_i + \sum_{j=1}^4 B_{ji} &= \sum_{j=1}^4 B'_{ji}, & B_i \alpha_{im} - \sum_{j=1}^4 B_{ji} \alpha_{jm} &= \sum_{j=1}^4 B'_{ji} \alpha'_{jm}, \\ B_i \vartheta_{im} + \sum_{j=1}^4 B_{ji} \vartheta_{jm} &= \sum_{j=1}^4 B'_{ji} \vartheta'_{jm}, & B_i \omega_{i1} - \sum_{j=1}^4 B_{ji} \omega_{j1} &= \sum_{j=1}^4 B'_{ji} \omega'_{j1}, \end{aligned} \tag{A.5}$$

$$\begin{aligned}
 \sum_{i=1}^4 C_i &= 0, & 4\pi \sum_{i=1}^4 \vartheta_{i1} C_i &= 0, \\
 4\pi \sum_{i=1}^4 \vartheta_{i2} C_i &= 0, & 4\pi \sum_{i=1}^4 \vartheta_{i3} C_i &= 1, \\
 C_i + \sum_{j=1}^4 C_{ji} &= \sum_{j=1}^4 C'_{ji}, & C_i \alpha_{im} - \sum_{j=1}^4 C_{ji} \alpha_{jm} &= \sum_{j=1}^4 C'_{ji} \alpha'_{jm}, \\
 C_i \vartheta_{im} + \sum_{j=1}^4 C_{ji} \vartheta_{jm} &= \sum_{j=1}^4 C'_{ji} \vartheta'_{jm}, & C_i \omega_{i1} - \sum_{j=1}^4 C_{ji} \omega_{j1} &= \sum_{j=1}^4 C'_{ji} \omega'_{j1}.
 \end{aligned} \tag{A.6}$$

A.2. Fundamental solutions corresponding to unit point force P_1 in the x -direction. When $z \geq 0$, the fundamental solutions are given by

$$\begin{aligned}
 \tau_{xm} = & -P_1 \omega_{5m} \left[D_5 \left(\frac{1}{\bar{R}_{55}(\bar{R}_{55} - \bar{z}_{55})} - \frac{y^2}{\bar{R}_{55}^3(\bar{R}_{55} - \bar{z}_{55})} - \frac{y^2}{\bar{R}_{55}^2(\bar{R}_{55} - \bar{z}_{55})^2} \right) \right. \\
 & \left. - D_{55} \left(\frac{1}{R_{55}(R_{55} + z_{55})} - \frac{y^2}{R_{55}^3(R_{55} + z_{55})} - \frac{y^2}{R_{55}^2(R_{55} + z_{55})^2} \right) \right] \\
 & + P_1 \sum_{i=1}^4 \omega_{im} \left[D_i \left(\frac{1}{\bar{R}_{ii}(\bar{R}_{ii} - \bar{z}_{ii})} - \frac{x^2}{\bar{R}_{ii}^3(\bar{R}_{ii} - \bar{z}_{ii})} - \frac{x^2}{\bar{R}_{ii}^2(\bar{R}_{ii} - \bar{z}_{ii})^2} \right) \right. \\
 & \left. - \sum_{j=1}^4 D_{ij} \left(\frac{1}{R_{ij}(R_{ij} + z_{ij})} - \frac{x^2}{R_{ij}^3(R_{ij} + z_{ij})} - \frac{x^2}{R_{ij}^2(R_{ij} + z_{ij})^2} \right) \right],
 \end{aligned}$$

$$\begin{aligned}
 \tau_{ym} = & -\omega_{5m} P_1 x y \left[D_5 \left(\frac{1}{\bar{R}_{55}^3(\bar{R}_{55} - \bar{z}_{55})} + \frac{1}{\bar{R}_{55}^2(\bar{R}_{55} - \bar{z}_{55})^2} \right) \right. \\
 & \left. - \sum_{j=1}^4 D_{55} \left(\frac{1}{R_{55}^3(R_{55} + z_{55})} + \frac{1}{R_{55}^2(R_{55} + z_{55})^2} \right) \right] \\
 & - P_1 x y \sum_{i=1}^4 \omega_{im} \left[D_i \left(\frac{1}{\bar{R}_{ii}^3(\bar{R}_{ii} - \bar{z}_{ii})} + \frac{1}{\bar{R}_{ii}^2(\bar{R}_{ii} - \bar{z}_{ii})^2} \right) \right. \\
 & \left. - \sum_{j=1}^4 D_{ij} \left(\frac{1}{R_{ij}^3(R_{ij} + z_{ij})} + \frac{1}{R_{ij}^2(R_{ij} + z_{ij})^2} \right) \right],
 \end{aligned}$$

$$\sigma_m = P_1 x \sum_{i=1}^4 \vartheta_{im} \left[\frac{D_i}{\bar{R}_{ii}^3} + \sum_{i=1}^4 \frac{D_{ij}}{R_{ij}^3} \right],$$

and when $z \leq 0$

$$\begin{aligned} \tau'_{xm} = & -P_1 \omega'_{5m} D'_{55} \left[\frac{1}{R'_{55}(R'_{55} - z'_{55})} - \frac{y^2}{R'^3_{55}(R'_{55} - z'_{55})} - \frac{y^2}{R'^2_{55}(R'_{55} - z'_{55})^2} \right] \\ & + P_1 \sum_{i=1}^4 \sum_{j=1}^4 D'_{ij} \omega'_{im} \left[\frac{1}{R'_{ij}(R'_{ij} - z'_{ij})} - \frac{x^2}{R'^3_{ij}(R'_{ij} - z'_{ij})} - \frac{x^2}{R'^2_{ij}(R'_{ij} - z'_{ij})^2} \right], \end{aligned}$$

$$\begin{aligned} \tau'_{ym} = & -P_1 \omega'_{5m} D'_{55} x y \left[\frac{1}{R'^3_{55}(R'_{55} - z'_{55})} + \frac{1}{R'^2_{55}(R'_{55} - z'_{55})^2} \right] \\ & - P_1 \sum_{i=1}^4 \sum_{j=1}^4 D'_{ij} \omega'_{im} x y \left[\frac{1}{R'^3_{ij}(R'_{ij} - z'_{ij})} + \frac{1}{R'^2_{ij}(R'_{ij} - z'_{ij})^2} \right], \end{aligned}$$

$$\sigma'_m = P_1 x \sum_{i=1}^4 \sum_{j=1}^4 \vartheta'_{im} \frac{D'_{ij}}{R'^3_{ij}},$$

where the coefficients D_i , D_{ij} , D'_{ij} are given by

$$\begin{aligned} \sum_{i=1}^4 \alpha_{im} D_i &= 0, & s_5 D_5 + \sum_{i=1}^4 s_i D_i &= 0, \\ 2\pi c_{44} s_5 D_5 - 2\pi \sum_{i=1}^4 \omega_{i1} D_i &= -1, & D_5 + D_{55} &= D'_{55}, \\ \alpha_{im} D_i - \sum_{j=1}^4 \alpha_{jm} D_{ji} &= \sum_{j=1}^4 \alpha'_{jm} D'_{ji}, & D_i + \sum_{j=1}^4 D_{ji} &= \sum_{j=1}^4 D'_{ji}, \\ \omega_{51}(D_{55} - D_5) &= -\omega'_{51} D'_{55}, & \omega_{i1} D_i - \sum_{j=1}^4 \omega_{j1} D_{ji} &= \sum_{j=1}^4 \omega'_{j1} D'_{ji}, \\ \vartheta_{im} D_i + \sum_{j=1}^4 \vartheta_{jm} D_{ji} &= \sum_{j=1}^4 \vartheta'_{jm} D'_{jm}. \end{aligned}$$

By simple coordinate transformation, solutions to the problem of unit point force P_2 in the y -direction can be easily obtained from the above solutions.

Appendix B: The constants L_s and the functions G_s and \bar{G}_s

The coefficients in Equations (27)–(31) are given by

$$\begin{aligned} Q_i^1 &= D_i s_i c_{44} + c_{44} A_i - e_{15} B_i - f_{15} C_i, & Q_i^2 &= c_{13} D_i - s_i (c_{33} A_i - e_{33} B_i - f_{33} C_i), \\ Q_i^3 &= e_{31} D_i - s_i (e_{33} A_i + \varepsilon_{33} B_i + g_{33} C_i), & Q_i^4 &= f_{31} D_i - s_i (f_{33} A_i + g_{33} B_i + \mu_{33} C_i), \end{aligned} \quad (\text{B.1})$$

$$\begin{aligned}
 L_{X1} &= c_{44}\omega_{51}s_5D_5, & L_{X2} &= c_{44}\omega_{51}s_5D_{55}, \\
 L_{11}^i &= \omega_{i1}Q_i^1, & L_{21k}^i &= \vartheta_{ik}Q_i^1, \\
 L_{Z1}^i &= \omega_{i1}Q_i^2, & L_{Z1k}^i &= \vartheta_{ik}Q_i^2, \\
 L_{D1}^i &= \omega_{i1}Q_i^3, & L_{D1k}^i &= \vartheta_{ik}Q_i^3, \\
 L_{B1}^i &= \omega_{i1}Q_i^4, & L_{B1k}^i &= \vartheta_{ik}Q_i^4, \quad k = 1, 2, 3.
 \end{aligned}
 \tag{B.2}$$

The coefficients

$$L_{12}^{ij}, L_{22k}^{ij}, L_{Z2}^{ij}, L_{Z2k}^{ij}, L_{D2}^{ij}, L_{D2k}^{ij}, L_{B2}^{ij}, \text{ and } L_{B2k}^{ij}$$

can be obtained correspondingly by taking

$$s_j, A_{ij}, B_{ij}, C_{ij}, \text{ and } D_{ij}$$

instead of $s_i, A_i, B_i, C_i,$ and D_i in the above equations, respectively.

And the functions \bar{G} s with different superscripts and subscripts are given by

$$\begin{aligned}
 \bar{G}_{ii}^{(1)} &= \frac{b-y}{(b-y)^2 + \bar{z}_{ii}^2} \left(\frac{a-x}{\sqrt{(a-x)^2 + (b-y)^2 + \bar{z}_{ii}^2}} + \frac{a+x}{\sqrt{(x+a)^2 + (b-y)^2 + \bar{z}_{ii}^2}} \right) \\
 &\quad + \frac{b+y}{(b+y)^2 + \bar{z}_{ii}^2} \left(\frac{a-x}{\sqrt{(a-x)^2 + (b+y)^2 + \bar{z}_{ii}^2}} + \frac{a+x}{\sqrt{(x+a)^2 + (b+y)^2 + \bar{z}_{ii}^2}} \right),
 \end{aligned}$$

$$\begin{aligned}
 \bar{G}_{ii}^{(3)} &= \frac{1}{\sqrt{(a-x)^2 + (b-y)^2 + \bar{z}_{ii}^2}} - \frac{1}{\sqrt{(a+x)^2 + (b-y)^2 + \bar{z}_{ii}^2}} \\
 &\quad - \frac{1}{\sqrt{(a-x)^2 + (b+y)^2 + \bar{z}_{ii}^2}} + \frac{1}{\sqrt{(a+x)^2 + (b+y)^2 + \bar{z}_{ii}^2}},
 \end{aligned}$$

$$\begin{aligned}
 \bar{G}_{ii}^{(4)} &= \frac{1}{(a-x)^2 + \bar{z}_{ii}^2} \left(\frac{b-y}{\sqrt{(a-x)^2 + (b-y)^2 + \bar{z}_{ii}^2}} + \frac{b+y}{\sqrt{(a-x)^2 + (b+y)^2 + \bar{z}_{ii}^2}} \right) \\
 &\quad - \frac{1}{(a+x)^2 + \bar{z}_{ii}^2} \left(\frac{b-y}{\sqrt{(a+x)^2 + (b-y)^2 + \bar{z}_{ii}^2}} + \frac{b+y}{\sqrt{(a+x)^2 + (b+y)^2 + \bar{z}_{ii}^2}} \right),
 \end{aligned}$$

$$\begin{aligned}
 \bar{G}_{ii}^{(6)} &= \frac{(y-b)(a-x)}{\sqrt{(a-x)^2 + (b-y)^2 + \bar{z}_{ii}^2}} \left(\frac{1}{(b-y)^2 + \bar{z}_{ii}^2} + \frac{1}{(a-x)^2 + \bar{z}_{ii}^2} \right) \\
 &\quad + \frac{(y-b)(a+x)}{\sqrt{(a+x)^2 + (b-y)^2 + \bar{z}_{ii}^2}} \left(\frac{1}{(b-y)^2 + \bar{z}_{ii}^2} + \frac{1}{(a+x)^2 + \bar{z}_{ii}^2} \right)
 \end{aligned}$$

$$-\frac{(y+b)(a-x)}{\sqrt{(a-x)^2+(b+y)^2+\bar{z}_{ii}^2}}\left(\frac{1}{(b+y)^2+\bar{z}_{ii}^2}+\frac{1}{(a-x)^2+\bar{z}_{ii}^2}\right) \\ -\frac{(y+b)(a+x)}{\sqrt{(a+x)^2+(b+y)^2+\bar{z}_{ii}^2}}\left(\frac{1}{(b+y)^2+\bar{z}_{ii}^2}+\frac{1}{(a+x)^2+\bar{z}_{ii}^2}\right).$$

The functions $\bar{G}_{ii}^{(2)}$ and $\bar{G}_{ii}^{(5)}$ can be obtained respectively from $\bar{G}_{ii}^{(1)}$ and $\bar{G}_{ii}^{(4)}$ by taking a , b , x , and y instead of b , a , y , and x , respectively. The functions G_s can be obtained by taking z_{ij} instead of \bar{z}_{ii} in \bar{G}_s .

References

- [Chue and Liu 2005] C. H. Chue and T. J. C. Liu, “Magneto-electro-elastic antiplane analysis of a bimaterial BaTiO₃-CoFe₂O₄ composite wedge with an interface crack”, *Theor. Appl. Fract. Mec.* **44**:3 (2005), 275–296.
- [Chung and Ting 1995] M. Y. Chung and T. C. T. Ting, “The Green function for a piezoelectric piezomagnetic anisotropic elastic medium with an elliptic hole or rigid inclusion”, *Phil. Mag.* **72** (1995), 405–410.
- [Crouch 1976] S. L. Crouch, “Solution of plane elasticity problems by the displacement discontinuity method”, *Int. J. Numer. Meth. Eng.* **10**:2 (1976), 301–343.
- [Ding et al. 2005] H. Ding, A. Jiang, P. Hou, and W. Chen, “Green’s functions for two-phase transversely isotropic magneto-electro-elastic media”, *Eng. Anal. Bound. Elem.* **29**:6 (2005), 551–561.
- [Gao and Noda 2004] C.-F. Gao and N. Noda, “Thermal-induced interfacial cracking of magneto-electro-elastic materials”, *Int. J. Eng. Sci.* **42**:13-14 (2004), 1347–1360.
- [Hou et al. 2005] P.-F. Hou, H.-J. Ding, and J.-Y. Chen, “Green’s functions for transversely isotropic magneto-electro-elastic media”, *Int. J. Eng. Sci.* **43**:10 (2005), 826–858.
- [Huang and Kuo 1997] J. H. Huang and W.-S. Kuo, “The analysis of piezoelectric/piezomagnetic composite materials containing an ellipsoidal inclusion”, *J. Appl. Phys.* **81**:3 (1997), 1378–1386.
- [Huang et al. 1998] J. H. Huang, Y.-H. Chiu, and H.-K. Liu, “Magneto-electro-elastic eshelby tensors for a piezoelectric-piezomagnetic composite reinforced by ellipsoidal inclusions”, *J. Appl. Phys.* **83**:10 (1998), 5364–5370.
- [Jiang and Pan 2004] X. Jiang and E. Pan, “Exact solution for 2D polygonal inclusion problem in anisotropic magneto-electro-elastic full-, half-, and bimaterial-planes”, *Int. J. Solids Struct.* **41**:16-17 (2004), 4361–4382.
- [Liu and Liu 2001] J. Liu and Y. Liu, X. and Zhao, “Green’s functions for anisotropic magneto-electro-elastic solids with an elliptical cavity or a crack”, *Int. J. Eng. Sci.* **39**:12 (2001), 1405–1418.
- [Murkami 1992] Y. Murkami, *Stress intensity factors handbook*, vol. 3, Pergamon, Oxford, 1992. v.3 published with the aid of The Society of Materials Science, Japan.
- [Neelakanta 1995] P. S. Neelakanta, *Handbook of electromagnetic materials: monolithic and composite versions and their applications*, CRC Press, Boca Raton, FL, 1995.
- [Pan 1991] E. Pan, “Dislocation in an infinite poroelastic medium”, *Acta Mech.* **87**:1-2 (1991), 105–115.
- [Pan 2002] E. Pan, “Three-dimensional Green’s functions in anisotropic magneto-electro-elastic bimaterials”, *Z. Angew. Math. Phys.* **53**:5 (2002), 815–838.
- [Pan and Amadei 1996] E. Pan and B. Amadei, “Fracture mechanics analysis of cracked 2-D anisotropic media with a new formulation of the boundary element method”, *Int. J. Fracture* **77**:2 (1996), 161–174.
- [Qin 2004] Q. H. Qin, “Green’s functions of magneto-electro-elastic solids with a half-plane boundary or bimaterial interface”, *Phil. Mag.* **84**:12 (2004), 771–779.
- [Sih et al. 2003] G. C. Sih, R. Jones, and Z. F. Song, “Piezomagnetic and piezoelectric poling effects on mode I and II crack initiation behavior of magneto-electro-elastic materials”, *Theor. Appl. Fract. Mec.* **40**:2 (2003), 161–186.
- [Song and Sih 2003] Z. F. Song and G. C. Sih, “Crack initiation behavior in magneto-electro-elastic composite under in-plane deformation”, *Theor. Appl. Fract. Mec.* **39**:3 (2003), 189–207.

- [Tian and Rajapakse 2005] W. Y. Tian and R. K. N. D. Rajapakse, “Fracture analysis of magneto-electroelastic solids by using path independent integrals”, *Int. J. Fracture* **131**:4 (2005), 311–335.
- [Wang and Mai 2003] B. L. Wang and Y.-W. Mai, “Crack tip field in piezoelectric/piezomagnetic media”, *Eur. J. Mech. A Solids* **22**:4 (2003), 591–602.
- [Wang and Shen 2002] X. Wang and Y.-P. Shen, “The general solution of three-dimensional problems in magneto-electroelastic media”, *Int. J. Eng. Sci.* **40**:10 (2002), 1069–1080.
- [Wang and Shen 2003] X. Wang and Y.-P. Shen, “Inclusions of arbitrary shape in magneto-electroelastic composite materials”, *Int. J. Eng. Sci.* **41**:1 (2003), 85–102.
- [Wen 1996] P. H. Wen, *Dynamic fracture mechanics: displacement discontinuity method*, vol. 29, Topic in Engineering, Computational Mechanics Publications, Boston, 1996.
- [Zhang et al. 2002] T. Y. Zhang, M. H. Zhao, and P. Tong, “Fracture of piezoelectric ceramics”, *Adv. Appl. Mech.* **38** (2002), 147–289.
- [Zhao et al. 1997a] M. H. Zhao, Y. P. Shen, Y. J. Liu, and G. N. Liu, “Isolated crack in three-dimensional piezoelectric solid, I: solution by Hankel transform”, *Theor. Appl. Fract. Mec.* **26**:2 (1997), 129–139.
- [Zhao et al. 1997b] M. H. Zhao, Y. P. Shen, Y. J. Liu, and G. N. Liu, “Isolated crack in three-dimensional piezoelectric solid, II: stress intensity factors for circular crack”, *Theor. Appl. Fract. Mec.* **26**:2 (1997), 141–149.
- [Zhao et al. 1998] M. H. Zhao, Y. P. Shen, Y. J. Liu, and G. N. Liu, “The method of analysis of cracks in three-dimensional transversely isotropic media: boundary integral equation approach”, *Eng. Anal. Bound. Elem.* **21**:2 (1998), 169–178.
- [Zhao et al. 2004] M.-H. Zhao, P.-Z. Fang, and Y.-P. Shen, “Boundary integral-differential equations and boundary element method for interfacial cracks in three-dimensional piezoelectric media”, *Eng. Anal. Bound. Elem.* **28**:7 (2004), 753–762.
- [Zhao et al. 2006a] M. H. Zhao, H. Wang, F. Yang, and T. Liu, “A magneto-electroelastic medium with an elliptical cavity under combined mechanical-electric-magnetic loading”, *Theor. Appl. Fract. Mec.* **45**:3 (2006), 227–237.
- [Zhao et al. 2006b] M. H. Zhao, F. Yang, and T. Liu, “Analysis of a penny-shaped crack in a magneto-electro-elastic medium”, *Phil. Mag.* **86**:28 (2006), 4397–4416.
- [Zhou et al. 2004] Z.-G. Zhou, B. Wang, and Y.-G. Sun, “Two collinear interface cracks in magneto-electro-elastic composites”, *Int. J. Eng. Sci.* **42**:11-12 (2004), 1155–1167.

Received 28 Nov 2006. Accepted 5 Nov 2007.

MINGHAO ZHAO: memhzhao@zzu.edu.cn

Department of Engineering Mechanics, Zhengzhou University, No. 100 Science Road, Zhengzhou, Henan Province 450001, China

NA LI: zhuofan8227@163.com

Department of Engineering Mechanics, Zhengzhou University, No. 100 Science Road, Zhengzhou, Henan Province 450001, China

CUIYING FAN: fcymaster@126.com

Department of Engineering Mechanics, Zhengzhou University, No. 100 Science Road, Zhengzhou, Henan Province 450001, China

TONG LIU: Liutung@zzu.edu.cn

Department of Engineering Mechanics, Zhengzhou University, No. 100 Science Road, Zhengzhou, Henan Province 450001, China

INFLUENCE OF VEHICULAR POSITIONS AND THERMAL EFFECTS ON STRUCTURAL BEHAVIOUR OF CONCRETE PAVEMENT

MOSTAFA YOUSEFI DARESTANI, DAVID P. THAMBIRATNAM,
ANDREAS NATAATMADJA AND DAKSH BAWEJA

Structural response of concrete pavements is influenced by the position of the axle loads and if critical load positions are not considered in concrete pavement analysis, the design may be inadequate and lead to early failure of the pavement. Whilst there has been a great deal of research conducted on concrete pavement performance and deterioration under vehicular loads and environmental forces, there is a lack of adequate information on effects of vehicular load positions on pavement responses.

Critical positions of different axle groups in uncurled and curled jointed concrete pavement with different configurations were determined in the current study. Results indicate that structural performance of concrete pavements is significantly affected by boundary conditions between concrete slab and base. Corner loading was found to be critical in bonded concrete pavement. Corner loading is also critical when a separation occurs between unbonded concrete slab and base. Furthermore, the benefits offered by unbonded boundary condition cease at a certain differential temperature. Hence, a particular care needs to be considered in projects constructed in extremes of heat or cold. In presence of high differential temperature together with axle loading, joint faulting in unreinforced concrete pavements is affected by concrete slab thickness.

1. Introduction

Although there has been a great deal of research conducted on concrete pavement performance and deterioration under vehicular loads and environmental forces, there is a lack of adequate information on effects of vehicular load positions on pavement responses. If the load positions which give the maximum response parameters are not considered in the analysis, the design may be inadequate and lead to early failure of concrete pavements. Structural response of concrete pavements is affected by vehicular load configurations, magnitude of applied loads and position of axle groups on the pavement as well as environmental effects. This paper treats the influence of vehicular load positions on pavement responses in terms of induced tensile stresses. Effects of configuration and magnitude of vehicular loads on concrete pavement responses have also been investigated and the findings will appear in another paper.

In concrete pavements, applied loads are generally transferred to base and subgrade layers by the bending action of concrete slab which results in a tensile stress at the top or the bottom surface layers of the concrete slab. The applied loads can be vehicular and/or environmentally related. Research conducted in the past for determination of the critical position of vehicular loads upon the concrete pavements can

Keywords: concrete pavement, concrete, tensile stress, thermal analysis, critical position, axle group loads, crack.

The original work of this study was sponsored by the Queensland University of Technology (QUT), Australia, and Readymix Holdings Pty Limited, under R & D project RD835.

be divided into two categories, with and without consideration of differential temperature effects. The most significant one in the absence of differential temperature is the work of [Packard and Tayabji \[1985\]](#).

A single traffic lane confined at one longitudinal edge by shoulder, subjected to single axle, tandem axle and triple axle loads was considered in Packard and Tayabji's research [\[Packard and Tayabji 1985\]](#) to determine the critical position of the above mentioned axle groups on uncurled concrete pavements. Although many jointed concrete pavements suffered from corner and longitudinal cracking [Packard and Tayabji \[1985\]](#), and [Heath et al. \[2003\]](#), found that the maximum vehicular induced tensile stress occurs when axle group loads are applied at the middle of the longitudinal joints between transverse joints. This leads to bottom-up mid-edge transverse cracking. Vehicular induced tensile stress in the absence of differential temperature gradients occurs at the deepest surface layer of the concrete slab, particularly when the load is applied at longitudinal joints [\[Ongel and Harvey 2004\]](#). Recommendation of American Association of States and Highway Officials [\[AASHTO 2003\]](#) for analysis of jointed concrete pavements is the use of a single lane with at least three concrete slab panels in the longitudinal direction. This is compatible with what [Packard and Tayabji \[1985\]](#) considered.

In addition to the traditional bottom-up mid-edge transverse fatigue cracking, environmental effects together with built-in temperature curling result in other failure modes [\[Hiller and Roesler 2005\]](#). Temperature fluctuation has different effects on concrete pavements. Nonuniform temperature distribution within concrete slab depth results in upward (nighttime) or downward (daytime) curling. Curling induced tensile stress occurs at the top surface layer of the concrete slab during nighttime and at the bottom surface layer of the concrete slab during daytime [\[Ongel and Harvey 2004\]](#).

Traditional methods of thermal analysis were based on a linear temperature distribution in pavement depth [\[Westergaard 1926; Bradbury 1938\]](#). However, [Choubane and Tia \[1995\]](#) showed that temperature distribution in pavement depth is nonlinear. [Mohamed and Hansen \[1997\]](#) developed an analytical method to estimate the induced tensile stress in concrete pavements subjected to a nonlinear temperature gradients. The concept of equivalent temperature distributions was then employed in concrete pavement analysis based on the plate theory [\[Ioannides and Khazanovich 1998\]](#). In their study, a plate consisting one or more layers (plate layers with no separation and compressible layers with possible separation using Totsky model [\[Totsky 1981\]](#) resting on an elastic foundation was investigated. Consequently, mathematical formulations for analysis of a typical concrete pavement subjected to a linear function, a quadratic function or multilinear function of differential temperature together with arbitrary wheel load were developed.

Results of [Mohamed and Hansen \[1997\]](#) and also [Heath and Roesler \[1999\]](#) indicated that nonlinear temperature distribution through the depth of concrete slab results in tensile stress that is lower than that of linear temperature distribution when concrete pavement is subjected to a positive temperature gradient (daytime) and produces tensile stress that is greater than that of linear temperature distribution when concrete pavements are subjected to negative temperature gradients (nighttime). [Liang and Niu \[1998\]](#) showed that concrete pavement responses are significantly affected by environmental forces. [Kuo \[1998\]](#) indicated curling induced stress is affected by temperature differential, self-weight of concrete pavement and support under concrete slab. Furthermore, [Kuo \[1998\]](#) recommended that (i) mid-slab loading in daytime curling and (ii) joint loading in nighttime curling should be considered in pavement analysis.

[Byrum and Hansen \[1994\]](#) contributed the influence function lines in analysis of jointed concrete pavement under environmental effects and wheel load. The wheel load was applied in a distance of

838 mm away from longitudinal joint. Their results indicated that (i) maximum stress occurs at some distance away from the joint when the load passes across the joint (ii) thermal, moisture and shrinkage gradients have a significant effect on the residual stresses of the concrete slab (iii) highway slabs are predominantly in the upward curled condition.

Several field tests were carried out in the past to determine the range of temperature gradient in depth of concrete slab. Richardson and Armaghani [1990] and Shoukry et al. [2002] reported that the differential temperature is about 10°C in a concrete slab with 225 mm thickness. Byrum and Hansen [1994] based on other research in this field used a temperature gradient between 0.087 and 0.109°C/mm during daytime and between 0.044 and 0.065°C/mm during nighttime. Darter et al. [1995] provided a range between 0.0219 and 0.656°C/mm whereas Ongel and Harvey [2004] reported monthly values of temperature gradient in concrete pavement for a period of 5 years with an average of 0.125°C/mm . As temperature gradient is strongly affected by air temperature, ratio of the top surface area of the concrete slab to its depth, duration and density of solar radiation, rain fall, thermal conductivity of concrete and wind speed, it is obvious that differential temperature changes from one location to other locations.

Since the top surface layer of concrete slab is exposed to solar radiation and wind, it dries and cures faster than other layers within the concrete slab depth and consequently results in nonuniform shrinkage which is the reason for concrete slab warping and top-down cracking [Ongel and Harvey 2004]. The effect of drying shrinkage on concrete pavement is similar to nighttime differential temperature effects. Hence, Reddy et al. [1963] recommended the use of equivalent nighttime temperature gradients between 0.065 and 0.13°C/mm in concrete pavement analysis to represent the effects of drying shrinkage in concrete pavement responses.

Results of Yu et al. [1998] on concrete pavement response to temperature and wheel loads suggested that corner loading may results in greater stress than mid-edge loading. Effect of single axle dual tyre (SADT), tandem axle dual tyre (TADT) and triple axle dual tyre (TRDT) on pavement response were then taken into account by Hiller and Roesler [2002] to develop a method for predicting concrete pavement deterioration. Since the assumptions considered by Hiller and Roesler [2002] are not compatible with concrete pavement construction in Australia, results of the current research may or may not agree with what they found. Reasons behind this can be absence of base layer, consideration of shoulder with 3000 mm width, concrete slab interaction, the use of 200 mm thickness for concrete slab and long distance between transverse joints (5800 mm) in their study.

In 2005, Hiller and Roesler [2005] used the influence stress lines to determine the critical location of fatigue damage under certain truck loads in a typical California concrete pavement having permanent built-in curling. They found that the critical damage location in the absence of environmental effects was at the bottom surface layer of the mid-slab edge for a load transfer efficiency of 70%. However, top-down transverse cracking near the mid-slab edge was the critical failure mode in the presence of a nighttime differential temperature of -16.5°C .

Buch et al. [2004] parametrically investigated the structural response of jointed concrete pavement under single axle (SA), tandem axle (TA), triple axle (TR), quad axle (QA), multi axles, together with differential temperature using influence stress line approaches. In addition, diverse truck loads (combination of different axle group loads) were also studied. Their results indicated that mid-edge loading results in bottom-up cracking and corner loading results in top-down cracking for SA, TA, TR and QA.

They also found that an increase in the subgrade reaction and thickness of the concrete slab increases and decreases the induced tensile stresses respectively.

Structural behaviour of curled concrete pavements depends on provision of debonding layer between concrete slab and base. If a full bonded condition between concrete slab and base is considered, a tensile stress will be produced at the interface of concrete slab and base during the first 28 days of concrete placement due to plastic and drying shrinkage. This subsequently results in early age cracking. Because of this, a debonding layer is placed between concrete slab and base to eliminate the early age cracking. The concept of frictional stress in concrete pavement analysis was introduced by [Wimsatt et al. \[1987\]](#) and [Wesevich et al. \[1987\]](#). It was also adopted in most finite element softwares developed for analysing concrete pavements. The frictional stress is a shear stress induced at each square metre of concrete slab and base interface. This parameter is highly independent of concrete slab thickness and bearing stress.

Different boundary conditions including bonded, unbonded and partially bonded may be created between concrete slab and base depending on types of debonding layer. While bonded boundary condition keeps concrete slab and subbase together with no vertical separation, fully unbonded boundary condition lets them to be separated under tensile force without inducing any shear force between these layers. Partially bonded boundary condition, on the other hand, keeps concrete slab and base together for a certain shear force. Beyond this shear force, a vertical separation will occur between these layers. Note that information on effects of debonding layer on concrete pavement behaviour does not lead to a specific conclusion as [Tarr et al. \[1999\]](#) indicated that unbonded condition could only be achieved by using a double layer of polyethylene sheets and [Yu et al. \[1998\]](#) stated that friction between concrete slab and base is sufficient to produce bonded behaviour even if polyethylene sheets are placed between them.

Whilst most research on concrete pavements is based on either fully bonded or fully unbonded boundary condition between concrete slab and base [[Heath and Roesler 1999](#)], effects of different boundary conditions on concrete pavement responses are not clearly understood. Since configuration and magnitude of vehicular loads have a significant effect on induced tensile stress in concrete pavements [[Yu et al. 1998](#); [Hiller and Roesler 2002](#)] and a variety of axle group configurations is employed in heavy vehicle industries, further study shall be carried out for other axle group types. Moreover, there is no inclusive information on critical positions of each individual axle group on curled and uncurled concrete pavement.

This study seeks to establish the critical positions of axle groups on jointed concrete pavement based on [Austroads \[2004\]](#) recommendations. Loads from different axle groups are separately applied at various locations on a number of pavement configurations—unconfined and confined by adjacent lanes and shoulders—to evaluate the critical design parameters of maximum tensile stress. Fully bonded and unbonded boundary conditions between concrete slab and base are considered. Different axle groups based on [Austroads \[2004\]](#) consisting of (i) Single Axle Single Tyre (SAST), (ii) Single Axle Dual Tyre (SADT), (iii) Tandem Axle Single Tyre (TAST), (iv) Tandem Axle Dual Tyre (TADT), (v) Triple Axle Dual tyre (TRDT) and (vi) Quad Axle Dual Tyre (QADT) are positioned at different locations of the pavement.

Curling and warping of concrete pavement were also taken into account. Effects of axle group loadings and differential temperature gradients on both bonded and unbonded concrete pavement will be separately studied. A sensitivity analysis on structural behaviour of unbonded and bonded concrete pavements subjected to diverse differential temperatures will be done to estimate the accuracy of superposition

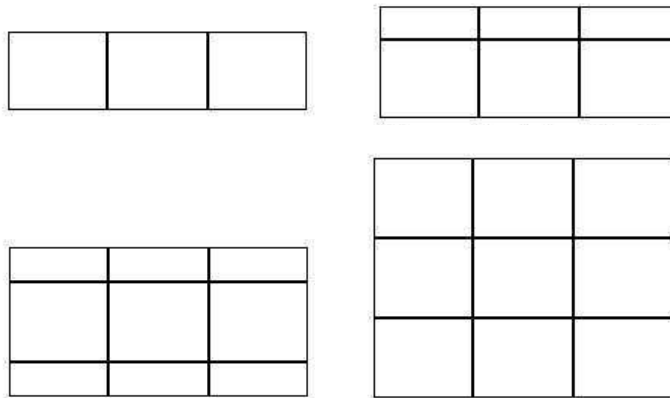


Figure 1. JPCP configurations considered in this research. Top left: single lane; top right: a lane confined at one longitudinal edge by shoulder (confined lane); bottom left: a lane confined at both longitudinal edges by shoulders (double confined lane); and bottom right: a lane confined by adjacent traffic lanes (full pavement).

of load and curling stresses. A full configuration of concrete pavement subjected to a combination of SADT and differential temperatures will then be studied. Effects of modulus of subgrade reaction and thickness of concrete slab on induced stress will subsequently be discussed. Results for different pavement configuration, namely, a single lane, a lane confined at one longitudinal edge by shoulder, a single lane confined at both longitudinal edges by shoulders and a single lane confined by adjacent traffic lanes called respectively in this paper a single lane, a confined lane, a double confined lane and full pavement (Figure 1) are evaluated and compared with those from existing research.

Results from the current study are also able to examine whether the findings of Packard and Tayabji [1985] and AASHTO [2003] can be extended when other axle groups, pavement configurations, curling and warping of concrete pavement and bonded or unbonded boundary conditions between concrete slab and base are considered.

2. Methodology

Diverse jointed plain concrete pavement (JPCP) configurations consisting of a single lane (top left in Figure 1), confined lane (top right), double confined lane (bottom left) and full pavement (bottom right) were analysed to determine the critical positions of the applied vehicular axle group loads on the pavement together with temperature curling effects. EverFE2.23 [Davids and Mahoney 1999] finite element program was employed in this study.

EverFE2.23 is a three dimensional finite element analysis software jointly developed by the universities of Maine and Washington to simulate the behaviour of jointed plain concrete pavements under axle group loads and environmental effects. This programme employs 20-noded quadratic solid elements, beam elements, shear spring and 8-noded dense liquid shell elements to simulate behaviour of concrete slab and base, dowels and tie bars, aggregate interlock and subgrade layers under applied loads respectively. This program is also able to simulate a tensionless property in the subgrade. This lets a separation occur between base and subgrade if the base curls.

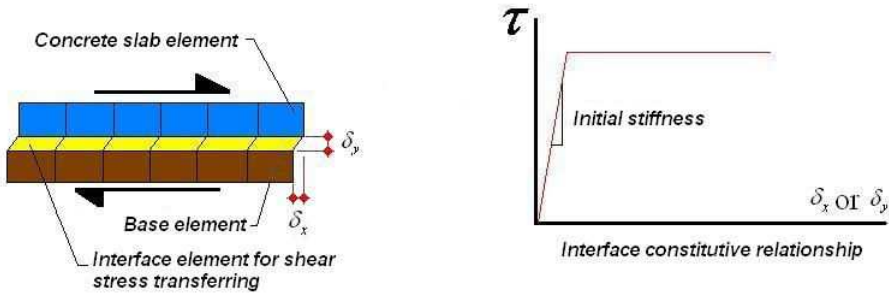


Figure 2. Schematic interface element behaviour and interface constitutive relationship [Davids and Wang 2003].

EverFE employs 16-noded zero thickness quadratic interface element for simulating the debonding layer between concrete slab and base. The element is capable to transfer the shear force between the concrete slab and the base. It is meshed in accordance with size of the mesh used in the concrete slab and the base. A bilinear constitutive relationship [Wimsatt et al. 1987; Wesevich et al. 1987] was considered to define the characteristics of the element under the applied load. Hence, the debonding layer can be defined by introducing initial distributed stiffness and slip displacement. Note that a free separation under tension occurs between the concrete slab and the base when unbonded boundary condition is selected. Figure 2 shows a schematic behaviour of the interface element used in the EverFE finite element program as well as the required information for its definition. Further information on this matter can be found elsewhere [Davids and Wang 2003].

In this study, distance between transverse joints and distance between longitudinal joints were considered to be 4600 mm and 3600 mm respectively. Tied shoulders with 1500 mm width [Austroads 2004] were considered. The slab thickness was considered to be 250 mm with modulus of elasticity and Poisson’s ratio of 28000 MPa and 0.2 respectively. A cement stabilized base of 150 mm thickness, 5000 MPa modulus of elasticity, and 0.2 Poisson’s ratio was considered beneath the slab and upon a subgrade with modulus of subgrade reaction of 0.03 MPa/mm (CBR ≈ 3.5). Transverse joints were doweled by eleven evenly spaced cylindrical bars having 32 mm diameter, 450 mm length and 1000 MPa dowel-slab support modulus. Tie bars with 13 mm diameter and 1000 mm length spaced at 1000 mm centre to centre were considered at longitudinal joints. The above mentioned values of the parameters are within the range recommended by [Austroads 2004]. These secure load transfer efficiency (LTE) of 95% in both transverse and longitudinal joints for bonded boundary condition and LTE of not less than 85% in

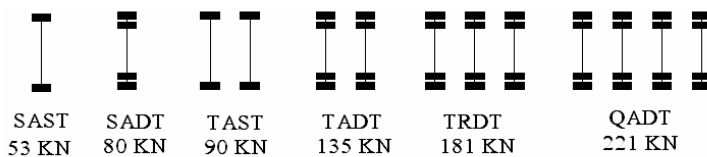


Figure 3. Axle groups type considered in this study based on [Austroads 2004].

transverse joint and 70% in longitudinal joints for unbonded boundary condition. Since information on behaviour of debonding layer provided in the literature did not lead to a specific conclusion, fully bonded and unbonded boundary conditions between concrete slab and base are taken into consideration in the current study to determine how provision of this layer as either bonded or unbonded affects concrete pavement responses.

In regards with effects of modulus of subgrade reaction and thickness of concrete slab on induced tensile stress of a curled pavement [Kuo 1998], different base thicknesses of 200, 250 and 300 mm and different modulus of subgrade reactions of 0.03, 0.05 and 0.07 MPa/mm were considered in a full pavement configuration.

SAST, SADT, TAST, TADT, TRDT, and QADT with average gross loads of 53 kN, 80 kN, 90 kN, 135 kN, 181 kN, and 221 kN (Figure 3) based on [Austroads 2004] were respectively applied as the vehicular loads at the centre, middle of the longitudinal edge and corner of the centre slab as shown in Figure 4. These load locations are respectively called a centre, mid-edge and corner loadings in this paper. A rectangular shaped tyre-pavement contact area based on the findings of Gillespie et al. [1992] was considered in the current study. Other assumptions for load configuration were as follows:

- Tyre inflation pressure: 750 kPa,
- Width-to-length ratio of tyre contact area: 0.7,
- Space between centre of dual tyres: 300 mm,
- Axle width: 1800 mm,
- Distance between axles in a given axle group 1250 mm.

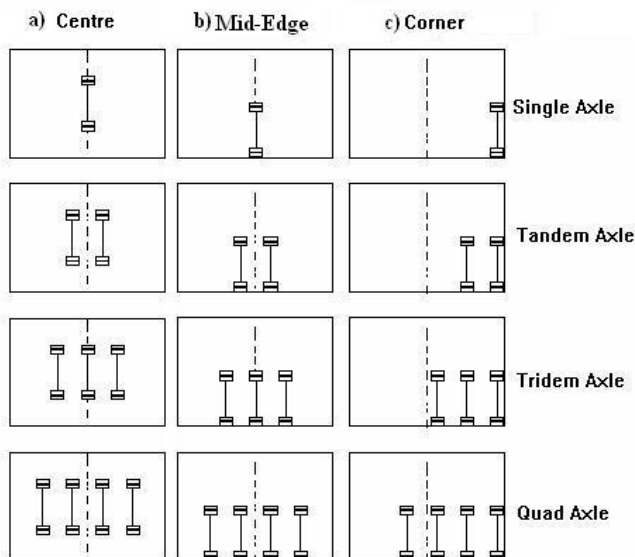


Figure 4. The position of applied loads for different axle groups on the centre concrete slab.

It should be noted that for those projects where valid statistical information on axle configuration are not available, research on critical axle group configurations [Darestani et al. \[2005\]](#) showed that the critical width-to-length ratio of tyre contact area is between 0.6 and 0.8 with average of 0.7, the critical distance between axles in a given axle group is between 1050 mm and 1150 mm with average of 1100 mm for all axle groups. In addition for TAST and TADT groups this value can also be between 1350 mm to 1450 mm with an average of 1400 mm. However, a value of 0.7 for width to length ratio of tyre contact area and 1250 mm distance between axles in a given axle group, as assumed by [Packard and Tayabji \[1985\]](#), have been chosen in the present study in order to compare present results with their results.

As high differential temperature (more than 25° C) would result in severe damage of unreinforced concrete slab of a normal thickness, linear differential temperature of -25° C (nighttime temperature) to 25° C (daytime temperature) were therefore considered between the top and the bottom surface layers of concrete slab. The concrete coefficient of thermal expansion was considered to be 1×10^{-5} mm/mm/° C.

3. Results and discussion

3.1. Axle group loadings. In the absence of differential temperature gradients, results of current study indicate that vehicular induced tensile stresses in unbonded concrete pavement due to mid-edge loading are greater than those from centre and corner loading for all pavement configurations when SAST, SADT, TAST and TADT are studied ([Figure 5](#)). In contrast, corner loading of QADT results in greater tensile stress than mid-edge loading for all pavement configurations. Corner loading of TRDT shows similar results for double confined lane. Furthermore, centre loading of QADT in double confined lane and full pavement configurations result in higher tensile stress than mid-edge loading.

Consideration of bonded boundary condition between concrete slab and base always results in lower tensile stress due to centre loading than other loading types ([Figure 6](#)). But, corner loading results in greater induced tensile stress than mid-edge loading for all axle groups except for SADT and SAST. This becomes predominant when traffic lane is confined by shoulders or adjacent traffic lanes.

Results of the current study reveal that the AASHTO recommendation [[AASHTO 2003](#)] is valid for fully unbonded boundary condition between concrete slab and base though this was not true for corner

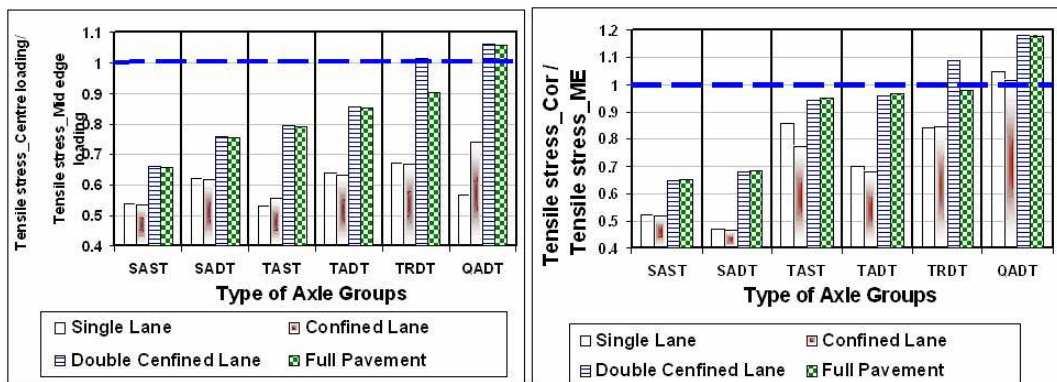


Figure 5. Vehicular induced stress in different pavement configurations for unbonded boundary condition.

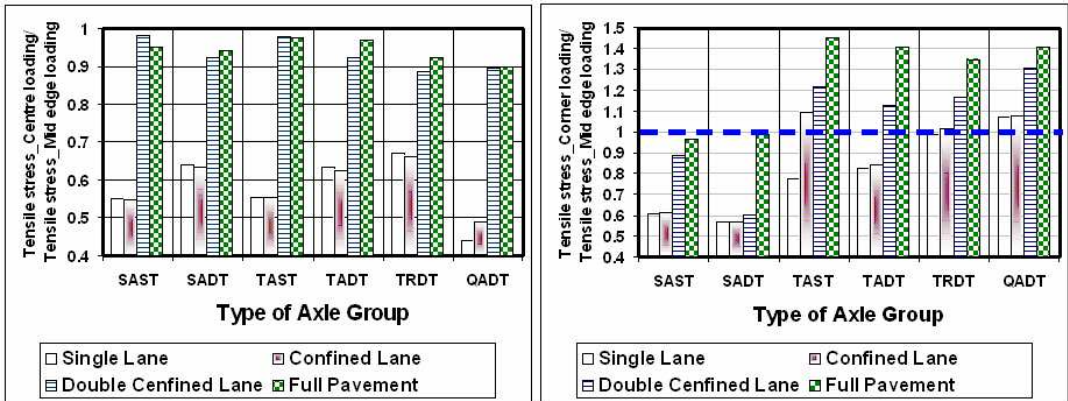


Figure 6. Vehicular induced stress in different pavement configurations for bonded boundary condition.

loading of SADT. While the bonded boundary condition is considered in the analysis, the AASHTO recommendation [AASHTO 2003] is not able to capture maximum vehicular induced tensile stress as induced tensile stresses in full pavement are greater than those tensile stresses produced in confined lane when vehicular loads are applied at the corner of the pavement (Figure 6).

As mentioned earlier, mid-edge loading was the critical loading case in research conducted by Packard and Tayabji [1985]. Results of the current study show that mid-edge loading, in the absence of differential temperature is the key factor for fatigue cracking of unbonded concrete pavements though this is not true for QADT. Corner loading results in greater vehicular induced tensile stress when fully bonded boundary condition is considered and TAST, TADT, TRDT and QADT are studied.

A comparison between vehicular induced stresses in bonded and unbonded boundary conditions between concrete slab and base shows that an unbonded boundary condition produces greater vehicular induced tensile stress in concrete pavement. This is due to loss of support in those locations of the concrete slab that were lifted-off. The minimum increase in the value of tensile stress is 30 per cent for corner loading of TRDT and the maximum increase is about 133 per cent for mid-edge loading of TAST. These results show that vehicular induced tensile stress is highly affected by the boundary condition between concrete slab and base.

3.2. Thermal induced stress. As mentioned earlier in this paper, the main reason for placing a friction reducer layer between concrete slab and base is to reduce the early age cracking in concrete slabs. Nevertheless, it plays a significant role in structural behaviour of concrete pavements during pavement life. As differential temperature and drying shrinkage tend to curl and warp concrete pavement, the location of neutral axis changes from its original location toward the top or the bottom surface layer of the concrete slab depending on the concrete slab curvature. Hence, the critical position of axle groups may be affected by consideration of environmental forces. For that purpose, daytime and nighttime differential temperature of 10° C and 25° C were considered in the current study.

Ongel and Harvey [2004] found that nighttime curling and warping are two reasons behind longitudinal cracking. Results of the current study show that the thermal tensile stress is at maximum along

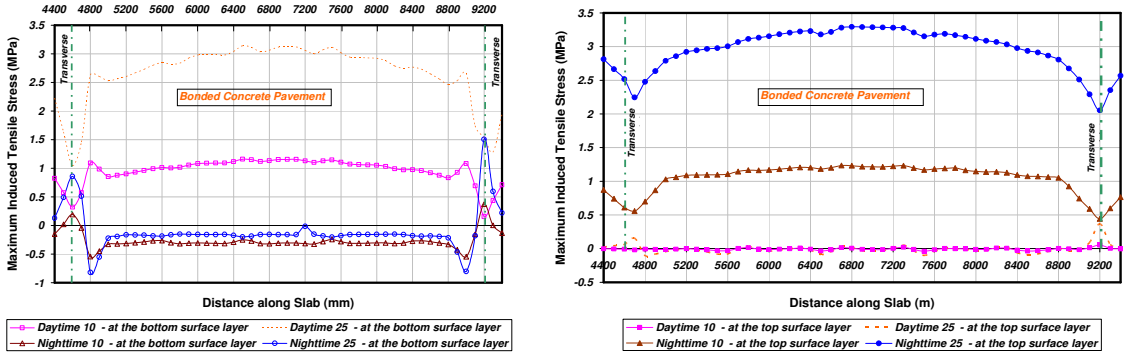


Figure 7. Curling induced stress in bonded concrete slab with full pavement configuration.

the longitudinal centreline of each traffic lane and decreases toward the edges of the traffic lane as expected. Furthermore, high daytime differential temperature results in bottom-up longitudinal cracking and consequently shall also be considered a reason for longitudinal cracking.

Figure 7 shows induced thermal stress at longitudinal joint along the wheel path for the centre panel of a full pavement configuration with the fully bonded boundary conditions between concrete slab and base. Figure 8 presents similar results for fully unbonded condition. In these Figures, Daytime and Nighttime represent daytime differential temperature and nighttime differential temperature, respectively. The number after Daytime or Nighttime indicates the absolute temperature difference between the top and the bottom surface layers of the concrete slab. For instance, Daytime 10 indicates a differential temperature between the top and the bottom surface layer of 10° C.

Results of the current study indicate nighttime temperature gradients produce greater tensile stress at the top surface layer of the concrete slab whereas daytime temperature gradients result in greater tensile stress at the bottom surface layer of the concrete slab as expected. When the top or the bottom surface layer of the pavement are individually studied, results indicate that daytime differential temperature may result in top-down cracking in the corner of the concrete slabs and bottom-up cracking at mid-edge of

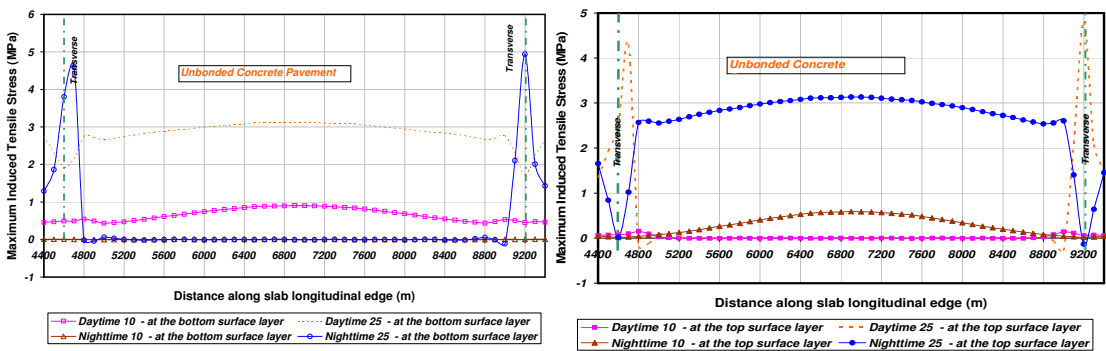


Figure 8. Curling induced stress in unbonded concrete slab with full pavement configuration.

the slab. Nighttime differential temperature, on the other hand, may produce bottom-up cracking in the corner of the slab and top-down cracking at the mid-edge of the slab.

In terms of absolute induced tensile stress, the critical location is mid-edge of the longitudinal joints for fully bonded boundary condition between concrete slab and base (Figure 7). In unbonded concrete pavement, however, the critical location depends on the magnitude of differential temperature. While concrete pavement is subjected to a low differential temperature, that is, 10° C, the middle of longitudinal joint is the critical location where the maximum thermal stress is produced. On the other hand, corner of the slab experiences greater tensile stress than mid-edge location when a higher differential temperature, i.e. 25° C, is considered (Figure 8).

When a single concrete slab is freely curled due to a differential temperature gradient and in the absence of the restraining factors such as subgrade and base resistant, vehicular loads and friction force at the interface of the concrete slab and base, a bending stress (flexural stress) is induced at the top or bottom surface layer of it due to its residual stiffness [Mohamed and Hansen 1997]. In this case, maximum induced tensile stress occurs at the centre of the slab and at the top surface layer during the day and at the bottom surface layer during the night. On the other hand, in the presence of the restraining factors another tensile stress will occur in the opposite sides of the residual tensile stress. In this condition, curling induced tensile stress occurs at the top surface layer of the concrete slab during nighttime and at the bottom surface layer of the concrete slab during daytime [Ongel and Harvey 2004].

Combination of these stresses together with the location of neutral axis in the concrete slab and provision of load transfer devices (dowels and tie bars) dictate a specific stress distribution in the slab depth. As it can be observed in Figure 8, the top surface layer of the concrete slab is subjected to tensile stress during nighttime and its bottom surface layer experiences greater tensile stress during daytime as expected. However, these statements are not valid in the area close to the transverse joints for unbonded concrete pavement subjected to high differential temperature. Provision of dowels in transverse joints tends to reverse concrete slab curvature in the area close to transverse joints. This consequently changes stress distribution regime in this area. For instance, the top surface layer of concrete slab is subjected to tensile stress if pavement is subjected to a nighttime differential temperature of 25° C. However, pavement curvature has to change in the area close to transverse joints due to availability of dowels. Hence, the top surface layer is subjected to compression stress. As a result, the magnitude of tensile stress at the top surface layer starts to decrease while the magnitude of tensile stress at the bottom layer increases. Consequently, the top and the bottom surface layers of the concrete slab are subjected to tensile stress at this area and finally form a transverse crack close to the transverse joints.

For the base dimensions selected, the critical location of thermal stress is at distance of about 400 mm from the transverse joints. Since this distance is a function of pavement length, varying the length by ± 2 metres may shift the location by ± 50 mm. This finding explains the reason behind the formation of transverse cracks commonly found near transverse joints. In addition to the finding by Ongel and Harvey [2004] (corner loading associated with nighttime curling and warping results in corner cracking), high daytime and nighttime differential temperature can also crack the concrete slab in the area close to transverse joints.

A comparison between thermal stresses in bonded pavement with those from unbonded pavement shows that unbonded boundary condition decreases the induced tensile stress when lower differential temperature is considered. In other words, the benefits offered by a consideration of the unbonded

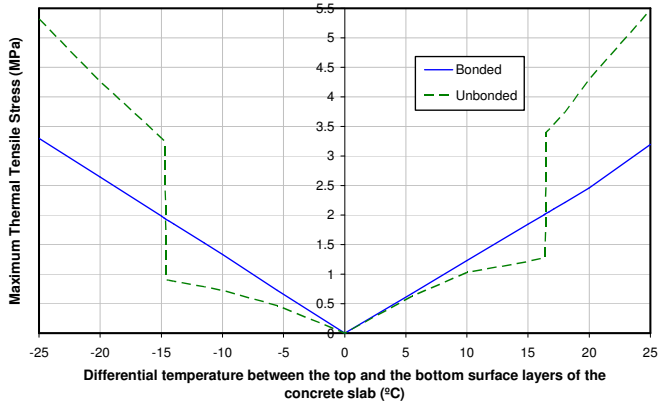


Figure 9. Comparison between thermal induced stresses for bonded and unbonded boundary conditions in single lane configuration.

boundary condition ceases at a certain value of differential temperature. Figure 9 shows an example of this finding in a single lane configuration. In this figure, negative values of differential temperature gradients represent nighttime differential temperatures and positive values represent daytime differential temperatures.

This finding suggests that with an increase in differential temperature, shear stress between slab and base increases until a full separation between concrete slab and base occurs. In this condition, the contact area between concrete slab and base rapidly decreases and consequently a significant bending stress is produced at the edge of the contact area. As a result, top-down corner cracking in upward curling or warping and bottom-up mid-slab transverse cracking in downward curling can be addressed by consideration of thermal induced stresses.

With regards to the significant effect of the boundary condition between concrete slab and base on induced thermal stress, Kuo's findings [Kuo 1998] will be modified as curling induced stress is affected by temperature differential, self-weight of concrete pavement, supported under concrete slab and boundary condition between concrete slab and base.

3.3. Combination of vehicular and thermal induced stresses. Information provided in Figure 9 indicates that the stress distribution in the concrete slab linearly changes with variations in differential temperatures in the presence of a fully bonded boundary condition between the concrete slab and the base. Similar results can be obtained in fully unbonded pavements subjected to a differential temperature greater than 16.5°C during daytime or lower than -14.5°C during nighttime. This suggests that accurate results can be expected when thermal induced stress at a certain location superimposed to vehicular induced stress at the same location. In the presence of fully unbonded boundary condition between the concrete slab and the base, however, the above mentioned consideration leads to inaccurate results when differential temperature during daytime and nighttime is lower than 16.5°C and greater than -14.5°C respectively, as the stress distribution in the above mentioned ranges seems to be nonlinear.

Figure 10 presents results of the current study for the bonded boundary condition between the concrete slab and the base when a full pavement configuration is subjected to temperature gradients of 10°C and

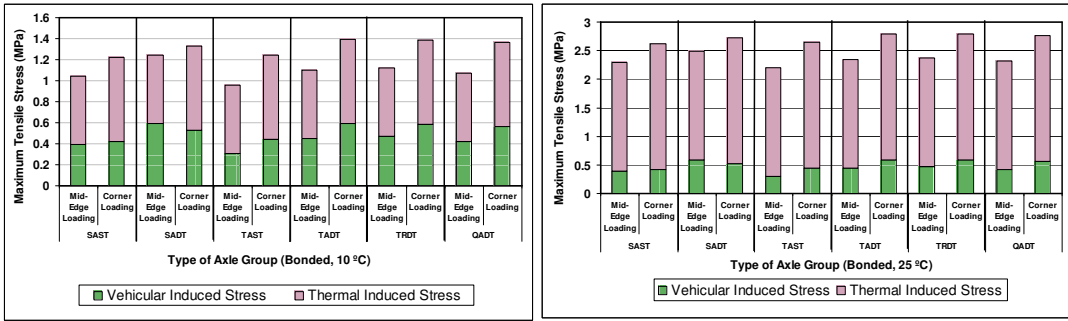


Figure 10. Vehicular and thermal induced tensile stresses in bonded concrete slab with full pavement configuration.

25° C. Vehicular induced tensile stresses for mid-edge and corner loadings have also been represented in this figure.

Results indicate that corner loading in the presence of thermal curling produces greater induced tensile stress than mid-edge loading if the bonded boundary condition is considered. In the unbonded boundary condition, higher differential temperatures change the critical location of axle groups toward an area close to the corner of the pavement (Figure 11). However, mid-edge loading results in greater induced tensile stress if pavement experiences lower differential temperatures.

Hiller and Roesler [2002] captured similar results when pavement was subjected to a nighttime differential temperature of 8.3° C which is very much lower than the differential temperature considered in the current study and moved the critical axle position from mid-edge toward corner of the concrete slab. This difference may be explained by taking into account the length of the pavement as 4.6 m in the current study and 5.8 m in the work of Hiller and Roesler [2002]. An increase in the pavement length increases the magnitude of shear stress between concrete slab and base or subgrade (in the absence of base) and consequently increases thermal induced stress. Consequently, the possibility of separation between layers in lower differential temperature increases. Hence, the aforementioned finding can be revised as corner loading will result in greater tensile stress than mid-edge loading if a separation due to environmental force occurs between concrete slab and base.

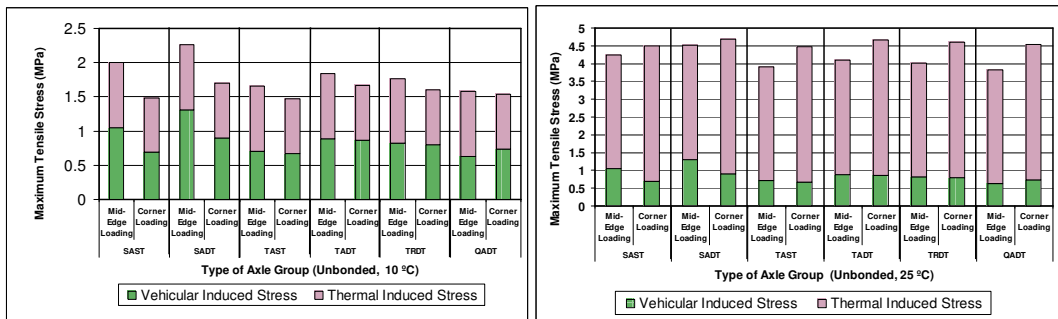


Figure 11. Vehicular and thermal induced tensile stresses in unbonded concrete slab with full pavement configuration.

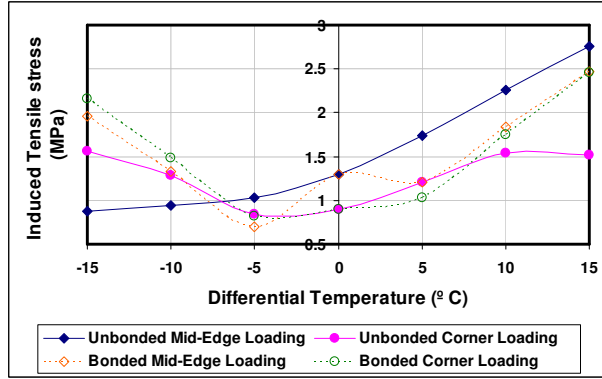


Figure 12. Combination of vehicular and thermal induced tensile stresses in a full pavement configuration subjected to SADT.

Since superposition law is not accurate enough when an unbonded pavement is subjected to small variation of temperature gradients, a full pavement configuration was examined for corner and mid-edge loadings together with differential temperature for better understanding of pavement behaviour under vehicular load and low or moderate differential temperature. SADT was considered in the analysis. Figure 12 compares thermal and vehicular induced tensile stresses due to mid-edge loading with the corresponding stresses of corner loading for bonded and unbonded pavements.

Results indicate that corner loading during nighttime produces greater tensile stresses than mid-edge loading in bonded concrete slab. By contrast, mid-edge loading during daytime results in greater tensile stress than corner loading. Nevertheless, corner loading is the critical loading condition when differential temperature exceeds 15°C. In fully unbonded pavement, on the other hand, mid-edge loading result in greater tensile stress than corner loading when a differential temperature greater than -5°C is considered. Further decrease in differential temperature results in greater tensile stresses in corner loading than mid-edge loading.

These can be explained by taking the pavement curvature into consideration. During daytime, thermal induced tensile stress similar to vehicular induced stress occurs at bottom surface layer of the slab with a maximum at mid-edge. As a result, mid-edge loading produces greater tensile stresses than corner loading regardless of boundary condition between concrete slab and base. However, further increase in differential temperature tends to lift-off the centre of the slab. As a result, a greater tensile stress at the bottom surface layer of the slab occurs due to corner loading than mid-edge loading. Note that provision

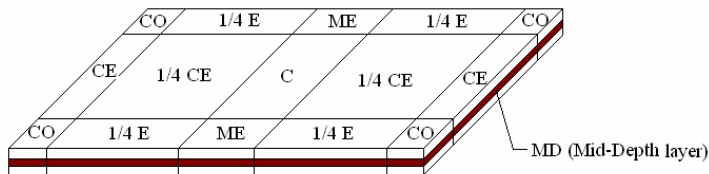


Figure 13. Information on location of fatigue cracking (see also Table 1).

of dowels at transverse joints together with slab weight results in a bending stress in the same direction of induced stress due to corner loading in daytime curling.

While nighttime differential temperature tend to lift-off transverse edges of the concrete slab, corner loading presses down the slab edge to return it to its original location. Consequently, tensile stress occurs at a location close to transverse joint and at the top surface layer of the slab due to cantilever action of the slab.

Crack location within the concrete slab is affected by vehicular loading conditions (corner, centre and mid-edge) and differential temperatures. To efficiently determine crack locations in concrete slab, the centre slab was divided into six areas (Figure 13). Table 1 presents the critical locations of concrete slab for fatigue cracking in a full pavement configuration subjected to combination of SADT and differential temperatures.

Interestingly, high differential temperatures result in joint faulting irrespective of the vehicular loading conditions and boundary conditions between the concrete slab and the base. This indicates that the finding of Ongel and Harvey [2004] – daytime and nighttime differential temperatures result in bottom-up and top-down cracking, respectively – is correct for a differential temperature lower than 15°C during daytime and greater than -15°C during nighttime. Furthermore, corner, centre and mid-edge loadings can result in different types of fatigue failure of the concrete slab depending on differential temperature.

These can be summarised as follows:

- While an unbonded pavement experiences a daytime differential temperature lower than 15°C , the maximum stress always occurs at the bottom surface layer of the slab where the vehicular load is applied.
- While an unbonded pavement experiences a nighttime differential temperature greater than -15°C ,
 - centre loading results in top-down cracking at the corner or an area between corner and mid-edge areas,
 - mid-edge loading results in top-down cracking at the location between corner and mid-edge areas,
 - corner loading results in top-down longitudinal cracking passing along the centre area of the slab.
- While a bonded pavement experiences daytime differential temperature lower than 10°C , the maximum stress always occurs at the bottom surface layer of the slab where the vehicular load is applied.
- While a bonded pavement experiences nighttime differential temperature greater than -15°C ,
 - centre loading results in longitudinal top-down cracking of the slab,
 - mid-edge loading results in mid-edge bottom-up transverse cracking,
 - corner loading results in top-down transverse cracking at a location between corner and mid-edge areas.

As mentioned earlier, Hiller and Roesler [2005] indicated that the nighttime differential temperature results in mid-edge top-down cracking. Results of the current study, however, indicate that this is not true when pavement experiences nighttime differential temperature lower than -20°C as joint faulting becomes the critical damage of concrete pavements in this case. Buch et al. [2004] mentioned that mid-edge and corner loadings result in bottom-up and top-down cracking respectively. Nevertheless, results

Slab thickness = 250 mm Modulus of subgrade reaction = 0.03 MPa/mm Axle group load = SADT		Temperature (°C)	Centre Loading	Mid-edge Loading	Corner Loading
	Daytime	25	<i>CE at MD</i>	<i>CE at MD</i>	<i>CO at MD</i>
		20	<i>CE at MD</i>	<i>CE at MD</i>	<i>CO at MD</i>
		15	<i>UW at B</i>	<i>ME at B</i>	<i>CO at B</i>
		10	<i>UW at B</i>	<i>ME at B</i>	<i>CO at B</i>
		5	<i>UW at B</i>	<i>ME at B</i>	<i>CO at B</i>
Unbonded		0	<i>UW at B</i>	<i>ME at B</i>	<i>CO at B</i>
	Nighttime	-5	<i>CO at T</i>	<i>1/4E at T</i>	<i>C at T</i>
		-10	<i>1/4E at T</i>	<i>1/4E at T</i>	<i>C at T</i>
		-15	<i>1/4E at T</i>	<i>1/4E at T</i>	<i>C at T</i>
		-20	<i>CO at MD</i>	<i>CO at MD</i>	<i>CO at MD</i>
		-25	<i>CO at MD</i>	<i>CO at MD</i>	<i>CO at MD</i>
	Daytime	25	<i>CO at MD</i>	<i>CO at MD</i>	<i>CE at MD</i>
		20	<i>CE at MD</i>	<i>CO at MD</i>	<i>CO at MD</i>
		15	<i>CE at MD</i>	<i>ME at B</i>	<i>CE at B</i>
		10	<i>UW at B</i>	<i>ME at B</i>	<i>CO at B</i>
		5	<i>UW at B</i>	<i>ME at B</i>	<i>CO at B</i>
Bonded		0	<i>UW at B</i>	<i>ME at B</i>	<i>CE at B</i>
	Nighttime	-5	<i>UW at B</i>	<i>ME at B</i>	<i>1/4E at T</i>
		-10	<i>C at T</i>	<i>ME at B</i>	<i>1/4E at T</i>
		-15	<i>C at T</i>	<i>ME at B</i>	<i>1/4E at T</i>
		-20	<i>CO at MD</i>	<i>CO at MD</i>	<i>CO at MD</i>
		-25	<i>CO at MD</i>	<i>CO at MD</i>	<i>CO at MD</i>

Table 1. Critical location of fatigue cracking in full pavement model due to different differential temperatures and SADT. Here, *UW*: under wheel; *B*: bottom surface layer; *T*: top surface layer; *CE*: centre area of transverse edge; *MD*: mid-depth Layer; *CO*: corner; *C*: centre area of the slab; *ME*: middle of the longitudinal edge; and *1/4E*: area at longitudinal edge between mid-edge and corner. See also [Figure 13](#).

of the current study show that mid-edge loading results in bottom-up cracking in the absence of nighttime differential temperatures or in the presence of daytime differential temperature lower than 15° C. In the presence of nighttime differential temperature, mid-edge loading can results in top-down cracking at the slab edge or joint faulting (Table 1). Furthermore, corner loading results in top-down cracking in the absence of daytime differential temperature or in the presence of nighttime differential temperature

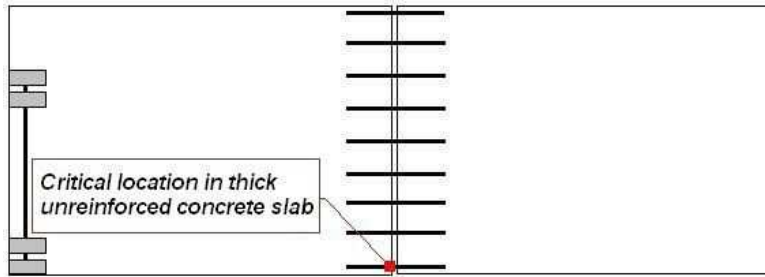


Figure 14. Position of the critical location in thick unreinforced concrete pavement.

lower than -20°C . In the presence of daytime differential temperature, corner loading results in bottom-up cracking at the corner. It should be noted that reasons behind joint faulting are presented later in this paper when effect of concrete slab thickness on pavement response is discussed.

Since [Austroads 2004] restricts the maximum distance between transverse joints in unreinforced concrete slab to 4600 mm, a separation between concrete slab and base in the absence of vehicular loads occurs when a differential temperature close to what presented in Figure 8 is considered. Vehicular loads can increase or decrease the critical value of differential temperature depending on position of vehicular loads and nature of differential temperature (daytime or nighttime).

Results of Hiller and Roesler [2002] were developed for unbonded boundary condition between concrete slab and base. Kuo's recommendation [Kuo 1998] is also valid for a certain range of differential temperatures and only unbonded boundary condition as mid-edge loading results in greater tensile stress than corner loading when lower nighttime differential temperature is considered or no separation occurs between concrete slab and base.

A comparison between induced tensile stresses in bonded and unbonded boundary conditions reveals that the unbonded boundary condition between concrete slab and base requires careful consideration when pavement is constructed in hot or cold weather where high differential temperature gradients may be produced in the concrete depth.

3.4. Effects of slab thickness on induced tensile stress. To find how slab thickness affects the results of the current study, a full pavement configuration subjected to different daytime and nighttime differential temperature gradients together with corner and mid-edge loadings was considered. Both bonded and unbonded boundary conditions were taken into account. Table 2 shows results of the current study for maximum induced tensile stress when modulus of subgrade reaction was held constant and SADT was applied on the centre concrete slab panel as either corner loading or mid-edge loading.

Results indicate that an increase in thickness of concrete slab decreases the magnitude of induced tensile stress regardless of boundary condition between concrete slab and base as mentioned by Buch et al. [2004]. However, the use of thicker concrete slab (300 mm thickness) associated with higher differential temperature (15°C) rapidly increases the value of induced tensile stress at mid-depth of the concrete slab for a node in unloaded transverse joint and close to the corner of the concrete slab (Figure 14). This can be explained by taking into account the concrete slab curvature together with location of axle group upon pavement.

Modulus of Subgrade Reaction = 0.03 MPa/mm Axle group load = SADT			Temperature (°C)	Slab Thickness (mm)		
				200	250	300
Unbonded	Corner loading	Daytime	5	1.627	1.213	0.876
			10	1.944	1.544	1.32
			15	2.172	1.52	4.52
		Nighttime	5	1.02	0.846	0.685
			10	1.6	1.282	1.009
			15	2.038	1.56	3.623
	Mid-edge loading	Daytime	5	2.296	1.744	1.333
			10	2.938	2.257	1.724
			15	3.514	2.758	2.044
		Nighttime	5	1.351	1.028	0.803
			10	1.328	0.945	0.704
			15	1.351	0.881	3.381
Bonded	Corner loading	Daytime	5	1.206	1.028	0.897
			10	2.025	1.745	1.524
			15	2.845	2.46	2.14
		Nighttime	5	0.922	0.825	0.722
			10	1.659	1.489	1.305
			15	2.404	2.16	1.9
	Mid-edge loading	Daytime	5	1.4	1.211	1.027
			10	2.12	1.837	1.557
			15	2.841	2.465	2.086
		Nighttime	5	0.839	0.703	0.623
			10	1.566	1.332	1.13
			15	2.298	1.965	1.674

Table 2. Effect of concrete slab thickness on maximum induced stress (MPa) due to different differential temperatures and SADT. Highlighted values occur very close to the corner of loaded concrete slab and at the middle of the concrete slab depth.

A downward curvature is produced during daytime temperature gradients. Corner loading associated with thermal curvature results in an increase in the area of separation between concrete slab and base toward the unloaded corners of the base. It ultimately induces a lifting-off at unloaded corners of the concrete slab. While thinner concrete slab is considered, the unloaded transverse edge of the concrete slab lifts off. In this case, induced bending stresses for transferring the weight of adjacent concrete panel are divided equally between all dowels located in unloaded transverse joint. Consequently, induced stress

at interface of dowel and concrete remains in the normal range. On the other hand, thicker concrete slab results in nonuniform lift-off of unloaded corners which ultimately induce higher bending stress in that dowel located close to lifted-off corner. Mid-edge loading, on the other hand, alleviates the severity of the problem.

Nighttime temperature results in upward curvature. Both corner and mid-edge loadings together with nighttime temperature enhanced the magnitude of induced stress in thick concrete pavement as describes above. This finding suggests a particular dowel arrangement at corner of the concrete slab or a maximum slab thickness that shall be considered in the design of unreinforced concrete pavement.

Hiller and Roesler [2002] showed that a change in the thickness of the concrete slab changes the magnitude of induced stresses due to corner and mid-edge loadings uniformly. However, results of the current study indicate a nonuniform change between corner loading and mid-edge loading induced stresses. For instance, the proportion of induced tensile stress due to corner loading to induced tensile stress due to mid-edge loading, when unbonded pavement is subjected to a nighttime differential temperature of 10°C , is 1.205, 1.357 and 1.433 for slab thickness of 200 mm, 250 mm and 300 mm respectively.

3.5. Effects of modulus of subgrade reaction on induced tensile stress. To determine effects of modulus of subgrade reaction on the results of the current study, a full pavement configuration was subjected to different daytime and nighttime differential temperature gradients together with corner and mid-edge loadings. Both bonded and unbonded boundary conditions were taken into account. Table 3 shows results of the current study for maximum induced tensile stress when concrete slab thickness was held constant and SADT was applied on the centre concrete slab panel as either corner loading or mid-edge loading.

Results shows that modulus of subgrade reaction has different effects on the pavement response when daytime or nighttime differential temperature, corner or mid-edge loading, and unbonded or bonded boundary condition between concrete slab and base are considered.

An increase in modulus of subgrade reaction in the presence of nighttime temperature increases the magnitude of induced tensile stresses in most case studies. This is compatible with the statement of Buch et al. [2004]. In contrast, induced tensile stresses in the bonded pavement and in the presence of daytime differential temperatures decrease when modulus of subgrade reaction is increased and SADT is applied at the corner of the concrete slab. An increase in modulus of subgrade reaction associate with higher daytime differential temperatures and mid-edge loading increases the magnitude of induced tensile stress regardless of boundary condition between concrete slab and base. In some cases such as when the unbonded pavement is subjected to daytime differential temperature and mid-edge loading, modulus of subgrade reaction has no effect on maximum induced tensile stress as axle load induced stress is in negative direction of thermal induced tensile stress.

Hiller and Roesler [2002] showed that an increase in modulus of subgrade reaction in the presence of nighttime differential temperature of 8.3°C increases the proportion of corner loading induced stress to mid-edge loading induced stress. Results of the current study for unbonded pavement subjected to nighttime differential temperature of 10°C shows similar result.

Slab thickness = 250 mm Axle group load = SADT			Temperature (°C)	Modulus of Subgrade Reaction (MPa/mm)		
				0.03	0.05	0.07
Unbonded	Corner loading	Daytime	5	1.213	1.18	1.2
			10	1.544	1.413	1.458
			15	1.52	1.58	1.649
		Nighttime	5	0.846	1.18	0.924
			10	1.282	1.377	1.434
			15	1.56	1.58	1.757
	Mid-edge loading	Daytime	5	1.744	1.686	1.632
			10	2.257	2.31	2.329
			15	2.758	2.781	2.853
		Nighttime	5	1.028	0.847	0.751
			10	0.945	0.791	0.826
			15	0.881	0.895	1.007
Bonded	Corner loading	Daytime	5	1.028	0.967	0.946
			10	1.745	1.651	1.581
			15	2.46	2.234	2.248
		Nighttime	5	0.825	0.848	0.864
			10	1.489	1.543	1.586
			15	2.16	2.248	2.315
	Mid-edge loading	Daytime	5	1.211	1.198	1.197
			10	1.837	1.859	1.885
			15	2.465	2.519	2.573
		Nighttime	5	0.703	0.705	0.709
			10	1.332	1.345	1.372
			15	1.965	2.015	2.075

Table 3. Effect of modulus of subgrade reaction on maximum induced stress (MPa) due to different differential temperatures and SADT.

4. Conclusions

Critical positions of different axle groups in uncurled and curled jointed concrete pavement with different configurations were studied. Results of the current study indicate that AASHTO recommendation [AASHTO 2003] -except for SADT-and results of Packard and Tayabji [1985] -except for QADT- are valid for the fully unbonded boundary condition between concrete slab and base and uncurled pavement. Results of the current study also show that pavement performance under combinations of vehicular loads

and differential temperatures is significantly affected by boundary condition between concrete slab and base.

The reasons behind longitudinal, transverse and corner cracking were addressed. The significant findings in this area were (i) corner loading is critical when there is a bonded boundary condition between concrete slab and base (ii) corner loading is also critical when a separation due to environmental forces occurs between the unbonded concrete slab and base. Furthermore, the benefits offered by consideration of the unbonded boundary condition cease at a certain value of differential temperature. Hence, a particular care needs to be given to those pavement projects constructed in hot or cold weather where high differential temperature gradients may be produced in concrete depth. Moreover, corner, centre and mid-edge loadings can result in different types of fatigue failure of the concrete slab depending on differential temperature.

There is an inverse relationship between induced tensile stress and thickness of concrete slab so that an increase in thickness of concrete slab decreases the magnitude of induced tensile stress. However, a maximum slab thickness or dowel arrangement at corners of the slab shall be considered in unreinforced concrete pavement as thicker slabs are sensitive to high differential temperature together with axle loading. An increase in modulus of subgrade reaction can increase or decrease the magnitude of tensile stress depending on boundary condition between concrete slab and base, corner or mid-edge loading and daytime or nighttime differential temperature.

Acknowledgment

Thanks are expressed to Glenn Carson for helping with project planning and execution.

References

- [AASHTO 2003] AASHTO, "Appendix QQ (Structural response models for rigid pavements) of guide for mechanistic-empirical design of new and rehabilitated pavement structures", Technical report, Transportation Research Board-National Research Council, ARA Inc., Illinois, U. S. A., 2003. Prepared for National Cooperative Highway Research Program.
- [Austroads 2004] Austroads Inc., *AUSTROADS pavement design guide*, Sydney, Australia: Austroads Inc., 2004.
- [Bradbury 1938] R. D. Bradbury, "Reinforced concrete pavement", Technical report, Wire Reinforcement Institute, Washington D.C., 1938. 34–41.
- [Buch et al. 2004] N. Buch, D. Gilliland, T. Van Dam, and V. K., "A parametric mechanistic evaluation of PCC cross-section using ISLAB2000", Final report, Michigan Department of Transportation, Lansing, MI, 2004.
- [Byrum and Hansen 1994] C. R. Byrum and W. Hansen, "Influence Function Approach to Analysis of Jointed Portland Cement Concrete Pavement", Technical report 1449, Transportation Research Record, TRB, Washington, 1994. 148–158.
- [Choubane and Tia 1995] B. Choubane and M. Tia, "Analysis and verification of thermal-gradient effects on concrete pavement", *J. Transp. Eng.* **121**:1 (1995), 75–81.
- [Darestani et al. 2005] M. Y. Darestani, D. T. Thambiratnam, A. Nataatmadja, and D. Baweja, "Sensitivity analysis of the structural response of rigid pavement to vehicular loads", pp. 17–32 in *Smart systems, postgraduate research conference*, Brisbane, Australia, 15 December 2005.
- [Darter et al. 1995] M. I. Darter, K. T. Hall, and C. M. Kuo, "Support under portland cement concrete pavement", Technical report Rep. 372, Transportation Research Board, National Research Council, Washington D.C., 1995. National Cooperative Highway Research Program.

- [Davids and Mahoney 1999] W. G. Davids and J. P. Mahoney, "Experimental verification of rigid pavement joint load transfer modelling with EverFE", Technical report 1968, Transportation Research Record, 1999. 81–88.
- [Davids and Wang 2003] W. G. Davids and Z. Wang, "3D finite element analysis of jointed plain concrete pavement with EverFE2.2", Technical report, Transportation Research Board, 2003. Annual Meeting CD-ROM.
- [Gillespie et al. 1992] T. D. Gillespie, S. M. Karamlhas, D. Cebon, M. W. Sayers, M. A. Nasim, W. Hansen, and N. Ehsan, "Effects of heavy vehicle characteristics on pavement response and performance", Final report, National Cooperative Highway Research Program- Transportation Research Board-National Research Council, The University of Michigan Transportation Research Institute, Michigan, U. S. A., 1992.
- [Heath and Roesler 1999] A. C. Heath and J. R. Roesler, "Shrinkage and thermal cracking of fast setting hydraulic cement concrete pavements in palmdale", Preliminary report, California Department of Transportation, California, 1999.
- [Heath et al. 2003] A. C. Heath, J. R. Roesler, and J. T. Harvey, "Modelling longitudinal, corner and transverse cracking in jointed concrete pavements", *Int. J. Pavement Eng.* **4**:1 (2003), 51–58.
- [Hiller and Roesler 2002] E. J. Hiller and J. R. Roesler, "Transverse joint analysis for mechanistic-empirical design of rigid pavements", Technical report 1809, Transportation Research Record, 2002. 42–51.
- [Hiller and Roesler 2005] J. E. Hiller and J. R. Roesler, "determination of critical concrete pavement fatigue damage locations using influence lines", *J. Transp. Eng.* **131**:8 (2005), 599–607.
- [Ioannides and Khazanovich 1998] A. M. Ioannides and L. Khazanovich, "Nonlinear temperature effects on multilayered concrete pavements", *J. Transp. Eng.* **124**:2 (1998), 128–136.
- [Kuo 1998] C. M. Kuo, "Effective temperature differential in concrete pavements", *J. Transp. Eng.* **124**:2 (March/April 1998), 112–116.
- [Liang and Niu 1998] R. Y. Liang and Y. Z. Niu, "Temperature and curling stress in concrete pavements: analytical solutions", *J. Transp. Eng.* **124**:1 (1998), 91–100.
- [Mohamed and Hansen 1997] A. R. Mohamed and W. Hansen, "Effect of nonlinear temperature gradients on curling stress in concrete pavements", Technical report 1568, Transportation Research Record, 1997. 65–71.
- [Ongel and Harvey 2004] A. Ongel and J. Harvey, "Analysis of 30 years of pavement temperature using the enhanced integrated climate model (EICM)", Draft report, California Department of Transportation, 2004.
- [Packard and Tayabji 1985] R. G. Packard and S. D. Tayabji, "New PCA thickness design procedure for concrete highway and street pavements", pp. 225–236 in *Concrete Pavement & Rehabilitation Conference*, Purdue, USA, 1985.
- [Reddy et al. 1963] A. Reddy, G. A. Leonards, and M. E. Harr, "Warping stress and deflections in concrete pavements, Part III", Highway Research Report 44, HRB, National Research Council, Washington D.C., 1963.
- [Richardson and Armaghani 1990] M. Richardson and J. M. Armaghani, "Stress caused by temperature gradient in Portland cement concrete pavements", Technical report 1121, Transportation Research Record, 1990. 7–13.
- [Shoukry et al. 2002] A. N. Shoukry, G. W. William, and M. Riad, "Characteristics of concrete contact stresses in doweled transverse joints", *Int. J. Pavement Eng.* **3**:2 (2002), 117–129.
- [Tarr et al. 1999] S. M. Tarr, P. A. Okamoto, M. H. Sheehan, and R. G. Packard, "Bond interaction between concrete pavement and lean concrete slab", Technical report 1668, Transportation Research Record, 1999. 9–17.
- [Totsky 1981] O. N. Totsky, "Behavior of multi-layered plates on Winkler foundation", *Stroitel'naya Mekhanika i Raschet Sooruzhenii* **6** (1981), 54–58. in Russian.
- [Wesevich et al. 1987] J. W. Wesevich, B. F. McCullough, and N. H. Burns, "Stabilised subbase friction study for concrete pavements", Research Report 459-1, Centre for Transportation Research, University of Texas, Austin, USA, 1987.
- [Westergaard 1926] H. M. Westergaard, "Analysis of stress in concrete pavements due to variations of temperature", pp. 201–205 in *Proc., 6th Ann. Meeting*, Washington D.C., 1926.
- [Wimsatt et al. 1987] A. W. Wimsatt, B. F. McCullough, and N. H. Burns, "Methods of analysing and influencing frictional effects of subbase", Research Report 459-2F, Centre for Transportation Research, University of Texas, Austin, USA, 1987.

[Yu et al. 1998] H. T. Yu, L. Khazanovich, M. I. Darter, and A. Ardani, "Analysis of concrete pavement responses to temperature and wheel loads measured from instrumented slabs", Technical report 1639, Transportation Research Record, 1998. 94–101.

Received 28 Aug 2006. Accepted 14 Dec 2007.

MOSTAFA YOUSEFI DARESTANI: m.yousefi@qut.edu.au

School of Urban Development, Queensland University of Technology, 2 George Street, Brisbane, QLD 4001, Australia

DAVID P. THAMBIRATNAM: d.thambiratnam@qut.edu.au

School of Urban Development, Queensland University of Technology, 2 George Street, Brisbane, QLD 4001, Australia

ANDREAS NATAATMADJA: a.nataatmadja@qut.edu.au

School of Urban Development, Queensland University of Technology, 2 George Street, Brisbane, QLD 4001, Australia

DAKSH BAWEJA: dbaweja@readymix.com.au

Rinker Australia, Tower B, Level 8, 799 Pacific Highway, Chatswood, NSW 2067, Australia

SUBMISSION GUIDELINES

ORIGINALITY

Authors may submit manuscripts in PDF format on-line. Submission of a manuscript acknowledges that the manuscript is *original and has neither previously, nor simultaneously, in whole or in part, been submitted elsewhere*. Information regarding the preparation of manuscripts is provided below. Correspondence by email is requested for convenience and speed. For further information, write to:

[Marie-Louise Steele](#)
Division of Mechanics and Computation
Durand Building, Room 262
Stanford University
Stanford CA 94305

LANGUAGE

Manuscripts must be in English. A brief abstract of about 150 words or less must be included. The abstract should be self-contained and not make any reference to the bibliography. Also required are keywords and subject classification for the article, and, for each author, postal address, affiliation (if appropriate), and email address if available. A home-page URL is optional.

FORMAT

Authors are encouraged to use L^AT_EX and the standard article class, but submissions in other varieties of T_EX, and, exceptionally in other formats, are acceptable. Electronic submissions are strongly encouraged in PDF format only; after the refereeing process we will ask you to submit all source material.

REFERENCES

Bibliographical references should be listed alphabetically at the end of the paper and include the title of the article. All references in the bibliography should be cited in the text. The use of B^IB_T_EX is preferred but not required. Tags will be converted to the house format (see a current issue for examples), however, in the manuscript, the citation should be by first author's last name and year of publication, e.g. "as shown by Kramer, et al. (1994)". Links will be provided to all literature with known web locations and authors are encouraged to provide their own links on top of the ones provided by the editorial process.

FIGURES

Figures prepared electronically should be submitted in Encapsulated PostScript (EPS) or in a form that can be converted to EPS, such as GnuPlot, Maple, or Mathematica. Many drawing tools such as Adobe Illustrator and Aldus FreeHand can produce EPS output. Figures containing bitmaps should be generated at the highest possible resolution. If there is doubt whether a particular figure is in an acceptable format, the authors should check with production by sending an email to:

production@mathscipub.org

Each figure should be captioned and numbered so that it can float. Small figures occupying no more than three lines of vertical space can be kept in the text ("the curve looks like this:"). It is acceptable to submit a manuscript with all figures at the end, if their placement is specified in the text by means of comments such as "Place Figure 1 here". The same considerations apply to tables.

WHITE SPACE

Forced line breaks or page breaks should not be inserted in the document. There is no point in your trying to optimize line and page breaks in the original manuscript. The manuscript will be reformatted to use the journal's preferred fonts and layout.

PROOFS

Page proofs will be made available to authors (or to the designated corresponding author) at a web site in PDF format. Failure to acknowledge the receipt of proofs or to return corrections within the requested deadline may cause publication to be postponed.

Journal of Mechanics of Materials and Structures

Volume 3, N^o 3 March 2008

- An extended mechanical threshold stress plasticity model: modeling 6061-T6 aluminum alloy**
BISWAJIT BANERJEE AND ANUP SATISH BHAWALKAR 391
- The effect of taper on section constants for in-plane deformation of an isotropic strip**
DEWEY H. HODGES, JIMMY C. HO AND WENBIN YU 425
- On large deformation generalized plasticity** VASSILIS P. PANOSKALTSIS, LAZAROS C.
POLYMENAKOS AND DIMITRIS SOLDATOS 441
- Advanced postbuckling and imperfection sensitivity of the elastic-plastic Shanley–Hutchinson model column**
CLAUS DENCKER CHRISTENSEN AND ESSEN BYSKOV 459
- Rolling contact with slip on a thermoelastic half-space: comparison with perfect rolling contact**
LOUIS MILTON BROCK 493
- A variational deduction of second gradient poroelasticity: part I — general theory** GIULIO
SCIARRA, FRANCESCO DELL’ISOLA, NICOLETTA IANIRO AND ANGELA MADEO 507
- Estimation of parameters of a three-layered sandwich beam** NILSON BARBIERI, RENATO
BARBIERI, LUIZ CARLOS WINIKES AND LUIS FERNANDO ORESTEN 527
- Extended displacement discontinuity method for crack analysis in three-dimensional two-phase transversely isotropic magnetoelectroelastic media**
MINGHAO ZHAO, NA LI, CUIYING FAN AND TONG LIU 545
- Influence of vehicular positions and thermal effects on structural behaviour of concrete pavement** MOSTAFA YOUSEFI DARESTANI, DAVID P. THAMBIRATNAM, ANDREAS
NATAATMADJA AND DAKSH BAWEJA 567